Contribution to numerical and experimental studies of flutter in space turbines : aerodynamic analysis of subsonic and supersonic flows in response to a prescribed vibratory mode of the structure

Hakim Ferria

KTH Industrial Engineering and Management

ÉCOLE CENTRALE LYON

N° d'ordre : 2011-02

Doctoral Thesis in Fluid Mechanics

presented for the award of degree of

Doctor of Philosophy

Ecole Centrale de Lyon (France) and Kungliga Tekniska Högskolan (Sweden)

prepared jointly at the Laboratoire de Mécanique des Fluides et d'Acoustique - UMR 5509, and the Heat and Power Technology Division

by

Hakim FERRIA

Contribution to Numerical and Experimental Studies of Flutter in Space Turbines. Aerodynamic Analysis of Subsonic or Supersonic Flows in Response to a Prescribed Vibratory Mode of the Structure.

Publicly defended on the first of February, 2011 at Ecole Centrale de Lyon

Supervisors:	P. Ferrand	Directeur de Recherche, CNRS, LMFA, Ecully, France
	T.H. Fransson	Professor, KTH, Royal Institute of Technology, Stockholm, Sweden
Opponent:	F. Moyroud	Docteur Ingénieur, General Electric, Le Creusot, France
Reviewers:	J.-C. Persson	Professor, KTH, Royal Institute of Technology, Stockholm, Sweden
	F. Thouverez	Professeur, LTDS, ECL, Ecully, France
	D. Vogt	Doctor, KTH, Royal Institute of Technology, Stockholm, Sweden
Examiners:	J. Herpe	Docteur, CNES, Evry, France
	M. Lance	Professeur, LMFA, Ecully, France
	M. Legros	Ingénieur, Snecma, Vernon, France
Invited Member:	S. Aubert	Docteur Ingénieur, Fluorem, Ecully, France

Ecole Doctorale Mécanique, Energétique, Génie civil, Acoustique
School of Industrial Engineering and Management, Energy Technology

ABSTRACT

Modern turbomachines are designed towards thinner, lighter and highly loaded blades. This gives rise to increased sensitivity to flow induced vibrations such as flutter, which leads to structure failure in a short period of time if not sufficiently damped. Although numerical tools are more and more reliable, flutter prediction still depends on a large degree on simplified models. In addition, the critical nature of flutter, resulting in poor well-documented real cases in the open literature, and the lack of experimental database typical of engine flows make its apprehension even more challenging.

In that context, the present thesis is dedicated to study flutter in recent turbines through aerodynamic analysis of subsonic or supersonic flows in response to a prescribed vibratory mode of the structure. The objective is to highlight some mechanisms potentially responsible for flutter in order to be in better position when designing blades. The strategy consists in leading both experimental and numerical investigations.

The experimental part is based on a worldwide unique annular turbine sector cascade employed for measuring the aeroelastic response by means of the aerodynamic influence coefficient technique. The cascade comprises seven low pressure gas turbine blades one of which can oscillate in a controlled way as a rigid body. Aeroelastic responses are measured at various mechanical and aerodynamic parameters: pure and combined modeshapes, reduced frequency, Mach number, incidence angle. In addition to turbulence level measurements, the database aims at assessing the influence of these parameters on the aerodynamic damping, at validating the linear combination principle and at providing input for numerical tools.

The numerical part is based on unsteady computations linearized in the frequency domain and performed in the traveling wave mode. The focus is put on two industrial space turbines:

- 2D computations are performed on an integrally bladed disk, also called blisk; its very low viscous material damping results in complex motions with combined modes and extremely high reduced frequency. The blisk operates at low subsonic conditions without strong non-linearities. Although the blades have been predicted aeroelastically stable, an original methodology based on elementary decompositions of the blade motion is presented to identify the destabilizing movements. The results suggest that the so-called classical flutter is surprisingly prone to occur. Moreover, the aerodynamic damping has been found extremely sensitive to the interblade phase angle and cut-on/cut-off conditions.
- 3D computations are then performed on a supersonic turbine, which features shock waves and boundary layer separation. In contrast, the blade motion is of elementary nature, i.e. purely axial. The blades have been predicted aeroelastically unstable for backward traveling waves and stable for forward traveling waves. The low reduced frequencies allow quasi-steady analysis, which still account for flutter mechanisms: the shock wave motion establishes the boundary between stable and unstable configurations.

Keywords:
flutter, space turbine, LRANS computation, flutter measurement, shock wave/boundary layer interaction, blisk, cut-on/cut-off condition, interblade phase angle, combined modes

RESUME

Les aubes des turbomachines modernes sont de plus en plus fines, légères et chargées aérodynamiquement. Cette tendance accroît l'apparition de phénomènes aéroélastiques tel que le flottement qui conduit à la rupture si l'amortissement est insuffisant. Bien que les outils numériques soient de plus en plus robustes, la fiabilité de sa prédiction demeure insuffisante. La nature critique du phénomène et le manque de données expérimentales pour des écoulements typiques de l'industrie encouragent des travaux de recherche.

Dans ce contexte, la présente thèse est dédiée à l'étude du flottement dans des configurations récentes de turbine à travers l'analyse aérodynamique des écoulements subsoniques ou supersoniques soumis à un mode de structure vibratoire imposé. L'objectif est de fournir des éléments de compréhension des mécanismes potentiellement générateurs de flottement pour une meilleure intégration lors de la conception des aubes. L'approche consiste à mener des travaux expérimentaux et numériques.

La partie expérimentale s'appuie sur un secteur de grille annulaire constitué de sept aubes dont une peut osciller de manière contrôlée. Les fluctuations de pressions instationnaires générées sont mesurées avec la technique dite des coefficients d'influence pour différents paramètres mécaniques et aérodynamiques : déformées modales pures et combinées, fréquence réduite, nombre de Mach, angle d'incidence. Complétée par des mesures de niveau de turbulence, la base de données vise à évaluer l'influence de ces paramètres sur la réponse aéroélastique, à valider le principe de superposition linéaire et à soutenir les codes numériques.

La partie numérique se base sur des calculs instationnaires linéarisés dans le domaine fréquentiel en utilisant la technique dite des "ondes propagatives" (traveling wave mode). Deux cas de turbines spatiales industrielles sont étudiés.

- Des calculs 2D sont réalisés sur une turbine monobloc ou blisk. L'amortissement mécanique quasi-nul entraîne des déformées complexes avec couplage de modes et des fréquences réduites très élevées. Bien que les aubes soient prédites stables, une méthodologie basée sur des décompositions géométriques élémentaires est présentée afin d'identifier les contributions déstabilisantes. Les résultats aboutissent étonnamment aux conclusions de la théorie du flottement classique : la torsion est une source potentielle d'instabilité. De plus, le coefficient d'amortissement aérodynamique a été trouvé extrêmement sensible au déphasage interaube et aux fréquences de coupure (modes cut-on/cut-off).
- Des calculs 3D sont ensuite réalisés sur une turbine supersonique. L'écoulement présente des ondes de chocs avec décollement de la couche limite et le mouvement de l'aube est de nature élémentaire, i.e. purement axial. Les aubes ont été prédites instables pour les modes rétrogrades et stables pour les modes propagatifs. En dépit des fortes hypothèses, des analyses quasi-stationnaires rendent compte des mécanismes de flottement : la phase entre le mouvement du choc et l'excitation établit la frontière entre configurations stable et instable.

Mots-clés :
flottement, turbine spatiale, LRANS, mesure expérimentale du flottement, interaction onde de choc/couche limite, blisk, fréquences de coupure, déphasage interaube, couplage de modes

ACKNOWLEDGEMENTS

After three years of intense work, it is a great pleasure to thank those who helped me. Since this probably will be the page of the report to have the widest audience, it is here I would like to spread how much I am thankful to all people I worked with. This is much more than a display of necessary politeness.

The thesis was initiated by the Centre National d'Etudes Spatiales and Snecma. Their financial support is gratefully acknowledged. As industrial partner, Fluorem joined the project and provided CFD codes and support. The academic partners were Ecole Centrale de Lyon (ECL) and Kungliga Tekniska Högskolan (KTH). The work was mainly performed at the Laboratoire de Mécanique des Fluides et d'Acoustique in France and the experimental work was conducted at the Division of Heat and Power Technology in Sweden. This collaboration began in November 2007 and led to fruitful teamwork. This thesis simply would not have been possible without all the people I worked with.

I offer my deepest thanks to my supervisors, not merely as protocol but through heartfelt gratitude:

- Doctor Pascal Ferrand, Research Director at the Centre National de la Recherche Scientifique at the Laboratoire de Mécanique des Fluides et d'Acoustique, Ecully, France. I would like to thank him for his support, for his guidance and for his availability in any circumstances. His extensive of knowledge helped me both scientifically and professionally. "Les professeurs ouvrent les portes mais vous devez entrer vous-même" (proverbe chinois). Merci Pascal d'avoir ouvert!
- Professor Torsten Fransson at the Chair of Heat and Power Technology at the Royal Institute of Technology, Stockholm, Sweden. I would like to thank him for having welcomed me to his lab. His great personality inspired me to work towards the best. Tack så mycket!

I thank all the committee members: Dr. François Moyroud for agreeing to be the "opponent"; Prof. Jan-Gunnar Personn, Prof. Fabrice Thouverez, and Dr. Damian Vogt for the review of the thesis; Dr. Julien Herpe, Prof. Michel Lance, Marc Legros, and Dr. Stéphane Aubert for agreeing to be on the committee.

I am infinitely grateful to the Fluorem team for their continuous help whenever I needed it: François Pacull, Thibault Turpin, Claire Rambeau, Lionel Gamet, Stéphane Aubert, Céline Sy, Thierry Rochemont, and Macumba N'Diyae. A very very special thank² to Laurent Delmas for his considerable help and patience when introducing me Turb'Lin™.

I am extremely grateful to Nenad Glodic who I performed the flutter measurements with early in the morning and late in the "eveni-ght". There exists an axiom when you perform experimental measurements: "nothing happens as you have planned". I most certainly had the chance to experience it with him. Thank you very much indeed for your contribution in this project!

I would like to thank Dr. Damian Vogt. It always is a great pleasure to work with him for his efficiency and his skill in the experimental field and in many others. I thank him for sharing his knowledge and taking care of the overall of his students, and although "the Swiss have obviously the watches but not necessarily time :-)", thank you for the support and the

unfailing enthusiasm. Also I would like to thank him for his review which has definitively enhanced this report.

I thank Jens Fridh for his help with the update of the hot-wire setup, for all the advices he provided me, and for having been a very nice company in the control room. "Bad luck is now over! Thank you for all". Special thanks to the lab engineers Leif Petterson, Stellan Hedberg, Christer Blomqvist and Mikael Schullström for their technical support.

It was a pleasure to share the office with Laurent Soulat and I thank him for the fruitful discussions and his friendship. Many thanks to Martin Buisson, and I would like to apologize for the noise due to the computations that he allowed me to perform on "ecully" without any hesitation. Thanks to my "brothers in arms" Jean-Michel Lenoir and Mickael Philit for good time and mutual motivation.

I salute all the persons I have met during these three years. I am thinking of all PhD and MSc students. But also all the administrators, teachers and researchers at both ECL and KTH for their generous help.

Finally, I would like to express my sincere gratitude to Futoon, LeVert, BigMac, Suzanne and LaBriouche. I was not easy to live with and I thank them for their unconditional support!

LIST OF CONTENTS

LIST OF FIGURES

LIST OF TABLES

NOMENCLATURE

Symbols	Parameters	Unit
Latin letters		
A	amplitude of vibration	[deg]
C_p	steady pressure coefficient	[-]
$\tilde{C}_p$	unsteady pressure coefficient	[-]
C_v	velocity coefficient	[-]
c	chord	[m]
c	speed of sound	[m/s]
ds	infinitesimal surface element	[m^2]
$\tilde{\vec{F}}$	unsteady force	[N]
f	frequency	[Hz]
$\tilde{\vec{h}}$	mode shape vector	[-]
i	imaginary unit, $i = \sqrt{-1}$	[-]
k	reduced frequency	[-]
k	turbulent kinetic energy	[J/kg]
M	Mach number	[-]
M_k	k^{th} order central moment	[-]
n	nodal diameter	[-]
N	number of blades	[-]
p	pressure	[Pa]
R	bending-to-torsion ratio $R = \frac{A_{bending}}{A_{torsion}}$	[-]
R	specific gas constant	[$m^2/s^2/K$]
T	oscillation period	[s]
Tu	turbulence level	[%]
t	time	[s]
V	velocity	[m/s]
W_{cycle}	work per oscillation cycle	[J]
$\vec{X}$	displacement vector	[m]
x, y, z	cartesian coordinates	[m]
Greek letters		
α	flow angle	[deg]
γ	specific heat capacity ratio	[-]
$\varepsilon_2, \varepsilon_4$	artificial dissipation coefficients used in the centered spatial scheme of Jameson	[-]
λ	thermal conductibility	[W/m/K]
μ	dynamic laminar viscosity	[Pa.s]
μ_k	k^{th} moment about the mean	[-]
Ξ	global aerodynamic damping coefficient	[-]
ξ	elementary aerodynamic damping coefficient	[-]
π	pressure ratio	[-]

π	number "pi" 3.14	[-]
ρ	density	[kg/m^3]
σ	interblade phase angle	[deg]
σ	standard deviation	[-]
φ	mode shape	[-]
ϕ	phase between bending and torsion for combined mode	[deg]
$\varphi_{p\to h}$	phase angle	[deg]
ω	circular frequency	[rad/s]
ω	specific turbulent dissipation	[1/s]

Subscripts

ae	aerodynamic
aero	aerodynamic
ax	axial
def	deformation
dw	downstream
dyn	dynamic
EA	ensemble average
infc	influence coefficient
max	maximal
min	minimal
r	value in the relative frame of reference
ref	reference
s	static
ste	steady
t	total
twm	traveling wave mode
uns	unsteady
up	upstream

Superscripts

^	complex
¯	steady, mean
~	unsteady
™	trademark

Symbols

δ	perturbation
$\Im$	imaginary part
$\Re$	real part

Abbreviations

2D	two dimensional
3D	three dimensional
A/D	Analog/Digital
AGARD	Advisory Group for Aerospace Research and Development

ASME	American Society of Mechanical Engineers
AUSM	Advection Upstream Splitting Scheme
ae	aerodynamic
arc	arcwise
ax	axial
BiCGStab	Bi Conjugate Gradient Stabilized
CFD	Computational Fluid Dynamics
CFL	Courant Friedrichs Levy condition
CNES	Centre National d'Etudes Spatiales (French Space Agency)
CNRS	Centre National de la Recherche Scientifique
CPU	Central Processing Unit
CTA	Constant Temperature Anemometry
circ.	circumferential
deg	degree
EA	Ensemble Average
ECL	Ecole Centrale de Lyon
EPFL	Ecole Polytechnique Fédérale de Lausanne
GPIB	General Purpose Interface Bus
GMRES	Generalized Minimal Residual Method
HPT	Heat and Power Technology
IBPA	InterBlade Phase Angle
INFC	Influence Coefficient
JST	Jameson-Schmidt-Turkel
HWA	Hot-Wire Anemometry
KT8000	Kayser Threde KT8000 data acquisition system
KTH	Kungliga Tekniska Högskolan (Royal Institute of Technology)
LMFA	Laboratoire de Mécanique des Fluides et d'Acoustique
LDA	Laser Doppler Anemometer
LE	Leading Edge
LTDS	Laboratoire de Tribologie et Dynamique des Systèmes
M04	operating point set to an outlet Mach number of 0.4
M06	operating point set to an outlet Mach number of 0.6
M08	operating point set to an outlet Mach number of 0.8
MUSCL	Monotone Upstream-centered Scheme for Conservative Laws
MW	Mega Watt
ND	Nodal Diameter
nom.	nominal
OP	Operating Point
off1	off-design1
off2	off-design2
PC	Personal Computer
PIV	Particle Image Velocimetry
PS	Pressure Side
PSD	Positive Sensitive Detector
PSI	Pressure System Inc.
PT	Platinum resistance thermometer
PVC	Polyvinyl chloride
pos.	position
rad	radian
RANS	Reynolds Averaged Navier Stokes

T3D	Turbo3D
TBF	Turb'Flow™
TBL	Turb'Lin™
TE	Trailing Edge
tors.	torsion
SMARTER	Sharp and Monotonic Algorithm for Realistic Transport Efficiently Revised
SS	Suction Side
TWM	Traveling Wave Mode

CONVENTIONS AND NORMALIZATIONS

The reduced frequency

Unless otherwise specified, the reduced frequency is based on the full chord and the outlet velocity taken 20% axial chord downstream of the blade.

$$k = 2\pi f \frac{c}{V} \qquad \text{Eq. 0-1}$$

The steady static pressure coefficient

The steady static pressure is normalized by a reference pressure taken upstream of the blade.

$$C_p = \frac{p_s - p_{s,ref}}{p_{t,ref} - p_{s,ref}} \qquad \text{Eq. 0-2}$$

The unsteady static pressure coefficient

The unsteady pressure is normalized by the amplitude of vibration and the dynamic pressure as follows,

$$\hat{C}_p = \frac{\hat{p}}{A \cdot p_{dyn}} \qquad \text{Eq. 0-3}$$

with

$$p_{dyn} = p_{t,ref} - p_{s,ref} \qquad \text{Eq. 0-4}$$

The stability parameter or aerodynamic damping coefficient

In the present context, the term "flutter stability" denotes the stabilizing character of the flow rather than the stability of the entire fluid-structure system. The terms "stability parameter" and "aerodynamic damping coefficient" are used with the same meaning and refers to the same concept: the flutter stability, which is described in Appendix A. A local and global stability parameter are defined. The first one corresponds to the infinitesimal force integrated within an infinitesimal surface element of the blade. This highlights therefore the local variations of the aerodynamic damping. Whereas the second one refers to the integration of the local forces along the complete blade profile.

Interblade phase angle in the blade-to-blade plane

Typically, when considering the phase of the unsteady pressure fluctuations in the blade-to-blade plane, two blades are displayed and the reference blade is at the bottom as illustrated in the figure below. Moreover, physical aspects related to the interblade phase angle are given in Appendix B.

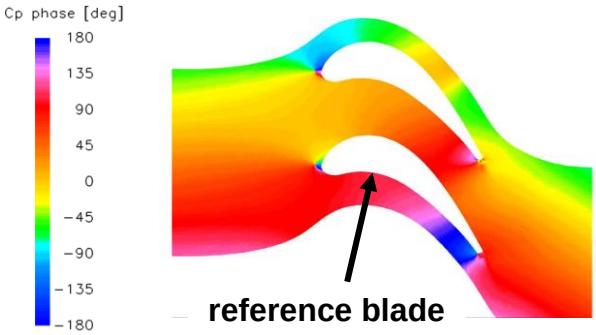

Figure 0-1: Reference blade in the blade-to-blade plane

1 INTRODUCTION

This first chapter describes the overall framework of the thesis. The flutter phenomenon is firstly introduced from a general point of view and then more specifically towards turbomachines. Afterwards, numerical methods commonly used for flutter prediction are given as well as setups for experimental investigations. Next, the specifities of space turbines are introduced. Finally the objectives are formulated and the strategy of investigation is detailed.

1.1 Introduction

"Among a variety of phenomena that cause concern in regard to blade failures, perhaps the most serious is flutter" (Srinivasan, 1997).

Flutter is an instability described as a self-excited and self-sustained vibration originating from the combination of aerodynamic, inertial and elastic forces in such a way that the structure and the flow around it interact with each other. The terms "self-excited" and "self-sustained" denote respectively "without unsteadiness coming from upstream or downstream" and "without external constraint". Flutter results in energy exchange between the fluid and the structure: when the structure is self-excited, its vibration induces an unsteady pressure field around the profile sustaining the vibration. Flutter usually starts from small aerodynamic or mechanical disturbance above a critical flow velocity, gives large vibration amplitudes and leads to damage in a short period of time. Basically, flutter appears when the mechanical damping is not high enough to overcome the aerodynamic excitations.

Currently, although numerical tools are more and more reliable, flutter prediction still depends on simplified models and systematic tests are the only guarantee for flutter-free engines. Moreover, thinner and lighter blades, higher velocities and loads, lower axial gaps, etc, all characterize the trend of new engines and inevitably give rise to increased sensitivity to flow induced vibrations. Flutter is thus a major concern for the designers regarding both the safety and costs. The security reasons are obvious and they do not need to be explained. In contrast, potential risks of failure lead to extra-costs for the manufacturers, especially when the engine is already at a later stage of development and fails the qualification tests. Cost reduction policies are also based, for instance, on the use of the so-called integrally bladed disks, also known as blisks. The particularities are the complex deformation of the blades, the high frequencies and the quasi non-existence of mechanical damping. As a result, the aerodynamic damping is the only source of damping. This is even much more critical for the designers since aeroelastic stability is based on the aerodynamic damping evaluation.

During the last thirty years, many experimental and numerical research efforts have focused on flutter prediction. Several flutters have been well defined and labelled with respect to their origin. However, although it has been established that flutter originates from a phase lag between excitation and response, the reasons why in some situations, this phase lag stabilizes the vibrations and in other amplifies them are still under investigations. The answer to this question would constitute a significant advance in the field. The present thesis contributes by investigating experimentally and numerically subsonic and supersonic flutters.

The report is organized as follows, around two main parts dedicated to experimental and numerical studies respectively:

- the current first chapter presents the general background. Flutter and important aspects for flutter prediction are described. Numerical methods and experimental setups commonly used are then introduced. A detailed state-of-the-art is not included, the goal is to provide basic and fundamental aspects as well as some specifities in order to introduce the flutter issue in a general framework. Finally the problem is formulated, and the objectives and the strategy of investigation are detailed.

- the part 1 is dedicated to the experiments and consists of two main chapters. The first one (chapter 2) presents the overall measurement setup of the experiments performed in the annular sector cascade at the Royal Institute of Technology, Sweden. Then chapter 3 includes the overall results. The steady state based on data and CFD is introduced. Finally the unsteady state results are given and discussed. This part is essentially experimentally based, however some CFD have been performed for the steady state only. No unsteady computations have been carried out.

- then two real industrial space turbines are numerically studied in the part 2, which also consists of two main chapters. It starts with chapter 4, which focuses on an industrial subsonic space turbine characterized by the use of blisk technology. Based on 2D numerical computations, the turbine is analyzed and a methodology is suggested to increase the flutter margin. Then chapter 5 presents the results of an industrial supersonic space turbine based on 3D computations. The problem is firstly exposed, then the numerical method is detailed. At last, the steady flow is described and the unsteady results are discussed.

- finally chapter 6 summarizes the main results and exposes some recommendations for future work.

- the report includes also appendices. In order to keep the manuscript more pleasant to read, some figures of the experimental results are annexed. On the other hand theoretical backgrounds are detailed in the first appendices, such as the determination of flutter stability, the interblade phase angle, the influence coefficient technique and the traveling wave mode. For each section related to CFD, the numerical parameters are briefly given in the text but are detailed in Appendix D.

The next section is dedicated to the description of flutter.

1.2 General description of flutter

1.2.1 A dynamic aeroelastic phenomenon

Flutter is defined as a dynamic aeroelastic instability. Aeroelasticity denotes the combination of aerodynamic, inertial and elastic forces in such a way that the structure and the flow around it interact with each other. Always present in turbomachines, these interferences are illustrated by the Collar's triangle (1946) below.

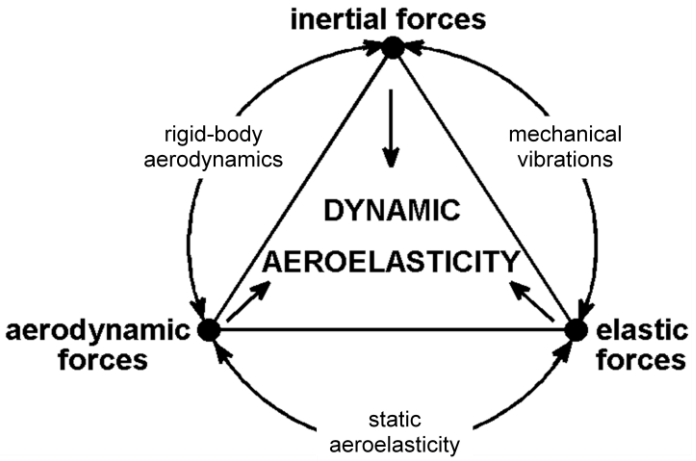

Figure 1-1: Collar's aeroelastic triangle

Aerodynamic, inertial and elastic forces each occupies a vertex in the aforementioned triangle and interact with each other or all together resulting in the following cases:

- Rigid-body aerodynamics describes the static aspects of the loading on a structure, i.e. inertial and aerodynamic forces act together. Such situations meet in external aerodynamic (lift, control and stability of the aircraft).

- The interaction between elastic and inertial forces leads to structural dynamics. No fluid acts around the structure, which only vibrates under the inertial and elastic forces.

- Static aeroelasticity denotes the combination of aerodynamic and elastic forces. No vibrations are implied. The steady aerodynamic load is responsible for the deformation or displacement of the structure.

- Finally, dynamic aeroelasticity defines the interaction of all three forces. A more accurate terminology would be "aero-elasto-dynamics" but the shorter term "aeroeasticity" is the usual terminology whereas it should only be used for what is generally known as "static aeroelasticity" (Platzer, 1990).

Aeroelasticity phenomena result from excitations whose the sources can originate from:

- forced response
  - convective unsteadiness, i.e. wakes, distortion
  - unsteady potential field (turbines)

- self-excited (flutter)
  - flow separation (fan, low pressure turbine)
  - shock impingement on blade (high pressure turbine)

Flutter must be distinguished from forced response like rotor/stator interaction or from unsteady natural phenomena like vortex-shedding. Indeed, the structure must undergo an instantaneous displacement around its steady state position in such a way that an instantaneous perturbation of the flow appears. As a result, an energy transfer between

the fluid and the structure takes place and, according to the nature of this transfer, will lead to either stable or unstable motion of the blade. Actually flutter phenomenon strongly depends on the flexibility of the structure and appears when the mechanical work is lower than the aerodynamic work, i.e. when the mechanical damping is too small to overcome the aerodynamic excitations. As a result, it is usual to separate flutters that occur in external flows (around wing airplanes for instance) and flutters in internal flows (turbomachines). In external flows, flutter appears when two vibrating modes (usually bending and torsion) interact together at distinct frequencies, whereas in internal flows, the structures being much more stiff, flutter often occurs due to the interaction between a vibrating mode (bending or torsion) and an unstable aerodynamic behavior, like a boundary layer separation, a shock wave motion. In any case, flutter exists because of strong interaction between the instantaneous motion of the blade and the instantaneous aerodynamic forces. The thesis focuses on flutter in axial turbomachines.

1.2.2 Flutter in axial turbomachines

In turbomachines, flutter is prone to occur in the fore part of compressors or aft part of turbines where blades are long and slim, and generally appears on blade eigenmodes. All the blades oscillate at the same frequency but are phase shifted in time. The flow experiences therefore the vibrations through:

- the blade profile: variation in incidence at the leading edge and vortex shedding at the trailing edge.
- the interblade channel: fluctuations of the passage section, blockage.
- the cylindrical nature of the flow itself apart from the cascade: cut-on/cut-off modes.

Performance and structural integrity of engines lead to reduce blade thickness and weight, which make them more sensitive to aeroelastic effects. Blades designs are conducted such as to avoid crossings of the operating line with flutter boundaries as shown in Figure 1-2. The surge line is reached when the compressor operates at high positive incidence angles; this results in high pressure amplitudes of low frequency. The chocked line is reached when decreasing the pressure level at a certain mass flow resulting in low positive or negative incidence angles and chocked flow, i.e. at a given mass flow the pressure ratio cannot decrease anymore. Flutter depends on the operating point and may occur during transient operation (acceleration, deceleration) and then intersect the flutter margin:

- Subsonic and transonic stall flutters (cases 1 and 2) are situated close to the stall line. They occur when the compressor is operating near surge. The flow conditions are characterized by high incidence angles and separated flow. The governing parameters are the Mach number, the reduced frequency and the incidence angle (Srinivasan, 1997). The mechanism for energy transfer between the flow and the structure does not rely on coalescence modes nor upon a phase lag between the motion of the structure and the aerodynamic response (Dowell et al., 2004). Although coupling between modes and phase lag may alter the results somewhat, stall flutter is essentially explained by non-linear phenomena.

- Choke flutter (case 3) appears near the choke line at negative incidence and part speed operation. The vulnerable components are mid and aft stages of compressors. The governing parameters are the Mach number, the reduced frequency and the incidence angle. The vibratory modes are bending or torsion modes (Srinivasan, 1997).

- Supersonic started flutter at low back pressure (case 4) is situated near the operating line and therefore can impose a limit on high-speed capability. Also referred as supersonic unstalled flutter, it usually appears on fan blades where the flow is supersonic and attached, and results in high stresses. The governing parameters are the Mach number, the reduced frequency, the interblade phase angle and the shock position. The vibratory modes are bending or torsion modes (Srinivasan, 1997).

- Supersonic started flutter at high back pressure (case 5) appears during high speed operation. As the back pressure increases, the shock waves move on the blade. Also referred as supersonic stalled flutter, it is probably characterized by a strong in-passage shock wave, together with a boundary layer separation (Fransson, 1999). The vulnerable components are usually the fan blades featuring high loads, supersonic tips and strong shocks. The governing parameters are the Mach number and the reduced frequency (Srinivasan, 1997).

- Classical flutter (case 6), contrary to stall flutter, is explained by the phase lag between the blade motion and the induced unsteady aerodynamic forces. Depending on the aforementioned phase lag, the blade will either absorb energy from the flow (unstable blade) or give energy to the flow (stable blade). Also called potential flutter, it can occur near the operating point for small incidence angles, the flow being attached all the time.

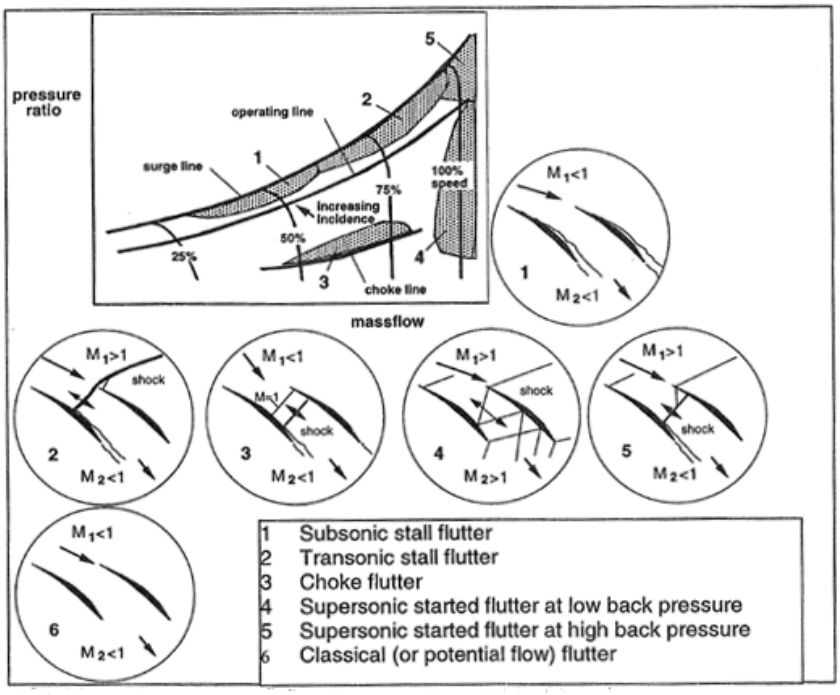

Figure 1-2: Operating map of a multistage compressor from Fransson (1999)

Flutter in compressors has been more extensively studied than flutter in turbines, however the same map as for compressor can be drawn. Figure 1-3 shows the characteristic line of a turbine. When the sonic Mach number is reached at the throat, the turbine is chocked, i.e. there is no longer variation of the flow and all the curves collapse (sonic blockage in

the stator). Moreover, contrary to compressors, surge does not occur in turbines. The present thesis focuses on the following turbine flutters:

- classical flutter in subsonic flow (case 1) will be studied experimentally and numerically. It appears near the operating point for small incidence angles.

- supersonic flutter with supersonic inflow (case 4) will be studied numerically. It can occur for high outlet Mach numbers. Moreover, such flow conditions can induce separation due to shock wave/boundary layer interaction.

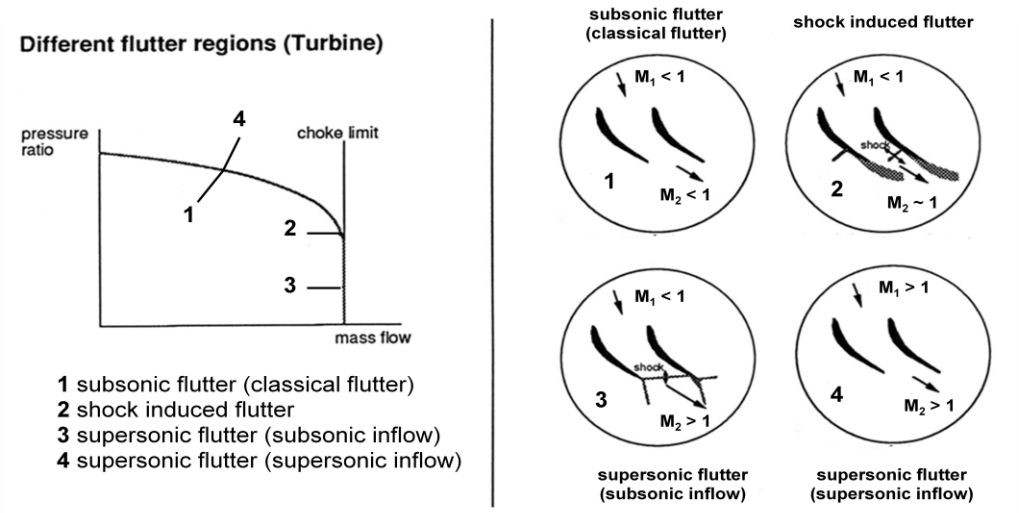

Figure 1-3: Flutter map for turbines from Ferrand (2007)

Flutter originates from the phase shift between the blade motion and the induced unsteady forces, i.e. between the excitation and the response respectively. However, the reason why the aforementioned time phase lag occurs is still not understood. Flutter is evaluated through the energy transfer between the blade and the flow ("energy" denotes the aerodynamic work, i.e. the work exchange between the fluid and the structure). Either, when oscillating, the blade transfers energy to the fluid: the flow acts thus stabilizing and this leads therefore to stable blade; or when oscillating, the blade receives energy from the fluid: the flow acts thus destabilizing, the vibrations is amplified and this leads to unstable blade. The most critical case occurs when the aerodynamic work is such that the flow transfers energy to the structure; nevertheless, this does not necessarily induce flutter especially if the mechanical damping is high enough to overcome the excitation. The potential of vibration for damage can only be evaluated through forcing and damping forces. In preliminary design, basic rules are usually applied in order to remain outside the flutter margin, as described in the next sub-section.

1.2.3 Parameters for flutter-free design

As the problem is of fluid-structure interaction nature, designers can work either on the structure, or on the aerodynamic field or on both of them in order to improve the engine in terms of stability. Structural parameters are for instance the modeshape, the nodal diameter and the reduced frequency: they characterize how the structure behaves. Besides, aerodynamic parameters such as the incidence angle and the Mach number defines the flow. Below, the parameters usually considered of main concern in flutter studies are described.

1.2.3.1 The modeshape

The modeshape is of high importance not to say the most important parameter. Long and slim structures exposed to high aerodynamic loads are sensitive to flutter, typically first stages of compressors and last stages of turbines. According to the nature of the structure itself, the modeshape may be of different levels of complexity. In external aerodynamic such airplane wings, modeshape can be a combination of the first eigenmodes of the structure (the involved modes must lie in frequency such that they can be coupled by the flow); whereas in internal flows, the modeshape are typically pure eigenmodes. The main difference between internal and external aeroelasticity is the material stiffness and is expressed through the so-called mass ratio defining the ratio between the mass of the structure and the mass of surrounding air inside a circle with radius half chord. In turbomachines, the blades are stiff and the mass ratio is consequently larger compared to airplane wings. As a result the flow is assumed not to modify the blade modeshape. Usually, the blades are mounted on a disk, the entire structure is thus called bladed disk assembly. The blades are mechanically coupled with each other through the disk. The advantage of such structures is the mechanical damping resulting from the interface between blades and disk (fir tree attachments). Nowadays, the trends is to manufacture turbine stage as a single piece. Called blisk (integrally bladed disk), the blades and disk is an integrally part machined out from a forging. The mechanical damping mentioned above does no longer exist and only a very low viscous damping remains. This can result in complex motions of the blade with couplings of modes.

The bending-torsion coupling was among others studied by Bendiksen and Friedmann (1980). The authors examined the effect of coupling between bending and torsion on the stability boundary and mentioned that the coupling can take three forms: structural coupling, inertial coupling and aerodynamic coupling. It has been shown that the two motions imply different responses regarding the location of the centre of torsion (Bendiksen and Friedmann, 1982). As stated by Panovsky and Kielb (2000), mode shape is of high importance in determining the stability of a blade. This has been confirmed by Tchernycherva et al. (2001) with a parametrical study on the effect of the reduced frequency and the mode shape towards the aeroelastic stability; a significantly larger influence of the mode shape has been shown. Vogt and Fransson (2007) analyzed the aeroelastic response of an oscillating blade included in an annular cascade of low pressure turbine blades for three pure orthogonal motions (axial bending, circumferential bending, and torsion). The results showed that the most stable modes are of axial bending type whereas the stability exhibits higher sensitivity to torsional modes. Furthermore, it has been highlighted that all modes tend to be more stable with increase in reduced frequency. Nevertheless only pure and rigid modes were considered. More recently, Glodic et al. (2009) studied aeroelastic properties of combined mode shape in the same facility. The validity of linear combination was experimentally verified at low subsonic flow.

1.2.3.2 The reduced frequency

The reduced frequency provides information on the unsteadiness through a ratio between steady and unsteady time scales. The unsteady time scale is determined through the natural frequency of vibration whereas the steady time scale is defined through the fluid particles velocity and a characteristic length scale, the chord for instance. The reduced frequency can be interpreted as the ratio of the time for a fluid particle to pass by the blade

to the time of one oscillation cycle. If the time for one blade oscillation is long enough, the flow can be considered as quasi-steady insofar as the flow is able to adapt to the changing conditions. Hence according to the reduced frequency, the flow will be quasi-steady, i.e. the time for a particle to travel across the blade chord is shorter than the time of one oscillation cycle, or unsteady, or the flow will feature strong couplings. This dimensionless parameter is useful in order to compare unsteady results at different flow velocities and blade geometries. Srinivasan (1997) reported typical reduced frequencies, based on full chord, for which flutter occurs in rotor blades of compressors: less than about 0.4 in the first modes, and between 0.4 and 0.7 for modes with a predominantly first torsion mode.

1.2.3.3 Aerodynamic parameters

The incidence angle and the flow velocity are part of the aerodynamic parameters and their influence on flutter phenomenon is well illustrated in Figure 1-2 and Figure 1-3. Off-design conditions can lead to either positive or negative incidence and then induce flutter. For instance, this can generate flow separation in compressors yielding to stall flutter. The inlet velocity becomes critical when supersonic with the presence of strong shocks. This can lead to the boundary layer separation which can interact with the shock and then irremediably affect the blade vibration. Transonic and supersonic flows result in strong and complex interactions between traveling pressure waves, shock motion, and fluctuating turbulent boundary layer. The interaction between shock waves with boundary layers developed on the structures can induce aeroelastically unstable states. Many numerical and experimental studies are dedicated to the understanding of the phase lags and high time harmonics occurring in the shock/boundary layer region. Ferrand (1984) studied choke flutter and highlighted that the shock motion can be critical for the self-exciting oscillations. Ferrand (1987) proposed a parametric study of choke flutter with a linear theory and showed that the shock wave movement depends strongly and weakly of up- and downstream flow respectively.

Excitations propagate as waves both up- and downstream of the excitation source. Either these waves are purely propagative without any decay or exponentially decaying (cut-on or cut-off respectively). This aspect is particularly important in flutter analysis by giving important information about the system perturbations. Waves can indeed brutally change in mode and hence produce strong discontinuities on the unsteady flow. The ability of the flow to damp or to amplify the blade motion is strongly affected by how unsteady perturbations are propagated from the cascade to the far-field. This depends on the steady aerodynamic field, the interblade phase angle, and the reduced frequency.

Atassi et al. (1995) and Ferrand et al. (1996) reported results explaining why transonic flows and high subsonic flows exhibit a rise of the unsteady pressure magnitude along the surface of an airfoil such that a significant bulge appears near the shock location. For such flows, upstream propagating acoustic disturbances are blocked and amplified: the near-sonic velocity acts as a barrier, known as acoustic blockage, which is similar to the shock in transonic flow preventing acoustic disturbances from propagating upstream. Bron et al. (2003) and Bron (2004) investigated on a transonic convergent-divergent nozzle and confirmed the acoustic blockage theory. It has been shown that there exist critical behaviors such that up- and downstream there are cut-on and cut-off mode respectively: outlet pressure perturbations are magnified when propagating into the near sonic flow region and can lead to the excitation of shock wave. This interaction creates a shift in the shock position and contributes to the system stability: it has a strong effect on the overall

unsteady forces affecting the flutter boundary as well, and thus causing large local stresses which may result in high cycle fatigue failure.

Flutter has been introduced. The next section is dedicated to the numerical methods used for its prediction.

1.3 Numerical methods for flutter prediction

Flows in turbomachines are complex, highly three dimensional, unsteady, compressible, turbulent. They feature non-linear aerodynamic effects difficult to model like shock/boundary layer interaction induced flow separation. Moreover, the constraint to take the structure into account in the aeroelastic problem adds non-linearities like friction damping at the blade attachment. The interaction between the flow and the structure is a coupled, non-linear problem. Despite the considerable progresses in terms of computing power and numerical codes, it is impossible to calculate the real value of the aerodynamic damping as well as a fine description of the unsteady flow because time and spatial schemes, turbulence models and numerical methods are not yet fully understood and controlled.

1.3.1 Standard numerical methods

The aeroelastic problem can be described by an equation representing a balance between structural and aerodynamic forces. The structural forces consist of modal mass, damping and stiffness matrices whereas the unsteady aerodynamic forces consist of two elements. The first element represents the aerodynamic disturbances from both up- and downstream of the blade row, typically the rotor-stator interaction. The second element represents the interaction between the blade and the flow. Within the framework of flutter analysis, only the forces induced by the blade motion have to be considered as described in the equations below,

$$[M]\{\ddot{X}(t)\} + [G]\{\dot{X}(t)\} + [K]\{X(t)\} = \{F_{ae}(t)\} \qquad \text{Eq. 1-1}$$

$[M]$, $[G]$ and $[K]$ are the modal mass matrix, the modal damping matrix and the modal stiffness matrix respectively. X represents the modal coordinate of the blade displacement and $\{F_{ae}(t)\}$ is the unsteady forces that consist of the two elements $F_{disturbance}$ and $F_{damping}$. For flutter analysis, Eq. 1-1 simplifies as follows,

$$[M]\{\ddot{X}(t)\} + [G]\{\dot{X}(t)\} + [K]\{X(t)\} = \{F_{damping}(t)\} \qquad \text{Eq. 1-2}$$

In that context, many numerical methods towards flutter prediction have been developed and a complete and detailed review is presented by Marshall and Imregun (1996). Below, different numerical methods are briefly described the complexity of which has increased over the years.

- The linearized potential methods solve inviscid and irrotational flows and neglect the viscous effects. The equations are non-linear but can be simplified by linearization assuming small amplitudes. The problem is considered as the superposition of a non-linear steady flow and a small perturbation about this latter. This leads to an acoustic waves equation if the frequency is imposed. The

assumptions are strong and its use is therefore restricted to weak shocks and low loads.

- The linear Euler methods extend the above approach to rotational flows. The equations are linearized either in the time or frequency domain. The main advantage compared to non-linear technique is the computation time. On the other hand, when comparing with the same mesh and spatial scheme, linear Euler methods lead to lower numerical dissipation. They therefore feature relatively high accuracy at high frequencies. However, the linearization prevent the prediction of a limit cycle of flutter and thus limit their applicability to a detailed flutter analysis. When flutter occurs, the non-linearities effect depends on the configuration and the validation of the linear solution is questionable. These methods are thus well adapted when the frequencies are high and when the problem needs an amount of computational effort.

- The non-linear potential and Euler methods are based on the previous approaches without assumption of linearity and thus without unique frequency. The problem is solved using time discretization of the unsteady terms and high loaded configurations with shocks can be considered by changing the outlet static pressure. It is also possible to include inviscid effects by using two models respectively close to and far from the walls.

- The Reynolds-Averaged Navier Stokes (RANS) equations taking into account all the viscous terms are widely use. The problem is closed by modeling the turbulence. They are a variety of turbulence models and the most used are one-equation models (Spalart-Allmaras) or two-equation models (Jones & Launder $k-\varepsilon$, Kok $k-\omega$). However they feature some limitations in steady computations: overproduction of turbulent energy and separation at the leading edge, laminar-turbulent transition in turbines, shock wave/boundary layer interaction. These limitations are reduced by using various numerical parameters such as flux limiters or threshold.

- The Linearized RANS (LRANS) equations are based on the same aforementioned assumption of small amplitude. The difference is the turbulence modeling and two approaches can be considered, either the turbulence is variable or frozen. This leads obviously to decreasing the computation time; however this indicates also two different configurations. When the turbulence is set to variable, the turbulence model is derived and this implies that the turbulence reacts quasi-steadily to the excitation generated by the blade vibration. This means that the frequency associated to the turbulence is higher than the one associated to the excitation. In contrast, if the excitation frequency is higher than the turbulence frequency, the turbulence will not react and will remain, i.e. frozen, in its steady state.

- The non-linear Unsteady RANS (URANS) equations are based on the above equations without the assumption of linearity and the turbulence is considered as quasi-steady. However, when the flow features separation region, the turbulence spectra becomes wider and the frequencies lower. This leads to the limits of steady (size of the separation zone) and unsteady (phase lag of the separation with respect to the excitation) turbulence models.

Many engineering approaches are based on the linearization (superposition of harmonics) and the decoupling (no change in structure is assumed) for the assessment of the aerodynamic damping, i.e. the stability parameter, which is considered as the most important information for the designers. This assumes small amplitudes and is justified from the point of view that all tendency towards flutter must be avoided, and if no self-excitations appear at small amplitudes, the amplitudes will never grow (Fransson, 1999). However, it shall be noticed that for flows featuring shock waves, the linearized approach leads to a shock moving up- and downstream of its mean position with the same amplitude of displacement. Actually, the non-linear behavior of shock waves can induce motion with different amplitudes up- and downstream of its mean position.

For the methods currently used (second-order scheme), 20 discretization points per wavelength have to be considered in order to capture the waves properly. When considering the same scheme, linearized methods are more accurate and thus more flexible from this point of view that non-linear methods. The technique used in the present thesis to evaluate stability is the so-called energy method, based on unsteady aerodynamics only, i.e. it calculates the aerodynamic response to a prescribed blade motion, usually its eigenmode. The coupling between unsteady aerodynamic response and the prescribed blade motion results in energy transfer between the fluid and the structure. The unsteady computations are based on linearization principle. The governing equations are linearized about a non-linear steady aerodynamic field. The unsteady flow is defined as a small perturbation, assumed to be harmonic in time with the frequency ω.

1.3.2 Numerical aspects related to meshes

In turbomachine applications, structured multi-blocks meshes are often used due to their efficiency in terms of accuracy, CPU time and memory requirement; however significant time is necessary to generate good quality structured grids on complex geometries. Thus in some cases unstructured grids are preferred, which are generally more dissipative than structured approaches. Conservative formulations are needed to properly take into account discontinuities and propagation of waves. The coupling of numerical schemes (often separated-fluxes based) with flux limiters (which decrease the order of the scheme across discontinuities) can also introduce interference. A flux limiter that is too sensitive can produce a too high spreading of discontinuities. Instead, an insensitive limiter will generate "overshoots fluctuating" in regions of strong gradients generating numerical parasite waves. Finally, a limiter too strong will make the convergence difficult and maintain a high level of noise signal. In transonic and supersonic flows significant differences may appear and even more for unsteady state. These problems can hardly be solved by unsteady adaptive mesh. Indeed, there are many waves present in the entire computation box. It is therefore important to have a regular mesh and refined both in critical zones and even in regions where steady gradients are weak.

1.3.3 Numerical aspects related to boundary conditions

Generally the flows are solved in computation boxes the in- and outlet boundaries of which are set arbitrarily. The real environment around the blade row is not taken into account due to high computation cost; the blade row is thus assumed to be part of an infinite cylindrical plenum. For unsteady computations, this can lead to very disturbing effects whether the boundaries are not transparent to acoustic waves. If not, a part of the acoustic waves are reflected and they propagate towards the blade changing its response. Various techniques

have been developed in order to minimize this effect. For instance, one of them is based on analytical formulation in the case of small perturbations of low frequency. In that case, the solutions can be expressed as the sum of exponentials that depend on the distance. The imaginary part corresponds to the oscillatory part whereas the real part corresponds to either a damping or an amplification. The boundary condition consists therefore in only keeping the terms that are not amplifying to the infinite since the terms which are amplifying are physically meaningless. This treatment is thus independent of the boundary position and split naturally the forward and backward waves. For discrete numerical methods, the same idea is applied on the boundaries by applying the so-called non-reflective boundary conditions. This non-reflective condition depends on the nature of the waves (vertical, acoustic, convective) and on the steady state (like the flow angle with respect to the normal at the boundary). Furthermore the cut-on/cut-off conditions appear as well very important. When conditions are cut-on, the waves are propagating and the damping term is null with respect to the distance, the wave magnitude will be maximal and the reflection potentially maximal. The nature of the waves in terms of cut-on/cut-off conditions can be easily determined analytically (Fang and Atassi, 1991), as described in the equation below. The subscript 0 denotes the mean base flow, and $\frac{D^2.}{Dt} = \frac{\partial.}{\partial t} + (V.\nabla).$ is the material derivative. Eq. 1-3 originates from Euler equations linearized around a steady base flow and assuming inviscid flow, small perturbations, potential, homentropic and uniform steady base flow in the far-field.

$$\frac{1}{c_0^2}\frac{D_0^2(\delta p)}{Dt^2} - \Delta(\delta p) = 0 \qquad \text{Eq. 1-3}$$

The boundary transparence is therefore very sensitive to the configuration. Each new configuration needs to be investigated with respect to the position of the in- and outlet boundaries in order to conclude on the independence of the unsteady solutions. Buffer zones with large size cells and high numerical viscosity minimize this effect.

A recurrent issue occurs when starting CFD computations regarding its initialization. The velocity and the turbulence profiles are in general not known prior CFD. A way to be in better position is obviously to perform experiments and then calibrate and initialize numerical computations. The next section is dedicated to the description of experimental setups commonly used for flutter investigations.

1.4 Experimental setups for flutter investigations

This section presents common experimental setups for flutter investigations. There exists different approaches to evaluate the aerodynamic damping:

- the motion of the test object is free (free flutter testing), i.e. the test object is exposed to a flow and the operating conditions are changed until self-induced oscillations occur. The aerodynamic properties vary (incidence, inflow velocity) while measuring their effect on the structure. This approach is used for real engine flutter tests.

- the motion of the test object is controlled (controlled flutter testing), i.e. the motion is prescribed and the aerodynamic response to that prescribed excitation is measured. This approach is widely used for investigating aerodynamic damping.

Each approach has its own advantage and inconvenience. The choice depends on the desired objectives and the cost. Free flutter testing in real engines obviously lead to a high degree of fidelity but remain prohibitive in terms of cost and are in general reserved for industries. All the experimental setups are limited by the risk of failure and when oscillation cycle starts, it is very difficult to control the damping such as not to yield to the breakdown. As a result many experiments are led in linear or annular cascade with an imposed and controlled vibration of the motion. Controlled flutter testing are lower in cost and allows investigating in a more intimate way both aerodynamic and mechanical effects. This approach is thus much more used for research and is often based on the linearized theories. In this category, two techniques can be employed:

- the traveling wave mode technique: all blades in the cascade vibrate with the same amplitude, the same frequency and constant interblade phase angle. The response is measured on one blade.

- the influence coefficient technique: only one blade vibrates but the response is measured on all blades in the cascade.

The first technique is more accurate with respect to real engines, however this remain complex and relatively heavy to use. Nevertheless, the data from the two aforementioned techniques can be related with each other assuming small perturbation and linear superposition as described in Appendix C.

One of the most complete and used compilations of flutter tests data is described in details by Bölcs and Fransson (1986) and has become the standard for unsteady cascade flows. The database consists of linear and circular cascades of compressor and turbine blades. Both the above techniques have been employed, i.e. traveling wave mode and influence coefficient, and validated leading to the conclusion that indeed the influence coefficient technique is valid for flutter testing considering small oscillation amplitudes.

In particular, in the 4th standard configuration, Bölcs and Fransson (1986) performed measurements in the annular cascade facility at EPFL with cambered turbine blades in transonic flows. The blade vibrated in the traveling wave mode at constant interblade phase angle and featured flutter instability in the first bending mode. The reduced frequencies ranged from 0.08 to 0.17 (based on full chord). The vibration was based on electromagnetic actuators: a spring type suspension was submitted to electromagnetic excitation. Further measurements were carried out on the same profile by Norryd and Bölcs (1997) in the linear cascade with 5 blades one of which oscillating in bending mode. The reduced frequencies were higher [0.22-0.61]. The effect of tip gap flow on the aeroelastic response was studied. It has been found that the local instantaneous response on the blade changed significantly, however the stability parameter was not modified.

A more advanced facility is suggested by Frey and Fleeter (1997). Oscillating blades are built into a rotating blade assembly providing results from a controlled blade vibration under rotation. A series of experimental influence coefficient technique was performed in order to quantify the effects of oscillation amplitude of a blade vibrating in torsion mode. It has been shown that amplitudes higher than 5deg leads to non-linear effects that are no longer negligible.

Körbächer (1996) conducted experiments of the unsteady flow in an oscillating annular compressor cascade with NACA3606 profile blades that could be vibrated independently. It has been shown that the superposition principle can be applied with a good accuracy for high subsonic flows and high incidence angles.

Numerical and experimental approaches for flutter prediction have been introduced. The next section is dedicated to the characteristics of space turbines.

1.5 Space turbines characteristics

As for all turbomachines, the main objective when designing rocket engines is to deliver a maximum of thrust using a minimum of fuel. Space turbine denotes here the turbines which are part of the turbopumps in liquid-propellants cryogenic rocket engines. The purpose of such turbopumps is to deliver the reactants to the thrust chamber at specified pressure. The cryogenic propellants, i.e. the fuel and the oxidizer, are typically liquid hydrogen and oxygen and are stored into two different tanks at very low temperature. A gas generator drives the turbine which drives the pumps. The propellants are thus pumped and then they are injected and burned in the combustion chamber. The combustion results in high-pressure and high-velocity stream of hot gases that are ejected through the nozzle. There exists different power cycles that defines how power is derived to feed propellants to the main combustion chamber; the more common types are included in Figure 1-4 (Olsson, 2006):

- the gas generator cycle: turbine exhaust gases are used to cool the nozzle and are then ejected to boost performance.
- the expander cycle avoids the turbine-drive gas losses of the gas-generator cycle by placing the turbine in series with the thrust chamber.

Liquid oxygen is widely used because it is a good oxidizer for a number of fuels giving high flame temperature and because it is reasonably dense and relatively inexpensive. It is often combined to liquid hydrogen as fuels because the combination provides high exhaust velocity with acceptable fuel consumption.

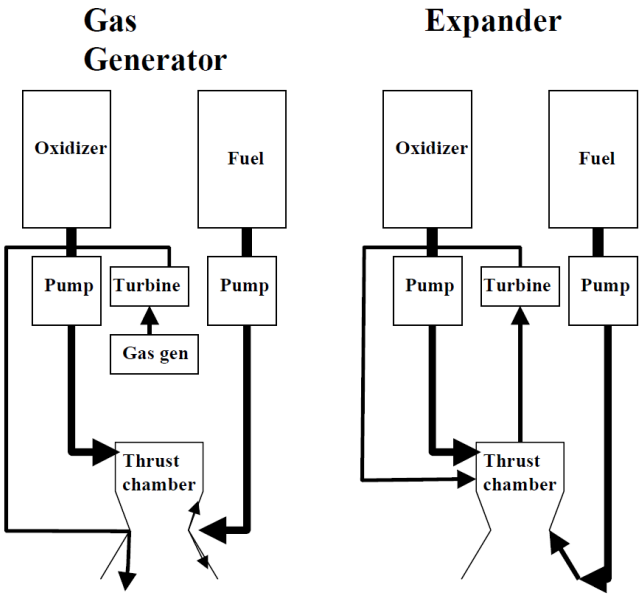

Figure 1-4: Liquid rocket engine cycles (Olsson, 2006)

At this point, the flutter issue has been identified and the existing tools for its prediction have been introduced. The next section is dedicated to formulate the problem and the strategy of investigation.

1.6 Objectives and method of attack

1.6.1 Objectives

Flutter in turbomachines remains immature because not well understood. Due to their high degree of complexity, the mechanisms responsible for its onset are at the limit or beyond the current capabilities of measurements and simulations. This results in uncertainties, which are difficult to accurately evaluate. Accordingly, a unique approach of the problem must be discarded in favor of methodologies accounting for various results from both analytical, experimental and numerical studies.

From an experimental point of view, aerodynamic damping measurement is limited by the use of simplified models that do not represent all the physics. For instance,

- the oscillation frequency reachable, due to mechanical issues of the actuator mechanism.
- the nature of the setup itself: circumferential modes and cut-on/cut-off conditions cannot be investigated in sector cascade.

From the numerical side, flutter prediction is limited by:

- the turbulence models: for situations where the turbulence is high such as separated flows, its applicability and relevance are still under investigations.
- computation of the propagating waves, especially for high frequencies, require spatial schemes with high degree of accuracy.
- the initialization of the simulations, especially the inlet boundary layer profiles.
- computational cost and power availability.

Furthermore, flutter is rather a critical issue for industries and does not provide a good advertising. This results in poor well-documented real cases. On the other hand, the lack of experimental data for 3D high subsonic flows makes the flutter apprehension even more challenging. As a result, though it seems pointless to state that the overall objective is to deeper understand flutter in turbomachines, it is indeed only a better knowledge that will enable to take it into account earlier in the design process. The present thesis contributes by investigating experimentally and numerically subsonic and supersonic flutters. First, this aims at highlighting primary aspects involved in the flutter mechanisms to better understand how to increase the aerodynamic damping for the future generation of industrial turbines and second, to provide a unique set of unsteady data for further investigations.

1.6.2 Method of attack

In the light of the aforementioned objectives, the study has been led as follows.

The experimental data will help the basic understanding of aeroelastic response to a prescribed motion in a 3D flow, and will also serve as a database for the validation of aerodynamic design tools. The aim is to experimentally obtain time-dependent pressures

on a vibrating turbine blade at realistic Mach numbers and reduced frequencies. A worldwide unique annular turbine sector cascade is employed, consisted of low pressure gas turbine profiles. The cascade is non-rotating. One blade in the cascade can be made oscillating at various modeshapes. The focus is put on two operating points defined through the outlet Mach number (0.4 and 0.8) and results in maximal reduced frequencies of 0.4 and 0.2 respectively. Different modeshapes are investigated, pure and combined modes in order to confirm the principle of linear superposition at different flow velocities and frequencies. Furthermore, hot-wire measurements are performed in order to also provide inlet conditions for numerical computations.

Then the aforementioned principle is applied on an industrial space turbine operated at low subsonic conditions. The choice of the turbine focuses on a typical new industrial configuration designed with blisk, which features both very high eigenfrequency and complex blade deformation originating from the blisk modeshape. The aim of using the linear superposition principle is to decompose the aerodynamic damping. The stability is analyzed with respect to the interblade phase angle and cut-on/cut-off modes.

Finally, after studying flutter in a "sane aerodynamic flow", but complex structural features, a second type of industrial space turbine is numerically investigated. The turbine consists of assembled bladed disk. The modeshape is of elementary nature, i.e. purely axial, however strong non-linearities come from the supersonic flow that implies shock wave/boundary layer interaction.

CFD computations are based on steady state computation (RANS) using Turb'Flow™ and unsteady computations, linearized in the frequency domain, using Turb'Lin™, which calculates the aerodynamic response to a prescribed motion of the blade assuming small perturbations.

Experimental and industrial turbines differ a lot and no direct comparisons are included. The main characteristics are summarize in Table 1-1. However, correlations are still possible:

- the experimental and the subsonic industrial turbine does not differ so much in terms of 2D blade shape and Mach number.

- the experimental and the supersonic industrial turbine are close in terms of reduced frequency.

	Experimental turbine	**Subsonic industrial turbine**	**Supersonic industrial turbine**
fluid	air (gas)	hydrogen (liquid)	oxygen (liquid)
Mach number	low to high subsonic	low subsonic	supersonic
aspect ratio	high	low	low
tip clearance	low	high	shrouded
reduced frequency	low	high	low

Table 1-1: Main characteristics of the different case studies

1.6.3 Contribution

The present thesis, started in November 2007, has been initiated by the "Centre National d'Etudes Spatiales", the French space agency (CNES) and Snecma with the goal to better understand aeroelastic instabilities in space turbines. The project involved different academic and industrial partners and was mainly carried out in the "Laboratoire de Mécanique des Fluides et d'Acoustique" (LMFA) at "Ecole Centrale de Lyon" (ECL), France, where the numerical part was performed using the numerical solvers Turb'Flow™ developed by the LMFA and Turb'Lin™ developed by the company Fluorem. The experimental part was conducted at the Division of Heat and Power Technology (HPT) at the Royal Institute of Technology (KTH), Sweden. The overall project was financially supported by CNES and Snecma.

Fluorem (2006) performed the computations before the beginning of this research project as well as the analytical decomposition presented in this thesis. The involvement of Fluorem consisted in performing CFD as well as discussing results. The involvement of HPT Division was to make accessible the flutter facility, to assist the different measurements and to provide post-processing programs for evaluation of the raw data.

The thesis has led to the following papers:

Ferria H.; Pacull F.; Aubert S.; Ferrand P.; Aknouche S.; Pouffary B.; 2009
”2D Elementary Geometric Decomposition to Study Flutter Motion of a Space Turbine Blisk”
Proceedings of ASME Turbo Expo 2009: Power for Land, Sea and Air, Orlando, Florida, USA.

Ferria H.; Ferrand P.; Delmas L.; Aubert S.; 2011
"Numerical investigation of supersonic flutter in space turbine based on unsteady computations linearized in the frequency domain in response to a prescribed blade motion"
International Forum of Aeroelasticity and Structural Dynamics, IFASD11, Paris, France.

Ferria H.; Ferrand P.; Pacull F.; Aubert S.; 2011
"Numerical investigation of flutter stability in subsonic space turbine blisk with emphasis on cut-on/cut-off modes and interblade phase angles"
The 10th International Symposium on Experimental and Computational Aerothermodynamic of Internal Flows, ISAIF10, Brussels, Belgium.

PART 1: EXPERIMENTAL APPROACH OF SUBSONIC FLUTTER

This first part is dedicated to experimental investigations of subsonic flutter. The test facility comprises an annular sector cascade of low pressure gas turbine profiles operated from low to high subsonic flows. One blade can be made oscillating at different 3D orthogonal modes as well as combination of two modes while the unsteady responses are measured in the influence coefficient domain.

This part is organized in two main chapters:

- the first chapter (chapter 2) presents the experimental setup of the unsteady pressure and hot-wire measurements.

- the second chapter (chapter 3) presents the experimental results. The steady and unsteady states are described and discussed.

Some minor CFD results are also presented for comparisons with measurements. However, only steady computations have been performed and therefore no correlations with unsteady experimental data are included. The focus has been put on the understanding of the aeroelastic response to a prescribed blade motion and more especially on the evaluation of the principle of linear superposition for different combined modes. The database will thus be used for further numerical investigations that are not part of the present thesis.

2 EXPERIMENTAL SETUP

This chapter presents experimental measurements for studying flutter in subsonic flows. The test facility is in use at the Division of Heat and Power Technology at the Royal Institute of Technology (KTH), Sweden; it has been designed and developed by Vogt (2005) for investigations of aeromechanic phenomena in low pressure turbine rotors. Aeroelastic responses are assessed in the influence coefficient domain by measuring the unsteady response to a prescribed motion originating from one blade oscillating in various 3D rigid-body modes (pure and combined). Turbulence measurements are also carried out to characterize the turbulence level at the inlet.

The chapter details successively the test facility, the test section, the test object, the conventions used, the blade oscillation mechanism. Then the hot-wire anemometry is described in the same manner.

2.1 Description of the test setup

This section is dedicated to the description of the test setup. First, the test facility, the test section and the test model are introduced and the conventions used are defined. Then the blade oscillation is described. Finally the measurement setup for flutter investigations are detailed.

2.1.1 Test facility

The tests have been performed in an exchangeable module connected to a large-scale screw compressor of 1MW power, providing a mass flow up to 5kg/s at 303K at a maximum 4bar pressure. A picture of the test facility is shown in Figure 2-1 whose the description is given in details by Vogt (2005).

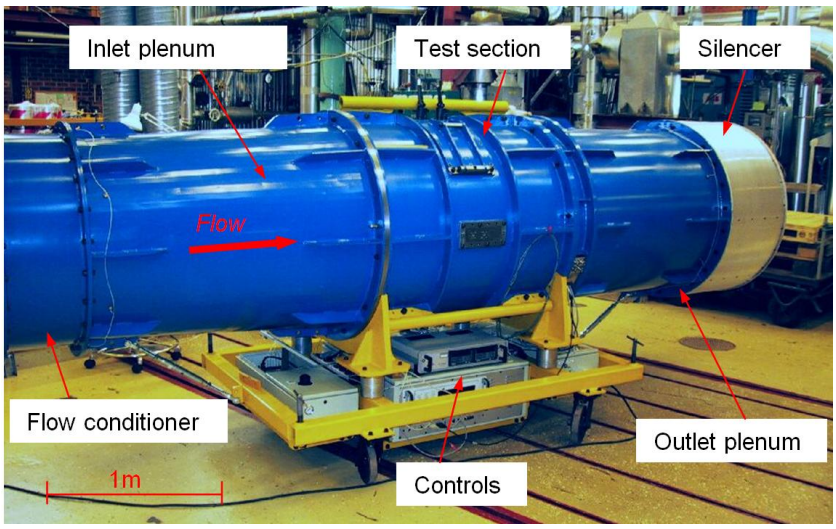

Figure 2-1: Test facility (Vogt, 2005)

The path of the flow through the facility is depicted in Figure 2-2 and is summarized below:

- the stationary flow conditions are first achieved in a fully circular plenum: the pressurized and pre-conditioned air is straightened and a setup of turbulence

meshes is used to reach a uniform turbulence level of about 0.5% and 2mm length scale.

- the flow is directed through a bell-mouth and a variable annular sector channel to the test section. The variability allows the control of inflow angle.
- the test section comprises seven freestanding blades with one full passage on either side, i.e. eight passages in total.
- the adjustable sidewalls are adapted such as to achieve periodic flow in the cascade.
- downstream of the cascade the flow discharges through an adjustable annular sector duct to a fully circular outlet plenum.

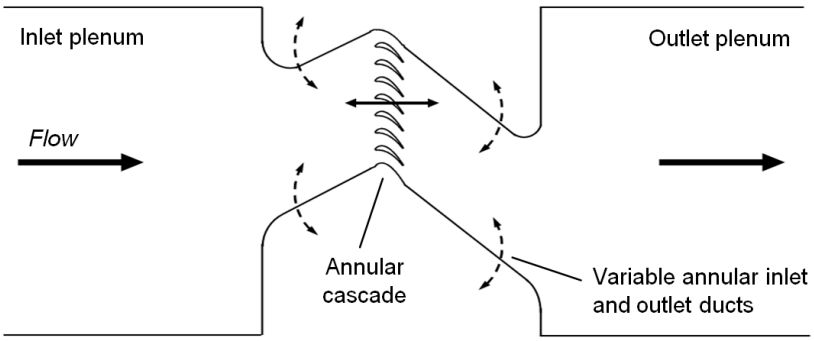

Figure 2-2: Flow path in the test rig (Vogt, 2005)

2.1.2 Test section

The test section includes an annular sector cascade of seven freestanding blades with one full passage on either side. The end walls are shaped as pressure and suction sides of the blade profile. The blade row is non-rotating that is to say there is no centrifugal forces as well as sheared flow conditions. Nevertheless, the annular shape of the setup leads to a radial pressure gradient. The test section has been designed such to allow fast exchange of the blades without dismantling the facility: the blade charging and locking mechanisms as well as the complete measurement system are located underneath the hub (Figure 2-3). All the blades feature a nominal tip clearance of 1% blade height and one of them can be made oscillating in controlled modes as rigid body.

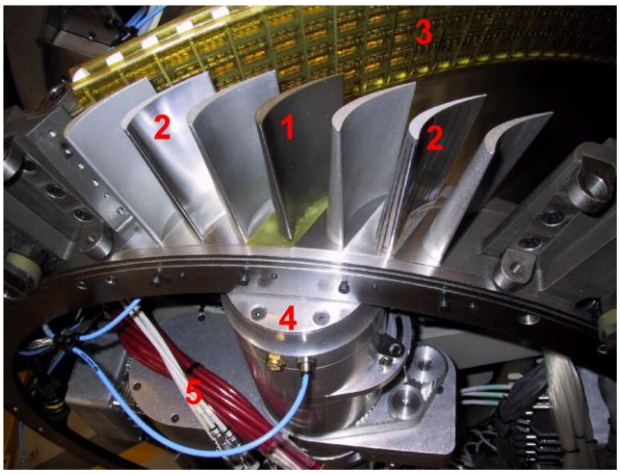

1: oscillating blade

2: non-oscillating blades

3: adjustable sidewall

4: actuator

5: instrumentations

Figure 2-3: Test section

2.1.3 Test model

The test object represents typical three-dimensional twisted and highly loaded low-pressure turbine rotor profiles. It is part of a blade row, which the geometry has been designed such to achieve realistic aerodynamic features in actual turbines. A set of non-oscillating blades and oscillating blades have been used: the first are milled from aluminium alloy (AI7075-T6) whereas the second are manufactured from titanium alloy (Ti6AI4V) and mounted by a swivel bearing onto a steel root. The blades have been hand polished in order to achieve a smooth surface with a maximum geometric deviation of 0.03mm (Vogt, 2005). The geometric parameters are given in Table 2-1. The test object and the 2D blade profile at 10%, 50% and 90% span are included in Figure 2-5. The model is also described in Figure 2-5 through:

- the passage width normalized by the pitch whose the minimum is around 35% axial chord.
- the section normalized by the section at the throat. A fluid particle flowing close to the suction side experiences the minimal section, i.e. the throat, at around 67% axial chord.

Parameter	Symbol	Value	Unit
real chord @ midspan	c	50	[mm]
axial chord @ midspan	c_{ax}	45	[mm]
span	S	97	[mm]
pitch @ midspan	p_c	4.5	[deg]
solidity @ midspan	p_c/c	0.68	[-]
aspect ratio	s/c	1.94	[-]
hub radius	R_{hub}	383	[mm]
shroud radius	R_{shr}	480	[mm]

Table 2-1: Blade profile parameters

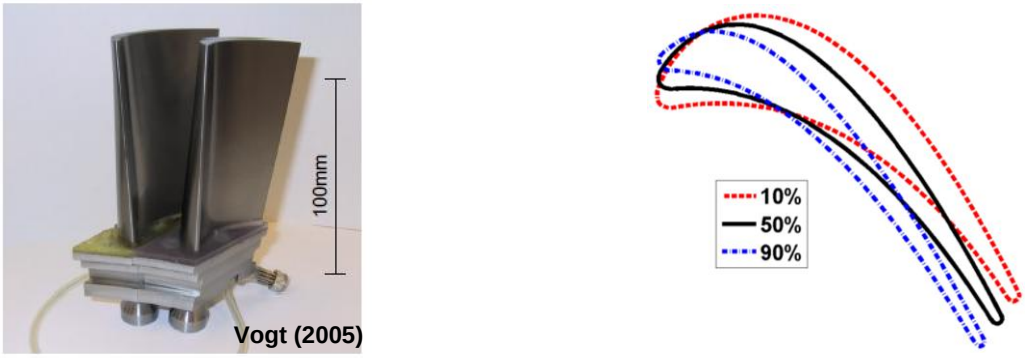

isometric view **profile sections**

Figure 2-4: Test object

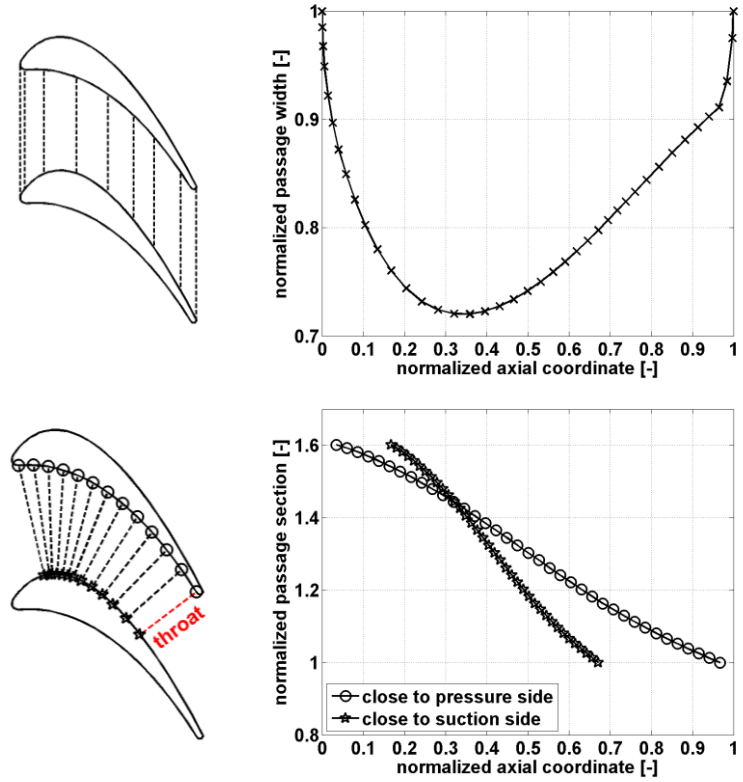

Figure 2-5: Flow passage characteristics

2.1.4 Conventions

Conventions of cascade coordinate, blade indexing, flow angles and blade oscillation are successively described below.

2.1.4.1 Test rig coordinate system

The cascade coordinates system is presented in Figure 2-6:

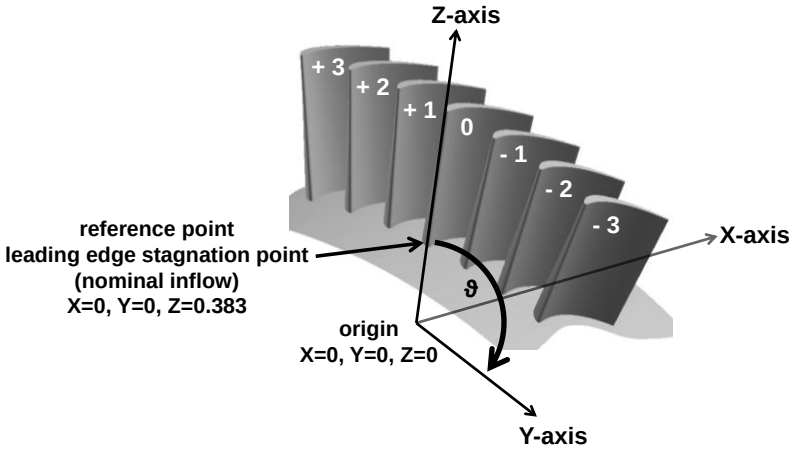

Figure 2-6: Test rig coordinate system

- the Z-axis is leading through the leading edge stagnation point at nominal inflow at hub of blade 0.

- the X-axis corresponds to the machine axis and is oriented in the main flow direction; the origin is located at the leading edge stagnation point at nominal inflow of blade 0.
- the Y-axis completes the coordinate system according to the right-hand rule.
- the polar angle ϑ of the respective cylindrical coordinate system is defined according to the right-hand rule from the X-axis in direction of negative blade indices.
- the radial direction is pointing from the origin outwards.

2.1.4.2 Cascade coordinates and blade indexing

The cascade contains seven blades indexing from -3 to +3 ascending in direction from pressure to suction side, i.e. in direction of negative polar angle ϑ. The oscillating blade corresponds to the center blade indexed 0. Figure 2-7 displays the indexing of blades in an unwrapped blade-to-blade view as well as the coordinate system based on axial, pitchwise and spanwise directions and normalized:

- the normalized axial coordinate results from the axial coordinate normalized by the axial chord at midspan.
- the normalized pitchwise results from the pitch normalized by the unwrapped blade pitch at respective radius.
- the normalized span results from the span normalized by the total local channel height.
- constant pitch lines correspond to stagnation lines.
- the direct surfaces of the oscillating blade, i.e. pressure side of blade +1 and suction side of blade -1, will be referred as primary surfaces.
- the surfaces facing away the oscillating blade, i.e. suction side of blade +1 and pressure side of blade -1, will be referred as secondary surfaces.

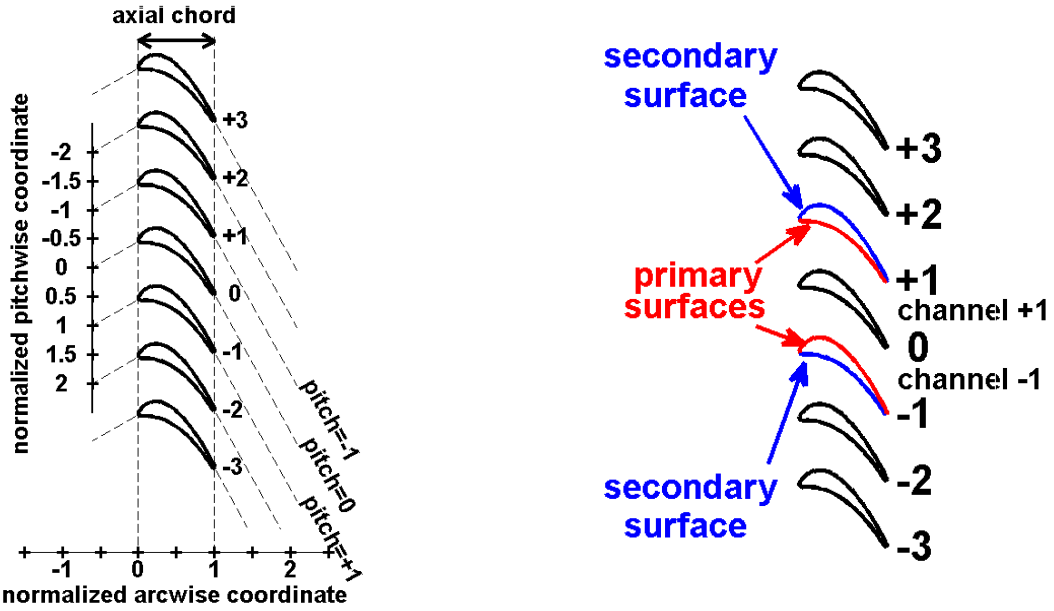

Figure 2-7: Cascade coordinates

2.1.4.3 Local coordinate system of blades

The blade surface is spanned by an arcwise local coordinate that follows the blade surface at constant span (Figure 2-8). The origin is set at the leading edge stagnation point (nominal inflow) at each span. Negative and positive branches span respectively the suction and pressure sides. The arcwise coordinate is normalized by the total local arc length.

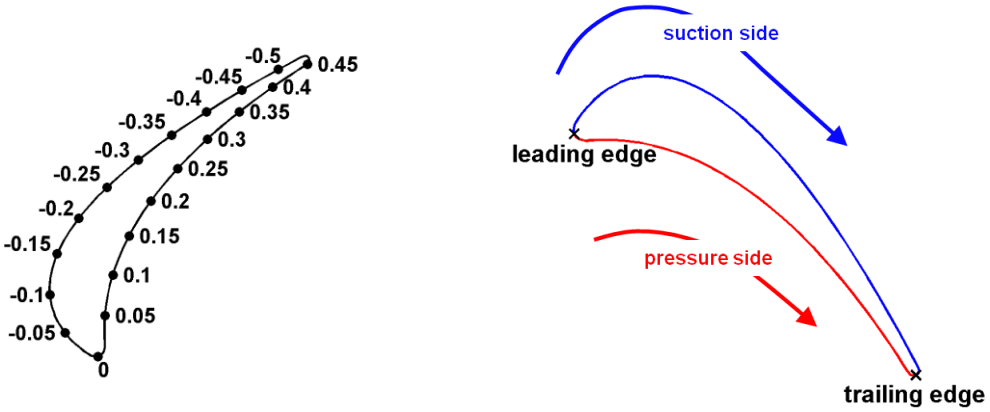

Figure 2-8: Arcwise coordinate at midspan

2.1.4.4 Convention of flow angles

The flow direction is characterized by yaw angle and pitch angle (Figure 2-9):

- the yaw angle α is the angle between the flow direction and the machine axis (positive in direction of positive polar angle ϑ).
- the pitch angle β is the angle of the flow direction in the axial-radial plane (positive in direction towards the blade tip).

Furthermore the 3 incidence angles investigated in the present thesis are also detailed. From nominal over off-design1 to off-design2, the incidence increases such that the boundary layer on the pressure side separates.

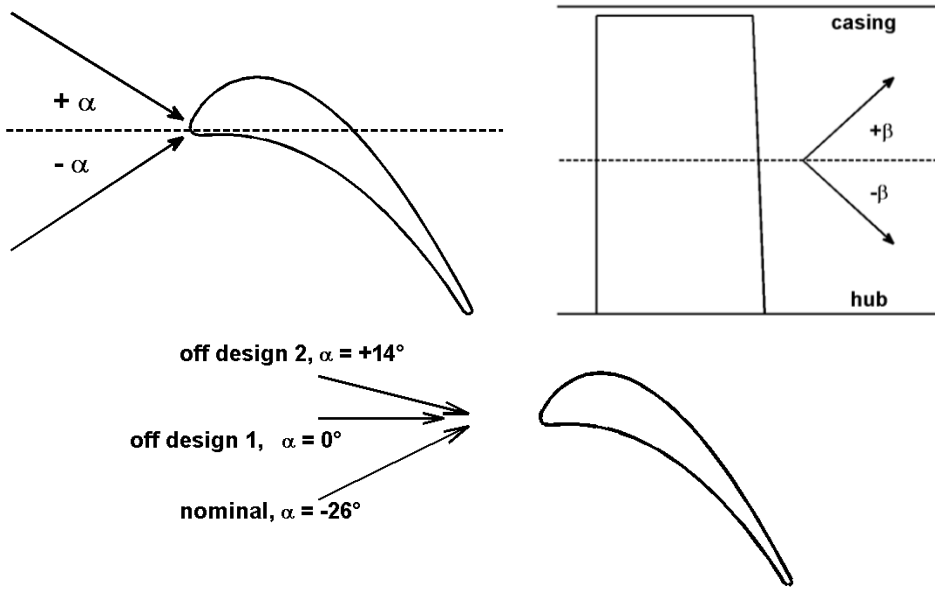

Figure 2-9: Definition of flow angles

2.1.4.5 Convention of blade oscillation

The blade motions are of pure-rigid nature and consist of a rotation around a rotation axis of the form

$$\alpha(t) = Ae^{i\omega t} \qquad \text{Eq. 2-1}$$

The directions of the three orthogonal modes are included in Figure 2-10:

- the center of rotation is defined with respect to the center of blade oscillation, i.e. the blade swivel bearing pivot point, located at X=0.0181m, Y=-0.0038m and Z=0.375m (global coordinates). In terms of local blade coordinates, the center of rotation is situated at 40% axial chord.
- bending modes oscillate around an axis of rotation lying normal to the radial direction that points to the center of blade oscillation.
- torsion mode oscillates aound an axis of rotation that collides with the radial direction pointing to the center of blade oscillation.

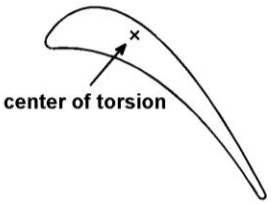

center of torsion located at 40% axial chord

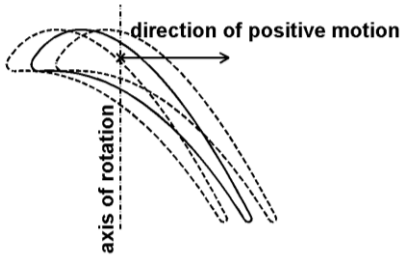

axial bending

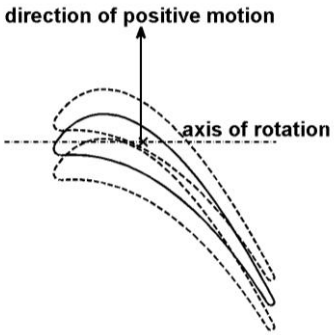

circumferential bending

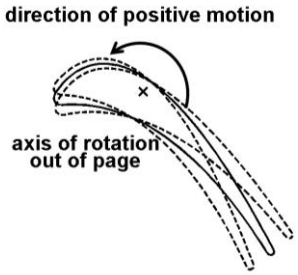

torsion

Figure 2-10: Blade oscillation convention

2.1.4.6 Convention of data presentation

The unsteady results are presented in a systematic way. The unsteady response is displayed along the normalized arcwise coordinate in terms of amplitude and phase as shown in Figure 2-11. The phase is defined positive when the unsteady pressure response is leading the blade motion and are treated such as to avoid 360deg jumps. The scale varies from plot to another for highlighting variations. The unsteady pressure is normalized by the blade oscillation in degrees for analyses of the unsteady response whereas for stability analyses, this is normalized on a per-mm and per-rad basis for bending and torsion modes respectively.

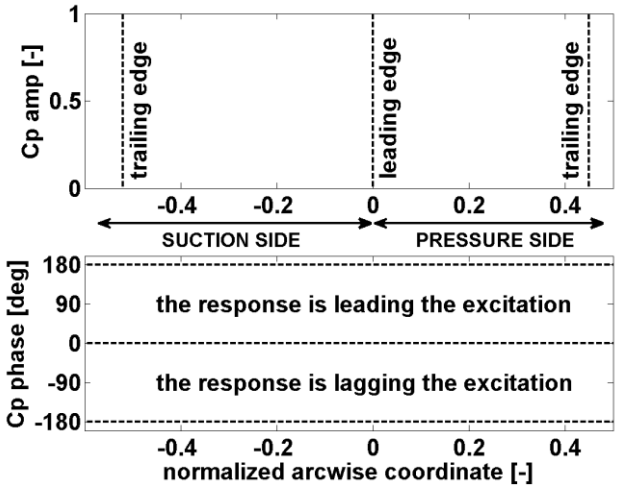

Figure 2-11: Convention of unsteady data presentation

2.1.5 Blade oscillation

2.1.5.1 Mechanical principle

Oscillations are achieved by pivoting the blade at a short distance below the hub. The blade can oscillate as rigid-body in torsion, bending or combination of torsion and bending. The setup is such that the bending amplitude increases from hub to tip and is of three-dimensional nature. The principle is sketched in Figure 2-12. The position of the swivel bearing is approximately on the stacking line of the profile at a radial distance of 8.2% blade span underneath the hub. As a result, oscillation of the blade is achieved without intruding parts into the test section. Vogt (2005) has developed the actuator mechanism and details can be found in (Vogt, 2005). A picture of the actuation mechanism is shown in Figure 2-13; it consists of two co-rotating circular eccentric cams actuating a guided actuator disk in a sinusoidal oscillatory movement. Pure bending modes are achieved by co-rotating the two cams at 0deg phase shift. The direction of the bending axis, i.e. axial or circumferential, can be set by turning the actuator. Combined bending and torsion modes are achieved by co-rotating the two cams at a phase shift between zero and 180deg. For the present measurements, the following modes have been considered:

- pure axial bending mode
- pure circumferential bending mode
- pure torsion mode
- combined axial bending/torsion
- combined circumferential bending/torsion

The combined modes are a combination of bending and torsion modes at 90deg out-of-phase and can be realized at different bending-to-torsion ratios.

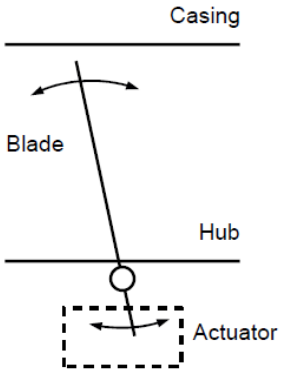

Figure 2-12: Blade oscillation principle (Vogt, 2005)

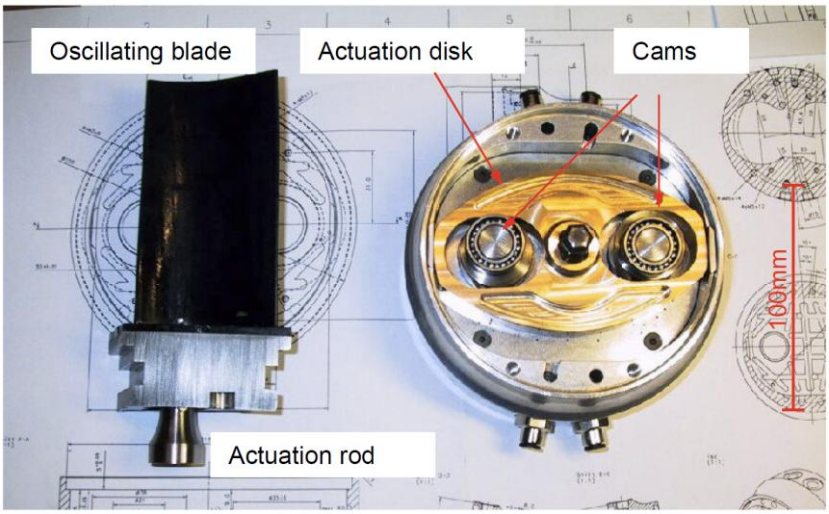

Figure 2-13: Oscillation actuator device (Vogt, 2005)

2.1.5.2 Measurement principle

The instantaneous dynamic geometry has been measured using time-resolved laser triangulation principle. The measurement setup is shown in Figure 2-14. Through the Plexiglas window, the laser beam is projected on one point of the blade surface. The reflected light is then projected back and a lens is used to create an image on a plane located on a positive sensitive detector (PSD). When the distance between the blade surface and the laser sensor changes, i.e. when the blade is oscillating, the angle between the laser beam and the reflected light varies as well.

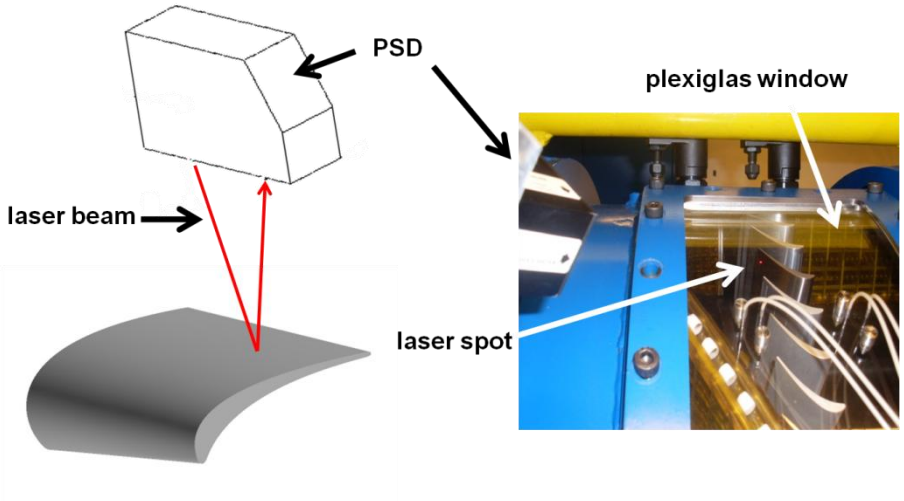

Figure 2-14: Measurement setup for laser triangulation

2.1.5.3 Calibration

Prior the unsteady pressure measurements a calibration has been performed for each pure mode in order to determine the relationship between the measured voltage from the laser and the angular motion about the torsion axis. Basically, it consists in measuring the blade motion by two different means: the first uses the aforementioned laser technique and returns a voltage whereas the second one uses an analog 0.1-20mm dial indicator,

also called "clock", which returns the motion amplitude in millimeters. The laser is thus calibrated by correlating the analog readout to the voltage. A measurement device has been manufactured to measure the blade motion while oscillating in pure axial, pure circumferential bending and pure torsion. A picture of the setup is shown in Figure 2-15, which also displays the position of the clock with respect to the measurement device according to the nature of the blade oscillation.

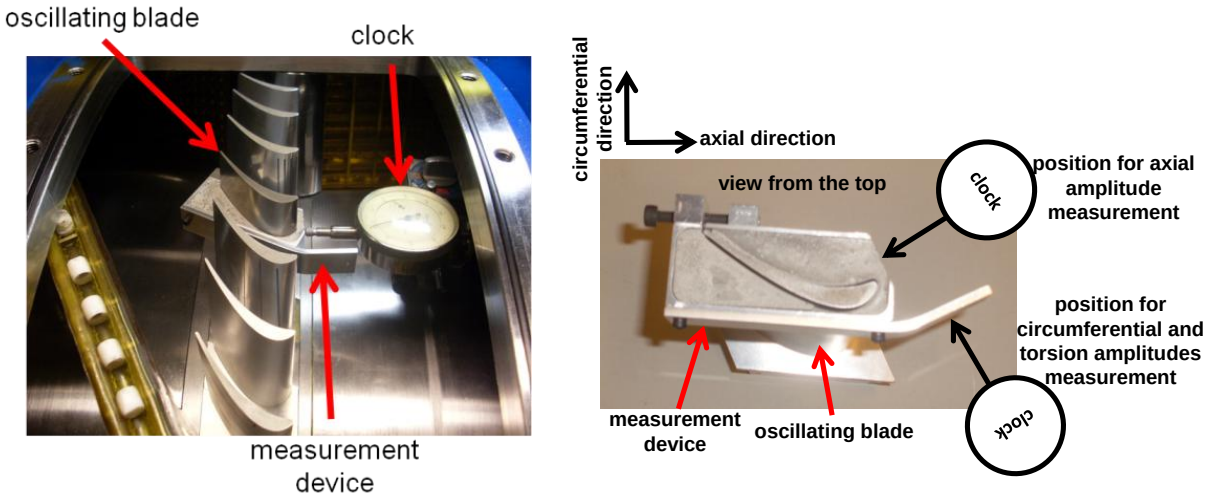

Figure 2-15: Principle of the laser calibration

The calibration curves are displayed in Figure 2-16. First, the laser signal in voltage is plotted versus the reading from the clock translated in degree at 3 runs for each modeshape.

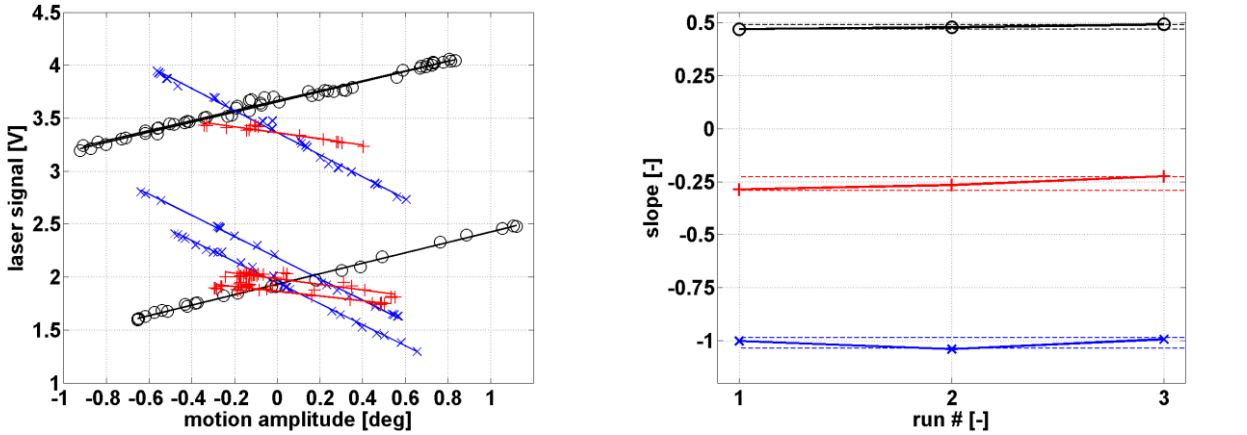

signals from the laser (in voltage) versus signal from the clock (in degree) at 3 different runs for each modeshape

the change in slope with respect to the runs and their respective standard deviation (dashed lines)

Figure 2-16: Calibration curves of the laser

The figure exhibits linear behaviors with rather small deviations of the motion amplitude range. It shall be noticed that:

- the number of runs has been limited to 3 due to mechanical considerations: the actuator mechanism deteriorates progressively while testing.

- each triplet of curves appear such that two of them are very close with each other whereas the third one is of different order of magnitude in terms of voltage. This is due to a change in cascade position.
- the effect of the Plexiglas window has not been evaluated due to the setup itself, the laser support being attached to the window.
- the main source of inaccuracy in such a measurement system is related to the laser spot on the blade surface. Firstly, since the laser beam goes through the Plexiglas window and secondly, since the blade surface quality may introduce changes in terms of size and reflectivity. This has not been evaluated.

2.1.5.4 Measurement during flutter test

While measuring the unsteady pressure induced by the blade oscillation, voltage issued from the laser is stored using the Kayser Threde KT8000 data acquisition system that is a digital high-speed data acquisition system. The system features 32 channels with programmable amplifiers, 14bit A/D conversion for each channel and a maximum sampling rate for 32 channels simultaneously of 200kHz. The sampling settings have been adjusted in such a way to have 200 periods for each oscillation frequency and the sampling frequency was set to 20kHz. The post-processing consisted of ensemble-averaging the data from each measurement position as shown in Figure 2-17 displaying signal of the blade oscillating at 43.75Hz. The oscillation appears sinusoidal and periodic with constant frequency that is well illustrated by a sharp peak.

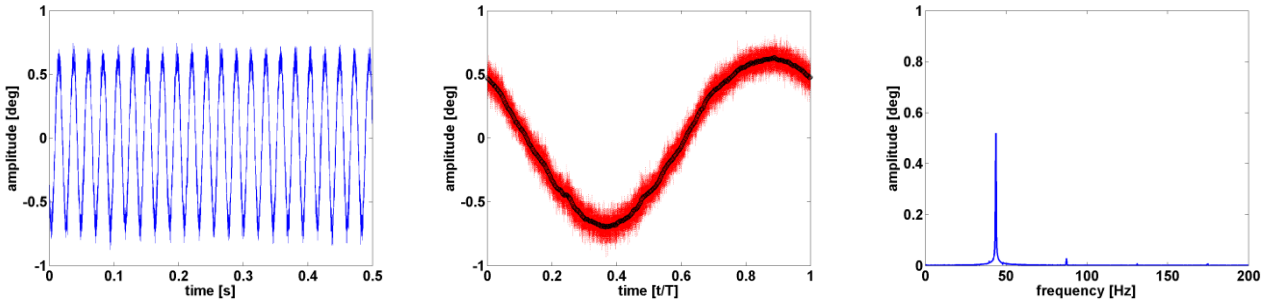

signal in time domain ensemble average signal in frequency domain

Figure 2-17: Blade oscillation signal

2.1.6 Measurement setup

The instrumentation of the test facility includes both steady and unsteady states measurement devices that are centrally controlled from an industrial master PC integrated to the test rig control unit and interfaced using Ethernet, GPIB and serial communications.

The steady state measurement includes the global flow parameters and blade loading. The global parameters, i.e. atmospheric pressure, mass flow, total inlet pressure, total inlet temperature and static outlet pressure are continuously monitored and logged for traceability purposes:

- The atmospheric pressure was monitored by means of Solartron high-sensitive barometer with an accuracy of 0.01%.
- The mass flow rate is measured by means of a standard differential orifice.

- Inlet total pressure and outlet static pressure were measured by 100kPa modules of a 16-channels PSI9016 system with an accuracy of 0.04% full scale (±40Pa) with atmospheric reference.
- A PT100 sensor connected in 4-wire circuit to a highly-quality conditioning module yielded total temperature data at 0.1K accuracy.

The blade loading is mapped by a total of 19 static taps of 0.4mm in diameter (0.8% chord) evenly distributed at midspan. The taps are connected by miniature stainless steel tubes (0.4mm inner diameter) to the lower end of the blade root and thereafter by Vinyl tubes (1.0mm and 1.6mm inner diameters) to the measurement equipment. Data have been acquired on blades ±1 at midspan (Figure 2-18) by means of a multi-channel PSI9010 system with atmospheric reference measured with the aforementioned Solartron barometer. Modules of 100kPa with an accuracy of 0.05% full scale (±50Pa) have been used.

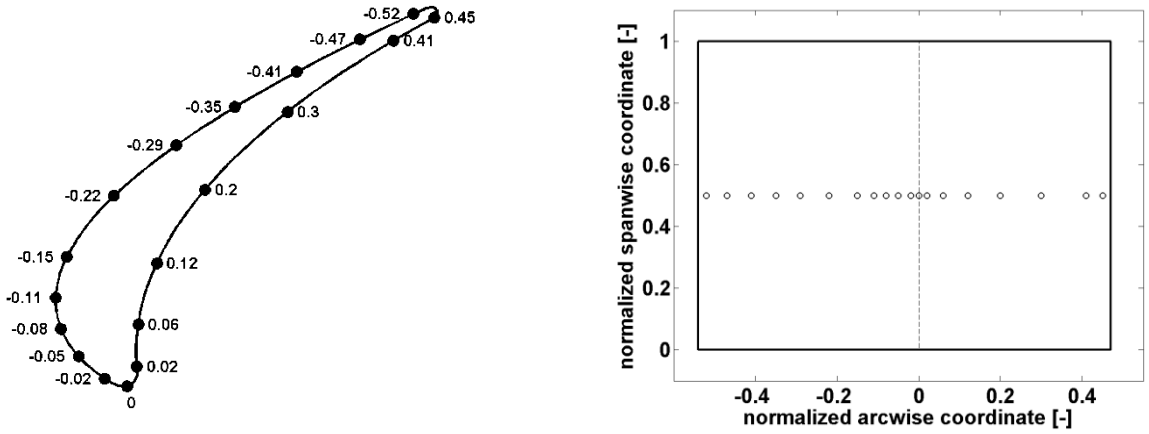

Figure 2-18: Arcwise distribution of static pressure taps at midspan

Fast-response pressure instrumentation is used for measuring the unsteady pressure on the blade surface. Due to space constraints and for practical reasons, recessed-mounted technique is employed: this avoids deterioration due to acceleration or temperature. The pressure transducers are placed underneath the blade hub, which is equipped with purpose-built receptable blocks (Figure 2-19), at typical distances of 50mm to 150mm from the measurement location.

The transfer coefficients provided by the non-oscillating neighbor blades are measured with the instrumented blades described above. This yields in 54 taps evenly distributed on 3 spanwise sections, i.e. 10%, 50%, and 90%, with 18 taps on each section. Data have been acquired on the two direct adjacent blades indexed ±1 at 10%, 50% and 90% span (Figure 2-20).

The oscillating blade is mapped by a total of 19 pressure taps of 0.4mm in diameter (0.8% chord) at midspan. The taps are connected by spark eroded miniature holes (0.9mm inner diameter) to the lower end of the blade and transferred by means of miniature PVC tubes (0.8mm inner diameter) to the lower end of the blade root. The PVC tubes are molded into the flexible transition part and harnessed such as to avoid any deteriorating effect during blade oscillation. Five taps are not useable for measurements due to poor transfer characteristics (Figure 2-21).

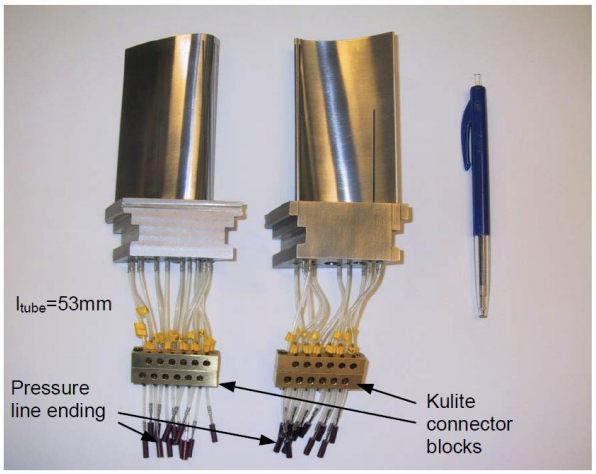

Figure 2-19: Instrumented non-oscillating blades (Vogt, 2004)

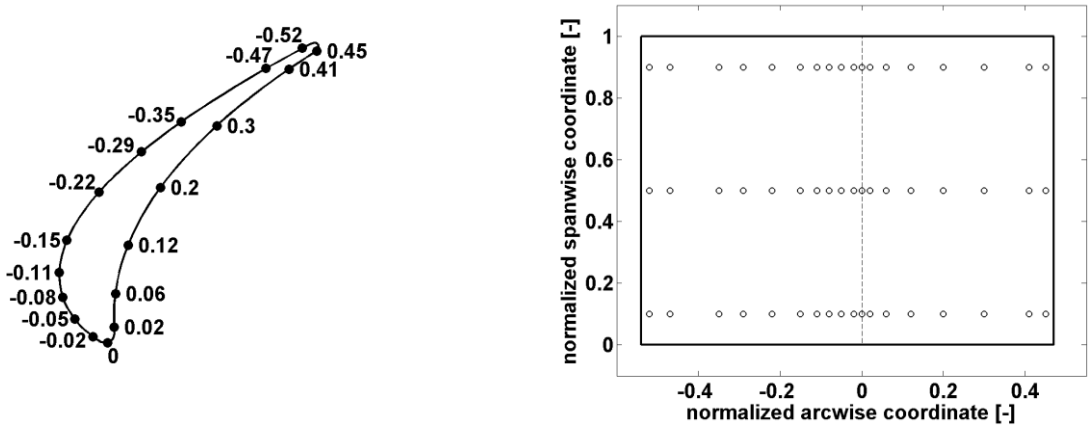

arcwise distribution at midspan mesh of taps on blade surface

Figure 2-20: Distribution of unsteady pressure taps on non-oscillating blade

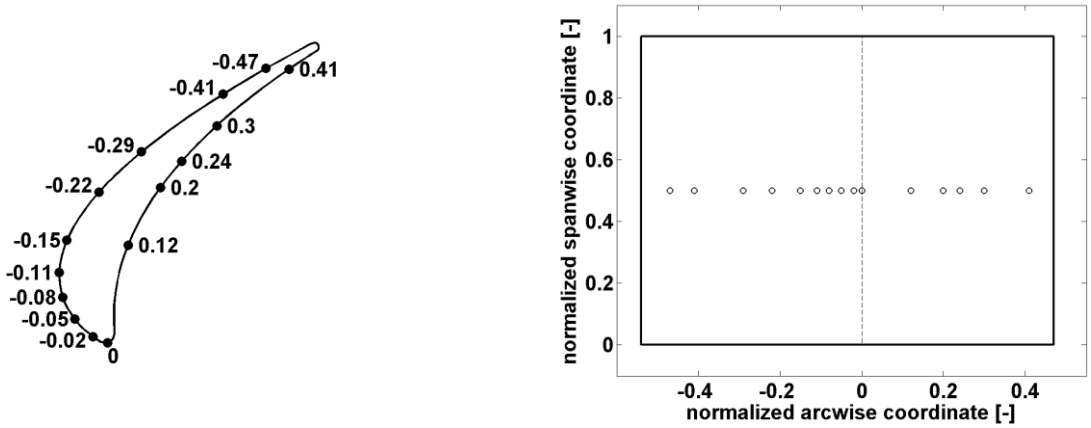

arcwise distribution at midspan mesh of taps on blade surface

Figure 2-21: Distribution of unsteady pressure measurement taps on oscillating blade

Kulite sensors of the type XCQ-062 and LQ-080 were used. The voltage from the sensors have been acquired with the aforementioned KT8000. The tests have been performed at a sampling of 20kHz. The accuracies of the sensors were determined to ±30Pa (Vogt, 2005) taking into account the static and dynamic transfer characteristic of the sensor. Furthermore, the resolution of the A/D-converted (30μV) adds ±50Pa and the transfer characteristic ±50Pa. As a result, the fast-response measurement setup presents ±130Pa accuracy. As mentioned, the instrumentation is such that Kulite transducers are placed underneath the hub. This technique leads to damping and lagging of the pressure fluctuation that must be determined with transfer functions through dynamic calibration. Dynamic calibration is performed with a in-house developed calibration apparatus (Vogt and Fransson, 2004). It consists of a nozzle air impacting on a rotating wheel with holes. The air pressure jet and the rotating speed of the motor can be controlled and thus allows a fine adjustment over the amplitude and frequency. A picture of the dynamic calibration unit and a sketch of the fluctuating pressure generator are shown in Figure 2-22.

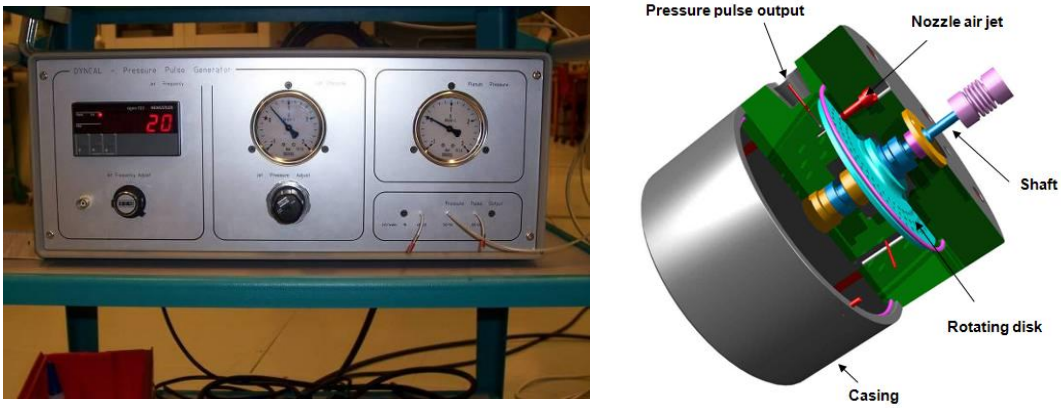

Figure 2-22: Dynamic calibration unit (left) and fluctuating pressure generator (right)

The signals from the sensor are treated such as to yield complex dynamic transfer properties in the frequency domain. The process consists in applying a periodic fluctuating pressure on the surface of the instrumented blade and then measuring both the input and the output signals. The dynamic calibration is performed up to 2kHz. Transfer characteristic at two arcwise positions (arc=-0.11 on suction side and arc=0.12 on pressure side) are included in Figure 2-23.

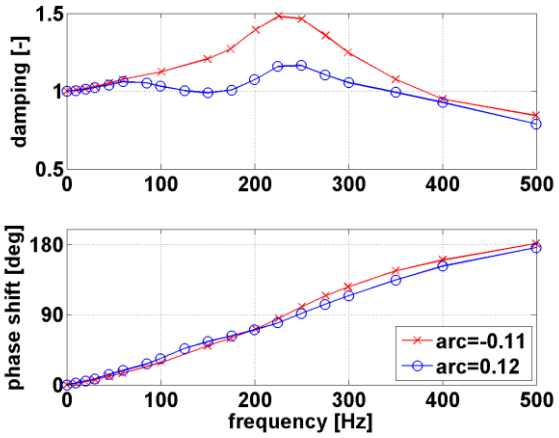

- amplitude ratio of 1 means that the measured amplitude and the amplitude at the tap are equal.
- amplitude ratio higher than 1 indicates an amplitude magnification.
- amplitude ratio lower than 1 denotes an amplitude damping.

Figure 2-23: Transfer characteristics at two arcwise positions

2.1.7 Data acquisition and data reduction procedure

Unsteady measurements were mastered by the main control unit and remotely acquired by a built-in PC of the aforementioned high-speed data acquisition system at a rate of 20kHz. The steps of the data reduction procedure are the following:

- determination of the exact blade oscillation (frequency and amplitude) from signal analysis of the laser signal.
- ensemble averaging of unsteady pressure data (N=200 periods) with respect to the oscillation period,

$$\tilde{p}_{EA}(x,y,z,t) = \frac{1}{N}\sum_{n=0}^{N} p(x,y,z,t_0 + nT) \qquad \text{Eq. 2-2}$$

- normalizing of the unsteady pressure by inlet dynamic head and oscillation amplitude in order to define the unsteady pressure coefficient. The reference dynamic head is defined as the difference between total pressure in the settling chamber and static pressure at 40% axial chord upstream of the cascade.

$$\tilde{C}_P(x,y,z,t) = \frac{\tilde{p}_{EA}(x,y,z,t)}{A \cdot p_{dyn,ref}} \qquad \text{Eq. 2-3}$$

- signal analysis of unsteady pressure coefficient in order to provide first harmonic amplitude and phase.

$$\tilde{C}_p(x,y,z,t) = \hat{C}_p(x,y,z) \cdot e^{i\left(\omega t + \varphi_{C_{p\to A}}\right)} \qquad \text{Eq. 2-4}$$

Figure 2-24 displays raw data signals from blade motion and two transducers located on the suction side at arc=-0.11 and on the pressure side at arc=0.12 (1st, 2nd and 3rd window respectively). They are plotted both in the time and frequency domains and show good sinusoidal shape. The pressure signals in time domain exhibit a slight modulation suggesting a frequency in addition to the fundamental natural frequency; however, in spectral domain the preponderance of the fundamental frequency is clearly evidenced.

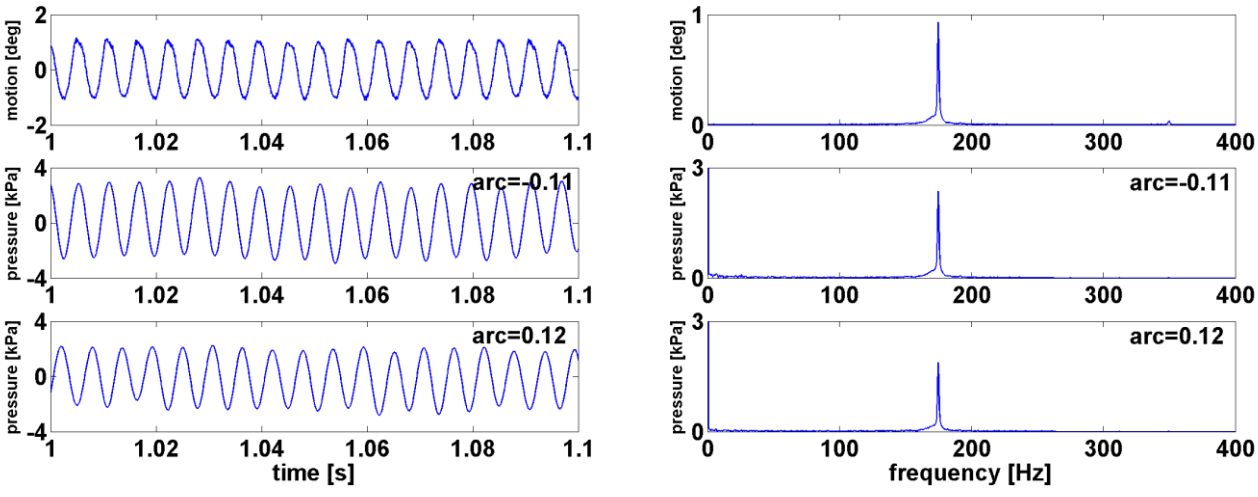

Figure 2-24: Raw signals of motion and pressures, f=175Hz

Finally, Figure 2-25 shows raw data from the aforementioned transducers and ensemble averaged-data: all samples, i.e. over 200 periods, are superposed in a single fundamental period. This highlights the scatter of the measurements through the size of the red band and demonstrates the high quality of the measures.

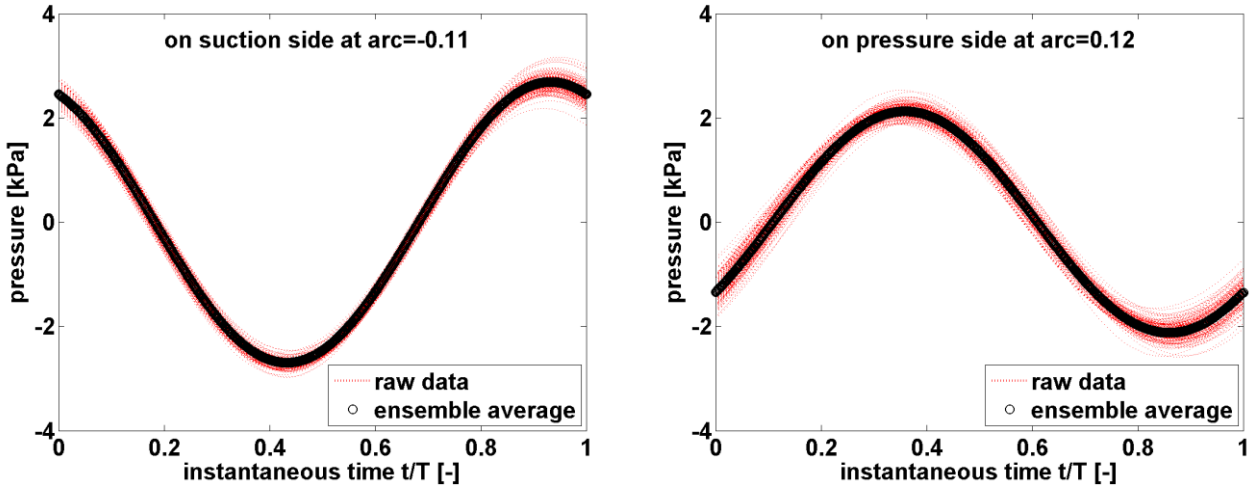

Figure 2-25: Ensemble average of raw data from pressure transducers

This section was dedicated to the description of the test setup. The test facility, the test section and the test model have been presented and the conventions used defined. Then the blade oscillation mechanism has been described. Finally the measurement setup for flutter investigations have been detailed. The next section is dedicated to the hot-wire anemometry for the evaluation of the inlet conditions.

2.2 Hot-wire anemometry

Constant Temperature Anemometry (CTA) has been employed to evaluate turbulence level and boundary layer profile upstream of the cascade. Although this is an intrusive technique, HWA is easy to put in place and is relative low cost: its strongest points are its high spatial and temporal resolutions. This section presents the HWA measurements carried out for the evaluation of the inlet conditions. First, a general description of the principle, the system and the probe are given. Then the probe calibration is introduced.

2.2.1 General description

2.2.1.1 Principle

Temperature anemometers measure the flow velocity by detecting the heat transfer of an electrically heated sensor exposed to a fluid flow. The system aims at keeping the temperature constant and the power necessary to keep the temperature constant is measured and is related to the flow velocity according to the calibration law. A CTA consists of a Wheatstone bridge and amplifier circuit that controls a tiny wire at constant temperature. As a fluid flow passes over the heated sensor, the amplifier senses the bridge off-balance and adjusts the voltage to the top of the bridge, keeping the bridge in balance. The principle is sketched in Figure 2-26:

- the adjustable resistor is set to the resistance desired during operation.
- the 2 other legs of the bridge have the same resistance.
- the servo amplifier keeps the error voltage to zero by adjusting the bridge voltage such that the current through the probe heats the sensor up to the temperature which gives the desired resistance.

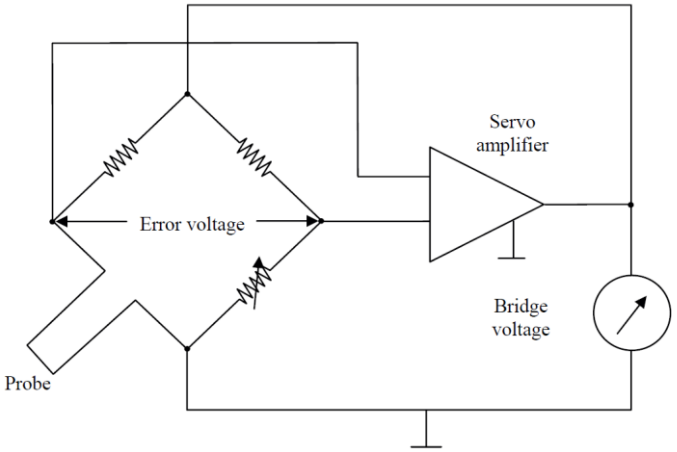

Figure 2-26: Principle of Constant Temperature Anemometers (TSI, 2000)

2.2.1.2 System overview

The IFA300 system is a fully-integrated, thermal anemometer-based system that measures mean and fluctuating velocity components as well as turbulence in fluid flows. The IFA300 system provides up to 300kHz frequency response, depending on the sensor used. The module is designed with a built-in thermocouple circuit for measuring fluid temperature and for making temperature corrections. Setup is software-controlled via a RS-232 interface. The IFA300 unit contains one microprocessor which controls settings of the anemometer. An RS-232 interface is used to send commands from the computer to the microprocessor. Each channel of anemometry contains a single bridge circuit and signal conditioner. The bridge circuit includes the Smartune technology (TSI, 2000) that automatically optimizes the frequency response and prevents oscillations which may damage the sensor. Therefore, the bridge does not require tuning for frequency response regardless of the type of sensor used and the length of the cable. Smartune constantly monitors the bridge voltage and feeds a signal back to the amplifier circuit maintaining the frequency response based on the operating temperature and sensor type. Automated overheat ratio control and Smartune bridge optimization simplify the overall package by eliminating the numerous potentiometer adjustments.

2.2.1.3 HWA probe

A picture of the probe used within this project is displayed in Figure 2-27. This is a 90deg sensor perpendicular to probe axis manufactured by Dantec (9055P0141) consisting of one single sensor, which is a thin wire suspended between two prongs also called needles. Wire sensors have high flow sensitivity and the highest frequency response. The prongs are made of stainless steel and tapered, providing end surface of around 0.1mm in diameter to which the wire are spot-welded. Miniature wire probe has been used (Figure 2-27) here: it has 5µm diameter, 1.25mm long platinum-plated tungsten wire sensor. The wire is welded directly to the prongs and the entire wire length acts as a sensor. This is

recommended for most measurements in one- or two-dimensional flows of low turbulence intensity (Dantec, 2005). Characteristics of the probe are summarized in Table 2-2.

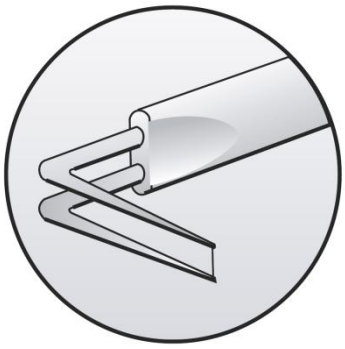

Figure 2-27: Miniature wire probe (Dantec)

sensor material	platinum-plated tungsten
sensor dimensions	5µm diameter(d), 1.25mm long (l)
aspect ratio (l/d)	250
maximal sensor temperature	300°C
maximum ambient temperature	150°C
minimum velocity	0.20m/s
maximum velocity	500m/s
frequency limit	150kHz

Table 2-2: Probe characteristics

2.2.2 Probe calibration

2.2.2.1 Calibration principle

A major step in any thermal anemometry measurement involves calibrating the probe in order to relate voltage and velocity. The conventional way of calibrating hot-wire probes consists of mounting the probe within a laminar flow as clean as possible. Then it consists in reading the output voltage of the anemometer over the velocity range of interest. The different flow velocities must be measured simultaneously by an independent device. Then the output voltage from the anemometer must be translated into velocity, the voltage varying non-linearly with velocity. Furthermore, when measuring, the effect of sensor orientation is negligible as long as the sensor is placed identically with respect to the flow during calibration and measurement. The misalignment is normally so small that it may be neglected as an error source (Jørgensen, 2002).

2.2.2.2 Calibration facility

Calibrations have been performed in the VM100 transonic wind tunnel facility, which in use at the Division of Heat and Power Technology at KTH. It consists of a settling chamber equipped with screens and honey combs, located 1.5m upstream of the test section, which is 100x110mm. A first contraction in the horizontal plane guides the air flow into a 250mm high and 100mm wide channel. A second contraction in the vertical plane then re-accelerates the flow 30mm upstream of the test section. The air supply facility consists of the aforementioned screw compressor. The mass flow as well as the pressure level are controlled by adjusting different valves as illustrated in Figure 2-28. As a result, different inlet Mach numbers can be reached (from 0 to 0.95). The velocity has been computed by measuring the total pressure in the settling chamber and the static pressure on the sidewall of the test section. The position of the probe has been fixed with the aim of a laser beam in order to position the probe as accurate as possible. The static pressure was

measured with the PSI-9016 system with an accuracy of ±0.05% of the full scale of its 16 channels. The pressures were measured with the 100kPa-range channels (±50Pa) with atmospheric reference. The atmospheric pressure was measured with the aforementioned Solartron high sensitive barometer with an accuracy of ±0.01% (±11.5Pa).

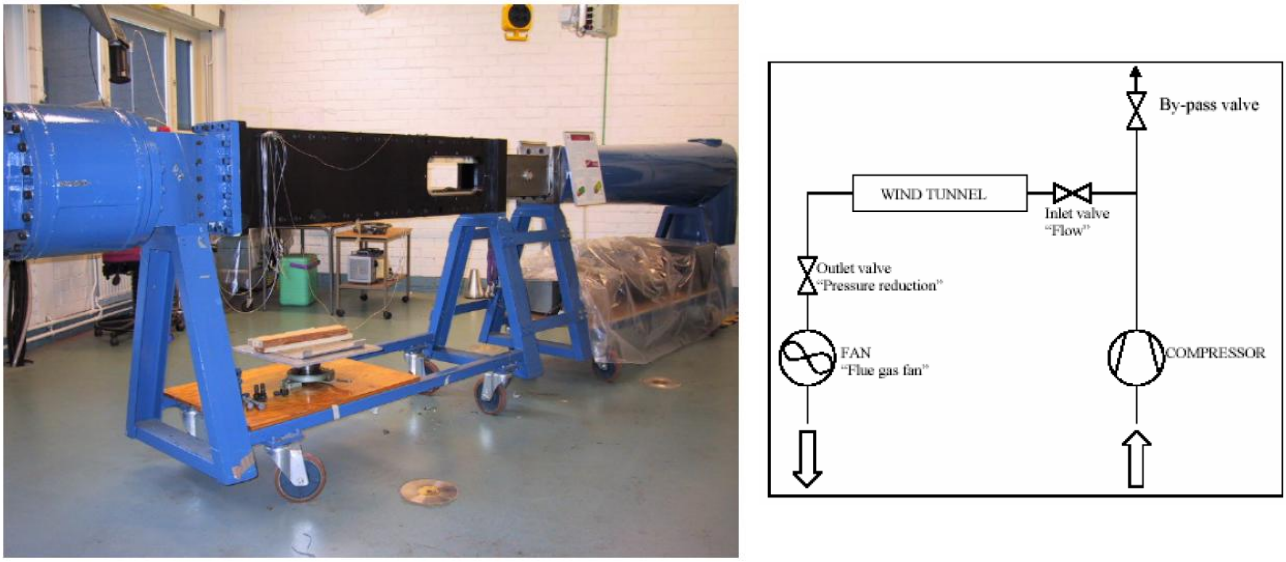

Figure 2-28: VM100 wind tunnel

2.2.2.3 Calibration curve

King's law is the most well-known of the heat transfer laws used in hot-wire anemometry (Bruun, 1995), the relationship is assumed to be of the form $E = f(V)$ (Eq. 2-5),

$$E^2 = K_1 + K_2 V^n \qquad \text{Eq. 2-5}$$

where E is the anemometer output voltage measured across the Wheatstone bridge, V is the fluid velocity, and K_1 and K_2 are constants. The fluid velocity is therefore obtained by carrying out an inversion process $V = f^{-1}(E)$. Polynomial curve fits can also be used as follows ($A, B, C, D, \ldots$ are constants),

$$V = A + BE + CE^2 + DE^3 + \cdots \qquad \text{Eq. 2-6}$$

Expressing the velocity in such way simplifies the computation of fluid velocity since this can be obtained directly from Eq. 2-6. Figure 2-29 shows the calibration curve within the expected velocity range, i.e. from 0 to 140m/s. The calibration data is curve fit with n-order polynomial, n varying from 4 to 9. The residuals are also plotted in the right hand side figure. The output voltage have been measured at 16 velocities. The more the data points, the higher the order. Calibration coefficients result finally from the 9th order polynomial.

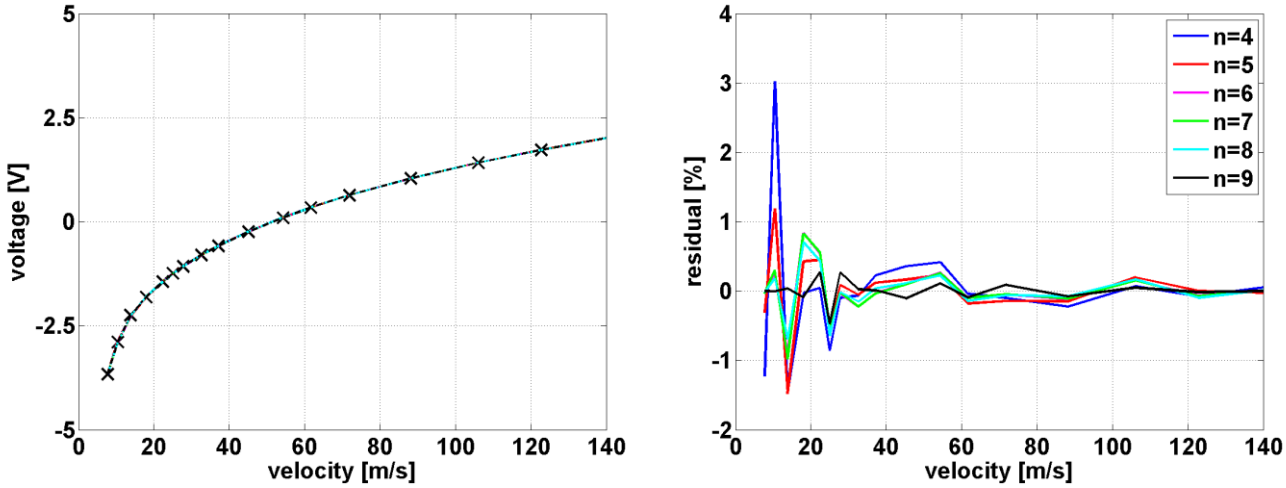

Figure 2-29: Calibration curve of hot-wire probe

2.2.2.4 Data reduction

Data measured with HWA are typically reduced to statistical quantities which remains the best way to characterize the behavior of scattered experimental data. Assuming stationary random processes as ergodic, i.e. a random process in which the statistical properties form a single time-serie will approach define limits independent of the particular series as the length of the series increases, the general formula for the k^{th} moment about the origin is given by

$$M_k(x_i, 0) = \frac{1}{n}\sum_{i=1}^{n} x^k \qquad \text{Eq. 2-7}$$

where x_i is the i^{th} data point in the sequence x of length x. The term x^k is the k^{th} power of x_i. As a result, the following statistical quantities are considered:

- the arithmetic mean: this denotes the average of a distribution,

$$\bar{x} = M_1 \qquad \text{Eq. 2-8}$$

- the normal stress or variance (second moment about the mean): this describes how far values lie from the mean,

$$\mu_2 = M_2 - M_1^2 \qquad \text{Eq. 2-9}$$

- the standard deviation, also called RMS (root-mean-square) is defined as the square root of the variance,

$$\sigma = \sqrt{\mu_2} \qquad \text{Eq. 2-10}$$

- the turbulence intensity,

$$Tu = \left(\frac{\sigma}{\bar{x}}\right) \times 100 \qquad \text{Eq. 2-11}$$

2.3 Conclusion

This chapter was dedicated to the overall description of the experimental setup. The test facility, the test section, the test object have been described as well as the different measuring techniques. Flutter investigations are based on unsteady pressure measurements in response to a prescribed blade motion. The inlet conditions in terms of turbulence level and boundary layer profiles are evaluated by mean of hot-wire anemometry. The next chapter is dedicated to the presentation of the overall test results.

3 EXPERIMENTAL RESULTS

This chapter presents the overall results of steady and unsteady measurements. It is organized as follows:

- the operating points are firstly described.
- the steady state is exposed through blade loadings and inlet conditions.
- unsteady responses are investigated at midspan with respect to the following parameters: modeshape, reduced frequency, velocity, incidence. Three-dimensional effects are also evaluated.
- then the linear combination principle is verified.
- finally, the unsteady response is discussed in terms of stability.

3.1 Operating conditions

The operating point is reached by adjusting the mass flow and consequently the inlet total pressure. The total temperature is kept constant. As mentioned previously, the experimental campaign presented in this thesis is based on previous measurements (Vogt, 2005; Glodic et al., 2009). As a result, operating points were set according to the aforementioned works. Four oscillation blade frequencies have been investigated resulting to the reduced frequencies range [0.05; 0.4]. The maximal oscillation frequency has been restricted to 175Hz due to mechanical issues. Two outlet Mach numbers have been considered 0.4 and 0.8, referenced M04 and M08 respectively. Moreover the incidence angle varied from nominal over off-design1 to off-design2, referenced nom, off1 and off2 respectively. An overview of the entire database is presented in Table 3-1, the shaded cells give the values from Vogt (2005).

PARAMETER	SYMBOL	M04			M08			UNIT
		nom	***off1***	***off2***	***nom***	***off1***	***off2***	
mass flow	$\dot{m}$	2.4	2.4	2.4	4.9	4.9	4.9	[kg/s]
		2.36	2.36	2.36	4.89	4.89	4.89	
total temperature	T_{t1}	303	303	303	303	303	303	[K]
		303	303	303	303	303	303	
inlet total pressure	P_{t1}	111.7	111.9	112.0	153.3	156.5	155.0	[kPa]
		112.3	112.6	112.8	160.6	163.7	165.0	
outlet static pressure	P_{s2}	102.0	102.0	102.0	106.4	106.4	106.4	[kPa]
		102.9	102.9	102.9	107.5	107.5	107.5	
pressure ratio	π	1.095	1.097	1.098	1.441	1.471	1.457	[-]
		1.091	1.094	1.096	1.494	1.523	1.535	
maximal reduced frequency	k_{max}	0.4	0.4	0.4	0.2	0.2	0.2	[-]
		0.5	0.5	0.5	0.3	0.3	0.3	

Table 3-1: Test conditions

Steady data have been assessed at midspan on blades ±1 at M04 and then completed with CFD computations. Unsteady responses have been acquired on oscillating blade 0 and its direct neighbors (blades ±1). The next section presents the steady state results.

3.2 Steady state results

To reduce the measurement efforts, steady state has been experimentally investigated at M04 on blades ±1 at midspan and nominal incidence angle, and then compared to CFD results. The very good agreement has confirmed this approach and the steady state analysis is therefore mostly based on simulations as well as on previous campaigns.

3.2.1 Blade loading

Steady blade loading data for the outlet Mach number 0.4 at nominal incidence angle and 50% span is shown in Figure 3-1 through the static pressure coefficient on blades ±1. The distribution shows a high decrease on the fore suction side around the leading edge due to the local blade curvature resulting in high flow acceleration. This is followed by a suction peak around arc=-0.11. This arcwise position corresponds to the minimal passage width. Then, the loading is slightly increasing from the suction peak to the trailing edge. On pressure side, the static pressure decreases from the leading to trailing edge due to steady flow acceleration. The static pressure deviation with respect to the mean value shows that the non-periodicity between the two blades is lower than 1%.

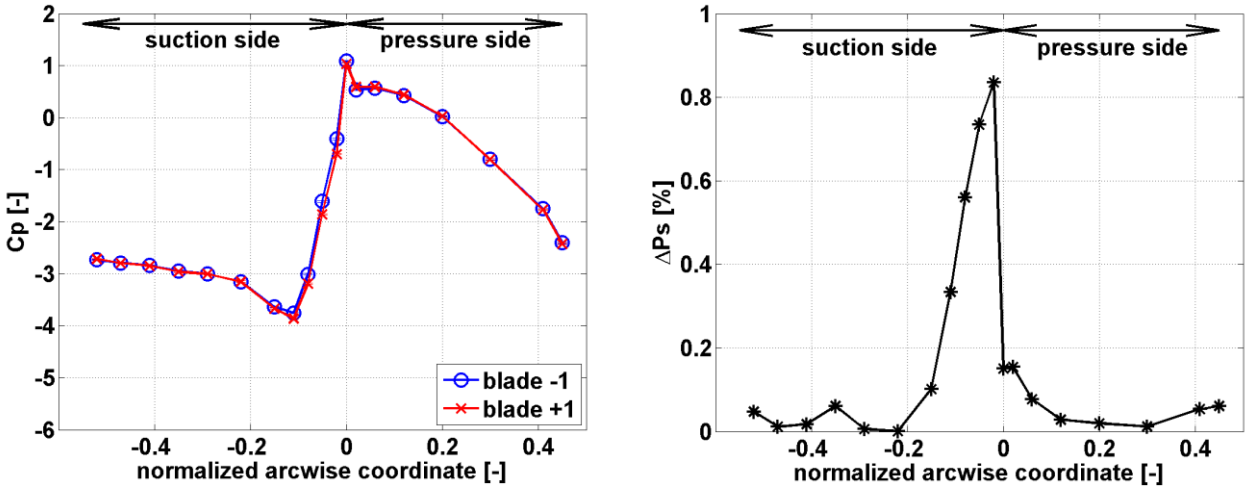

Figure 3-1: Steady blade loading at midspan, M04, nom

The steady state at midspan, nominal and M04 only has been considered; it has been decided as a strategy to put the measurements effort on the unsteady part because of previous recent steady measurements (Glodic et al., 2009); the results from the different set of steady data (Glodic et al., 2009; Vogt, 2005) have shown very similar features with each other. Therefore, in order to better understand the unsteady response presented in the next section, the main features reported by Vogt (2005) from pressure measurements and flow visualizations are summarized below:

- the blades exhibit uniformly high loading with suction peak at arc=-0.11. Flow visualizations highlighted that this arcwise position coincides to flow transition from laminar to turbulent.

- the fore suction side is characterized by strong acceleration of the flow from the leading edge to the aforementioned suction peak.
- the presence of a radial pressure gradient results in increasing the blade loading with increasing span.
- a corner vortex is generated at the hub leading to an upwash of the boundary layer onto the suction side.
- a tip corner vortex is generated driven by the jet-like leakage flow over the blade tip.
- a separation bubble is present on the fore suction side starting at the leading edge and limited to a small region close to the hub.

3.2.2 Numerical results

Computations parameters are described in Appendix E. The steady computations at M04 are included in Figure 3-2 in terms of steady static pressure coefficient and Mach number at midspan and in Figure 3-3 with the steady static pressure coefficient (at 10%, 50% and 90% span) along the normalized arcwise coordinate as well as on the blade surface in a 3D view. The aforementioned experimental data is also superposed. The figures suggest the following:

- numerical results and test data are in very good agreement.
- the static pressure gradually increases from hub to tip due to the radial pressure gradient resulting from the annular shape of the cascade.
- the peak position on the fore suction side moves from arc=-0.08 over arc=-0.11 to arc=-0.15 at 90%, 50% and 10% span respectively due to the 3D twisted shape of the blade and reveals the extent of the acceleration zone originating from the blade curvature.
- on suction side, right downstream the suction peak, the static pressure slightly increases towards the trailing edge.
- on pressure side, the static pressure decreases from the leading to trailing edge. Close to hub, the coefficient drops locally at arc=-0.014. Vogt (2005) reported this behavior and interpreted it, through flow visualizations, as a small local separation bubble due to the fact that the inflow is constant over the span resulting in negative incidence close to the hub.

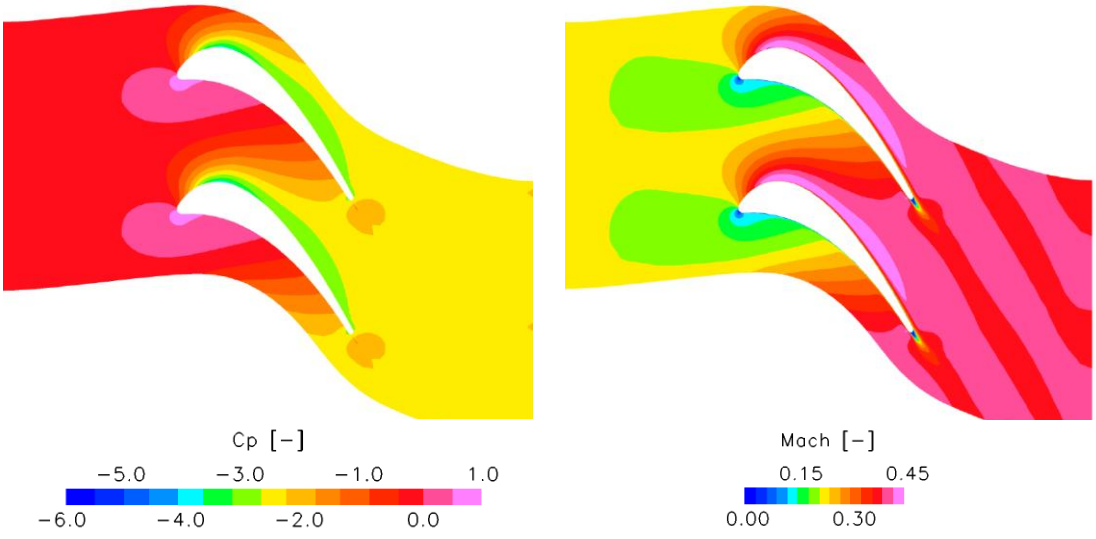

Figure 3-2: Steady Cp and Mach number, M04, nom, 50%span (CFD)

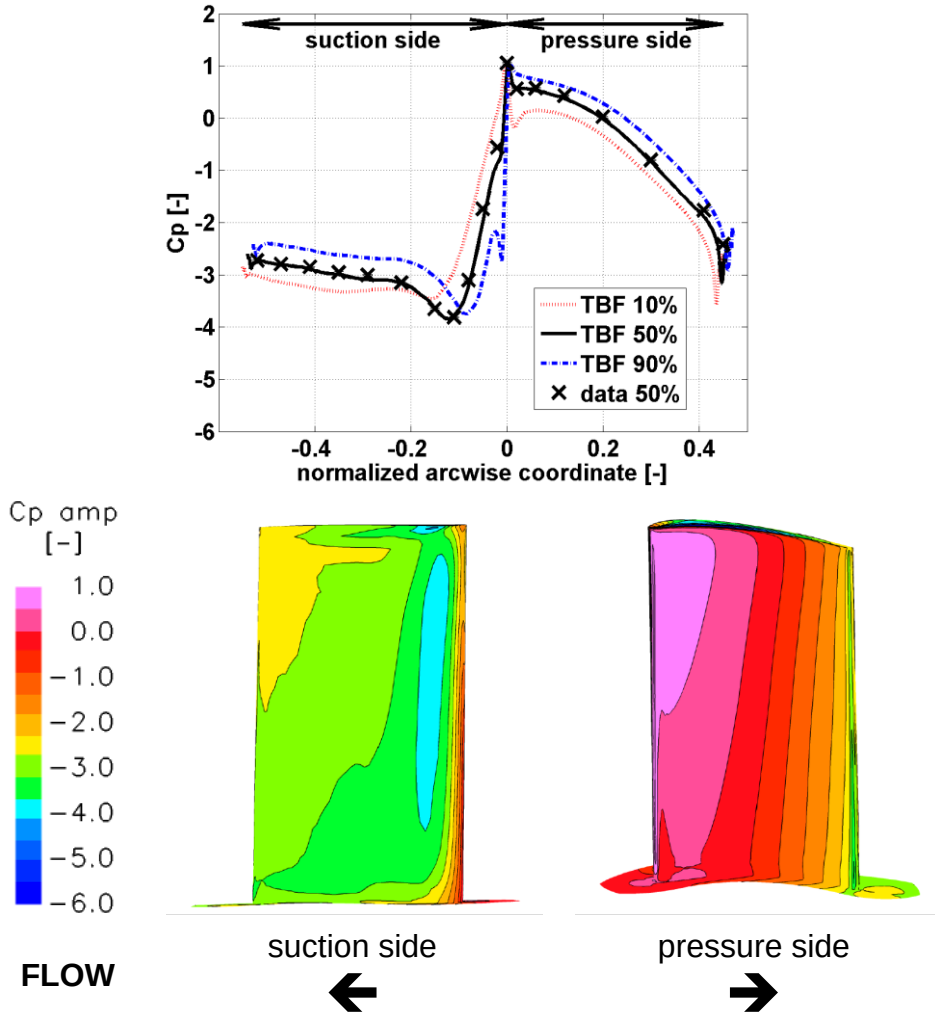

Figure 3-3: Steady blade loading at M04, nom

In the same way as above, the steady static pressure coefficient at M08 is displayed in Figure 3-4 at three span positions, i.e. 10%, 50% and 90% span, along the normalized arcwise coordinate as well as on the blade surface in a 3D view. The figure suggests the following:

- again the presence of radial pressure gradient results in increasing pressure with increasing span.
- the aforementioned suction peak on the fore suction side moves from arc=-0.09 to arc=-0.12 at 90% and 50% span respectively. This is much less pronounced close to the hub, the "peak" suction appears at arc=-0.16, then the pressure remains slightly constant and decreases significantly up to arc=-0.35.

The suction peak has been identified through flow visualizations (Vogt, 2005) as the laminar-turbulent transition; this cannot be numerically caught by Turb'Flow™ since it is a fully turbulent solver without models to capture the transition.

The three dimensional nature of the blade and the presence of tip gap result in highly 3D flow close to the walls. Corner vortices develop close to the tip and hub and are displayed in Figure 3-5. They are superposed to the steady static pressure coefficient. Close to the hub the corner vortices developed up to 15% span on the aft suction side, whereas close

to the tip it extends on 17% span from the tip. This shows on the other hand that the flow at midspan is not disturbed by the aforementioned features.

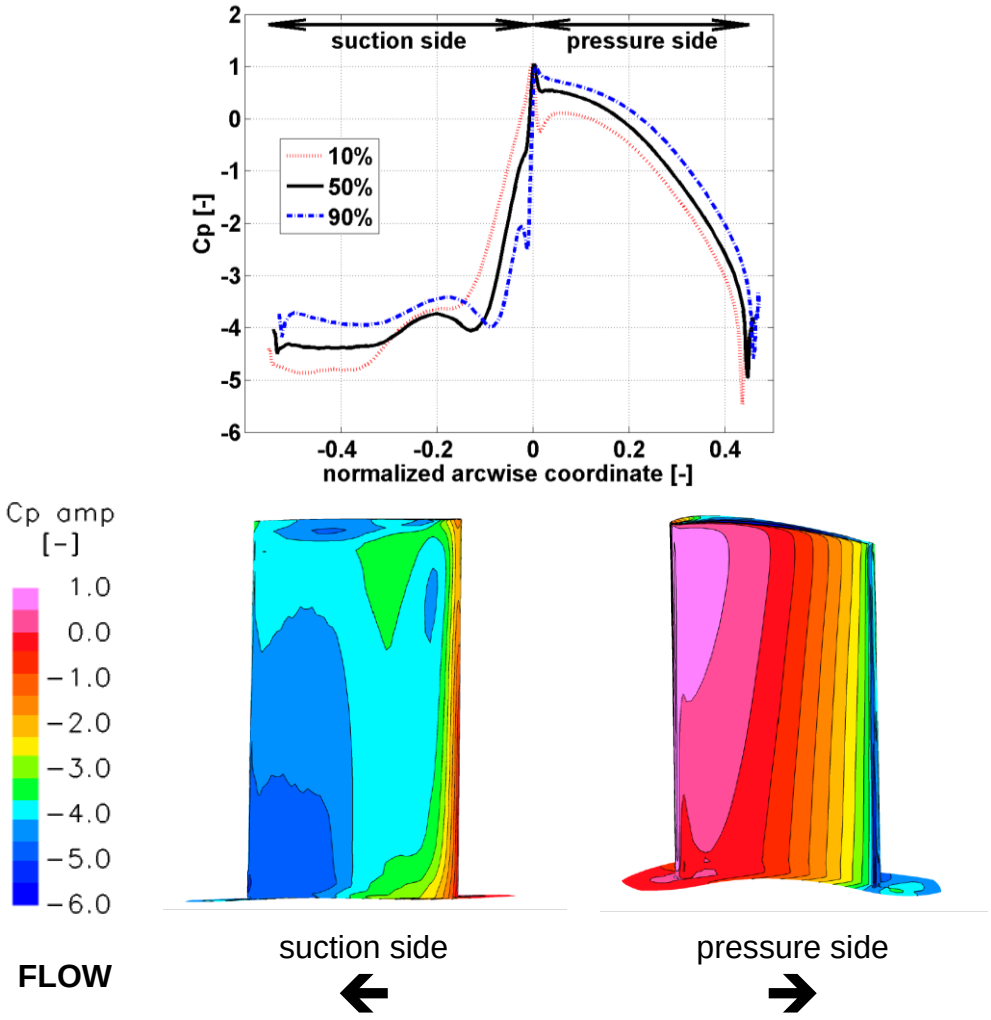

Figure 3-4: Steady blade loading at M08, nom, numerical results

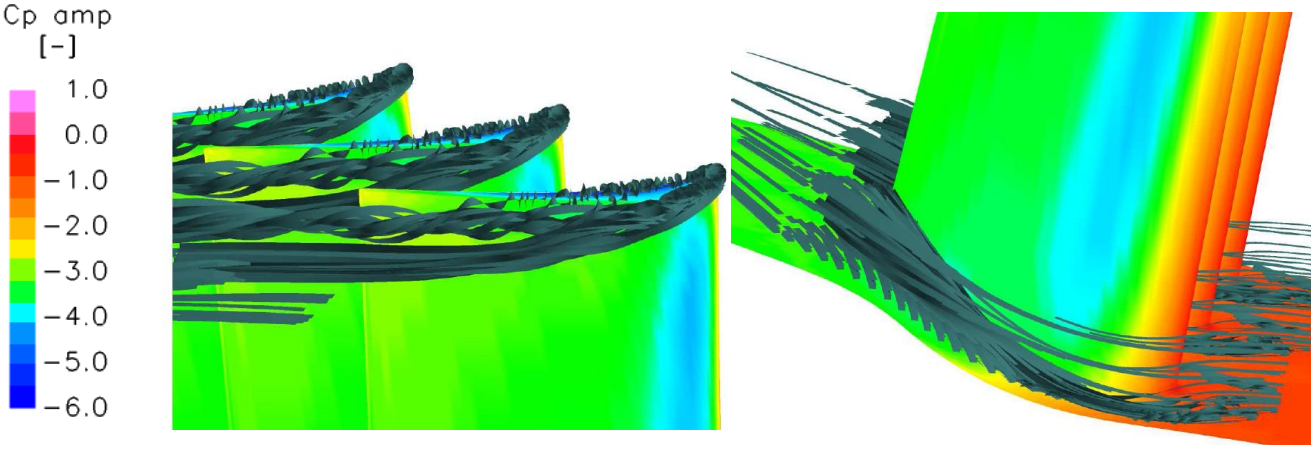

Figure 3-5: Visualization of corner vortices, M04, nom

The above computations have been performed prior the measurements. A systematic issue arises when starting simulations about the initialization and especially the turbulence level. The next sub-section addresses this point through hot-wire measures.

3.2.3 Evaluation of the inlet conditions

Turbulence measurements using hot-wire anemometry technique are exposed below. The focus is put on the boundary layer thickness and the assessment of the turbulence level. The results are presented as follows:

- first, the boundary layer profile and the turbulence intensity along the span at M04 and 20% axial chord upstream of the cascade are evaluated with respect to the circumferential positions, i.e. at 3 different normalized pitch coordinates:
  - at pos. +0.5, i.e. between blade -1 and blade 0
  - at pos. 0, i.e. in front of blade 0
  - at pos. -0.5, i.e. between blade 0 and blade +1
- then the turbulence level at 50% axial chord upstream of the cascade at M04 and M08 is given in order to provide inputs for further computations.

The radial traverses are displayed in Figure 3-6 below. The velocity and the turbulence intensity profiles along the normalized span at M04 at 20% axial chord upstream and at the 3 aforementioned circumferential positions are included in Figure 3-7. The radial traverses have been restricted from 5 to 95% span. The velocity profiles highlight the potential effect due to the presence of downstream blade, which induces a deviation lower than 7% with respect to the velocities at pos. ±0.5. The same order of deviation is found for the turbulence intensity. The measurements (averaged) are summarized in Table 3-2. The velocity profile appears wavy due to small temperature fluctuations of the order of 2% measured in the test rig.

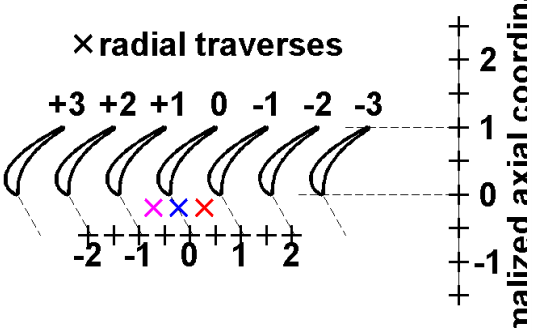

Figure 3-6: Definition of hot-wire probe traverses

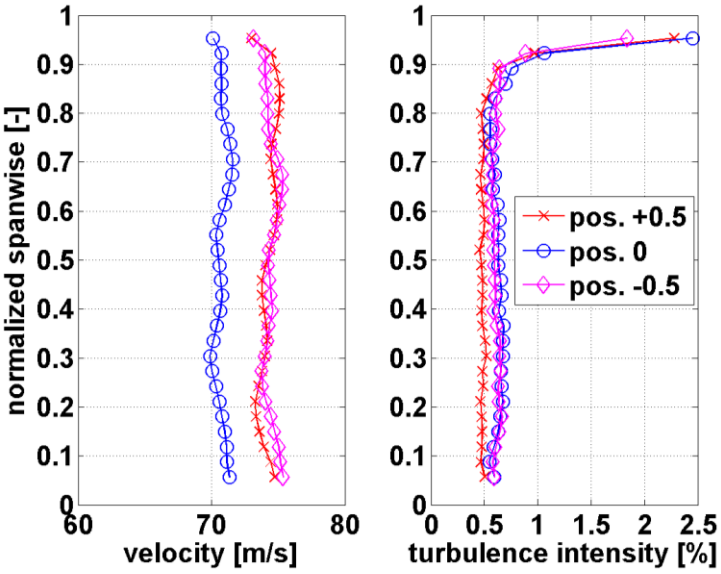

Figure 3-7: Velocity and turbulence intensity, M04, 20%c_{ax} upstream

	pos. -0.5		pos. 0		pos. +0.5	
	V [m/s]	*Tu [%]*	*V [m/s]*	*Tu [%]*	*V [m/s]*	*Tu [%]*
data	74.2	0.57	70.8	0.63	74.4	0.66

Table 3-2: Velocity and turbulence intensity, M04, 20%c_{ax} upstream

The turbulence intensity along the normalized span at M04 and M08 is included in Figure 3-8. The traverses have been performed at the normalized pitch coordinate -0.5 at 50% axial chord upstream of the cascade. Different measurements have been carried out for each operating point and are superposed in order to highlight the quality in terms of repeatability. The boundary layers at hub and tip are well captured and both feature the same thickness, i.e. about 12% and 5% of span at tip and hub respectively. Excluding the boundary layers at the walls, the resulting non-disturbed flow exhibits approximately turbulence levels equal to 0.37% and 0.57% at M04 and M08 respectively: the flow is more turbulent at M08 than at M04. Furthermore a slight gradient along the span is observed that is more pronounced at M08.

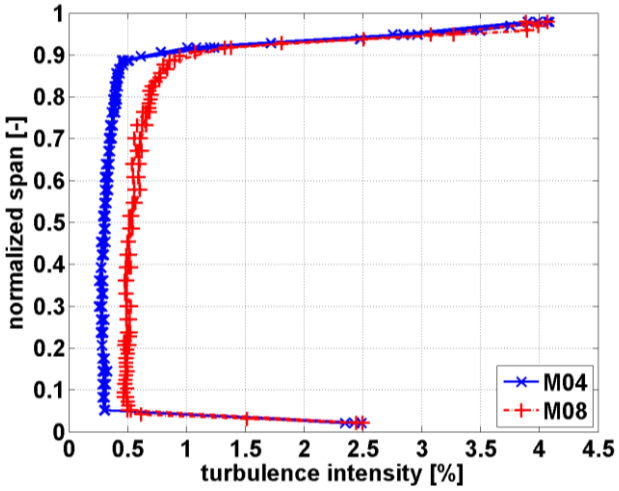

Figure 3-8: Turbulence intensity, M04 and M08, 50%c_{ax} upstream of the cascade

3.2.4 Summary of steady results

To reduce the measurement efforts, steady loading has been measured at M04 and midspan on blades ±1, then data have been compared to CFD results. A very good agreement has been found and this has enabled to be more confident in the use of CFD for analysis. Steady-state was based on the aforementioned CFD as well as previous measurements from (Vogt, 2005). Thus numerical data for M08 have been afterwards presented and finally the inlet conditions have been described. The main results are summarized below:

- the blade profile presents high loading with a suction peak located at arc=-0.11 at midspan, slightly upstream and downstream close to tip and hub respectively. This arcwise position coincides to flow transition from laminar to turbulent.
- the profile on the fore suction side induces a strong acceleration of the flow from the leading edge to the aforementioned suction peak.
- the presence of a radial pressure gradient results in increasing the blade loading from hub to tip.

- corner vortices are generated at the hub and tip.
- the extent of vortices (generated at the corners and over the blade tip) does not affect the flow at midspan.
- the boundary layers at hub and tip are about 12% and 5% of span tick respectively for both Mach numbers, whereas the levels of turbulence are about 0.37% and 0.57% at M04 and M08 respectively.

The next section is dedicated to the unsteady state test data.

3.3 Unsteady state results

Vogt (2005) has investigated and presented in details flutter test data through blades -2 to +2 for nominal subsonic case at reduced frequency of k=0.1. Parametric studies have been performed with respect to the modeshape (axial bending, circumferential bending and torsion), the reduced frequency (from k=0.1 to k=0.5), the flow velocity (M04, M06 and M08) and the flow incidence (nominal and two off-design points). Glodic et al. (2009) have studied the aeroelastic response for combined axial bending/torsion mode at low subsonic condition in order to assess the validity of linear assumption. The present work aims at investigating aeroelastic response for high subsonic flow at reduced frequency of k=0.2 for the following modeshapes:

- pure axial bending
- pure torsion
- pure circumferential bending
- combined axial bending/torsion
- combined circumferential bending/torsion

Vogt (2005) has showed that responses on blades ±2 are of minor magnitude compared to blade 0 and its direct neighbors. As a result, flutter data have here been acquired on blades 0 and ±1. The analyses presented in this chapter are adapted from Vogt (2005).

The section is thus organized as follows:

- first the focus is put on one operating point, i.e. M08, k02 at midspan and nominal inlet angle. For that operating point:
  - aeroelastic responses are presented for the three pure modes.
  - the data are then analyzed from a quasi-steady point of view.
  - aeroelastic responses for the two combined modes are finally introduced.

- secondly, the effect of reduced frequency on the aeroelastic response is exposed for the five modeshapes at M08 and nominal, the reduced frequency ranging from 0.05 to 0.2, followed by the effect of flow velocity and incidence angle.

- thirdly, the 3D effects are considered through the measures at 10%, 50% and 90% span, on blades ±1 for the three pure modes as well for the combined axial bending/torsion mode. Being instrumented at midspan only, the oscillating blade 0 is thus not included.

- fourthly, the linear superposition principle is detailed.

- finally, unsteady responses are discussed in terms of stability.

3.3.1 Unsteady response to pure modes

Unsteady responses are measured on blades 0 and ±1 at midspan and are successively presented below for each pure mode at M08 and nominal. The oscillation is set to 175Hz and yields to 0.2 as reduced frequency.

3.3.1.1 Pure axial bending mode

The unsteady responses measured on blades -1 through +1 for the pure axial bending mode are included in Figure 3-9 and suggest the following:

- The major response is located on blade 0 and its direct adjacent surfaces, i.e. the pressure side of blade +1 and suction side of blade -1 (primary surfaces), whereas the response is of minor amplitude on the surfaces facing away the oscillating blade, i.e. the suction side of blade +1 and pressure side of blade -1 (secondary surfaces).
  All the blades exhibit a 180deg jump in phase at the leading edge.

- On blade -1, the fore suction side features high pressure fluctuations and a maximum located at arc=-0.15, then the amplitude decreases towards the trailing edge.
  On suction side, the phase starts in-phase at the leading edge and then tends to lie out-of-phase with respect to the blade motion: this suggests that positive blade motion induces a decrease in pressure. Further downstream, the phase rotates to about 40deg at arc=-0.35; geometrical analysis shows that the passage throat is located around this position. Response on pressure side is of minor magnitude and the phase is therefore not discussed.

- On blade 0, the suction side depicts similar feature than blade -1: a response peak of the same order of magnitude and then a decrease towards the trailing edge. Nevertheless the maximum previously located at arc=-0.15 on blade -1 is here at arc=-0.08. At the leading edge, a local response peak of the same order of magnitude than the one on suction side is observed, then the response tends to linearly decreases towards the trailing edge.
  The phase lies out-of-phase on the pressure side, whereas it starts in-phase and rotates continuously to about 100deg on the suction side. This suggests two opposite behaviors: a positive blade motion induces increase and decrease in pressure on suction and pressure side respectively.

- On blade +1, a local response peak is present at arc=0.02 then the amplitude drops, remains at moderate level and decreases towards the trailing edge.
  The phase starts in-phase and remains rather constant (30deg) along the pressure side suggesting that positive blade motion induces an increase in pressure. The fore suction side exhibits strong phase variation from 165deg at the leading edge to 33deg at arc=-0.11, i.e. at the peak suction mentioned in the steady results section, although the response is of minor magnitude.

- The surfaces facing with each other display consistent phases, i.e. phases on suction side of blade 0 and pressure side of blade +1 agree as well as phases on pressure side of blade 0 with suction side of blade -1.

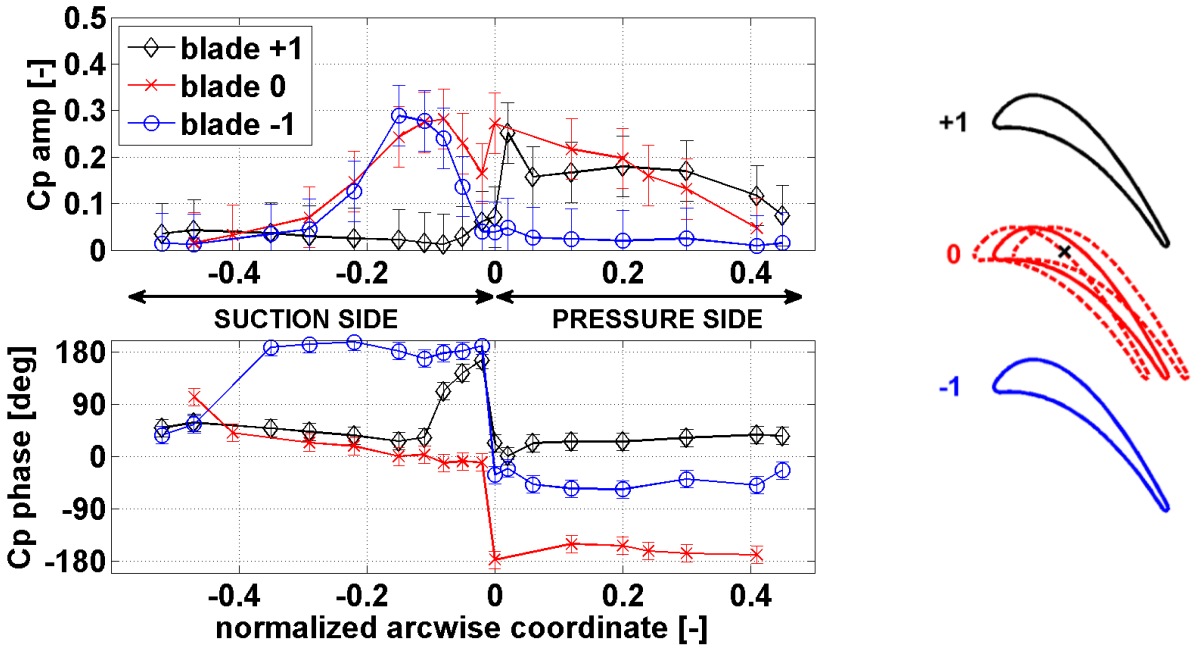

Figure 3-9: Unsteady response, M08, k=0.2, 50%span, nom, pure axial bending

3.3.1.2 Pure torsion mode

The unsteady responses measured on blades -1 through +1 for the pure torsion mode are included in Figure 3-10 and suggest the following:

- The major response is located on blade 0 and on suction side of blade -1. As for pure axial bending mode, pressure side of blade -1 is of minor magnitude. Surprisingly, both sides of blade +1 exhibits relatively high amplitudes. It was expected lower levels on the surfaces facing away, i.e. the suction side. It is believed to be due to the oscillating wake of blade 0 that may interfere with the one from blade +1 and change locally the pressure distribution. This could be verified by measuring on blade +2. Moreover, Vogt and Fransson (2000) have highlighted that a change in flow direction downstream of the cascade results in local pressure variations and this effect have been found predominant for torsion on the positive indexed neighbors of the oscillating blade.
  Furthermore, the aforementioned 180deg jump in phase at the leading edge is also observed on blades 0 and -1, whereas blade +1 shows a 90deg jump.

- On blade -1, a response peak arises at arc=-0.15 as for the axial bending but sharper, then the amplitude decreases significantly towards the trailing edge.
  The phase remains out-of-phase along the suction side with a drop at the trailing edge. This indicates that a positive blade motion induces a decrease in pressure.

- On blade 0, no pronounced response peak appears on the fore suction side like the one observed at arc=-0.11 for the pure axial bending mode. The level appears rather constant with a decrease towards the trailing edge on each side.
  The phases display similar feature than the axial bending: phases lie out-of-phase and in-phase on pressure and suction side respectively.

- On blade +1, the unsteady response starts with very small amplitude at the leading edge and increases significantly towards the trailing edge on each side.
  The phase response, starting at -90deg, remains afterwards slightly constant and in-phase on the aft part of pressure and suction sides indicating that a positive blade motion induces an increase in pressure.

- The surfaces facing with each other display again consistent phases: phases on suction side of blade 0 and pressure side of blade +1 agree as well as phases on pressure side of blade 0 with suction side of blade -1.

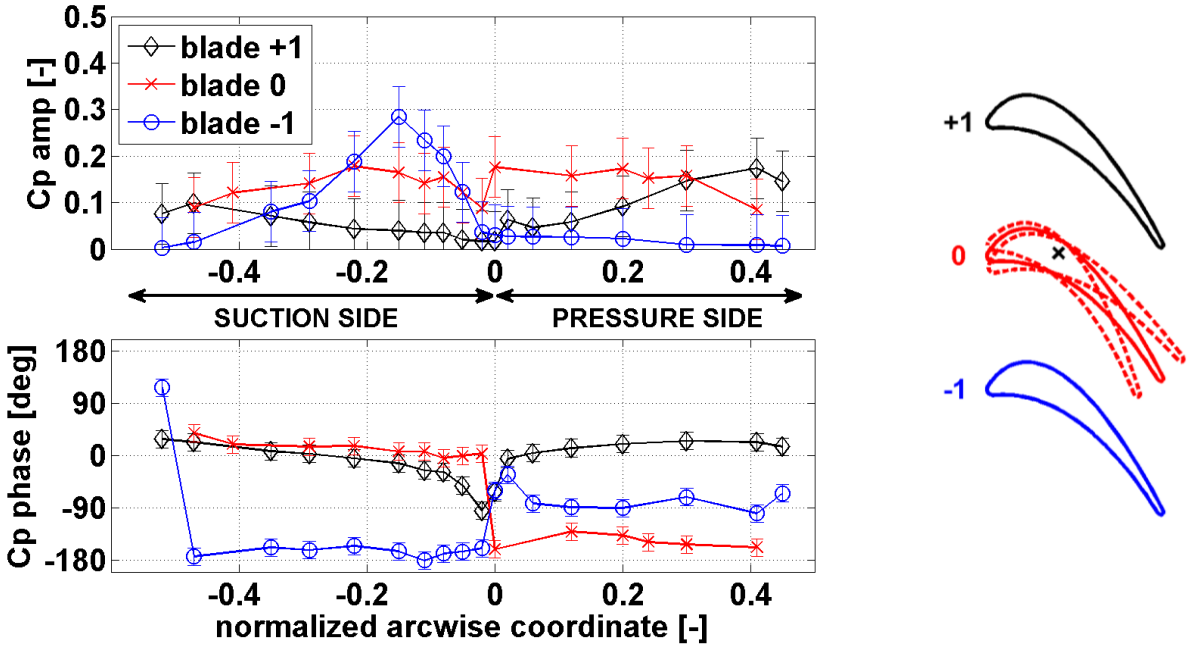

Figure 3-10: Unsteady response, M08, k=0.2, 50%span, nom, pure torsion

3.3.1.3 Pure circumferential bending mode

The unsteady responses measured on blades -1 through +1 for the pure circumferential bending mode are included in Figure 3-11 and suggest the following:

- Again, the major responses appear on the surfaces facing the oscillating blade. Nevertheless, the amplitudes are much lower than the ones observed for the two previous modes. Moreover, the levels on the oscillating blade and on its direct surfaces are of the same order of magnitude.
  The aforementioned 180deg jump in phase at the leading edge appears on blade 0 and -1 but not on blade +1, as for the torsion mode.

- On blade -1, the response "peak" on suction side is much less sharp.

The phase displays out-of-phase behavior, i.e. positive blade motion induces decrease in pressure.

- On blade 0, both the aft suction and pressure sides tend to be in-phase with respect to the blade motion. On the fore suction side, the phase displays strong variations, it starts at about 90deg and then decreases linearly to 0deg at arc=-0.15.

- On blade +1, the magnitude increases up to arc=0.3 then it decreases towards the trailing edge. The phase tends to lie out-of-phase.

- Contrary to the two previous modes, the surfaces facing with each other do not display consistent phases: on suction side of blade 0 and on pressure side of blade +1 phases do not agree. There is almost 180deg difference.

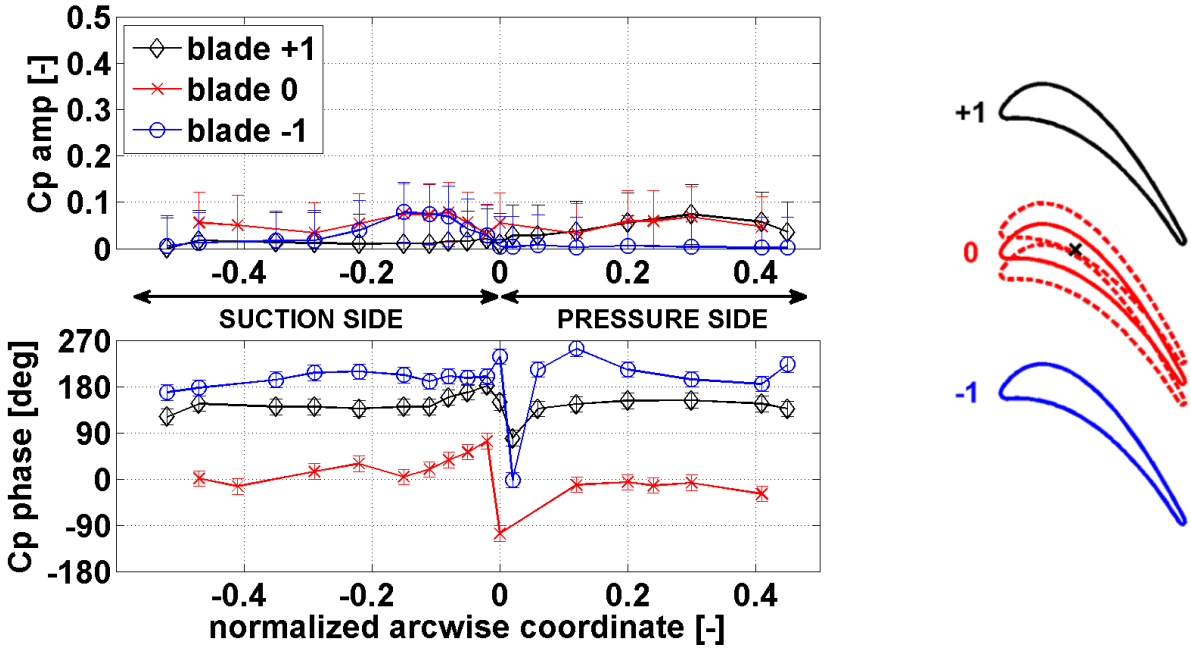

Figure 3-11: Unsteady response, M08, k=0.2, 50%span, nom, pure circ. bending

3.3.1.4 Summary

The unsteady responses to pure modes at midspan, M08, nominal and k=0.2 have been described. This has highlighted the following similar features:

- the major response is located on blade 0 and its direct adjacent surfaces.
- all modes exhibit a response peak on the fore suction side of blades 0 and -1.
- the surfaces facing with each other display consistent phases.
- the leading edges display 180deg jump in phase.

However, the following particularities shall be noticed:

- the suction side of blade +1 when blade 0 is oscillating in torsion exhibits also relatively high amplitude whereas this is not a direct neighbor surface.
- the peak response on the fore suction side is much less pronounced for the circumferential bending. Moreover, the surfaces facing with each other do not display consistent phases.

- a 90deg rather than 180deg jump in phase at the leading edge occurs on blade +1 when blade 0 is oscillating either in torsion or in circumferential bending.

The similarities pointed out so far suggest that axial bending and torsion lead to comparable mechanisms. The next sub-section analyses the above results from a quasi-steady point of view, i.e. infinitely slow blade motion.

3.3.2 Quasi-steady analysis

As mentioned by Vogt (2005), the above aeroelastic responses can be analyzed from a quasi-steady point of view. Consider the channel +1 between blades 0 and +1 with blade 0 oscillating in torsion mode. When blade 0 is reaching its maximum amplitude (in positive direction), it implies a reduction of the flow passage section at the throat (counterclockwise defines positive direction of motion).

In subsonic flows, when only a single channel is studied, a contraction of section leads to an increase in velocity and therefore a decrease in pressure. As a result, a positive motion involves a negative pressure fluctuation. In other words, motion and pressure are out-of-phase and this disagrees with Figure 3-10, which displays in-phase behavior on suction side of blade 0.

Actually, the quasi-steady analysis must be done by considering firstly the entire cascade and secondly the blockage phenomenon induced by the blade motion. Figure 3-12 illustrates this approach for an extreme blade position when oscillating in torsion mode. This represents a harmonic sinusoidal excitation, i.e. the blade motion δ(motion), that generates a harmonic response, i.e. the pressure fluctuations δ(pressure). Channels ±1 are successively considered:

- in channel +1, the blade motion, δ(motion)>0, implies a reduction of the section at the throat and less fluid particles are therefore able to pass through, increasing the blockage, δ(blockage)>0, within the channel and hence the pressure, δ(pressure)>0. As a result, motion and pressure are in-phase as depicted on the suction side of blade 0 and pressure side of blade +1 in Figure 3-10.

- in channel -1, the same blade motion, δ(motion)>0, implies an expansion of the section at the throat and more fluid particles are therefore able to pass through, decreasing the blockage, δ(blockage)<0, within the channel and hence the pressure, δ(pressure)<0. As a result, motion and pressure are out-of-phase as depicted on suction side of blade -1 and pressure side of blade 0 in Figure 3-10.

A parallel can be drawn to the rotating stall phenomenon for which the blockage appears due to the boundary layer separation, which induces a reduction of the flow passage.

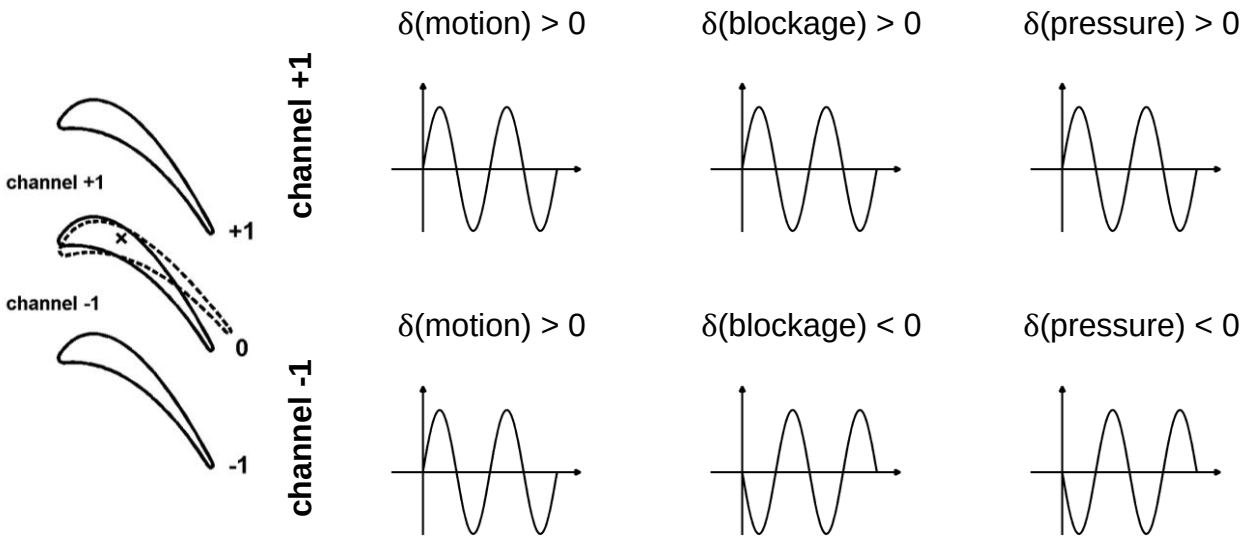

Figure 3-12: Quasi-steady analysis, torsion mode, positive fluctuation of blade motion

It has been observed that the circumferential bending differs in some extent from the axial and torsion modes. In order to put some light, the same quasi-steady analysis is suggested. A positive blade motion induces respectively an increase and decrease of the blockage within channels +1 and -1, i.e. an increase and decrease in pressure. As a result, pressure on suction side of blade 0 must be in-phase with respect to the blade motion and out-of-phase on the pressure side. This disagrees with Figure 3-11. Furthermore, pressure side and suction side of blade 0 experience opposite features, i.e. according to the direction of motion, one channel is narrowing while the second one is widening. This is indeed well illustrated by the phases at the leading edge (180deg jump); but then, the phases rotate to 0deg on each side. Moreover, the lower amplitude on the fore suction side of blades 0 and -1 compared to axial bending and torsion is believed to be due to the suction peak location that is prone to be more disturbed while blade 0 is oscillating in axial and torsion than circumferential mode.

Another aspect that can be put forward is the notion of isolated blade (Kerrebrock, 1977), i.e. only blade 0 is considered without its neighbors and this results in cancelling the effect of change in section (see Appendix B). While vibrating, the incidence angle is also changing and the aerodynamic forces acting on the blade as well. Particularly at the highest position of the blade, the incidence angle raises and generates higher aerodynamic forces suggesting that motion and pressure are in phase. This is observed in Figure 3-11 on the aft blade 0.

The change in incidence is also present during axial bending and torsion but the unsteady response mainly results from the change in flow passage at the throat. Figure 3-10 displays rather constant phase along the pressure and suction sides whereas the fluid particles experience different features though the channel since the axis of torsion is located 40% axial chord downstream of the leading edge. Indeed, considering a positive blade movement, the motion is such that the flow passage at the inlet increases whereas it decreases at the throat. It is therefore expected to have variation of the phase along the pressure and suction sides. It is believed that the relative change in section at the throat controls the unsteady pressure since the change is much higher than at the inlet as summarized in Table 3-3. The latter presents the change in percentage of the current

section for 1deg amplitude while the blade is oscillating in torsion which corresponds to 1mm amplitude when the blade is oscillating in bending modes. For instance, a positive blade motion in axial bending mode induces a change in flow passage of 0.06% of the section at the inlet whereas this involves a change of 4.92% and 4.68% at the throat in channels +1 and -1 respectively. Furthermore, Table 3-3 highlights the ratio of the changes in section at the inlet and throat. For axial and torsion modes, this ratio is high whereas the changes for circumferential bending are of the same order of magnitude. This could explain why the unsteady response to such a mode differs from the two others. On the other hand, as mentioned by Vogt (2005), the fact that the axial bending mode and torsion mode display similar features is explained by the largest impact on throat size due to these two modes.

δ(motion) > 0	**section at**	**channel +1**	**channel -1**
axial	*inlet*	+0.06%	+0.06%
	throat	-4.92%	+4.68%
torsion	*inlet*	+0.94%	-0.91%
	throat	-1.56%	+4.26%
circumferential	*inlet*	-2.89%	-2.92%
	throat	-3.66%	-3.48%

Table 3-3: Relative change in flow passage at the inlet and at the throat

At this point, phase data have highlighted that the response primarily involves a flow passage and its respective surfaces. This agrees with findings from (Vogt, 2005). The next sub-section is dedicated to the unsteady responses for the following combined modes:

- combined axial bending/torsion
- combined circumferential bending/torsion

3.3.3 Unsteady response to combined modes

It is recalled that the combined modes are a combination of bending and torsion modes at $\phi = 90deg$ out-of-phase, the phase reference is set according to the bending mode. Furthermore, the investigated combined modes were set to amplitude ratio of 1, i.e. the amplitudes of bending and torsion are of the same order of magnitude.

$$\tilde{C}_{p,combined} = \tilde{C}_{p,bending} + \tilde{C}_{p,torsion} \cdot e^{i\phi} \qquad \text{Eq. 3-1}$$

Unsteady responses are measured on blades 0 and ±1 at midspan and are successively presented below for each combined mode at M08 and nominal. The oscillation frequency is 175Hz and yields to a reduced frequency of 0.2. The above parameters are consistently the same as the pure modes.

3.3.3.1 Combined axial bending/torsion mode

The unsteady responses measured on blades -1 through +1 for the combined axial bending/torsion mode are included in Figure 3-13 and suggest the following:

- All the blades feature relatively high amplitudes on each side, except the pressure side of blade -1 whose the response is of minor magnitude.

- On blade -1, the response peak remains located at arc=-0.15 but is higher than the ones measured for the pure modes, then the amplitude decreases significantly towards the trailing edge.
  The phase response lies out-of-phase on the fore suction side and then decreases to 47deg towards the trailing edge. This evolution has been also observed for both the pure modes, i.e. slight constant phase on the fore suction and then a drop close to the trailing edge.

- On blade 0, a strong local response peak rises at the leading edge, then the amplitude gradually decreases on pressure side towards the trailing edge. On suction side, the response displays similar feature than pure modes with a major response on the fore part.
  The phase on pressure side lies out-of-phase as observed for pure modes, whereas it starts about -38deg and slightly varies up to -55deg towards the trailing edge.

- On blade +1, the response suggests clearly the occurrence of both modes: the two branches with increasing amplitude on each side characterize the torsion whereas the local high response peak on the fore pressure side (arc=0.02) characterizes the axial bending.
  Like for the pure modes, the phase displays strong variations on the fore suction side and rotates of 90deg from the leading to trailing edge.

- The surfaces facing with each other do not display clear consistent phases as observed for the pure modes.

3.3.3.2 Combined circumferential bending/torsion mode

The aeroelastic responses measured on blades -1 through +1 for the combined circumferential bending/torsion mode are included in Figure 3-14 and suggest the following:

- Pressure side of blade -1 still shows response of low magnitude whereas all other surfaces displays major response. Nevertheless, the amplitudes are lower than the combined axial bending/torsion mode.

- On blade -1, the local response peak at arc=-0.15 is higher than the ones measured for the pure modes, then the amplitude decreases towards the trailing edge.
  The phase response is qualitatively very close to the pure circumferential bending mode.

- On blade 0, the amplitude is rather constant along each side, the strongest variations being located on the fore suction side.
  The phases tend to be equal to 90deg and -90deg on pressure and suction side respectively, like the pure torsion but 90deg shifted.

- On blade +1, pressure side exhibits the aforementioned branch with increasing amplitude towards the trailing edge (characteristic of both pure torsion and pure circumferential); as well as on suction side indicating the occurrence of torsion.

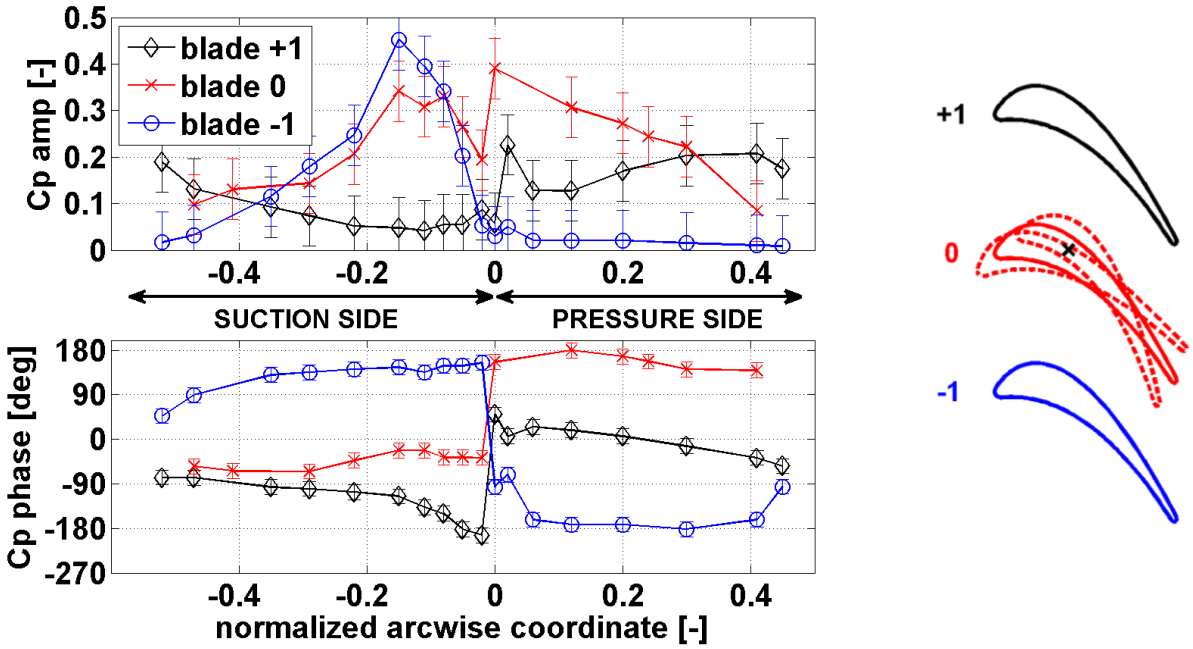

Figure 3-13: Unsteady response, M08, k=0.2, 50%span, nom, combined axial/torsion

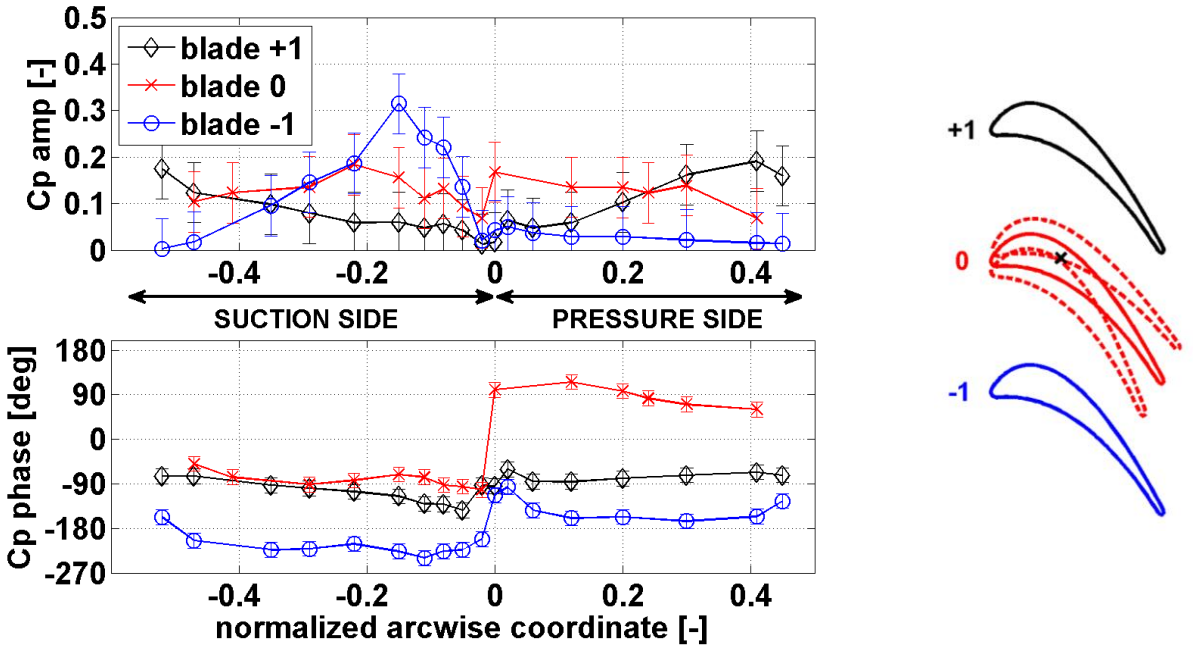

Figure 3-14: Unsteady response, M08, k=0.2, 50%span, nom, combined circ./torsion

The unsteady responses to combined modes at midspan, M08, nominal and k=0.2 have been described and led to the following:

- Pressure side of blade -1 features low response whatever the combined modes. This is consistent with the previous results for pure modes, i.e. the pressure side of blade +1 is less disturbed by the oscillating blade.
- Only blade +1 clearly evidences the occurrence of each mode when looking at the amplitudes.

At this position, the effects of modeshape on unsteady response have been described. It has been highlighted that according to the nature of blade motion, the unsteady response can either be very similar or not. In order to evaluate how important is this effect from a overall point of view, the next sub-sections will focus on the effects of other major parameters such as the reduced frequency, the flow velocity and the incidence angle. Thus, the next sub-section is dedicated to the effect of reduced frequency on the unsteady response.

3.3.4 Effect of reduced frequency on unsteady response

The effect of reduced frequency on unsteady response is presented below. Data have been acquired on blades -1 through +1 for each modeshape, at midspan, M08, and nominal. The blade 0 is oscillating at 4 various frequencies summarized in Table 3-4.

	reduced frequency [-]	
oscillation frequency [Hz]	**M04**	**M08**
43.75	0.1	0.05
87.5	0.2	0.1
131.25	0.3	0.15
175	0.4	0.2

Table 3-4: Oscillation frequencies and corresponding reduced frequencies

In order to keep this part as an -easy to read- section, the data are annexed in Appendix F and analyzed below.

- At pure axial bending, pressure side of blade +1 shows increased magnitudes with increasing reduced frequency but the phases remain quasi unchanged. In contrast, suction side displays constant and lower magnitudes but the phases strongly vary.
  On blades 0 and -1, the effect of reduced frequency on magnitude is apparent on the fore suction side: the suction peak becomes much less sharp and the amplitude lower with increasing frequency, whereas the phases in that region appear quasi perfectly constant and start to vary downstream of the throat.

- At pure torsion, magnitudes on blade +1 are fairly unaffected, whereas phases feature strong variations. In particular, the phase at the lowest frequency tends to remain in-phase along the entire blade surface while the others drop around -90deg on the fore suction side.
  On blade 0, magnitude tends to decrease with increasing frequency. As observed for the pure axial bending, phase on fore suction side is distinctly less disturbed.

On blade -1, the suction peak amplitude increases with decreasing reduced frequency and does not seem to vary linearly. The fluctuations appear as a pair: the two lowest and highest frequencies remain very close to each other and this is clearly evidenced through the phase.

- Pure circumferential bending appears less disturbed. On blade +1, the response varies only little on the aft pressure side. Nevertheless, the changes in phase are more pronounced on both sides.
  On blade 0, whereas the phase remains unchanged on pressure side, the amplitude decreases with increasing frequency.
  Primary surface of blade -1 appears insensitive both in terms of magnitude and phase.

- Combined axial bending/torsion mode differs from the respective pure modes as illustrated with the high sensitivity observed on each side of blade +1. Except on the fore pressure side, the magnitude tends to decrease with increasing frequency and the sensitivity gets stronger when approaching the trailing edge. In contrast, the phase displays the opposite trend, i.e. on the fore suction side, the magnitude shows small variations whereas the phase is strongly disturbed and gets weaker towards the trailing edge.
  On blade 0, whereas phase are fairly unaffected on both sides, strong variations arise on suction side and on aft pressure side characterized by a decrease in magnitude with increasing reduced frequency.
  On blade -1, the response is very similar to the pure torsion mode. However, the phase on suction side displays smaller changes.

- Combined circumferential bending/torsion shows similar characteristics than the combined axial bending/torsion. However it shall be noticed that the magnitudes on each blade at k=0.1 and k=0.15 are very close with each other without being clearly explained.

The influence of reduced frequency on unsteady response has been described. The effect is largest on the suction peak region at axial bending, torsion and both combined modes, whereas pure circumferential bending is much less affected. This is believed to be due to the motion of transition point that is more prone to be disturbed when blade 0 oscillates at low frequency and features a part of axial or torsion motion. This is observed in terms of magnitude and does not necessarily result in large change in phase. Nevertheless, drastic changes in phase appear both on primary and secondary surfaces when circumferential bending is involved in the blade motion, especially on blade +1.

The reduced frequency results in major effects on unsteady response, and strong changes in magnitude do not lead necessarily to strong changes in phase. Furthermore, the response magnitude seems not to vary linearly with reduced frequency. In order to put some light, unsteady responses to pure torsion mode on blades 0 and -1 at midspan at M04 and M08 are displayed in Figure 3-15 and Figure 3-16 respectively. The effect of reduced frequency on the unsteady response level is clearly evidenced at M08 whereas at M04 the effect is of much lower order of magnitude. However, it shall be noticed that the lowest frequency exhibits distinct higher amplitude on blade -1 at M04. Whereas the magnitude is much more affected at M08 rather than the phase, the opposite is observed at M04, i.e. the phase are strongly disturbed whereas the magnitude not.

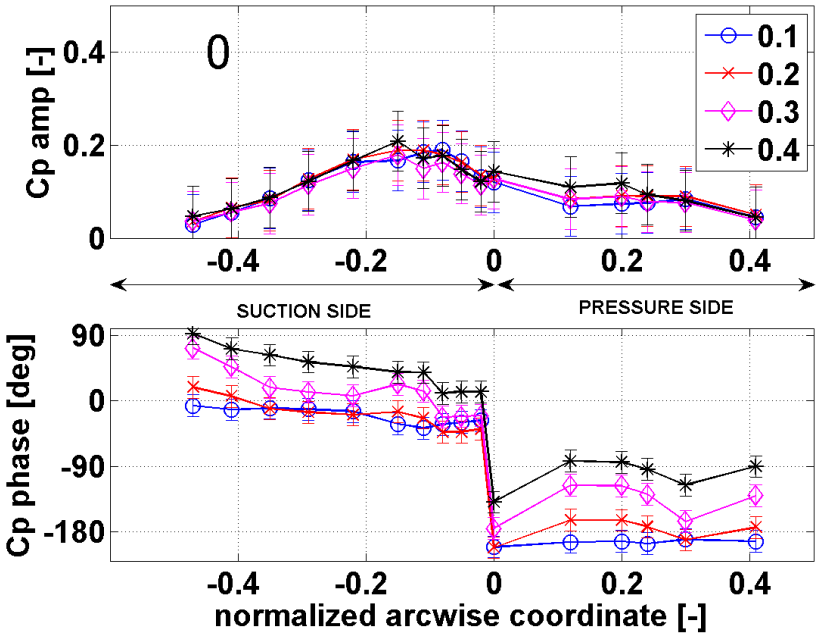

M04, nominal, pure torsion

blade 0

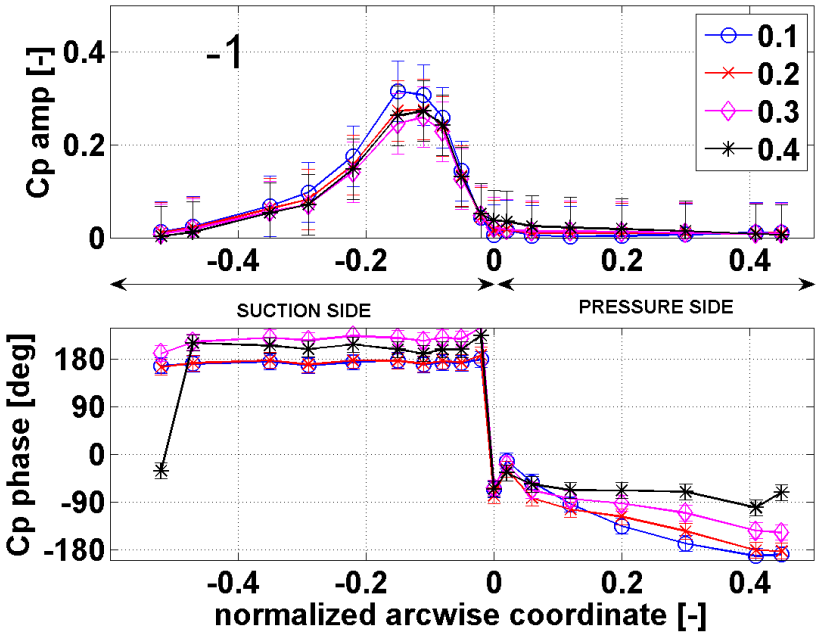

M04, nominal, pure torsion

blade -1

Figure 3-15: Effect of reduced frequency, nom, pure torsion, M04

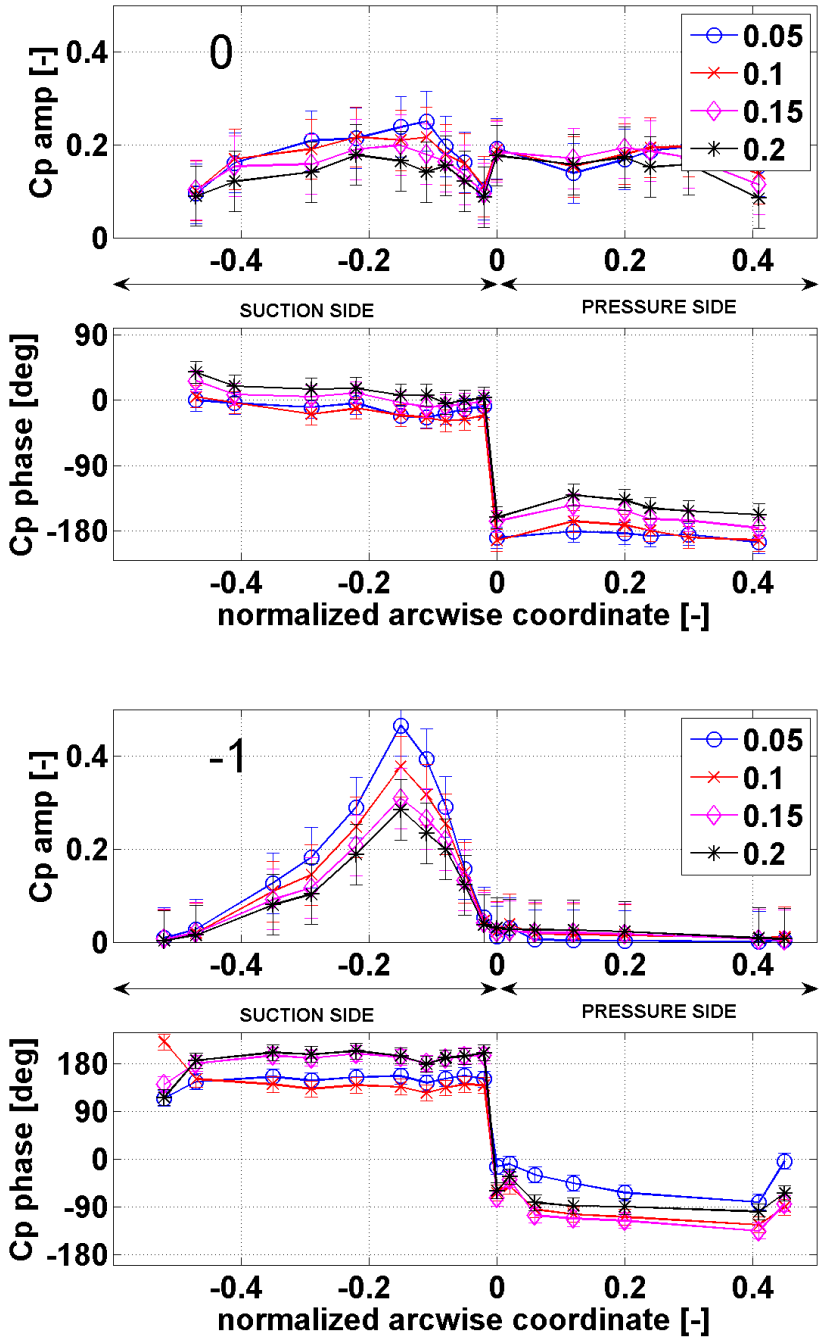

Figure 3-16: Effect of reduced frequency, nom, pure torsion, M08

The effect of reduced frequency has been discussed. The next focus is put on the effect of flow velocity, which is presented in the following sub-section.

3.3.5 Effect of steady flow velocity on unsteady response

The effect of flow velocity on unsteady response is presented through data acquired on blades -1 through +1 for each modeshape, at midspan and nominal. Two outlet Mach numbers have been considered, 0.4 and 0.8 referenced as M04 and M08 respectively.

The data are annexed in Appendix G and analyzed below. As forewords it shall be recalled that the unsteady pressure coefficient is normalized by the dynamic head, as a result when comparing two responses of the same amplitude at different Mach numbers must be interpreted as an increase of the absolute response with velocity.

- At pure axial bending, similar behaviors emerge when comparing the blades with each other. On pressure sides, the response magnitudes increase with increasing velocity, whereas the fore suction sides display the opposite. This is clearly evidenced on oscillating blade. The phases are quasi unaffected; the major effects occur on the aft pressure sides of blades 0 and -1 and on the aft suction side of blade -1 from arc=-0.35, i.e. close to the throat.

- Pure torsion mode is also affected. The fore suction side of blade +1 shows a response that slightly increases with decreasing velocity whereas the phase strongly deviates, it rotates from about 0deg at M04 to 90deg at M08. Then, from arc=-0.22 and arc=0.12 respectively on suction and pressure sides towards the trailing edge, the opposite trend is observed, i.e. the response increases with increasing velocity. It shall be noticed that the arcwise position arc=-0.22 is close to the axis of rotation.
  Similar features are observed on suction side of the oscillating blade; however the phase on the fore part is much less affected.
  On blade -1, the change in trend of amplitude on suction side occurs further upstream than blades 0 and +1, i.e. at arc=-0.11, whereas the phase remains rather unaffected on the fore part.

- At pure circumferential bending, blade +1 shows unaffected response magnitude on the entire blade surface whereas the phases display almost constant 45deg difference.
  On oscillating blade, the response on suction side increases with decreasing velocity and the reverse is observed on the aft pressure side. The major change in phase occurs downstream of the throat on aft suction side.
  The effect on blade -1 is also of low order of magnitude like blade +1. The amplitude is unchanged but the phase strongly varies on the fore pressure side.

- Combined modes display similar features than their respective pure modes.
  Blade +1 shows response close to pure torsion with an increase in magnitude with flow velocity on the aft blade.
  The response on oscillating blade differs on both sides: the magnitude increases with increasing velocity. However the fore suction side appear fairly unaffected both in terms of magnitude and phase. This is also suggested on blade -1.

The effect of flow velocity on the unsteady response has been described and the main outcomes are summarized below.

- pressure side of blade -1 is of much lower order of magnitude and is quasi-unaffected whatever the modeshape. However, despite this very small level, it results in significant changes in phase.
- phases on suction side of blade -1 suggest two different features inside the blade-to-blade channel. Whereas the fore blade is not affected by the flow velocity, the aft blade displays stronger variations.

The next sub-section is dedicated to the effect of inflow incidence angle.

3.3.6 Effect of incidence angle on unsteady response

The effect of inflow incidence angle on unsteady response is presented through data acquired on blades -1 through +1 for each modeshape, at M08. Three incidence angles have been considered, -26deg, 0deg and 14deg referenced as nominal (nom), off-design1 (off1) and off-design2 (off2) respectively.

At this point, a note shall be made on the following off-design data. Some measurement points appears doubtful on fore suction side of the oscillating blade. However, the data are still presented and short analysis is performed with respect to (Vogt, 2005). This region is critical since separation occurs. Steady measurements on these off-design points are thus recommended for short-term action. The following is a qualitative description since no steady measurements and no CFD results are presented.

The data are annexed in Appendix H and analyzed below.

- Pure axial bending shows considerable changes in magnitude on each blade. Fore pressure side of blade +1 displays increase in magnitude with incidence angle from arc=0 to arc=0.2 where all the curves intersect. This is believed to be due to separation bubble as reported in (Vogt, 2005). However, the change in phase is surprisingly of much lower order of magnitude, quasi non-existent. In contrast, the suction side of blade +1 is unaffected apart a small region at leading edge.
  This strong increase in magnitude is also observed on the fore pressure side of oscillating blade. However, the amplitude at off1 and arc=0.12 is doubtful, this peak has been reported between nom and off2 in (Vogt, 2005). This peak is also correlated to the separated flow in this region, which increases with increasing incidence. On fore suction side just downstream the leading edge, the magnitude decreases significantly when increasing the incidence. Furthermore, phase does not feature variations.
  On blade -1, the suction peak at arc=-0.15 gets much sharper with increasing incidence but the phase remains rather unchanged. In contrast, the second peak arising on the fore pressure side results in strong phase variation.

- Pure torsion mode features rather similarly to the above pure axial bending both in terms of phase and amplitude.

- Pure circumferential bending is much less affected than the two previous modeshapes.
  On blade +1, the changes are within the measurement accuracy, the magnitude is small, however phase changes on pressure side.
  The magnitude on blade 0 behaves without clear correlation, however the change in incidence results in noticeable phase deviation on fore blade.
  The magnitude on blade -1 features similarly to the pure axial bending with increasing magnitude on the fore pressure side and sharper peak on the fore suction side. Furthermore, the phases are drastically affected in the separated region.

- Combined modes display similar features than their respective pure modes.

The effect of incidence angle on unsteady response has been clearly evidenced. The main outcome is the drastic change in phase in the separated region. The next sub-section is dedicated to the 3D effects on unsteady response.

3.3.7 Three-dimensional effects on unsteady response

Three dimensional effects are assessed for the three pure modes as well as for the combined axial bending/torsion mode on blades ±1. Data on oscillating blade, being instrumented at midspan only, are not presented as well as the combined circumferential bending/torsion mode. Aeroelastic responses at M08, nominal and k=0.2, at 10%, 50% and 90% span are presented.

The data are annexed in Appendix I and analyzed below.

- Pure axial bending features the most disturbed response among the modeshapes. The effects are mainly observed on the primary surfaces. The aforementioned response peak on suction side of blade -1 increases significantly from hub to tip. The same growth occurs also on the aft pressure side of blade +1.
  The phases on both primary surfaces appear unaffected except close to hub at arc=-0.35 where a distinct peak rises that has been reported as probably due to secondary flow (Vogt, 2005).

- Pure torsion is much less affected. The noticeable difference is observed on the fore suction side close to tip where the aforementioned suction peak extends slightly upstream. It is believed to be due to the twisted shape of the blade profile whose the effect is strengthened by the torsion motion.
  Whereas the effect is rather weak on the amplitudes, it is more pronounced on the phases especially on suction sides: the phase increases from hub to tip and from tip to hub on blade +1 and -1 respectively. The largest difference being located in the leading edge region, this variation could also be due to the blade profile.

- Pure circumferential bending displays low magnitudes, however the 3D effects remain noticeable. The aft pressure side of blade +1 exhibits local response maximum increasing from hub to tip around arc=0.3; the phase at 90% span are clearly out-of-phase with respect to the blade motion whereas it is about 40deg lower at 10% and 50% span.
  The same trend in amplitude is observed on the fore suction side of blade -1 with local response maximum located at the aforementioned suction peak, i.e. around arc=-0.11. This region displays rather constant phase over span but varies significantly from arc=-0.22 towards the trailing edge. The main variation occurs at 90% span. The particular features of phase at 90% span is believed to be due to the tip leakage flow.

- Combined axial bending/torsion depicts qualitatively very similar feature than pure torsion mode.

This sub-section has presented the 3D effects on the unsteady response at M08, k=0.2 and nominal. The data have been acquired on blades ±1 since oscillating blade is

instrumented at midspan only. The main effect occurs on primary surfaces at pure axial bending mode with increasing response amplitude from hub to tip. This is also observed at pure circumferential bending but in much lower extent and much stronger disturbed phase on the aft suction side of blade -1.

The unsteady response has been evaluated according to the reduced frequency, the flow velocity and the incidence angle. This has led to the following main conclusions:

- an increase in reduced frequency results in decreasing response. The major response is located on oscillating blade, on suction side of blade -1 and in a lower extent on pressure side of blade +1. The effect is higher for pure axial bending, pure torsion and both the combined modes. Strong changes in response magnitude do not necessarily induce strong changes in phase.
- the flow velocity strongly affects the oscillating blade and leads to similar features whatever the modeshape, i.e. the phases on aft suction side are highly disturbed whereas the aft part is much less affected.
- separated flow leads to change in phase and considerable response in magnitude. However, no clear picture can be drawn at this point since steady state misses for deeper investigations (analysis can rely on Glodic et al., 2009; Vogt, 2005).
- measurements at different span positions have highlighted the occurrence of 3D effects. Pure axial bending mode are the most affected in terms of magnitude and phase.

At this point the effects of reduced frequency, flow velocity, incidence angle on the unsteady response have been assessed. The next sub-section introduces the linear superposition principle. This aims at validating the combination of the modes.

3.3.8 Linear superposition principle

This sub-section presents the linear superposition principle based on the experimental data previously introduced. The superposition consists simply in adding the pure modes results for comparison to the measured combined modes. As described in Eq. 3-2, the combined modes are a combination of pure bending and pure torsion at bending-to-torsion ratios $R = 1$ at 90deg out-of-phase denoted by ϕ. Glodic et al. (2009) have presented similar tests at low subsonic flow (M04) for the combined axial bending/torsion mode at different bending-to-torsion ratios and showed very good agreement.

$$\tilde{C}_{p,superposed} = \tilde{C}_{p,bending} + \frac{1}{R}\tilde{C}_{p,torsion} \cdot e^{i\phi} \qquad \text{Eq. 3-2}$$

As mentioned in sub-section 2.1.5, calibration has been performed for each pure mode; the vibration amplitude for combined modes is therefore calculated from the aforementioned calibration. Again, the actuation mechanism consists of two co-rotating circular eccentric cams actuating a guided actuator disk in a sinusoidal oscillatory movement. Pure bending and torsion modes are achieved by co-rotating the two cams at 0deg and 180deg phase shift respectively. Setting of the oscillation amplitude is illustrated in Figure 3-17. It gives the theoretical amplitude of motion according to the cam phase lag when the blade is oscillating either in bending or torsion mode. Combined modes are achieved by co-rotating the two cams at a phase shift between 0 and 180deg. The present tests have been performed by setting the cam phase lag to 108deg, which corresponds to

a bending-to-torsion amplitude ratio of $R = 1$. The setting is done manually by controlling the position of an internal planetary gear.

$$R = \frac{A_{bending}}{A_{torsion}} \qquad \text{Eq. 3-3}$$

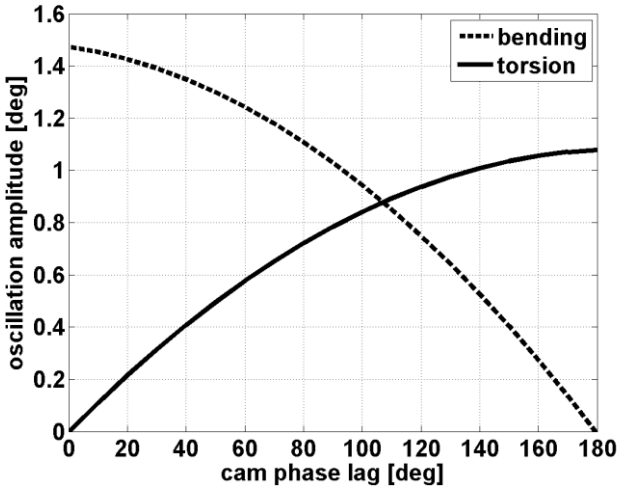

Figure 3-17: Setting of the oscillation amplitude

As a result, the unsteady response to combined modes is first normalized by the amplitude of pure bending, then correction is applied with a factor defined as follows,

$$factor = \frac{oscillation\ amplitude\ @0deg\ cam\ phase\ lag}{oscillation\ amplitude\ @108\ deg\ cam\ phase\ lag} \qquad \text{Eq. 3-4}$$

Linear superposition for combined axial bending/torsion and circumferential bending/torsion are displayed in Figure 3-18 to Figure 3-20 and in Figure 3-21 to Figure 3-23 respectively. The operating point is set to M08, nominal at k02. For each blade, i.e. blade 0 and blades ±1, amplitude and phase of the normalized unsteady pressure to pure and combined mode as well as superposition are included:

- pure bending (measured), pure torsion (measured) and combined bending/torsion (measured) refer to measured tests presented above.

- superposed bending/torsion (analytical) refers to the analytical superposition of the measured pure modes tests resulting from Eq. 3-2.

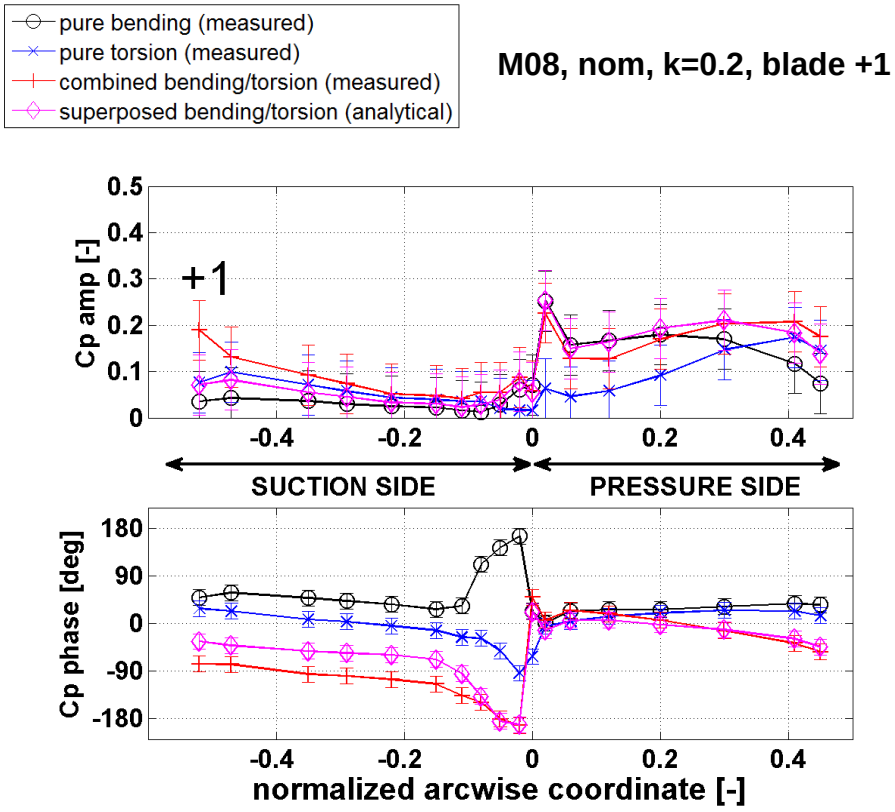

Figure 3-18: Linear superposition, combined axial bending/torsion, blade +1

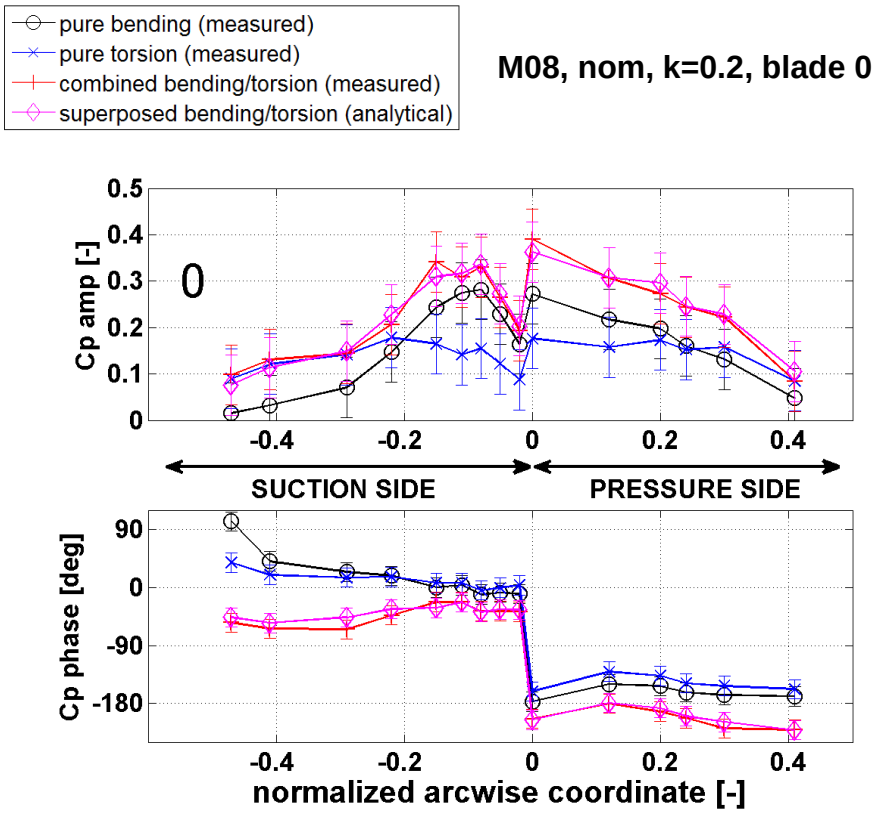

Figure 3-19: Linear superposition, combined axial bending/torsion, blade 0

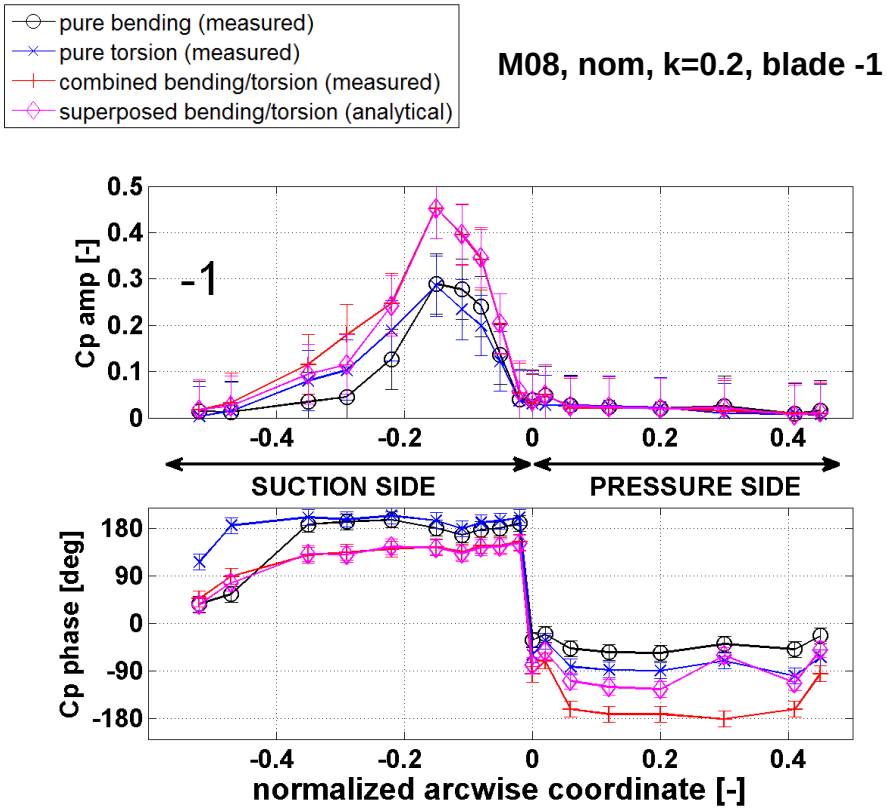

Figure 3-20: Linear superposition, combined axial bending/torsion, blade -1

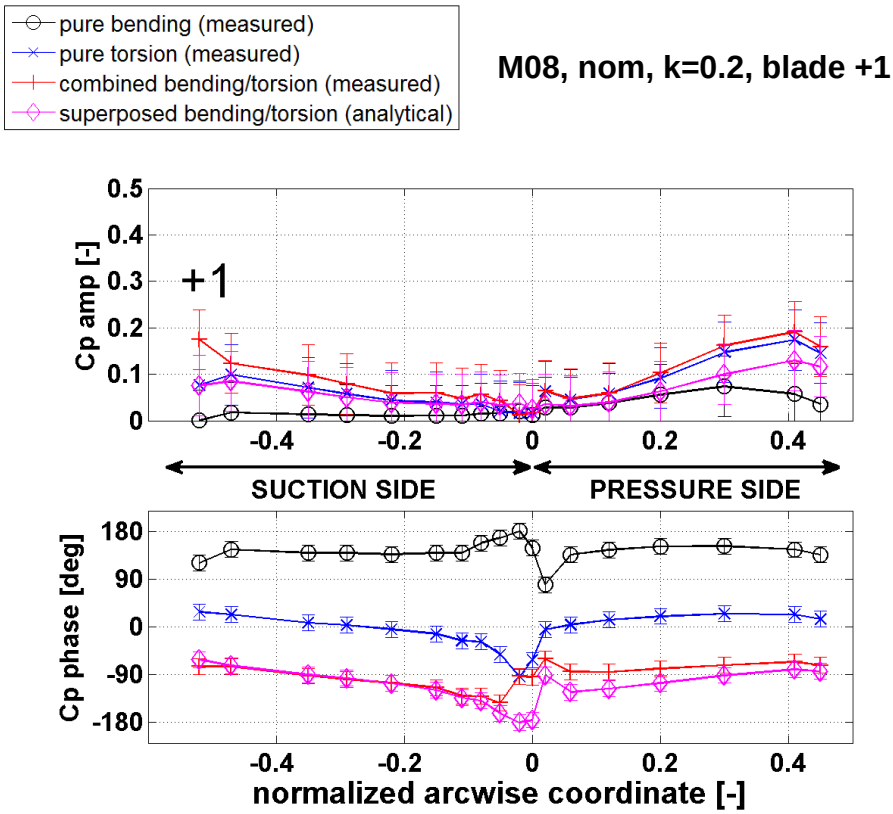

Figure 3-21: Linear superposition, combined circumferential bending/torsion, blade +1

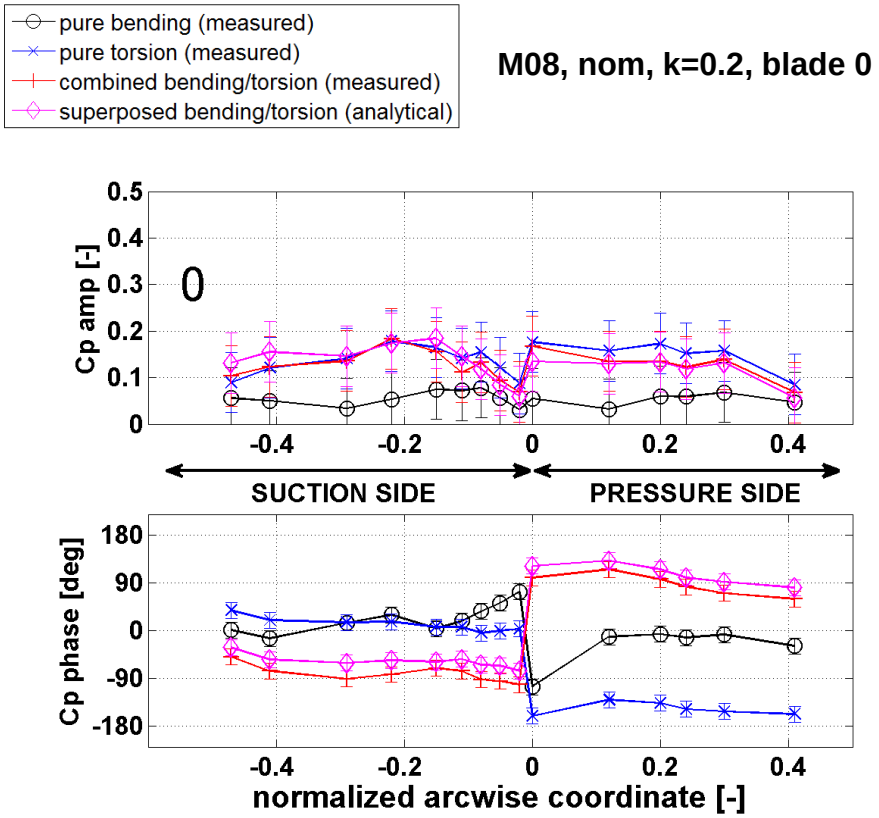

Figure 3-22: Linear superposition, combined circumferential bending/torsion, blade 0

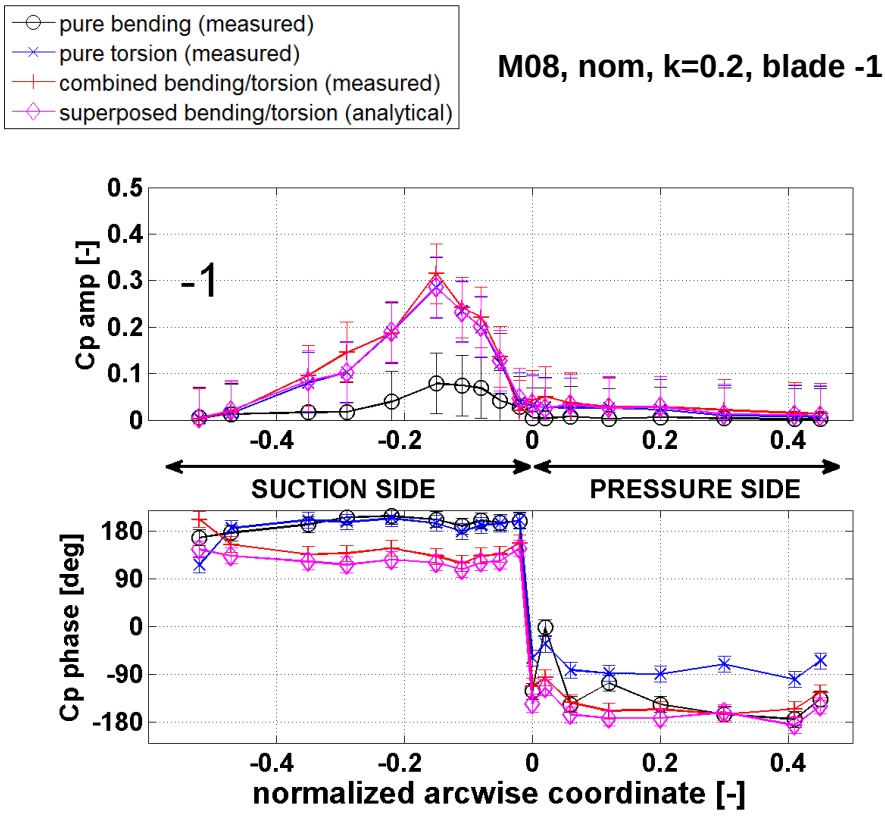

Figure 3-23: Linear superposition, combined circumferential bending/torsion, blade -1

The figures show that:

- for the combined axial bending/torsion mode, there is a good agreement between the amplitudes of the measured combined and superposed modes. The biggest discrepancies are observed on blade +1 on the aft suction side and on the fore pressure side. The phases present higher differences up to about 100deg on pressure side of blade -1; however, the amplitudes are rather low. Furthermore, the phases on the oscillating as well as on its direct surfaces reveal high degree of agreement.
- for the combined circumferential bending/torsion, the amplitudes agree rather well expect again on blade +1 which exhibits the highest differences. The phases show the same trend but a shift of about 30deg appears on the oscillating blade.

The main differences in phase occur on secondary surfaces, i.e. suction and pressure side of blades +1 and -1 respectively, whereas very good agreement is achieved on primary surfaces. This has to be correlated to the fact that unsteady response on secondary surfaces are of much lower degree of magnitude.

The linear superposition principle described above provides promising perspectives. This drives to easier understanding of aeroelastic problems by investigating on elementary effects and thus to identify potential destabilizing contributions. In that context, the next section is dedicated to the study of unsteady pressures from a stability point of view.

3.3.9 Flutter stability

The term stability refers to the stabilizing/destabilizing character of the flow rather than the stability of the fluid-structure system. As described in Appendix A the stability is evaluated through the work per oscillation cycle, it is computed by considering the 2D blade section at midspan with the blades oscillating in the traveling wave mode. The evolution of the stability parameter with respect to the interblade phase angle for each mode is discussed: its sign, positive or negative, indicates directly the stabilizing or destabilizing character of the flow respectively.

The focus is put on the following operating point: M08, nominal and k=0.2. Each of the blade motion results in specific response on the blades 0 and ±1 that is integrated along the complete arcwise coordinate such to achieve the unsteady force with one single value per blade and per IBPA, i.e. the blade influence coefficients. The imaginary parts of the aforementioned influence coefficients versus the IBPA are included in Figure 3-24. Each plot gives the influence of one mode on the orthogonal directions of interest as described in Eq. 3-5,

$$[F] = \begin{bmatrix} f_{xx} & f_{xy} & f_{xz} \\ f_{yx} & f_{yy} & f_{yz} \\ f_{zx} & f_{zy} & f_{zz} \end{bmatrix} \qquad \text{Eq. 3-5}$$

The first index refers to the mode causing the force and the second to the direction in which the force is acting. The diagonal terms correspond therefore to the influence of the mode on itself whereas the off-diagonal terms refer to the coupling contributions, i.e. the influence of a mode on other directions. The results appear like a perfect sinusoid since only the direct adjacent blades ±1 are considered:

- the influence of reference oscillating blade 0 is a constant value. The influence of the vibrating blade on itself, i.e. eigen-influence, is therefore independent of the interblade phase angle.
- the influence of adjacent blades corresponds to a harmonic contribution which can be considered as first harmonic oscillation.

The figure on the left displays the imaginary part of the axial component of the unsteady force over the IBPA for the blades 0 and ±1. For the combined motion, the two component of interest are displayed.

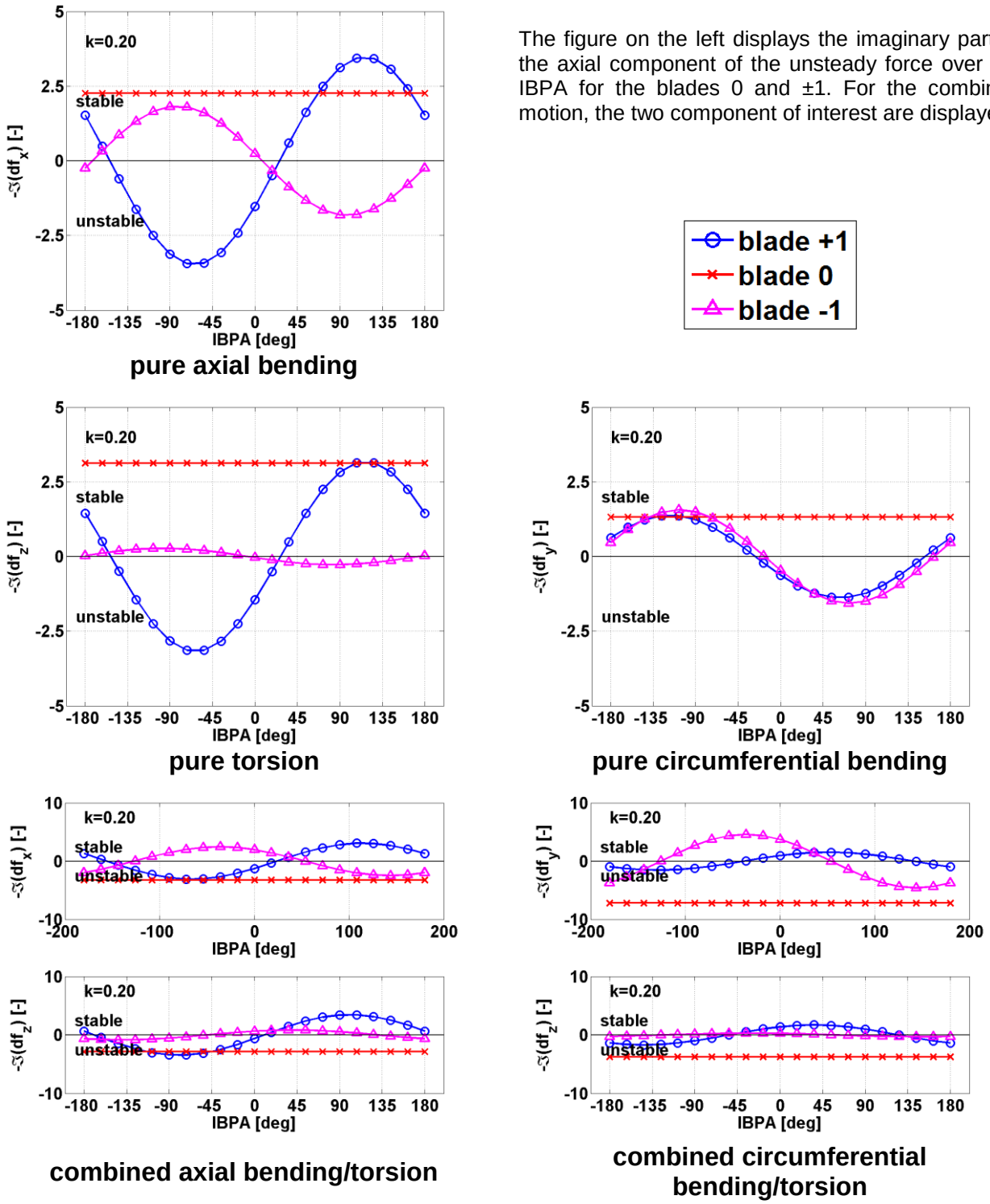

Figure 3-24: Unsteady force coefficients, M08, nom, k=0.2

Figure 3-24 indicates the following:

- for all pure modes, the oscillating blade is stabilizing over the entire range of IBPA, whereas for combined modes, blade 0 acts destabilizing.
- for pure axial bending and pure torsion, the adjacent blades ±1 act in an opposite way, i.e. for a given IBPA when blade +1 acts stabilizing, blade -1 acts destabilizing expect around 18deg and -160deg. This is not observed for the pure circumferential bending, which shows very similar evolutions of the adjacent blades. They act destabilizing in almost the entire range of positive IBPA: the least stable appears between 54deg and 72deg.

The unsteady blade surface pressures reduced to blade-specific influence coefficients are superposed to traveling wave mode and displayed versus the interblade phase angle, at two reduced frequencies (k=0.05 and k=0.2), M08 and nominal in Figure 3-25. The figure suggests the following:

- for each reduced frequency, the oscillating blade acts stabilizing except at the lowest one when the blade is oscillating in pure torsion mode.
- when oscillating in pure axial bending, the blade row is stable over the entire range of interblade phase angle for the two frequencies.
- the increase in reduced frequency results to an increase in stability. This is highlighted by a shift towards positive values revealing an increasingly stabilizing oscillating blade.
- the unstable range of IBPA at the lowest frequency for the pure torsion becomes entirely stable when the frequency increases whereas for circumferential bending, the unstable range of IBPA is reduced only.

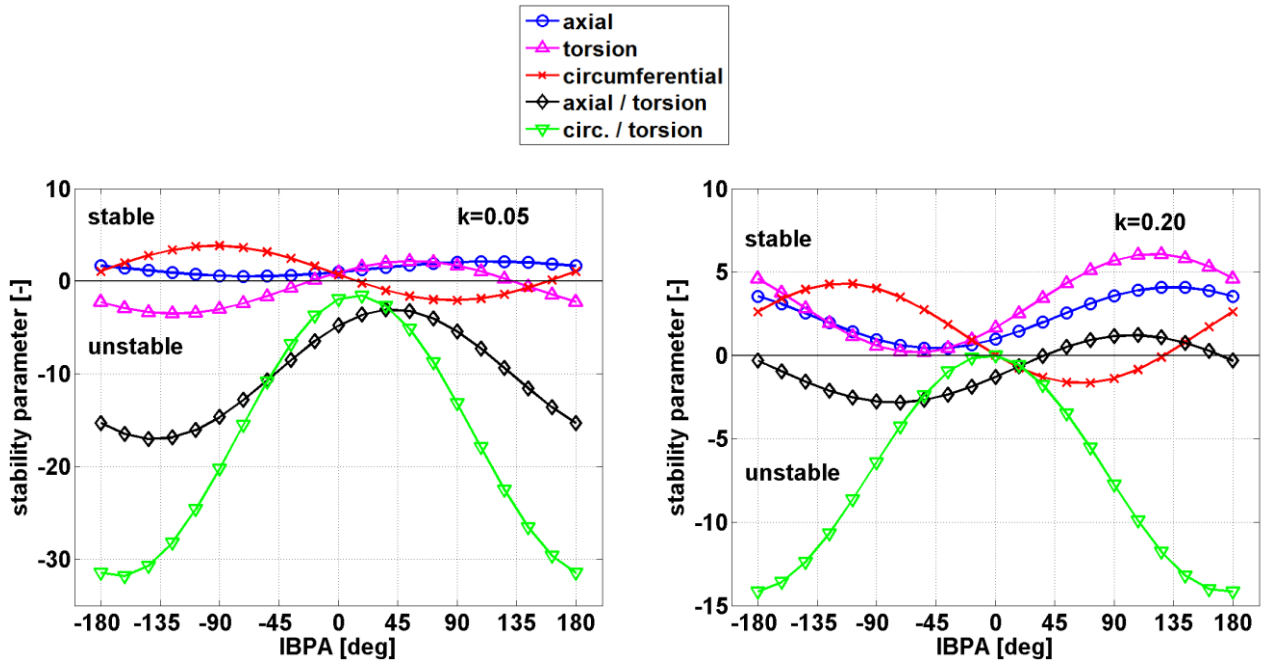

Figure 3-25: Effect of reduced frequency on stability, M08, nom

3.3.10 Discussion

The influences of the phase angle between bending and torsion as well as the ratio bending-to-torsion amplitude on the stability parameter are addressed in Figure 3-26 over

the interblade phase angle for the combined axial bending/torsion mode at M08, nominal and k=0.2. The pure axial bending mode and the pure torsion are analytically superposed (Eq. 3-2).

- The influence of the phase angle is suggested for three phase angles at a constant amplitude ratio (R=1). Figure 3-26 (a) shows that the negative phase angle, i.e. the torsion is lagging the bending, leads to instability for negative IBPA, whereas for in-phase combined mode and positive angle, the system becomes stable over the entire IBPA range. Moreover, the evolutions over the IBPA for these two last angles are very similar with each other.

- The influence of the ratio bending-to-torsion amplitude is suggested for three amplitudes at a constant phase angle ($-\pi/2$), R=0.5 means that the bending part is dominant in the combination whereas R=2 indicates that the torsion is dominant. Figure 3-26 (b) shows that dominant torsion is stabilizing for out-of-phase combined mode. Furthermore, the range of IBPA between 36deg and 72deg appears independent of the ratio.

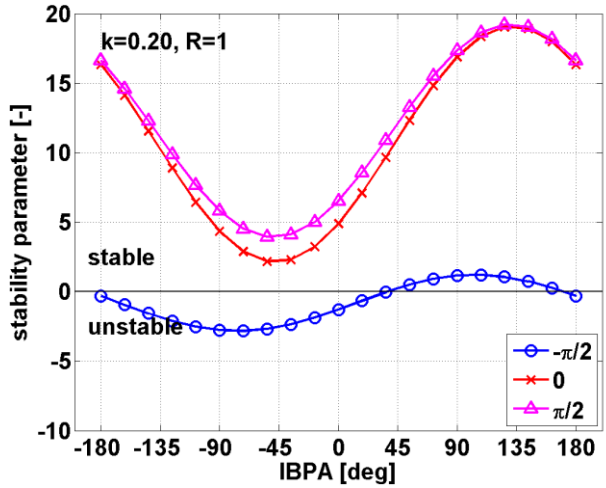

(a)

Influence of the phase angle between bending to torsion. Combined axial bending/torsion

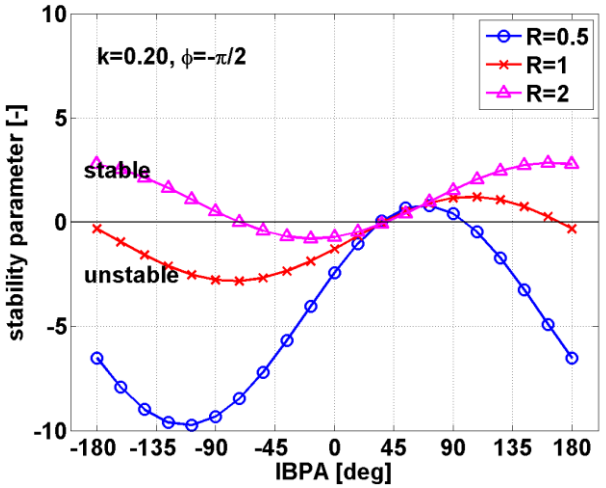

(b)

Influence of the ratio bending-to-torsion amplitude. Combined axial bending/torsion

Figure 3-26: Influence of phase angle and amplitude ratio in combined mode

The nature of combined modes appears finally essential in the overall stability. This highlights the need to perform further measurements from a parametrical point of view.

3.4 Conclusion

Experimental investigations of subsonic flutter in low-pressure turbine has been presented. Flutter test data have been acquired in an annular sector cascade comprising seven blades which one is made oscillating in controlled way as rigid-body. The tests included 3 pure modes as well as combination of them, i.e. pure axial bending, pure circumferential bending, pure torsion, combined axial bending/torsion and combined circumferential bending/torsion. The unsteady responses to blade excitations were measured through

blade -1 to blade +1 in the influence coefficient domain, from low to high subsonic outlet Mach numbers (0.4 and 0.8 respectively), with the blade oscillating at 4 distinct frequencies yielding to a maximal reduced frequency of 0.4 and 0.2 at M04 and M08 respectively. The incidence angle was varying from nominal to two off-design conditions such as to force the boundary layer on pressure side to separate. The inlet conditions were evaluated though hot-wire measurements in order to provide input for further numerical computations.

The main conclusions are summarized below:

- the major aeroelastic response occurs on oscillating blade, on blade +1 and on suction side of blade -1 whose the pressure side always shows relatively much lower response.
- the major aeroelastic response results from pure axial bending, pure torsion or when one of them is part of a combination. Response at pure circumferential is of lower order of magnitude.
- quasi steady analysis at M08 is still valid to interpret unsteady responses at axial bending and torsion, whereas circumferential bending behaves differently. Two mechanisms are responsible: the change in section at the throat and the steady gradient present inside the blade-to-blade channel.
- the effect of reduced frequency has shown that the lowest reduced frequency involves distinct high response at pure axial and pure torsion. An increase in reduced frequency results in decreasing response at M08. The major response is located on oscillating blade, on suction side of blade -1 and in a lower extent on pressure side of blade +1. The effect is higher for pure axial bending, pure torsion and both the combined modes.
- the flow velocity strongly affects the oscillating blade and leads to similar feature whatever the modeshape. On blade -1, the phases on aft suction side are highly disturbed whereas the aft part is much less affected.
- separated flow leads to change in phase and considerable response in magnitude. However, steady state is needed for deeper investigations.
- the 3D effects measurements at different span positions have highlighted the occurrence of 3D effects. Pure axial bending mode are the most affected in terms of magnitude and phase.
- the linear superposition principle has led to good agreement and therefore this will allow decomposing more complex motions into elementary movements.
- the data were finally processed such as to achieve blade individual work coefficients, then the data were recombined in the traveling wave mode such as to assess the stability parameter. This has highlighted that the oscillating blade 0 becomes much more critical at combined modes by considerably destabilizing the system.
- the stability strongly depends on the nature of the combined modes in terms of phase angle and amplitude ratio between the involved pure modes.

The presented experimental investigation has highlighted the effect of the structure in terms of motion and the effect of the aeodynamic in terms of incidence and velocity on the aeroelastic response. In the light of these results, an application towards recent industrial turbines is suggested in a second part. The focus is put on two turbines chosen according to the aforementioned experimental results. The goal is to investigate real turbine from two

perspectives: structural and aerodynamic. Accordingly, a blisk is firstly chosen to investigate from a structural point of view. The blisk implies complex deformation of the blades and thus the linear combination principle will be used to decompose the problem. Secondly, a supersonic turbine is chosen to investigate from an aerodynamic point of view: the blade motion is of elementary nature, i.e. purely axial, but the flow features strong non-linearities such as shock wave/boundary layer interaction.

PART 2: NUMERICAL APPROACH OF SUBSONIC AND SUPERSONIC FLUTTER

This part is dedicated to numerical investigations of industrial space turbines. Spacecrafts, being propelled by combustion gases of hydrogen and oxygen, require the use of turbopump units to achieve the desired combustion chamber conditions. Space turbines delivering power to pump are continuously developed to higher loads. Although the design life time of such a turbopump may be just a few minutes they can fail within seconds because of aeroelastic problems: the absolute aerodynamic load can be very high because of the high absolute pressure levels in the machine.

CFD computations are based on steady state computation (RANS) using Turb'Flow™ and unsteady computations linearized in the frequency domain using Turb'Lin™, which calculates the aerodynamic response to a prescribed blade motion assuming small perturbations.

This part consists of two distinct chapters:

- the first chapter (chapter 4) focuses on 2D numerical simulations of a blisk characterized by very low mechanical damping. This results in complex deformation of the blades. The steady non-linear field is firstly introduced and the unsteady response to a prescribed blade motion is presented with respect to a given IBPA range. Afterwards a particular IBPA is chosen and analyzed in details. Then, in order to simplify the analysis, a 2D methodology is proposed based on the linear combination principle. Finally, the effect of the IBPA and cut-on/cuff-off modes are correlated to the aerodynamic damping.

- the second chapter (chapter 5) focuses on 3D numerical simulations of a supersonic assembled bladed disk. The motion is of elementary nature, i.e. purely axial. However the flow is highly severe featuring shock wave/boundary layer interaction. The complexity comes here from the aerodynamic side. First, the steady state is introduced and the flow field is described. Afterwards, the unsteady response to a prescribed blade motion is computed over a restricted nodal diameters range. The backward modes are found all unstable. Then, the most stable and unstable cases are investigated and correlations of the aerodynamic damping to the IBPA and cut-on/cut-off modes are suggested.

Due to confidentiality reasons, the following data are voluntarily not given:

- the blade geometries have been scaled such that the actual shape is not displayed.
- the aspect ratio, chord, tip gap
- the number of blades
- the blade material
- the operating point

4 2D NUMERICAL APPROACH OF SUBSONIC FLUTTER

In this chapter a 2D methodology for flutter analysis is presented. The approach is based on an industrial modern type of space turbine using integrally bladed disk (blisk) instead of individual blades attached to the disk. The turbine is studied numerically and the stability is computed within a restricted range of its nodal diameters. In order to simplify the analysis, investigations are based on principles of elementary decompositions. The chapter is therefore organized as follows. First, the characteristics of the turbine are given and the numerical computations are described. Then, the steady state is introduced and the aerodynamic damping is displayed over the interblade phase angles. Afterwards, a specific interblade phase angle is investigated in details. Finally the method based on the aforementioned elementary decomposition is developed and the effects of the IBPA as well as cut-on/cut-off modes are examined.

4.1 Presentation of the case study

The study focuses on flutter prediction of the axial turbine blades of a turbopump working with liquid hydrogen in an expander cycle engine. The turbine operates at low subsonic conditions, at high inlet pressure with low pressure ratio and moderate mass flow. Fluid properties are summarized in Table 4-1.

Parameter	Symbol	Value	Unit
specific gas constant	R	4321.78	[$m^2/s^2/K$]
specific heat capacity ratio	γ	1.383	[-]
dynamic laminar viscosity	μ	7.99E-6	[Pa.s]
thermal conductibility	λ	0.1807	[W/m/K]
density	ρ	1.312	[kg/m^3]

Table 4-1: Fluid properties

The subsonic turbine consists of an unshrouded rotor blisk comprising N blades made in high stiff material with smooth walls. The blisk is characterized by large tip gap and small aspect ratio. An isolated blade is considered whose the 2D profile is plotted in Figure 4-1 as well as:

- the section normalized by the section at the geometric throat. A fluid particle flowing close to the suction side experiences the minimal section around 67% axial chord.
- the passage width normalized by the pitch whose the minimum is around 42% axial chord.

The blade shape has been voluntarily scaled such that the actual shape is not displayed.

The blade motion originates from the blisk eigenmode corresponding to a 13 nodal diameters pattern, which is expected to be aeroelastically unstable. This eigenmode is characterized by very complex deformation of the blades, very high eigenfrequency, greater than 40kHz, and implies therefore extreme reduced frequency (k=6.4). The modeshape has been calculated outside of this work through modal analysis using 3D finite element model and then provided. Afterwards, it has been projected on a 2D cylindrical surface, unwrapped at constant radius, i.e. midspan, of the blade row. The 2D

blade motion is displayed in Figure 4-1 and cannot be clearly labelled because it originates from the blisk modeshape instead of the blade itself. However it appears like a torsion mode combined to an axial flexion, the amplitude of motion being essentially located at the trailing edge.

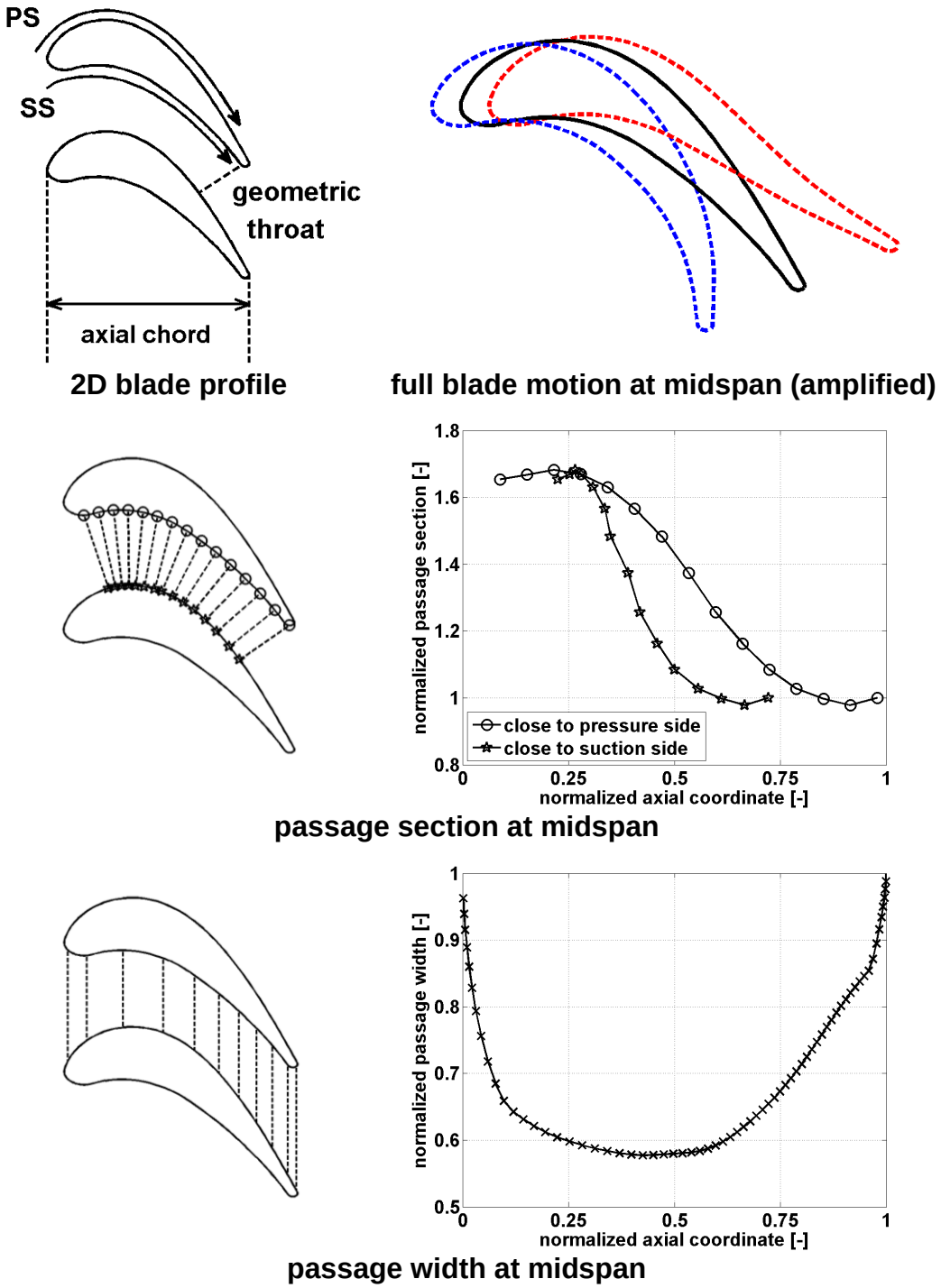

Figure 4-1: Geometric characteristics of the blade

The case study has been presented and the blade motion described. This latter will be the source of unsteadiness in the unsteady computations. The next section is dedicated to the numerical parameters.

4.2 Numerical parameters

This section summarizes the numerical parameters and complementary details are included in Appendix D. The simulations have been performed with the package Flow'Design™ v1.5.8-04SA which contains the solvers Turb'Flow™ (steady computation) and Turb'Lin™ (unsteady computations linearized in the frequency domain).

4.2.1 Computation grid

A periodic multi-blocks structured grid is used to mesh one blade sector. The O-grid is extruded from the blade profile, starting from a first cell size of about 0.01% of the pitch. The H-grids are then added up- and downstream of the blade. Two different mesh sizes have been used for the steady and unsteady computations respectively:

- the computation box for steady state is such that the mesh is extended five axial chords upstream and six axial chords downstream of the blade (11785 nodes);
- whereas the mesh is extended about 36 axial chords for unsteady state (25473 nodes).

Computation boxes and the mesh around the blade are included in Figure 4-2.

Such a long computation domain is used in order to damp outgoing unsteady waves and thus to avoid unphysical reflection from the in- and outlet boundaries towards the blade. Mesh size sensitivity studies (Fluorem, 2006) showed that steady results were very close with each other and therefore did not depend on the computation box. In contrast, the linearized responses showed significant differences on the aerodynamic damping coefficient within the IBPA range. It has been highlighted that, according to the IBPA, the number and amplitude of waves propagating from the blade to the computation box boundaries change (due to cut-on/cut-off modes as described in further section). The imposed boundary conditions are thus not completely non-reflective: a part of these waves comes back towards the blade with a phase related to the computation box size. As a result, they interfere with the waves from the blade itself and induce amplitude and phase that depend on the configuration.

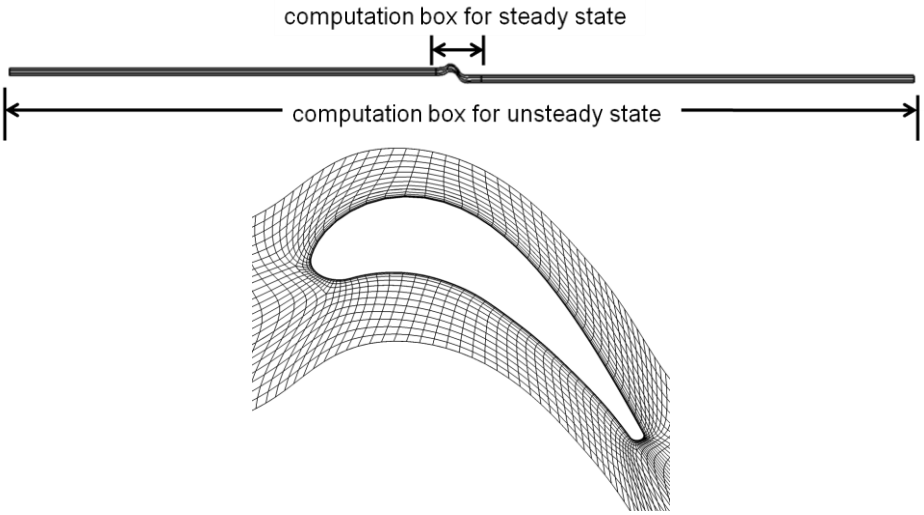

Figure 4-2: Two-dimensional structured mesh (1 every 2 points)

4.2.2 Steady computations

The simulations have been performed with periodic boundary conditions. During computations, the total pressure, total temperature and angle are imposed at the inlet and the static pressure is prescribed at the outlet. Moreover the walls are constrained to adiabatic conditions. The second order upwind Roe spatial scheme has been used combined to an implicit temporal scheme with a CFL condition of 10. The RANS equations system is closed with the Kok $k-\omega$ turbulence model with a limiter of kinetic energy production.

4.2.3 Linearized unsteady computations

The simulations have been performed in the traveling wave mode domain applying phase-lagged periodic boundary condition in order to take the IBPA into account. In addition to the very extended domain, non-reflective conditions are imposed at the in- and outlet in order to avoid unphysical reflections at the boundaries towards the blade. Second order centered Jameson scheme with 4th order artificial dissipation $(\varepsilon_2 = 0, \varepsilon_4 = 0.15)$ without limiter is used and the linear system is solved with GMRES deflated method. Furthermore, computations are executed with frozen turbulence. The unsteadiness, i.e. the blade motion, has been applied through transpiration boundary condition (see Appendix D). As the objective is to evaluate the unsteady response over a large nodal diameters range and because of the high frequency, it has been judged relevant to consider the aforementioned parameters, i.e. frozen turbulence and transpiration boundary condition. Moreover, this reduces significantly the computation time.

The industrial case has been presented. The blade motion has been described and the linearized unsteady computations introduced. The next sections are dedicated to the results. First the focus is put on the steady-state.

4.3 Steady state results

The steady state results from 2D RANS computations and a single channel is considered. The static pressure coefficient both in a blade-to-blade plane and along the blade surface versus the normalized axial coordinate is included in Figure 4-3. The figures depict typical pressure evolution in a turbine channel such as convergent-divergent channel with the minimal section passage at the throat:

- the stagnation point is located about 6% downstream of the minimal axial coordinate. This is also highlighted in the blade-to-blade plot (Figure 4-4) of the relative Mach number.
- on the pressure side, up to about 40% axial chord, the pressure appears as quasi constant, then it decreases significantly towards the trailing edge.
- the variations in pressure close to the trailing edge are due to two contra rotating vortices displayed in Figure 4-5.
- on the suction side, the static pressure reaches a minimum at about 20% and then slightly increases towards the trailing edge.

The flow is now characterized in terms of losses and turbulence. The relative total pressure normalized with its value at the inlet, i.e. one axial chord upstream of the cascade, is included in Figure 4-6 and the ratio of the turbulent dynamic viscosity (mut) over the laminar dynamic viscosity (mul) is displayed in Figure 4-7. The figures show that

the main losses are located in the wake. The boundary layer is very thin and does not disturb the main flow. At the throat the boundary layer thickness represents about 6.6% of the throat section. Figure 4-7 shows the increasing level of the turbulence along the channel and the consistency with the boundary layer.

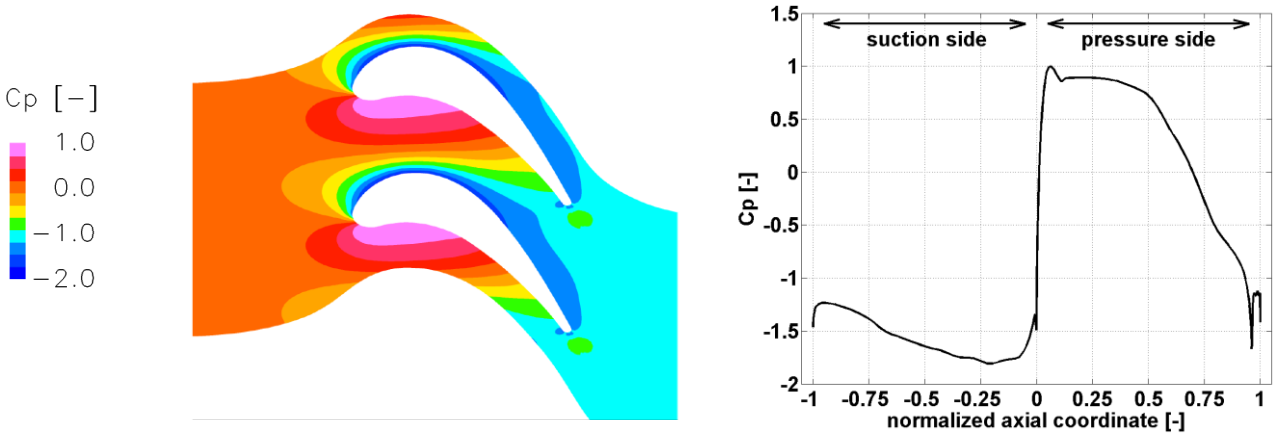

Figure 4-3: Static pressure coefficient

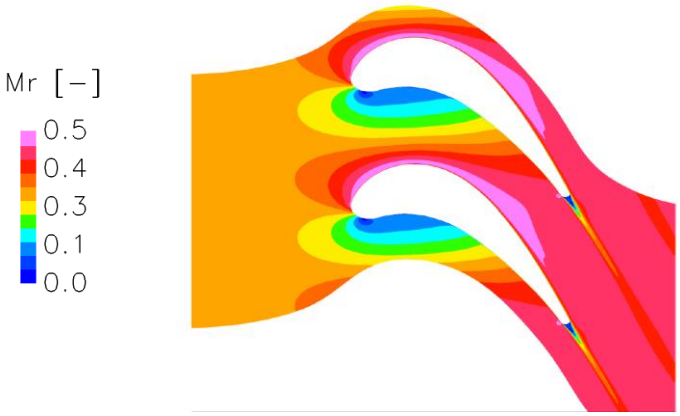

Figure 4-4: Relative Mach number

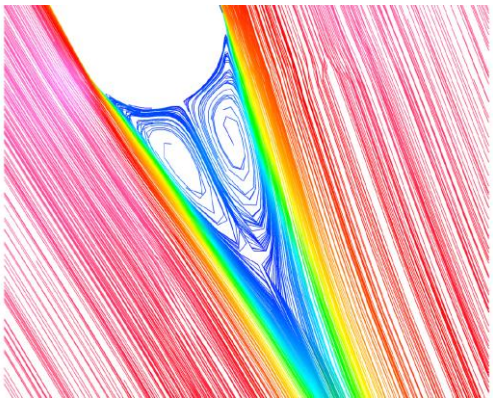

Figure 4-5: Trailing edge vortices

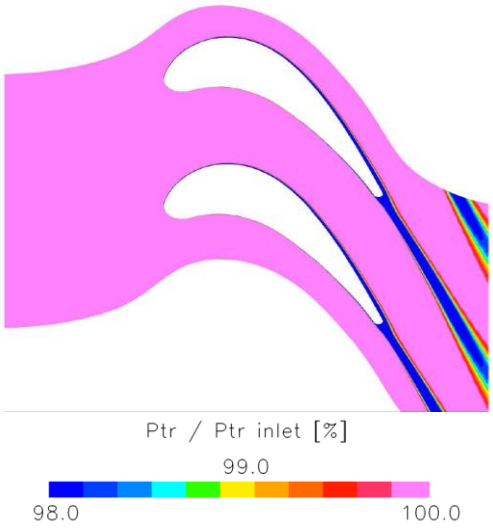

Figure 4-6: Relative total pressure

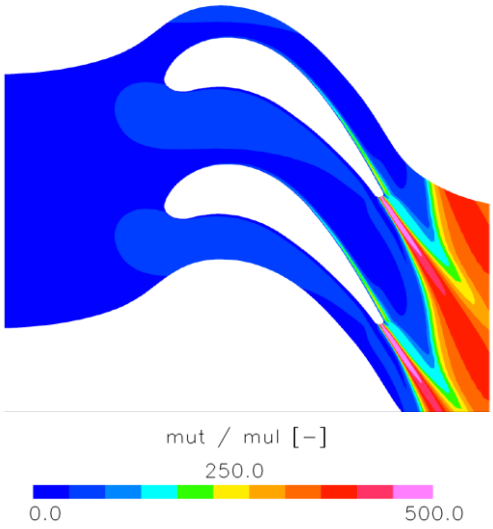

Figure 4-7: Dynamic viscosities ratio

The goal of this sub-section was to briefly describe the steady flow in order to highlight that the aerodynamic field does not feature strong non-linearities. This steady field will be the reference field for the unsteady computations and the next section is dedicated to the unsteady results.

4.4 Unsteady state results

The unsteady results are presented as follows:

- as the most important parameter from the designer point of view and being of high concern since it is the main damping source for the blisk, the aerodynamic damping coefficient is firstly presented over a restricted range of its nodal diameters.
- the aerodynamic damping coefficient as an integrated value does not provide detailed and useful information on the stability except the stability itself in terms of positive/negative values. Therefore, the particular case of +13ND is analyzed in details: this nodal diameter is expected to be aeroelastically unstable.
- then, the stability is investigated with respect to the blade motion itself (elementary decomposition) and the boundary conditions in terms of propagating waves (cut-on/cut-off modes).

4.4.1 Stability parameter

The stability parameter versus the nodal diameters is included in Figure 4-8. The coefficient is predicted positive, the fluid acts therefore as a damper. The evolution differs completely from sinusoidal curve without any understandable consistency. The figure reveals instead discontinuities between -20ND and -19ND, between -12ND and -11ND and between +11ND and +12ND. These violent changes are rather critical since sudden and large deviations in stability occur; for instance, from -20ND to -19ND, the stability parameter increases of 172%. In that case, this is not as critical as mentioned because this acts in a stabilizing manner, however the reverse would be obviously destructive. In order to investigate in a more intimate way the aerodynamic damping, the focus is now put on the aforementioned +13ND because, as mentioned, it was foreseen unstable.

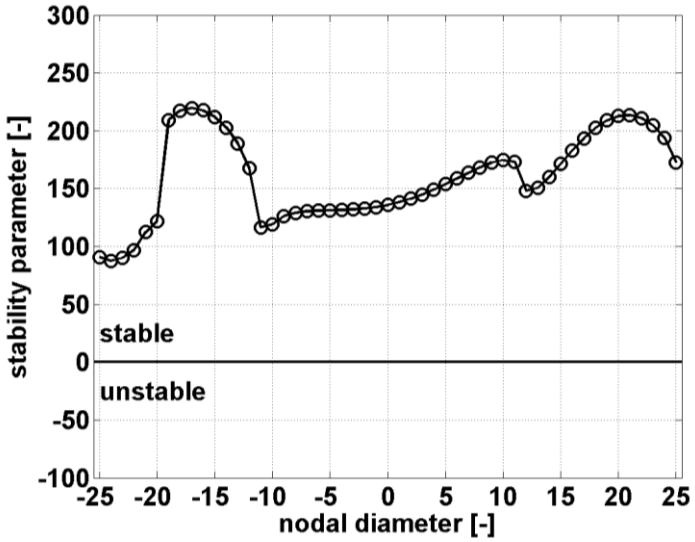

Figure 4-8: Stability parameter versus nodal diameter

4.4.2 Analysis of the 13 nodal diameters pattern

This sub-section is dedicated to the specific nodal diameter 13ND. First, the local stability parameter, i.e. along the blade, is introduced in order to highlight how the stability behaves along the surface. Then the unsteady pressure coefficient is presented and the cut-on/cut-off conditions as well.

4.4.2.1 Local stability parameter

The stability parameter along the blade surface is included in Figure 4-9. As already mentioned the global value is positive and thus the blade is aeroelastically stable. Nevertheless, when looking at the local values, destabilizing regions appear. This is especially observed on the pressure side from 25% to 79% axial chord and in a lower extent on the leading edge region; however, the suction side is stabilizing enough to overcome the destabilizing pressure side. Furthermore, the last 20% axial chord is stabilizing for both surfaces and exhibits the highest stable parts. Despite of its global stable character, the blade features local destabilizing contributions and thus provides useful information to the designers on how to increase the stability. Being calculated from the integration of the unsteady static pressure fluctuations along the blade surface, the stability analysis is completed by the unsteady response examination, which is presented in the next sub-section.

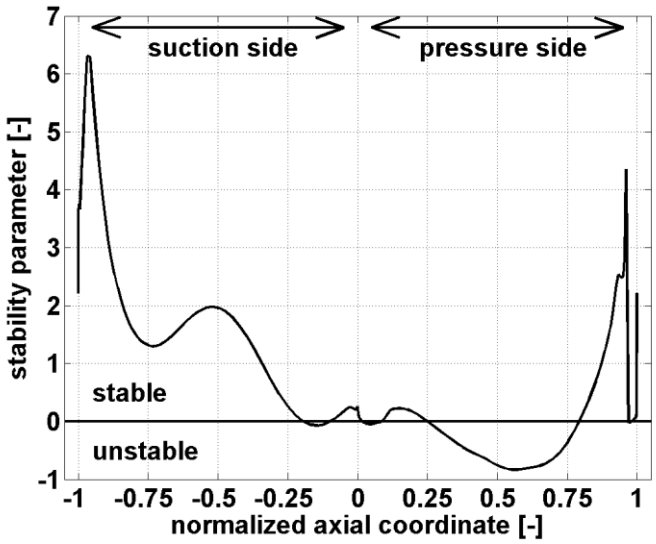

Figure 4-9: Stability parameter along the blade surface, 13ND

4.4.2.2 Unsteady response

A note shall be made on the presentation of results. The complex data are presented in terms of magnitude and phase. In blade-to-blade planes, the phases are displayed in the range [-180; 180]deg using a circular color map without discontinuity at ±180deg. When plotted along the normalized axial coordinate, the phases are also treated such as to avoid ±180deg jumps and the scale differs from plot to another in order highlight local variations.

It is recalled that the unsteady response, i.e. the static pressure fluctuations, is generated by the aforementioned prescribed blade motion through a transpiration boundary

condition, i.e. the blade motion velocity is imposed on its surface as illustrated in Figure 4-10: the right hand side figure shows what is imposed in the linearized solver whereas the left hand side figure focuses on the velocity fluctuations in a blade-to-blade plane resulting from the computations (except on the blade surface itself). The fluctuations are normalized by the steady reference velocity, i.e. one axial chord upstream of the cascade. As mentioned above, the trailing edge is characterized by higher amplitude of motion. The region of leading edge features strong velocity fluctuations but the strongest appear in the wake and interfere with the trailing edge of adjacent blade. On the suction side, the region just upstream the throat is characterized by low fluctuations.

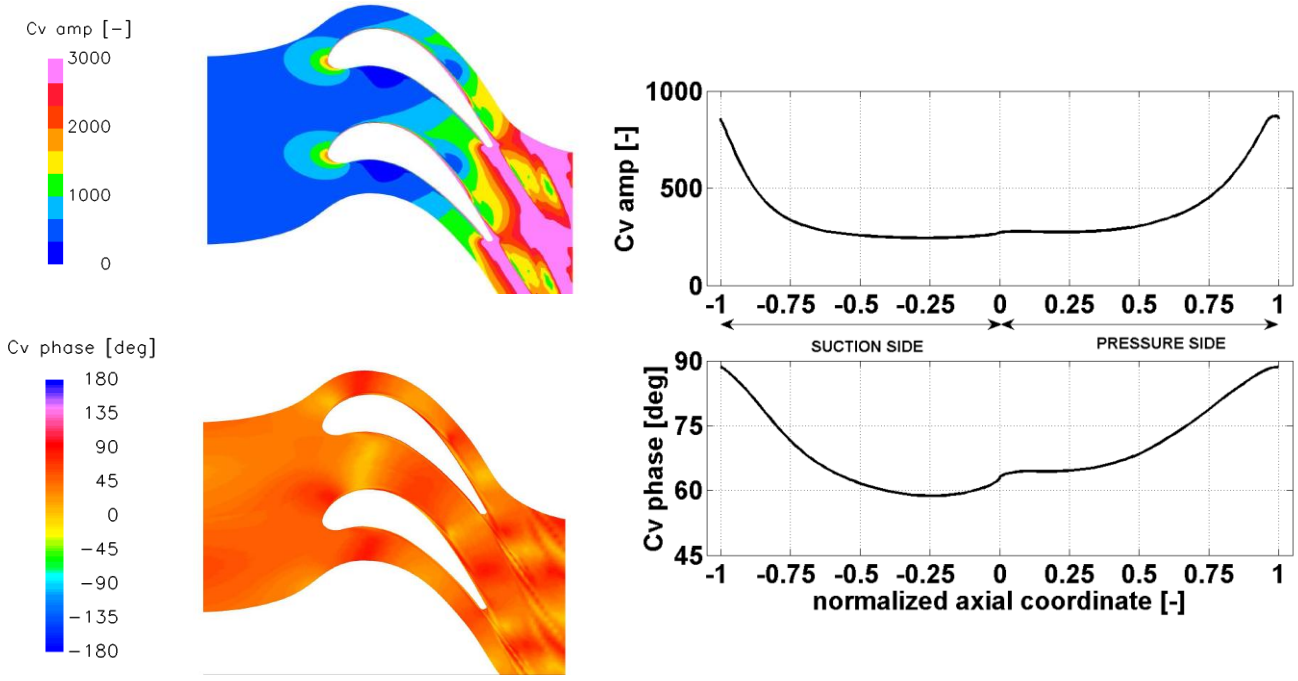

Figure 4-10: Unsteady velocity fluctuations, 13ND, magnitude and phase

The unsteady pressure in terms of magnitude and phase in the blade-to-blade plane as well as on the blade surface along the normalized axial coordinate is included in Figure 4-11. This suggests the following:

- significant unsteady pressure fluctuations arise inside the channel between 10% and 70% axial chord.
- on the suction side the highest levels appear firstly close to the mid-axial-chord at 42%, this corresponds to the minimum passage width, and secondly at the trailing edge. The fluctuations reach a minimum in between at 75% axial chord: this corresponds to the throat. The change in section passage at the throat modifies the unsteady response as shown on the phase plots through a stripe centered on it: from 66% to 84% axial chord, the phase rotates from 89deg to 47deg.
- on the pressure side, the level is rather constant on almost the entire surface. A strong and shark peak rises at 96% axial chord in the same way than on the pressure side.
- these large peaks observed close to the trailing edge both on the pressure and suction sides are believed to be due to the two aforementioned steady contra rotating vortices. The blade motion induces a slip of these vortices and thus create a change of the local pressure gradient.

- the front of the blade is characterized by low pressure fluctuations which is revealed by a severe variation in phase.
- furthermore, the blade-to-blade plot of the magnitude shows that the level of the pressure waves decreases significantly towards the inlet whereas it remains almost constant towards the outlet. On that account, the high pressure level appears as an amount of energy confined inside the channel.
- the phases behave linearly on both sides after the aforementioned strong variations at the blade front.
- on the suction side, the phase starts increasing linearly from about -13deg at 10% to 89deg at 66% axial chord. Then it decreases from the throat up to 84% and then it starts again increasing towards the trailing edge.
- on the pressure side, the linear variation is much less pronounced. From about 15% to 50%, the phase is rather constant and equal to -250deg, and then it starts to increase towards the trailing edge with a higher slope than on the suction side.

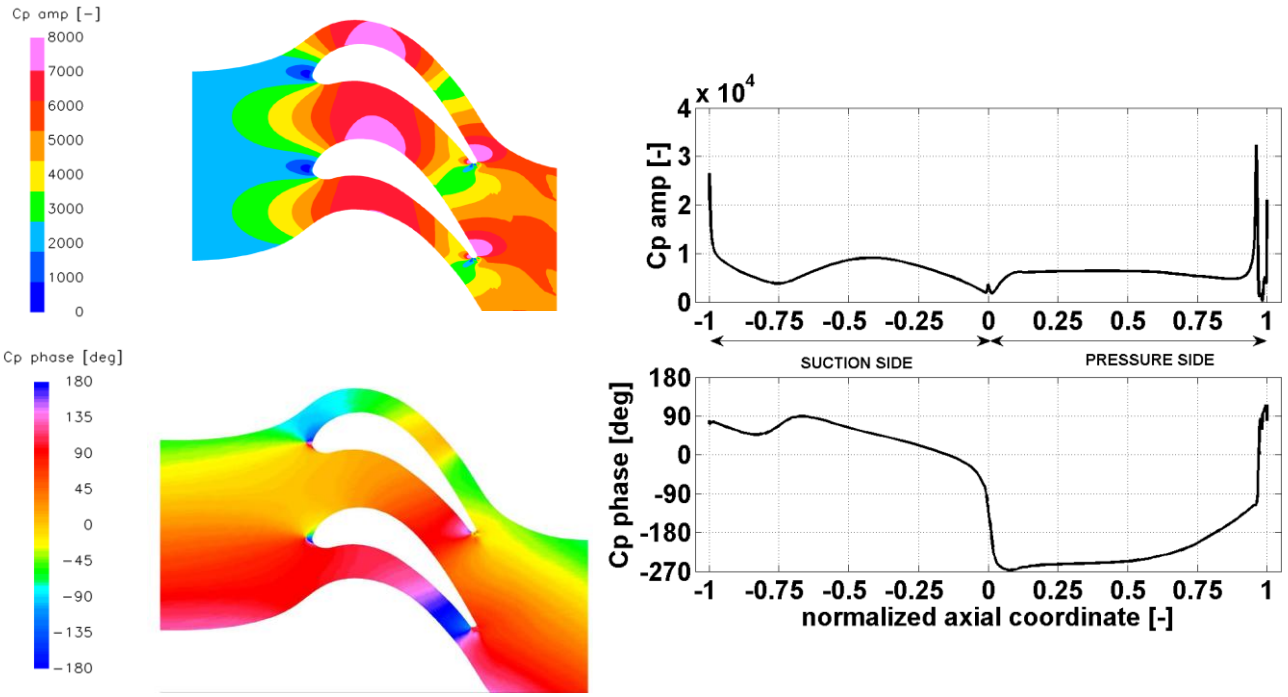

Figure 4-11: Unsteady static pressure, 13ND, magnitude and phase

The level of pressure fluctuations at the leading edge appears as correlated to the level of velocity fluctuations. High velocity fluctuations lead to low pressure fluctuations (in a lower extent, this also appears at the minimal width in the passage). Furthermore the blade motion nature at the leading edge is very close to an axial translation. In that context, Figure 4-12 displays the axial component of the steady velocity normalized by the reference steady velocity and expressed in percentage. This shows negative component in the leading edge region due to the stagnation point position (6% downstream of the minimal axial coordinate), while highest values appear around the minimal width passage. This highlights antagonist behavior: the overall axial velocities (steady and unsteady) at the leading edge and at the minimal width passage are out-of-phase.

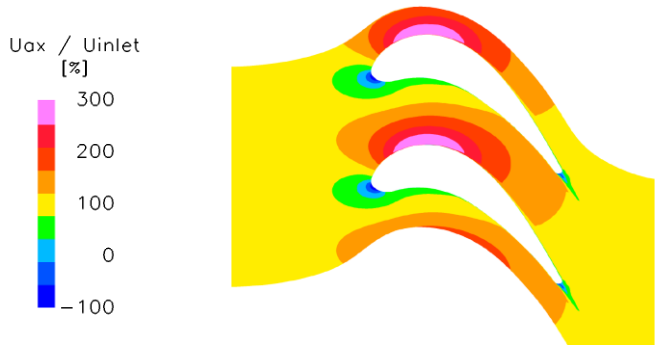

Figure 4-12: Axial component of the steady velocity

The unsteady response in terms of magnitude and phase of the static pressure fluctuations has been presented. The blade-to-blade plane suggests that the waves stagnate inside the blade-to-blade channel. In that context, the next sub-section is dedicated to the nature of propagating waves.

4.4.2.3 Cut-on/cut-off modes

This sub-section is dedicated to evaluate the nature of the waves propagating from the cascade. Such an approach provides fundamental knowledge about the perturbations which can either propagate to the far-field (cut-on mode) or decay (cut-off mode). It is expected that the ability of the flow to damp or to amplify the blade motion is strongly affected by how unsteady perturbations are transferred from the cascade to the far-field. In that context, Figure 4-13 exposes the unsteady pressure coefficient along a streamline taken at mid-channel and illustrates how the propagating waves in the far field are assessed. This are displayed versus the normalized axial coordinate on 4 axial chords up- and downstream of the blades, the extend of that box was judged large enough to be considered as far-field. As a result, the propagation is evaluated from 2 axial chords from the blades. At the inlet, the amplitude decays and thus suggests cut-off mode, whereas the amplitude purely propagates at the outlet indicating cut-on condition.

4.4.2.4 Summary

At this position, the results showed that the blade is aeroelastically stable. The information itself on the stability parameter is not sufficient to answer why. The blade is not entirely stable or unstable along its surface; it features local deviations that must be related to the unsteady pressure fluctuations. Furthermore, high amplitudes does not mean high destabilizing effect. The suction side exhibits the highest fluctuations level and remains stable while the pressure side displays almost quasi-constant and slightly of the same order of amplitude but this results in destabilizing situation. On the other hand and despite any clear correlation, it is expected that the boundary conditions in terms of cut-on/cut-off modes are of high importance in the pressure fluctuations magnitude. Besides, the phases suggest at this point a relation with the throat where the section is changing due to the blade motion. Finally, a deeper understanding of the physics, i.e. a better control of stability, requires simplification of the problem. The approach suggested in the following is thus based on the decomposition of the aforementioned blade motion.

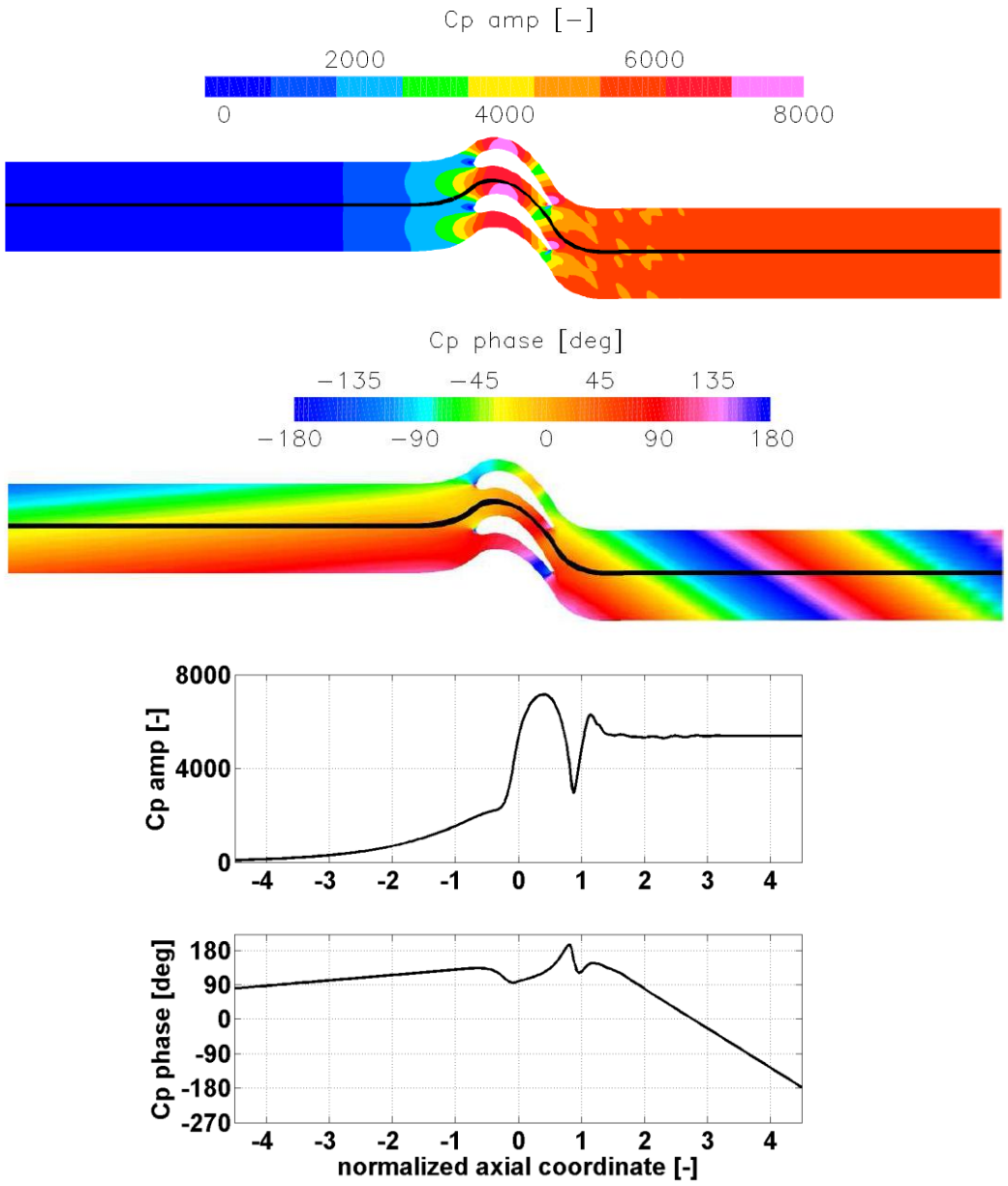

Figure 4-13: Propagation of pressure disturbances in the far-field, 13ND

4.5 Elementary decomposition

This section is dedicated to the aforementioned elementary decomposition. This introduces first the geometric decomposition based on the blade motion and the experimental results presented in part 1. Then the linearized computations approach is described and the results are analyzed and discussed.

4.5.1 Geometric decomposition

The goal is to determine in a more intimate way the destabilizing effects by decomposing the blade vibration into elementary geometric movements, after that the blade relative motion has been projected on a 2D cylindrical surface, unwrapped at midspan. Then, similarly to the physical bending/torsion couple traditionally considered, a geometrical translation/rotation couple is used to decompose the unsteady harmonic perturbation

corresponding to the blade relative motion. This periodic deformation is decomposed into two translations along the respective 2D referential axis and one rotation. A decomposition into translations along the axial chord axis and the axis perpendicular to the axial chord is also possible but the relative blade motion is here mostly tangential to the machine axis. The deformation vector remaining after the translation/rotation decomposition corresponds to the blade distortion. Regarding the disturbance, it is expected that the blade distortion will be of lower order than the three other elementary movements. The centre of rotation is thus calculated by minimizing the distortion. The full blade motion F is therefore decomposed as follows,

$$F = T_X + T_y + R + D \qquad \text{Eq. 4-1}$$

where T_X, T_y, R and D are the translation motion along the x axis, the translation motion along the y axis, the rotation motion and the distortion respectively (Figure 4-14). Furthermore, the translation is such that it cannot be shifted and the decomposition being unique, the translation/rotation couple is thus unique as well. Moreover, the phase shift between the translation and the rotation has been found lower than 10deg.

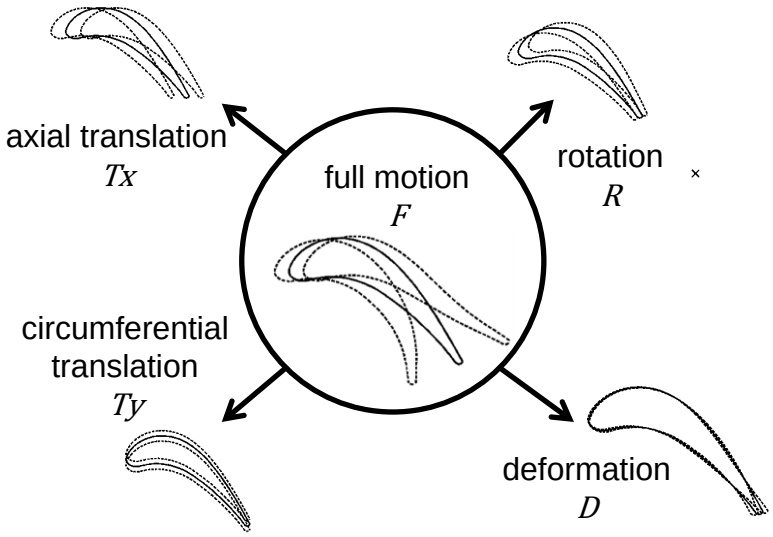

Figure 4-14: Decomposition of the full blade motion (not scaled)

4.5.2 Linearized unsteady computations

The aerodynamic response to a prescribed elementary blade motion is calculated. The steady flow field is the one previously obtained with Turb'Flow™. Then the unsteady linearized fields corresponding respectively to the axial translation, the circumferential translation, the rotation and the distortion are computed using Turb'Lin™. Such an approach takes advantage of the linearity of the unsteady operators: if the harmonic perturbation is decomposed into a sum of distinct components, the sum of the unsteady fields generated respectively by each of these components is equal to the full unsteady field. It is expected that some elementary relative blade movements appear to be more or less stabilizing; thus in order to study the coupling between these elementary movements, the bilinearity property of the damping coefficient with respect to both the pressure

disturbance δP and the velocity perturbation δV is introduced. If δP_1 and δP_2 are two unsteady pressure fields and δV_1 and δV_2 are two velocity perturbations, then,

$$\zeta(\delta P_1 + \delta P_2, \delta V_1 + \delta V_2) = \zeta(\delta P_1, \delta V_1) + \zeta(\delta P_1, \delta V_2) + \zeta(\delta P_2, \delta V_1) + \zeta(\delta P_2, \delta V_2) \quad \text{Eq. 4-2}$$

The damping coefficient can indeed be decomposed into different components that each corresponds to a pressure disturbance, resulting from the different linearized RANS computations, and a velocity perturbation, coming explicitly from the blade geometric movement,

$$\delta\vec{V} = 2\pi i f \delta\vec{X} \quad \text{Eq. 4-3}$$

A subscript notation is now introduced (Eq. 4-4) in which the first subscript refers to the unsteady pressure term, i.e. the mode causing the unsteady aerodynamic force, and the second one refers to the velocity perturbation, i.e. the motion,

$$\zeta(\delta P_1, \delta V_1) = \zeta_{P_1,V_1} \quad \text{Eq. 4-4}$$

Moreover the additivity property of the linearized method ensures Eq. 4-5 and the blade relative motion decomposition implies Eq. 4-6,

$$\delta p_F = \delta p_{T_x} + \delta p_{T_y} + \delta p_R + \delta p_D \quad \text{Eq. 4-5}$$

$$\delta V_F = \delta V_{T_x} + \delta V_{T_y} + \delta V_R + \delta V_D \quad \text{Eq. 4-6}$$

Once the coefficient is decomposed (Eq. 4-7), it is finally presented as an array (Table 4-2). The columns correspond to the different elementary movements applied to the unsteady field which is itself displayed row-wise. The diagonal terms represent therefore the influence of the motion on the unsteady pressure field generated by this motion. The off-diagonal terms are the influence of the others motions on that unsteady pressure field.

$$\begin{aligned}\zeta &= \zeta_{F,F} \\ &= \zeta_{T_x,T_x} + \zeta_{T_x,T_y} + \zeta_{T_x,R} + \zeta_{T_x,D} \\ &+ \zeta_{T_y,T_x} + \zeta_{T_y,T_y} + \zeta_{T_y,R} + \zeta_{T_y,D} \\ &+ \zeta_{R,T_x} + \zeta_{R,T_y} + \zeta_{R,R} + \zeta_{R,D} \\ &+ \zeta_{D,T_x} + \zeta_{D,T_y} + \zeta_{D,R} + \zeta_{D,D}\end{aligned} \quad \text{Eq. 4-7}$$

	$\boldsymbol{\delta V_{T_x}}$	$\boldsymbol{\delta V_{T_y}}$	$\boldsymbol{\delta V_R}$	$\boldsymbol{\delta V_D}$
$\boldsymbol{\delta p_{T_x}}$	ζ_{T_x,T_x}	ζ_{T_x,T_y}	$\zeta_{T_x,R}$	$\zeta_{T_x,D}$
$\boldsymbol{\delta p_{T_y}}$	ζ_{T_y,T_x}	ζ_{T_y,T_y}	$\zeta_{T_y,R}$	$\zeta_{T_y,D}$
$\boldsymbol{\delta p_R}$	ζ_{R,T_x}	ζ_{R,T_y}	$\zeta_{R,R}$	$\zeta_{R,D}$
$\boldsymbol{\delta p_D}$	ζ_{D,T_x}	ζ_{D,T_y}	$\zeta_{D,R}$	$\zeta_{D,D}$

Table 4-2: Aerodynamic damping coefficients array

The framework and the basics of the approach have been introduced. The next sub-section is dedicated to the presentation of the results.

4.5.3 Results

The unsteady responses resulting from the elementary decomposition at 13ND is presented below in 3 sub-sections (the results related to the deformation is discussed separately):

- a first sub-section compares each elementary unsteady field generated by the elementary blade motions, i.e. the axial translation, the circumferential translation and the rotation. They are displayed in terms of magnitude and phase of the unsteady static pressure fluctuations in blade-to-blade planes and then along the blade surface.
- for each of the aforementioned elementary pressure field, an elementary blade motion is analytically combined in order to compute the elementary stability parameter. This is exposed in a second sub-section.
- finally the last sub-section presents the deformation case since, as expected, the level is of lower magnitude.

4.5.3.1 Elementary unsteady pressure fields

The elementary unsteady pressure field generated by the axial and circumferential translations as well as the rotation are displayed in Figure 4-15. The magnitude of the unsteady pressure coefficients and its phase are respectively included on the top and the bottom of the figure. This indicates the following:

- the axial translation and the rotation induce the highest pressure fluctuations level that are located inside the channel for each of them especially on the suction side (between 20% and 70% axial chord approximately).
- the low fluctuation amplitudes on the leading edge region is again observed for both cases but the magnitude differs.
- upstream of the cascade, the flows do not exhibit strong differences according to the blade motion. In contrast, the downstream flow appear much more affected and consequent strong changes in amplitude occur at the throat, the strongest appearing for the circumferential translation.
- as already observed for the full blade motion, the phases display also strong variations in the leading and trailing edge regions and in a lower extent for the circumferential, which displays besides the lowest pressure fluctuation at that position.

The elementary unsteady pressure fields on the blade surface are displayed along the normalized axial coordinate in Figure 4-16. The unsteady pressure field generated by the full blade motion and presented above is also superposed for comparison. The figure shows the following:

- on the suction side up to 75% axial chord, the rotation and the axial translation induce the highest pressure fluctuations, higher than the full motion, with a maximum at 40% and 47% axial chord respectively, whereas the circumferential translation results in level of the same order than the full motion. Furthermore, all the curves exhibit a minimum at the same location, i.e. 75% axial chord.
- on the pressure side, the rotation still involves the highest fluctuations level especially from 50% axial chord as well as the circumferential translation, whereas

the axial translation shows the lowest level from the leading edge to 75% axial chord.

- the phases resulting from the axial translation and the full motion are close to each other and behaves rather similarly. In a lower extent, this is also observed on the suction side for the circumferential translation from 25% axial chord. In contrast, the rotation differs completely and tends to feature out-of-phase.

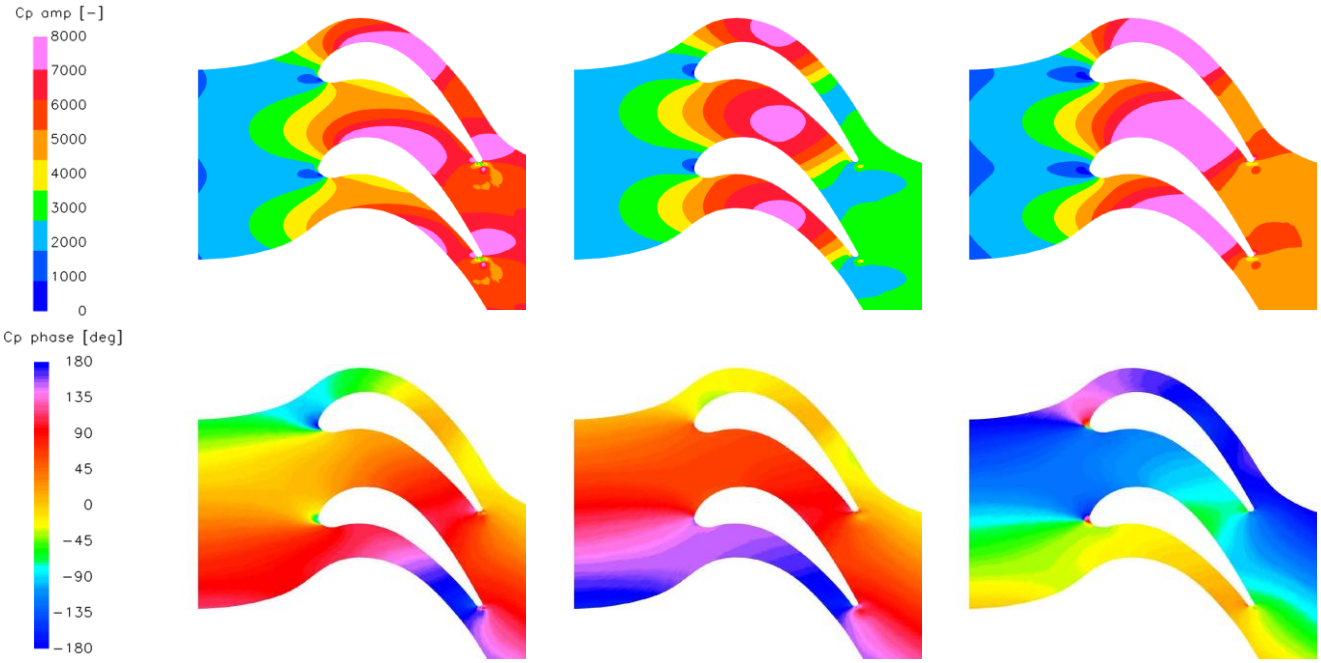

axial translation circumferential translation rotation

Figure 4-15: Elementary unsteady pressure fluctuations, 13ND

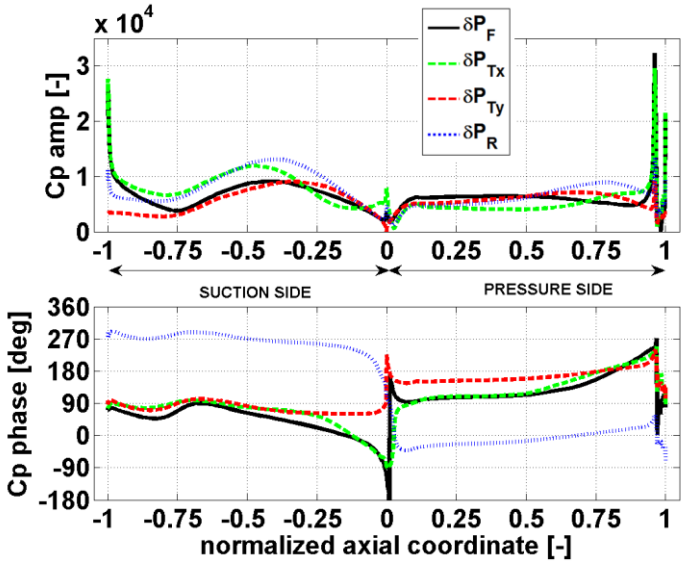

Figure 4-16: Elementary unsteady pressure fluctuations on the blade surface, 13ND

4.5.3.2 Elementary stability parameter

The different elementary unsteady pressure fields have been computed and presented. For each of them each elementary blade motions is analytically combined through the velocity fluctuations and thus the elementary stability parameters can be calculated. The results are summarized in Figure 4-17. The elementary stability parameters are shaded in the array according to the configuration in order to make the reading clearer. For instance, the case of an unsteady pressure field generated by the axial translation is successively combined to:

- δV_x: the velocity fluctuation results from the axial translation and this provide the elementary stability parameter ζ_{T_x,T_x}
- δV_y: the velocity fluctuation results from the circumferential translation and this provides the elementary stability parameter ζ_{T_x,T_y}
- δV_R: the velocity fluctuation results from the rotation and this provides the elementary stability parameter $\zeta_{T_x,R}$
- δV_D: the velocity fluctuation results from the distortion and this provides the elementary stability parameter $\zeta_{T_x,D}$. Although the unsteady pressure field due to the deformation has not been presented in the previous sub-section, it is considered here in order to highlight its relative low level, nevertheless more details on that case are given in the next sub-section.

Figure 4-17 indicates the following:

- the deformation motion applied on each elementary pressure field results in levels lying well below the other terms.
- the region corresponding to the trailing edge thickness does not contribute to the stability: each curve drops to zero. It appears locally as a dead zone.
- the different elementary motions applied to the pressure fields generated by the axial and the circumferential translations result respectively in similar features in terms of evolution but the magnitudes change, that is to say the stable and unstable regions remain respectively stable and unstable when comparing the two aforementioned pressure fields. However, a difference is noticed regarding the axial translation motion which exhibits stable then unstable behaviors in the leading edge region when the blade is axially oscillating whereas it is unstable when the blade is circumferentially oscillating.
- on the aft pressure side, each term crosses the stability limit, i.e. the zero stability, at the same axial position. This is observed for the unsteady pressure fields generated by the translations: the zero stability occurs at 76% axial chord. This is slightly upstream for the pressure field issued from the rotation, i.e. at 69% axial chord. These two axial positions correspond to a change in phase which crosses 180deg and 0deg respectively (Figure 4-16).
- when applying the axial translation motion on each elementary pressure field, the stability crosses the stability limit at the same location, i.e. between 22% and 26% axial chord, on the fore pressure side whereas the circumferential translation remains monotonic.
- the fluid particles flowing on the suction side and experiencing stronger gradients imply much higher stability levels than the pressure side.
- from a global point of view, the plot of the unsteady pressure field generated by the rotation appears as the reverse of the two other plots, i.e. a change from stable to unstable as observed in Figure 4-16 with the phases.
- this suggests that the overall stability parameter is finally the result of how the two translations and the rotation compensate with each other.

	δV_{T_x}	δV_{T_y}	δV_R	δV_D
$\boldsymbol{\delta p_{T_x}}$	$\boldsymbol{\zeta_{T_x,T_x}}$	$\boldsymbol{\zeta_{T_x,T_y}}$	$\boldsymbol{\zeta_{T_x,R}}$	$\boldsymbol{\zeta_{T_x,D}}$
δp_{T_y}	ζ_{T_y,T_x}	ζ_{T_y,T_y}	$\zeta_{T_y,R}$	$\zeta_{T_y,D}$
δp_R	ζ_{R,T_x}	ζ_{R,T_y}	$\zeta_{R,R}$	$\zeta_{R,D}$

the unsteady pressure field is generated by the **axial translation**

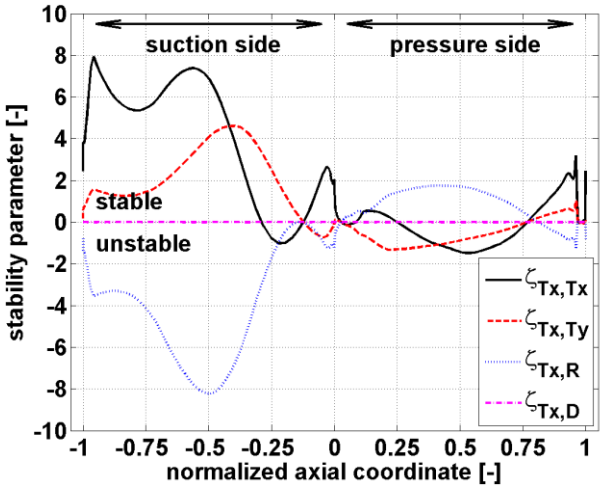

	δV_{T_x}	δV_{T_y}	δV_R	δV_D
δp_{T_x}	ζ_{T_x,T_x}	ζ_{T_x,T_y}	$\zeta_{T_x,R}$	$\zeta_{T_x,D}$
$\boldsymbol{\delta p_{T_y}}$	$\boldsymbol{\zeta_{T_y,T_x}}$	$\boldsymbol{\zeta_{T_y,T_y}}$	$\boldsymbol{\zeta_{T_y,R}}$	$\boldsymbol{\zeta_{T_y,D}}$
δp_R	ζ_{R,T_x}	ζ_{R,T_y}	$\zeta_{R,R}$	$\zeta_{R,D}$

the unsteady pressure field is generated by the **circumferential translation**

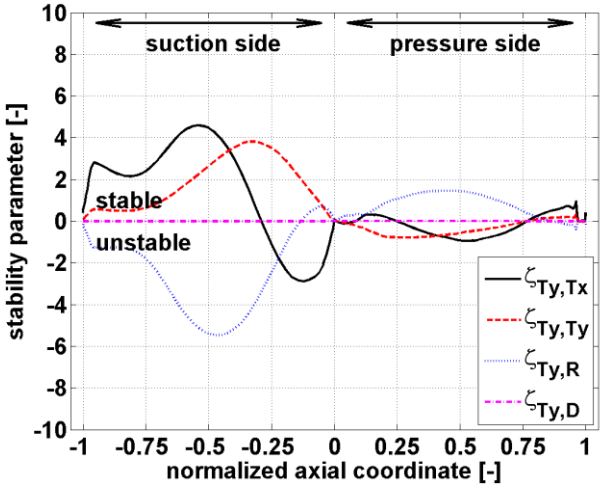

	δV_{T_x}	δV_{T_y}	δV_R	δV_D
δp_{T_x}	ζ_{T_x,T_x}	ζ_{T_x,T_y}	$\zeta_{T_x,R}$	$\zeta_{T_x,D}$
δp_{T_y}	ζ_{T_y,T_x}	ζ_{T_y,T_y}	$\zeta_{T_y,R}$	$\zeta_{T_y,D}$
$\boldsymbol{\delta p_R}$	$\boldsymbol{\zeta_{R,T_x}}$	$\boldsymbol{\zeta_{R,T_y}}$	$\boldsymbol{\zeta_{R,R}}$	$\boldsymbol{\zeta_{R,D}}$

the unsteady pressure field is generated by the **rotation**

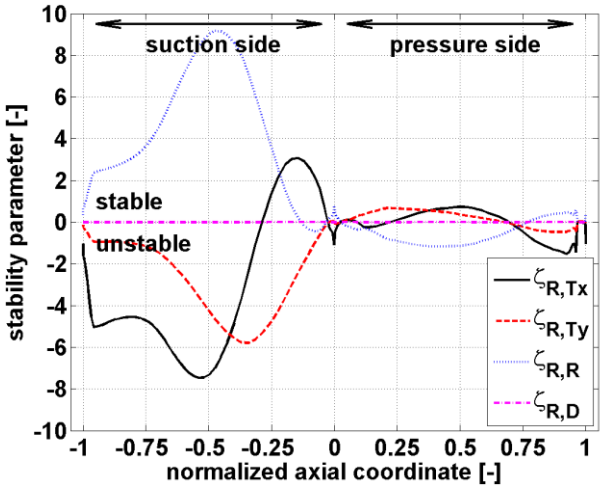

Figure 4-17: Elementary stability parameters, 13ND

4.5.3.3 Evaluation of the deformation

This sub-section exposes the elementary unsteady pressure field generated by the deformation D. Each elementary motion is then applied to the aforementioned field to calculate the following stability parameters: ζ_{D,T_x}, ζ_{D,T_y},

$\zeta_{D,R}$, $\zeta_{D,D}$. Although the deformation is of negligible order in the stability, local effects remain. Furthermore, it is expected that the major effect occurs in the trailing edge region because of the higher magnitude of deformation. Figure 4-18 displays the unsteady pressure fluctuations in the blade-to-blade plane and along the blade surface. The scales used are different from the previous one given the relative low level of magnitude:

- as observed in Figure 4-15, the major part of the energy appears inside the channel.
- the low pressure fluctuations in the front of the blade is located slightly downstream compared to the other motions.
- two spots of strong pressure fluctuations arise on both sides close to the trailing edge.
- the suction side features strong variations of the phase starting at the leading edge from about 0deg, it rotates up to 360deg when approaching the trailing edge.

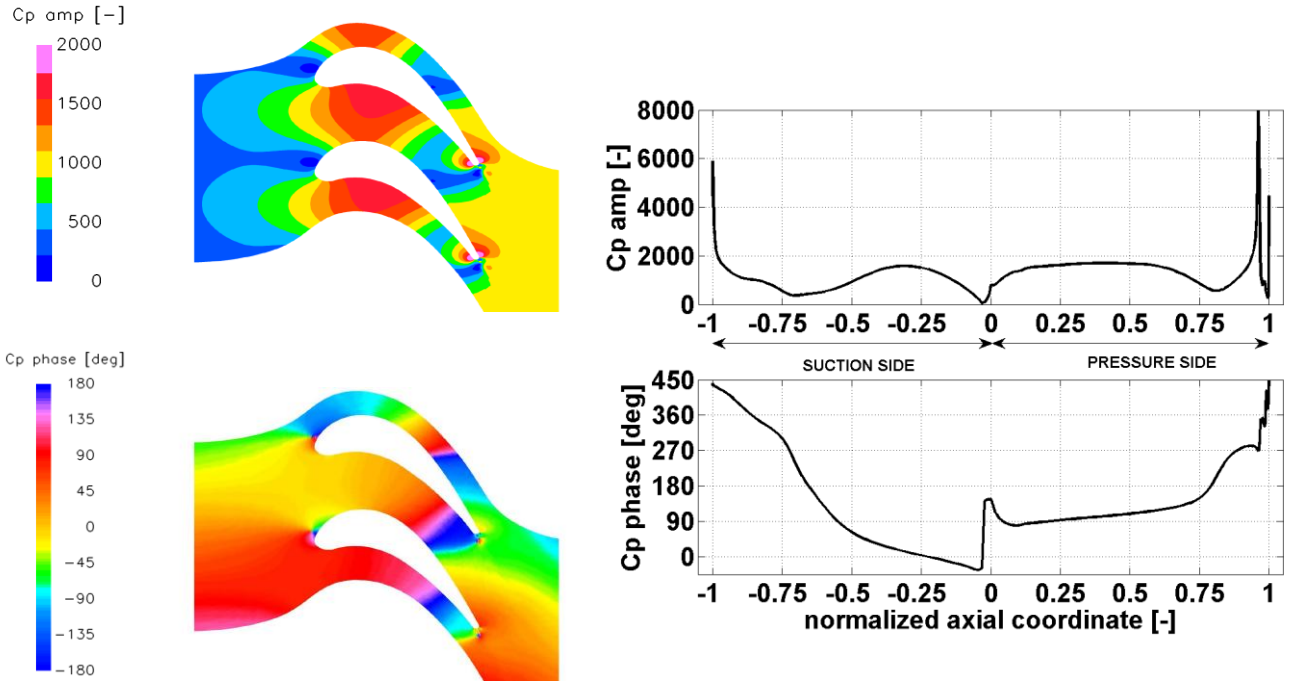

Figure 4-18: Unsteady pressure fluctuations due to the deformation, 13ND

The elementary stability parameters are displayed in Figure 4-19 and indicates the following:

- again rotation and translations behave in a opposite manner.
- the pressure side exhibits higher level whereas for the other motions this occurs on the suction side.

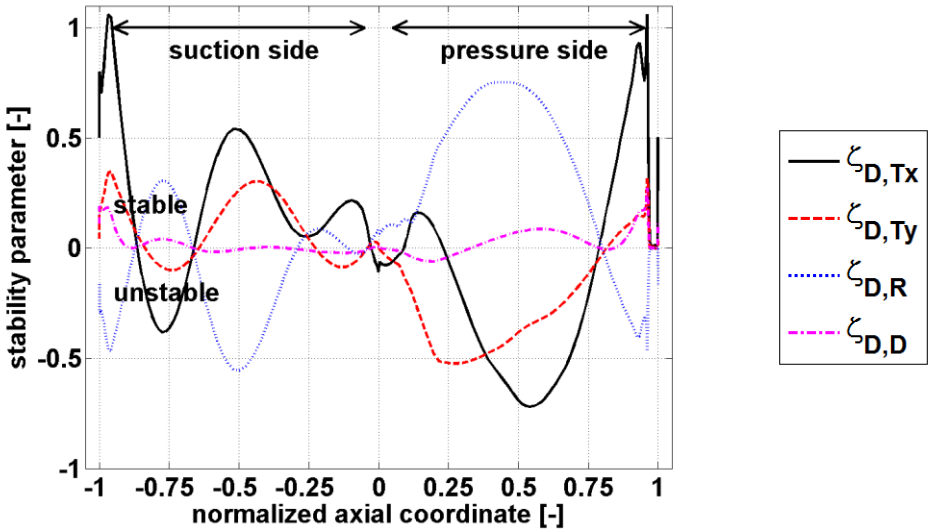

Figure 4-19: Elementary stability parameters, δp generated by the deformation, 13ND

4.5.4 Conclusion

4.5.4.1 Synthesis

Figure 4-20 presents the absolute values of the damping coefficient for the full motion on one hand and for the elementary motions on the other hand. The values correspond to the response to each elementary motion on an unsteady pressure field generated by the axial translation, the circumferential translation, the rotation and the distortion respectively, i.e. this gives the sum of each row of Table 4-2. This shows clearly the low contribution of the distortion, the main contributions coming from the axial translation and the rotation. This also highlights that the overall damping results from nontrivial balances of different contributions which add or cancel with each other.

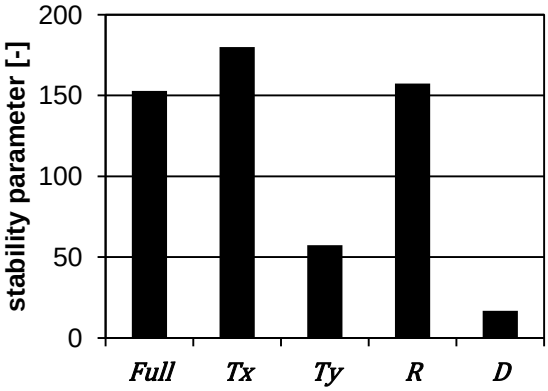

Figure 4-20: Elementary stability parameters, absolute values, 13ND

The aerodynamic damping coefficients involving the distortion D are negligible compared to the ones involving the three other elementary movements, this has been checked for each nodal diameter. As a result, the focus is put on the translation/rotation couple in the aerodynamic damping coefficients array.

The decomposition of the aerodynamic damping coefficient is presented in the form of a 3D histogram (Figure 4-21). The plot displays useful information but requires some explanation. The in-depth axis represents the pressure perturbation δP and the abscissa the elementary movement δV applied to δP. If the cone is upward (resp. downward), the damping coefficient is positive (negative) and the couple is stable (unstable). The sum of each contribution corresponds to the overall aerodynamic damping coefficient which has been found positive.

Figure 4-21 shows that the diagonal terms are all stabilizing; however they are not predominant. This was not expected due to the blade stiffness. All the coupled terms involving the rotation are destabilizing, the terms $\zeta_{T_x,R}$ and ζ_{R,T_x} are by the way the most destabilizing whereas the aerodynamic damping coefficients from coupled modes with translation are all positive. That feature is in line with the classical bending-torsion flutter theory, namely the torsion is a potential source of instability.

Figure 4-21 identifies the different contributions in the aeroelastic stability computation. This gives an answer to the influence of an elementary motion on an elementary unsteady pressure field. For instance, the influence of the torsion on an unsteady pressure field generated by the flexion in the axial direction is given by the term noted $\zeta_{T_x,R}$. According to Figure 4-21 this coupled mode is unstable and the torsion is destabilizing. As a result, the way to increase the stability of the blade is to minimize the effect of the torsion on the flexion by modifying for example the amplitude involved in the destabilizing elementary motion.

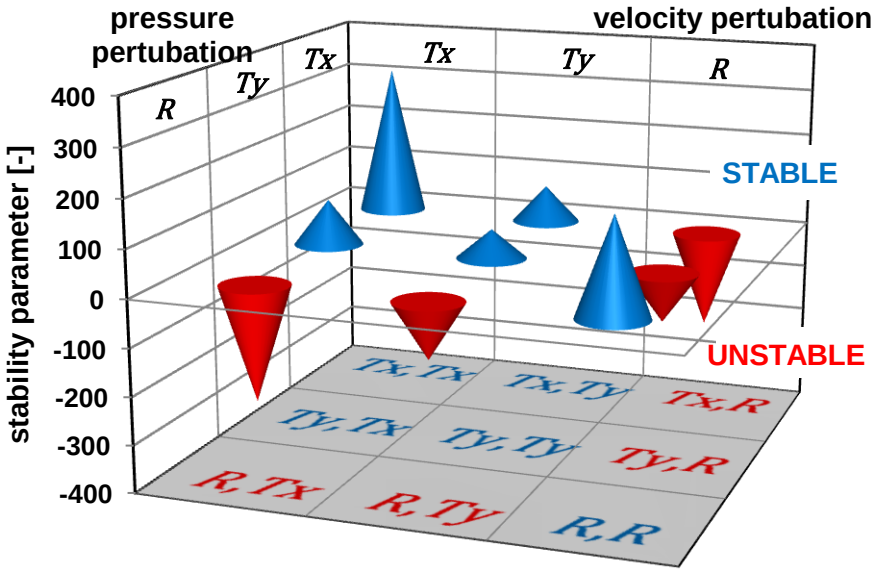

Figure 4-21: Elementary aerodynamic damping coefficients, 13ND

4.5.4.2 Discussion

The amplitude A used in the damping coefficient corresponds commonly to the vibration amplitude of the prescribed motion. Two amplitudes are actually involved here: the first one, $a_{\delta p}$, comes from the motion which generates the unsteady pressure field and the second one, $a_{\delta V}$, from the motion applied to that pressure field. Consequently in order to be able to compare each elementary damping coefficient with each other in terms of

contribution in the full coefficient, the same amplitude for each calculation has been considered, i.e. the vibration amplitude of the full blade motion as stated previously. This is the reason why each elementary damping coefficient can be added. The aeroelastician fellowship usually calculates the aerodynamic damping coefficient for each prescribed elementary motion by considering the amplitude of vibration of each motion. The difference of these two approaches is the following: starting here from the full blade motion, the aerodynamic work is then calculated to get the full aerodynamic damping coefficient and finally it is split into elementary contributions; whereas within the traditional way (Bölcs and Fransson, 1986), the elementary aerodynamic works are normalized with their respective amplitude motion. In order to link the two methods, Table 4-3 gives the relative extent of each couple in terms of amplitude of vibration by calculating the ratio given by Eq. 4-8 assuming that the dimensionless amplitude of the full blade motion A is 1. The columns give the amplitude of motion $a_{\delta p}$ that generates the unsteady pressure field whereas the rows give the amplitude of motion $a_{\delta V}$ applied to that pressure field (the shaded cells highlight the symmetry of the matrix).

$$\frac{a_{\delta p} a_{\delta V}}{A^2} \qquad \text{Eq. 4-8}$$

$$\zeta_{tradtional} = \frac{-W_{cycle,elem}}{p_{dyn} \cdot a_{\delta p} a_{\delta V}} \qquad \text{Eq. 4-9}$$

	$\boldsymbol{\delta V_{T_x}}$	$\boldsymbol{\delta V_{T_y}}$	$\boldsymbol{\delta V_R}$
$\boldsymbol{\delta p_{T_x}}$	1.15	0.61	0.78
$\boldsymbol{\delta p_{T_y}}$	0.61	0.32	0.41
$\boldsymbol{\delta p_R}$	0.78	0.41	0.53

Table 4-3: Relative amplitudes of the elementary motions

Table 4-3 and Eq. 4-9 provide the way to connect the two methods. They identify the couple which implies the largest amplitude of vibration. Both approaches show that the axial flexion is large enough to damp the destabilizing effect of the torsion and thus to have a global stable motion.

The notion of elementary damping coefficient has been presented and discussed for one specific nodal diameter, i.e. one specific IBPA. The following suggests to lead a similar approach for the entire range of nodal diameters.

4.6 Effect of interblade phase angle

This section is dedicated to the effect of the IBPA on the stability parameter. First, the IBPA is also decomposed in order to separate the effect of the change in incidence, typically when the IBPA is equal to 0deg, and the change in section, i.e. when the IBPA is different from 0deg. Then each elementary damping coefficient are assessed over the IBPA range as well as cut-on/cut-off conditions.

4.6.1 Decomposition of the IBPA effects

The aerodynamic damping coefficient computation for the IPBA corresponding to 13ND on the one hand and equal to 0ND on the other hand allow evaluating separately the effect of the change in incidence and the effect of change in section of the flow passage (Kerrebrock, 1977; see Appendix B). The aerodynamic damping coefficient can thus be considered as the sum of a first coefficient only related to the change in incidence (IBPA=0deg) and a second coefficient only related to the change in section as follows,

$$\zeta = \zeta_{incidence} + \zeta_{section} \qquad \text{Eq. 4-10}$$

4.6.1.1 Global damping coefficient

The aerodynamic damping coefficients along the blade surface according to Eq. 4-10 is included in Figure 4-22 and suggest the following:

- the two nodal diameters 13ND and 0ND exhibit both stable features in the trailing edge region, i.e. from 80%, on each side. From the leading edge to the aforementioned position, the trends are reversed, i.e. the pressure side is unstable at 13ND whereas it is stable at 0ND and the suction side is stable at 13ND whereas it is unstable at 0ND.
- the destabilizing region on the pressure side at 13ND results from the change in section although the change in incidence is stabilizing. Nevertheless the high degree of stabilizing effect is high enough to overcome the destabilizing part due to the change in section at the trailing edge.
- the stabilizing suction side results from the change in section whereas the change in incidence contributes to destabilization on almost 80% axial chord.

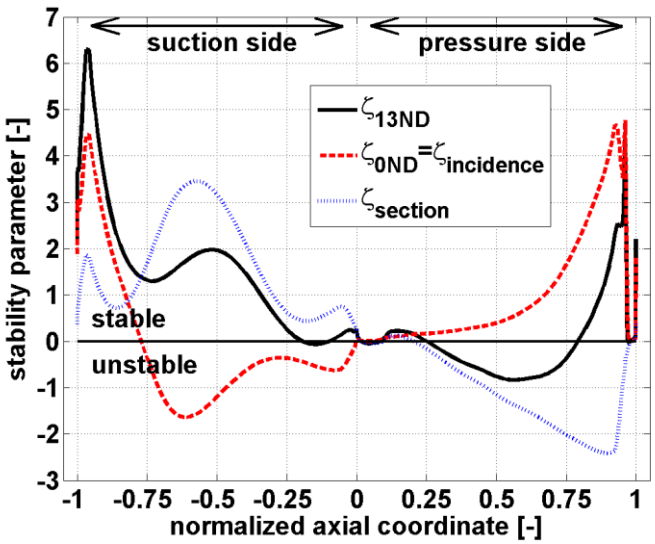

Figure 4-22: Decomposition of the IBPA effects, 13ND

4.6.1.2 Elementary damping coefficients

In the same way, Figure 4-23 displays the elementary aerodynamic damping coefficients for each case:

- (a) presents the decomposition of the 13ND as already introduced in Figure 4-21
- (b) presents the decomposition of the 0ND computation
- (c) presents the elementary coefficients resulting from (a) and (b) (Eq. 4-10).

The global feature remains the same for all cases, i.e. the diagonal terms as well as the combined modes only involving the translations are all positive whereas the torsion leads to negative coefficients. The change in incidence implies higher level and acts stabilizing compared to change in section which leads to negative total damping due to the much lower level of the stabilizing term ζ_{T_x,T_x}; indeed the ratio $\zeta_{T_x,T_x}/\zeta_{T_x,R}$ is lower than 1 for the latter.

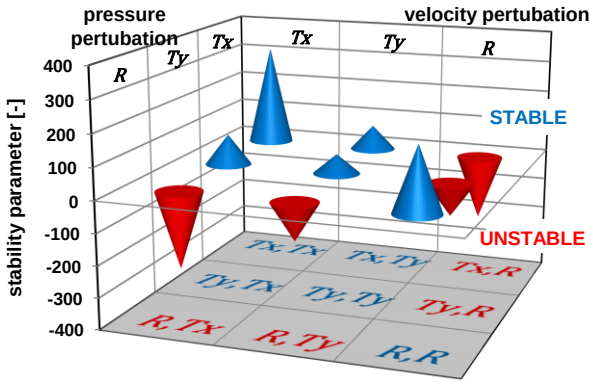

ζ_{total} = 98.1	δV_{T_x}	δV_{T_y}	δV_R
δp_{T_x}	321.2	79.2	-202.9
δp_{T_y}	97.2	62.4	-102.5
δp_R	-242.7	-118.1	204.3

(a) 13ND – effect of change in incidence and section

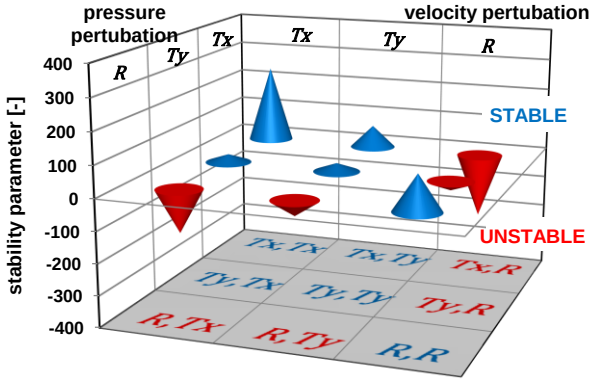

ζ_{total} = 107.5	δV_{T_x}	δV_{T_y}	δV_R
δp_{T_x}	245.3	71,7	-164,6
δp_{T_y}	26,1	27.3	-27,8
δp_R	-136.3	-47,4	113.2

(b) 0ND – effect of change in incidence

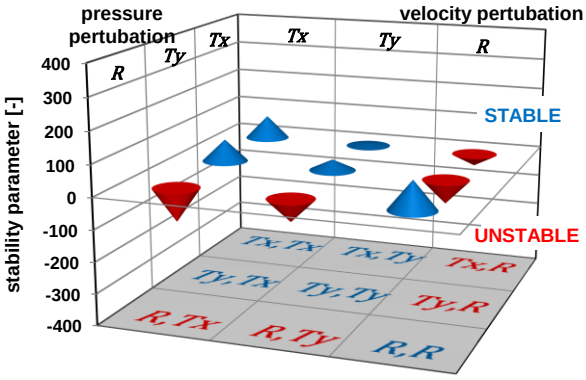

ζ_{total} = -9.4	δV_{T_x}	δV_{T_y}	δV_R
δp_{T_x}	75.9	7.5	-38.3
δp_{T_y}	71.1	35.1	-74.7
δp_R	-106.4	-70.7	91.1

(c) Effect of change in section

Figure 4-23: Decomposition of the IBPA effects, 13ND

4.6.2 Evolution over the IBPA range

The diagonal terms of the damping coefficients matrix (Table 4-2), i.e. the four self-applied elementary movements, versus the nodal diameter are included in Figure 4-24:

- the evolution differs completely from sinusoidal curve.
- each isolated elementary motion is stabilizing expect at -20ND for which the rotation R and the circumferential translation T_y are both self-exciting.
- the damping coefficients associated to the distortion are again not significant compared to the other movements.
- the curves exhibit strong and rough variations which occurs at the same nodal diameter regardless the motion.

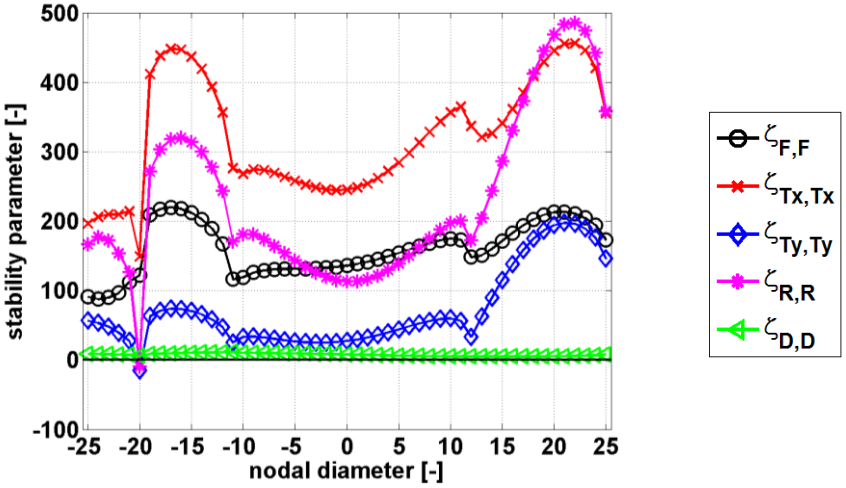

Figure 4-24: Diagonal damping coefficients versus nodal diameter

The off-diagonal terms of the damping coefficients matrix (Table 4-2), excluding the deformation, versus the nodal diameter are included in Figure 4-25:

- all the coefficients exhibit again a dependence with respect to the IBPA.
- the most stabilizing coefficients are the terms coupling both the translations, i.e. ζ_{T_x,T_y} and ζ_{T_y,T_x}. Nevertheless, the former is destabilizing from the nodal diameter -25 to -18, whereas the latter is stabilizing over the entire range.
- the combined modes involving the rotation are all destabilizing within the entire range, except $\zeta_{T_x,R}$ and ζ_{R,T_y}, which are stabilizing from -25 to -20 and at -20 respectively.

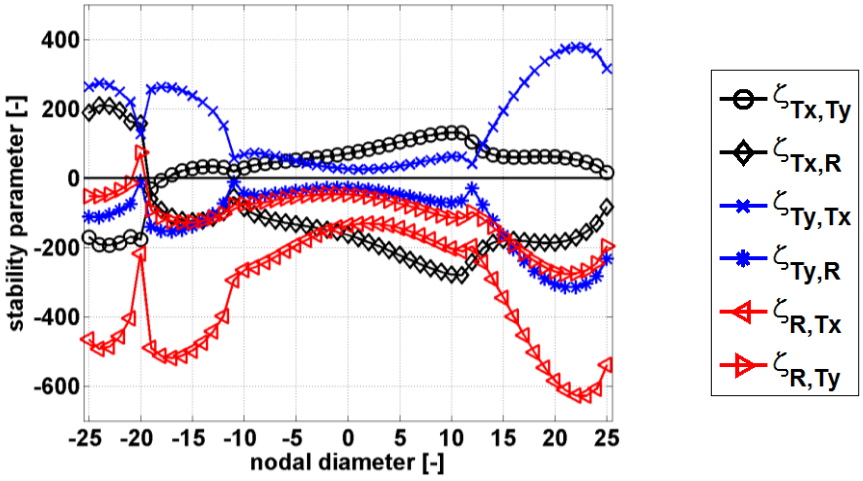

Figure 4-25: Off-diagonal damping coefficients versus nodal diameter

4.6.3 Cut-on/cut-off modes

In order to investigate this behavior, the nature of the waves is studied in the same way as in 4.4.2.3. The goal is to describe the pressure disturbance in the far-field as a function of the IBPA. Figure 4-26 exposes the unsteady pressure coefficient along a streamline taken at mid channel for 5 IBPA chosen between the discontinuities. This are displayed versus the normalized axial coordinate on 4 axial chords up- and downstream of the blades:

- -23ND: both at the in- and outlet, the amplitude decays and suggests cut-off mode.
- -13ND: at the inlet, the amplitude purely propagates whereas at the outlet it decreases indicating cut-on and cut-off modes respectively.
- 0ND: both at the in- and outlet, the pressure disturbances simply propagate leading to cut-on modes.
- 13ND: the perturbations at the inlet decline whereas they purely propagate at the outlet. This implies cut-off and cut-on modes respectively.

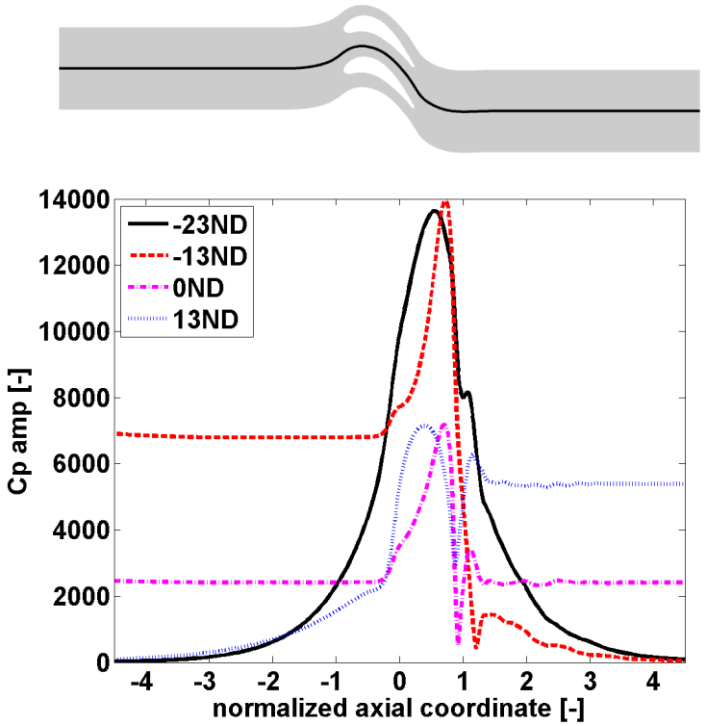

Figure 4-26: Pressure disturbances in the far-field, mid channel, full motion

The above observations highlight the correlation between the propagation of waves and the IBPA. The nature of acoustic modes leaving the cascade are summarized in Table 4-4:

- at the outlet, modes are cut-off in the range [-25ND; -11ND] whereas waves are released downstream by the blades within the range [-10ND; +25ND].
- at the inlet, waves propagate upstream in the range [-20ND; +11ND] and they decay in the ranges [-25ND; -21ND] and [+12ND; +25ND].
- the least stable configurations correspond to the case for which the waves decay, i.e. cut-off at the in- and outlet.
- the in- and outlet feature the same conditions in the range [-10ND; +11ND] for which the waves are propagating, i.e. cut-on modes, and the corresponding stability parameter presents slight variations compared to the others.

nodal diameter [-]	inlet	outlet
$-25 \leq n \leq -21$	cut-off	cut-off
$-20 \leq n \leq -11$	cut-on	cut-off
$-10 \leq n \leq +11$	cut-on	cut-on
$+12 \leq n \leq +25$	cut-off	cut-on

Table 4-4: Cut-on/cut-off conditions

The cut-on/cut-off conditions only depend on the steady field, the reduced frequency and the IBPA; as a result, the elementary unsteady pressure fields lead to the same conclusions than in Table 4-4. Nevertheless, their respective level is expected to be different. In that context, Figure 4-27 gives the propagation of the pressure disturbances in the far-field for each elementary unsteady pressure field and shows that the axial translation always exhibits higher amplitude than the full motion regardless the IBPA. This is also observed for the rotation for backward modes whereas the forward modes feature levels of the same order than the full motion. The magnitudes induced by the circumferential translation are below the ones from the full motion. These observations show that the major contributions originate from the axial translation and the rotation.

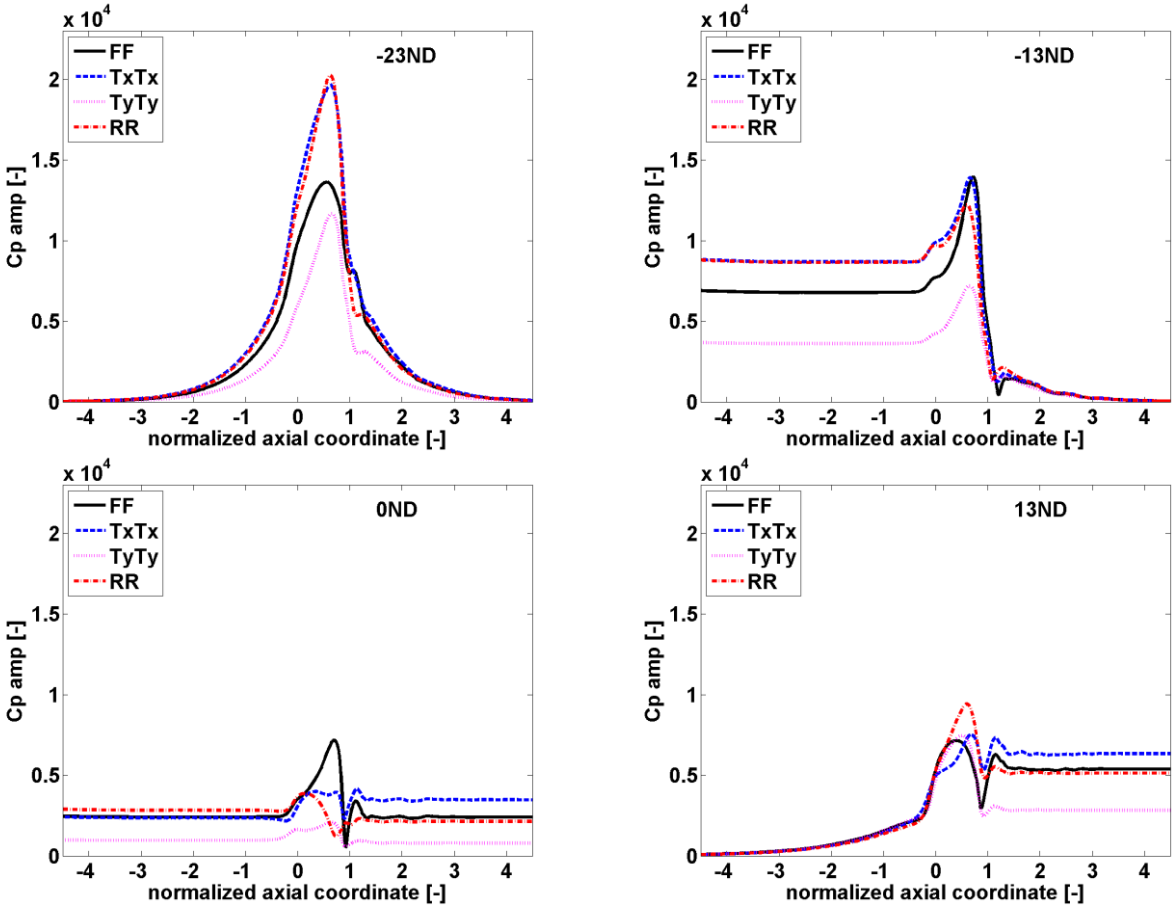

Figure 4-27: Pressure disturbances in the far-field, mid channel, elementary motions

Finally, as a summary, Figure 4-28 displays the damping parameter from the full blade motion versus the nodal diameter as well as the change in cut-on/cut-off modes highlighted with the vertical black lines. The least stable configuration corresponds to cut-off mode both at the inlet and outlet. Although there is no direct relation between the cut-on/cut-off condition and stability, the figure evidences a clear correlation between them. In this specific case, the configuration is prone to be unstable without outgoing waves from the cascade.

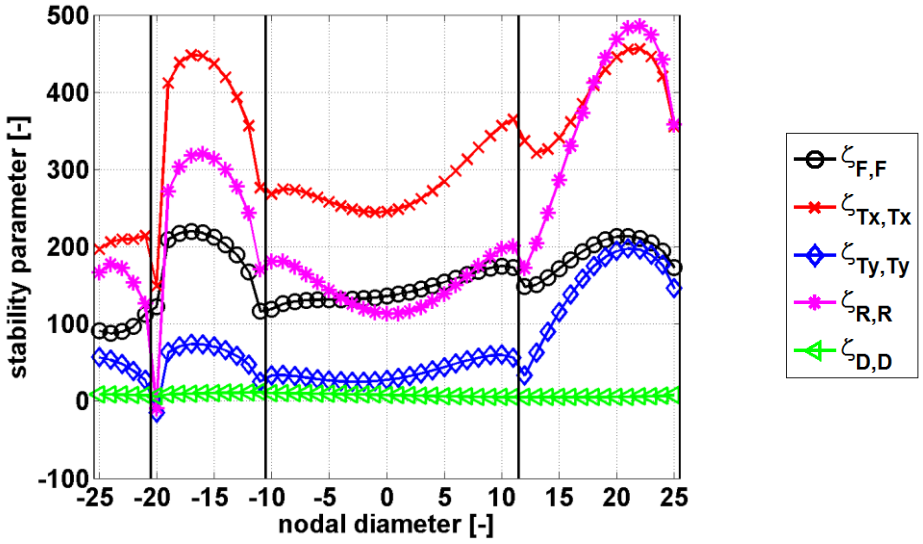

Figure 4-28: Correlation between damping coefficient and cut-on/cut-off modes

4.7 Conclusion

An isolated blade from an industrial space turbine has been numerically studied based on 2D unsteady computations linearized in the frequency domain. The blade was part of a blisk and featured combined modes and high reduced frequency.

The steady results have shown that the aerodynamic field did not present strong non-linearities that could induce flutter. And indeed, the linearized unsteady computations have established that the blade was aeroelastically stable over the studied range of IBPA. However the stability parameter presented discontinuities and strong variations over the IBPA and despite the stable character of the blade, a better understanding on why such discontinuities appear will obviously lead to increase the flutter margin.

As a result, the focus has been put on a specific IBPA (13ND). First it has been shown that the pressure side was rather destabilizing (from 25% to 75% axial chord), however the suction side has been found stabilizing enough to overcome it. This highlights the need to privilege studies of local values instead of global, since stability results from a balance between stable and unstable features. Then the unsteady pressure fluctuations have been investigated, they displayed the highest amplitudes at the minimal passage width and strongest phase variations occurred in the region of leading edge.

Based on the linear superposition principle from the experimental results presented in part 1, the blade motion originating from the blisk eigenmode, has been decomposed into elementary geometric movements such as in the experimental campaign, i.e. into axial

and circumferential translations, and rotation; the center of rotation is calculated by minimizing the deformation which has been found much less significant than the three other elementary motions. Then the aerodynamic response to a prescribed elementary motion has been computed using LRANS solver. This approach leads to elementary stability parameters, each coefficient corresponding to a pressure disturbance, resulting from the different LRANS computations, and a velocity perturbation, coming explicitly from the blade geometric motion. The results have shown that the combined coefficients involving the rotation were all destabilizing whereas the others were all stabilizing. This conclusion is in line with the classical flutter, i.e. the torsion is a potential source of instability. The most unstable coefficient results from the combination of the axial flexion and torsion. Accordingly, the elementary decomposition puts some light on the global stability and drives the designers towards the stability improvement.

Based on the approach proposed by Kerrebrock (1977), the interblade phase has been also decomposed in order to evaluate the effect of change in incidence (0deg IBPA) and the effect of change in section (all other IBPA). It has been highlighted that stability is indeed a balance between stable and unstable features, the change in section being in that context destabilizing.

Finally, cut-on/cut-off modes have been analyzed over the IBPA range and have shown that the least stable configuration corresponded to cut-off conditions both at the in- and outlet. Moreover, although no direct relation has been established, a clear correlation has been evidenced between the cut-on/cut-off modes and the strong discontinuities observed on the stability parameter over the IBPA range.

The next chapter is dedicated to recent real industrial space turbine that features much simpler deformation of the blades but rather more complex aerodynamic flow field. The focus is thus put on a supersonic assembled bladed disk. The blades are connected to the disk through fir tree attachments and therefore much more mechanical damping is present. The motion of the blade is of elementary nature, i.e. purely axial, however complexity of the problem comes from the supersonic flow field itself, which involves shock wave/boundary layer interaction, compression and expansion regions. The study is based on 3D simulations and presented in the next chapter.

5 3D NUMERICAL APPROACH OF SUPERSONIC FLUTTER

The industrial turbine presented in the previous chapter is an example of the recent advanced technologies in terms of structure: the flow does not involve strong non-linearities but the blade motion features combined modes resulting in destabilizing effects. Flows in turbomachines are often much more complex and the velocities are higher (supersonic flow, boundary layer separation, shock wave, etc). Numerous papers are thus dedicated to supersonic flutter (Mårtensson, 2006; Groth et al., 2008; Meingast et al., 2009). In that context, an industrial supersonic turbine is numerically studied and the results are presented in this chapter. The flow implies strong non-linearities whereas the blade motion remains of elementary nature, that is to say a pure mode rather than a composition of different movements. This supersonic turbine has been previously numerically computed outside of this research project with a different linearized CFD code called Turbo3D (Gerolymos and Vallet, 1996; Gerolymos et al., 1998): the goal was to identify the most unstable nodal diameter found during experimental campaigns; thus numerical results have been validated according to test data. Here, the objectives are to validate the numerical tools used in this project for flutter prediction in case of supersonic flows, and mainly to highlight the mechanisms responsible for flutter.

The chapter is therefore organized as follows. First, the characteristics of the turbine are given and the numerical computations are described. A validation of the numerical tools are then suggested through a comparison of the aforementioned previous computations and the ones performed in the framework of the present study. Afterwards, the steady state is introduced and the unsteady state, restricted to the first seven nodal diameters (backward and forward modes), is finally presented and discussed.

5.1 Presentation of the case study

The study focuses on flutter prediction of the axial turbine blades of a turbopump working with liquid oxygen in a gas generator cycle. The turbine presents intense turning and is characterized by very high flow velocity and aerodynamic load. Fluid properties are summarized in Table 5-1.

Parameter	Symbol	Value	Unit
specific gas constant	R	2171.0	[$m^2/s^2/K$]
specific heat capacity ratio	γ	1.369	[-]
dynamic laminar viscosity	μ	0.1711E-4	[Pa.s]
thermal conductibility	λ	0.242E-1	[W/m/K]
density	ρ	4.475	[kg/m^3]

Table 5-1: Fluid properties

An isolated shrouded blade which is part of the first stage rotor of a supersonic turbine is considered. The row comprises N blades that are connected to the disk through fir tree attachments. The turbine is characterized by large disk and short blades both made in very high stiff material. The modeshape originates from the disk vibration, it has been calculated previously outside of this work through modal analysis using 3D finite element

model of one blade and its segment of the disk, and then provided. The modal analysis established that the blades move according to two families of modes which are conjugated:

- one is rotating in the same direction than the machine and is referenced as forward mode,
- the second is counter-rotating and is referenced as backward mode.

The pair shares the same eigenfrequency but the modal shapes are conjugated. The nodal diameter range is restricted to [-7ND; +7ND]. The eigenfrequencies versus the nodal diameter are presented in Figure 5-1: this highlights the structure (disk and attached blades) to behave like ideal disk (disk mode). The nodal diameters, absolute and reduced frequencies are included in Table 5-2: the high velocities induce low reduced frequencies.

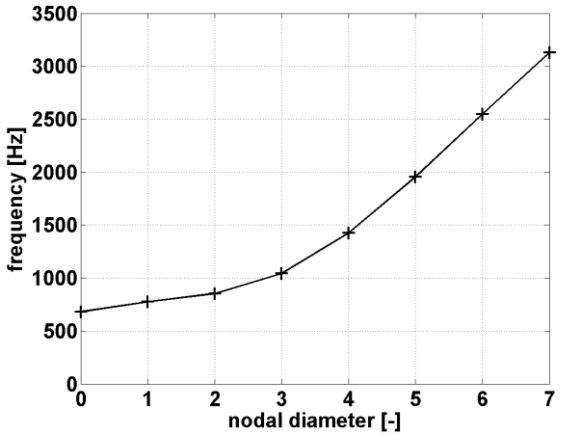

Figure 5-1: Frequencies versus nodal diameters

ND [-]	f [Hz]	k [-]
0	680.7	0.063
1	774.3	0.071
2	854.0	0.078
3	1041.2	0.096
4	1425.3	0.131
5	1956.4	0.180
6	2547.2	0.234
7	3128.1	0.287

Table 5-2: Nodal diameters and corresponding frequencies

The modal displacements are shown in Figure 5-2 over the normalized span; the amplitude of displacement is normalized according to Eq. 5-1. The prescribed motion is of pure axial rigid nature and will be implemented in the linearized computations as a pure axial translation along the machine axis.

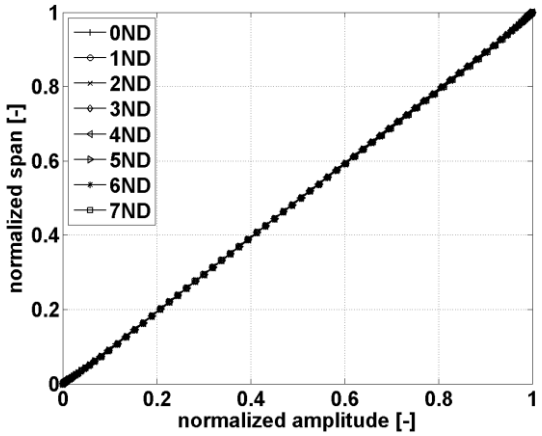

Figure 5-2: Modal displacements

$$A_{normalized} = \frac{A - A_{min}}{A_{max} - A_{min}} \quad \text{Eq. 5-1}$$

The 2D blade profile is plotted in Figure 5-3, the dimensions have been voluntarily scaled such that the actual shape is not shown. The figure displays also the evolution through the channel of:

- the passage width normalized with the pitch.
- the section normalized with the maximal section, i.e. at trailing edge.

The section is not strictly such a convergent-divergent channel. For a fluid particle close to pressure side, the section starts to decrease up to 25% axial chord (convergent), then it increases and remains constant up to 70% and finally it decreases slightly before to increase (divergent).

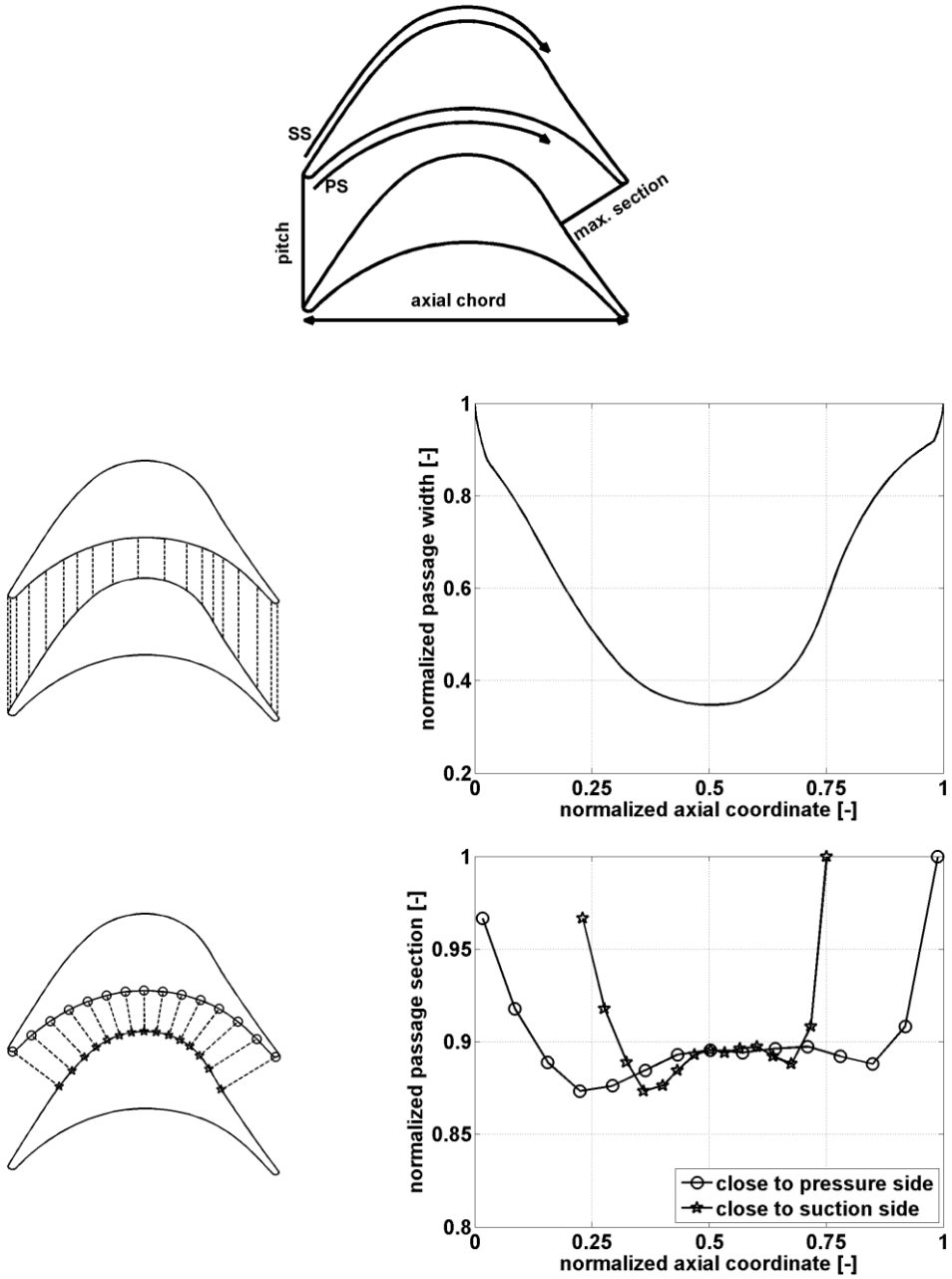

Figure 5-3: 2D blade profile

Considering all the data introduced so far and given the robust character of the blades that are short and stiff, implying therefore high natural frequencies, the risk of flutter remains

due to high pressure levels and strong shocks. The next section is dedicated to the presentation of numerical parameters.

5.2 Numerical parameters

This section is dedicated to the presentation of the numerical parameters. First the mesh is described, then the characteristics of the steady and unsteady computations are introduced. More details are presented in Appendix D.

5.2.1 Computation grid

A periodic multi-blocks structured grid is used to mesh one blade sector. The O-grid is extruded from the blade profile, starting from a first cell size of about 0.05% of the pitch. The H-grids are then added up- and downstream of the blade. Two different meshes in terms of size are used but each counts 61 nodes along the span:

- for steady computations, the mesh is extended about 1 and 1.6 axial chords up- and downstream of the blade respectively (718 763 nodes in total).
- for unsteady computations, the mesh is extended about 20 axial chords at each side (841 739 nodes in total) in order to damp outgoing unsteady waves and thus to avoid unphysical reflection from the in- and outlet boundaries towards the blade as mentioned previously.

Midspan section of the computation boxes and mesh around the blade are included in Figure 5-4.

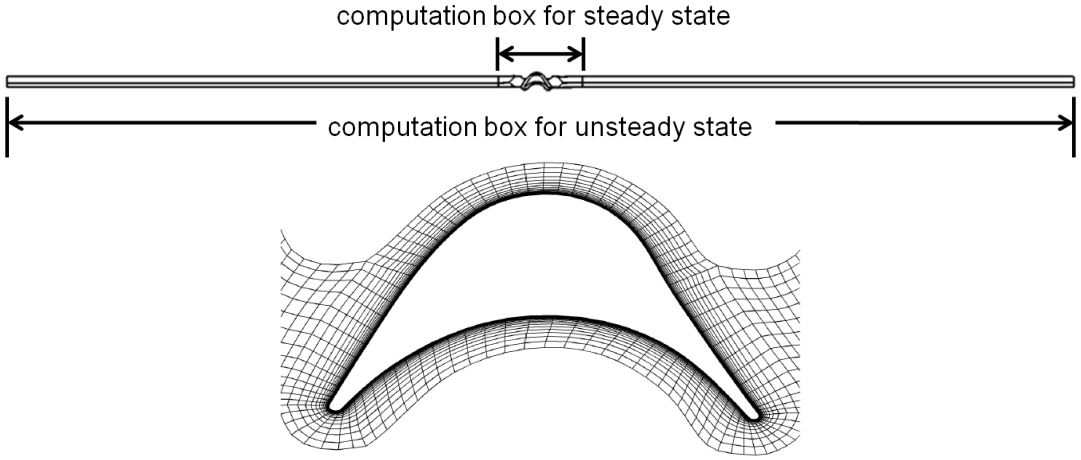

Figure 5-4: Computation boxes and mesh around (1 every 2 points)

The normalized first cell size is displayed in Figure 5-5 at 10%, 50% and 90% span in order to estimate the near wall mesh density: values below 15 are acceptable.

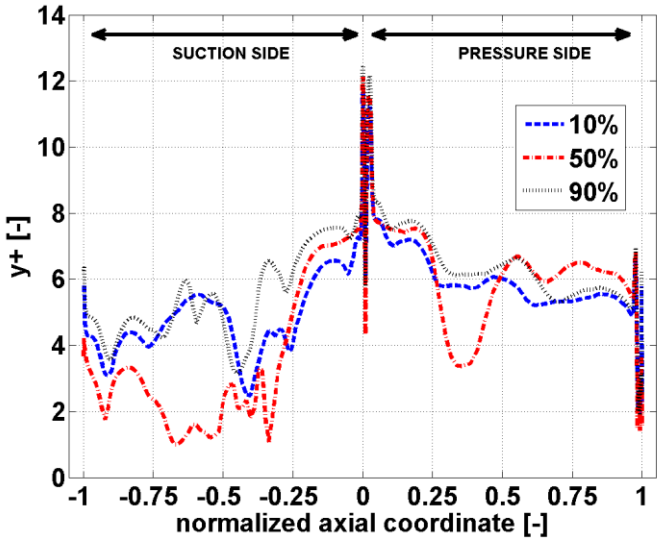

Figure 5-5: Normalized first cell size

5.2.2 Steady computations

Steady computations were performed with the solver Turb'Flow™ v1.7.1-3 with one passage modeled and applying periodic boundary conditions. During computations, as inlet boundary conditions, the relative total pressure, total temperature and angle are imposed, whereas at the outlet, a radial static pressure profile is prescribed. The second order spatial scheme AUSM+ of Liou is used combined to the SMARTER limiter. Explicit temporal scheme is adopted with 5-steps Runge-Kutta scheme and a CFL condition of 0.5. The RANS equations system is closed with the Kok $k-\omega$ turbulence model combined to a limiter of kinetic energy production.

5.2.3 Linearized unsteady computations

Based on the aforementioned steady calculations, unsteady computations linearized in the frequency domain were performed with the solver Turb'Lin™ v1.5.8-05SA in the traveling wave domain and applying phase lagged periodic boundary conditions in order to take into account the interblade phase angle. Given the low oscillation frequencies, a first sub-section suggests to assess the relevance of using the transpiration boundary condition only without moving mesh. Then, given the purely axial nature of the blade motion, a simplification towards the stability analysis is proposed. Finally the LRANS numerical parameters are described.

Evaluation of the transpiration boundary condition

As mentioned previously, transpiration boundary condition is usually used in order to simplify the numerical computations, especially when the amplitudes are small and the frequencies high. The frequencies being relatively low, the relevance of the use of transpiration boundary condition is assessed. Thus Eq. 5-2 gives the ratio of the section variation over the minimal section, i.e. at the throat, which is approximated as the ratio between the maximal vibration amplitude and the minimal section. Furthermore, Eq. 5-3 defines the velocities ratio, i.e. the ratio of the velocity fluctuation coming from the blade vibration over the outlet relative velocity. This ratio is given in Table 5-3 for each reduced

frequency (Eq. 5-4), the velocity is taken one axial chord downstream of the blade. Table 5-3 indicates that the section ratio is preponderant compared to the velocity ratio meaning that computations with moving mesh is necessary.

$$\frac{\delta S}{S_{min}} = \frac{A_{max}}{S_{throat}} = 3.87\% \qquad \text{Eq. 5-2}$$

$$\frac{\delta V}{V_{r,ax,out}} = \frac{A_{max} \times 2\pi f}{V_{r,ax,out}} \qquad \text{Eq. 5-3}$$

$$k = 2\pi f \frac{c_{ax}}{V_{r,ax,out}} \qquad \text{Eq. 5-4}$$

nodal diameter [-]	absolute frequency [Hz]	reduced frequency [-]	$\frac{\delta V}{V_{r,ax,out}}$ [%]
0	680.7	0.0625	0.05
1	774.3	0.0711	0.06
2	854.0	0.0784	0.07
3	1041.2	0.0955	0.08
4	1425.3	0.1308	0.11
5	1956.4	0.1795	0.15
6	2547.2	0.2337	0.20
7	3128.1	0.2871	0.24

Table 5-3: Velocity ratios versus the nodal diameters

Blade motion

The modeshape is considered as purely axial. As a result and in order to go beyond the sign of the aerodynamic damping coefficient, the expression of the work is simplified. The passage to complex formula gives,

$$\delta\vec{X} = \Re\left(\widetilde{\delta\vec{X}}\right) \rightarrow \begin{cases} \Re(\ \ ) \neq 0 \\ \Im(\ \ ) = 0 \end{cases}$$

The velocity fluctuation is then deduced from the above blade displacement,

$$\widetilde{\delta\vec{V}} = i\omega\widetilde{\delta\vec{X}} \rightarrow \begin{cases} \Re(\ \ ) = 0 \\ \Im(\ \ ) \neq 0 \end{cases}$$

$$\Im\left(\widetilde{\delta\vec{V}}\right) = \delta X\omega\cos(\omega t) = \delta X\omega\sin\left(\omega t + \frac{\pi}{2}\right) \qquad \text{Eq. 5-5}$$

The work, assuming the deformation negligible,

$$W_{aero} = \frac{1}{2}\Re\left(\widetilde{W}_{mvt} + \widetilde{W}_{def}\right) = \frac{1}{2}\Re\left(T \oint_{wall} \delta\tilde{p}_S^* \cdot \bar{\bar{S}} \cdot \widetilde{\delta\vec{V}}\right) \quad \text{Eq. 5-6}$$

simplifies finally as follows,

$$\begin{aligned} W_{aero} &= \frac{\pi}{\omega}\oint_{wall} \Im\left(\widetilde{\delta p_s}\right) \cdot \Im\left(\widetilde{\delta\vec{V}}\right) \cdot \vec{n} dS \\ &= \frac{\pi}{\omega}\oint_{hub}^{tip}\left[\oint_{blade} \delta p_s \cdot sin\left(\varphi_{\widetilde{\delta p_s}}\right) \cdot dy\right] \cdot \omega \cdot \delta X \cdot dr \end{aligned} \quad \text{Eq. 5-7}$$

The sign of the work can be deduced from the sign of dy in Eq. 5-7. The different cases are summarized in Figure 5-6. The wall is divided into four regions delimited by points where the sign of dy changes, i.e. where the tangent to the profile is horizontal in (x, y) plane (the blade is swept in clockwise direction).

For regions where dy is positive:

- Eq. 5-7 indicates that the flow is stabilizing if the imaginary part of the static pressure fluctuations is negative, i.e. if its phase is comprised between -180deg and 0deg. Furthermore, for a phase equals to -90deg, velocity and pressure fluctuation are out-of-phase (Eq. 5-5) and this agrees with stable configuration that is to say the pressure decreases with increasing velocity.
- In contrast, if the imaginary part of the static pressure fluctuation is positive, i.e. if its phase is comprised between 0deg and 180deg, the flow is destabilizing. Likewise, for a phase angle of 90deg, velocity and pressure fluctuations are in-phase and this agrees with unstable configuration: the pressure increases with increasing velocity.

Regions where dy is negative lead obviously to the opposite conclusions.

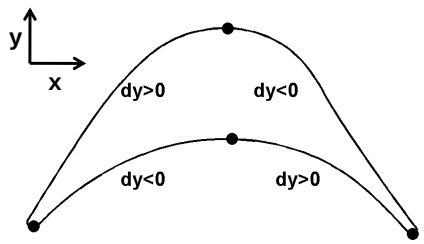

dy	$sin\left(\varphi_{\widetilde{\delta P_s}}\right)$	→	$\varphi_{\widetilde{\delta P_s}}$	W_{aero}	Ξ
> 0	> 0	→	$0° \leq \varphi_{\widetilde{\delta P_s}} \leq 180°$	> 0	< 0
	< 0	→	$-180° \leq \varphi_{\widetilde{\delta P_s}} \leq 0°$	< 0	> 0
< 0	> 0	→	$0° \leq \varphi_{\widetilde{\delta P_s}} \leq 180°$	< 0	> 0
	< 0	→	$-180° \leq \varphi_{\widetilde{\delta P_s}} \leq 0°$	> 0	< 0

Figure 5-6: Partition of the blade wall and sign of the work

Numerical parameters

The computations were performed on the grid displayed in Figure 5-4 with 1 every 2 points deleted in each direction, thus the total number of nodes is now of 112 747. A mesh sensitivity is further suggested in order to evaluate its influence on the results.

In addition to the extended computation box, non-reflective conditions are imposed at the in- and outlet in order to avoid unphysical reflections at the boundaries towards the blade. Second order centered Jameson scheme with 4th order dissipation (ε_2=1, ε_4=1/32) with

pressure sensor limiter is used. The linear system is solved with BiCGStab method combined to GMRES method for partitionning. On the other hand, the computations have been performed with frozen turbulence.

All the numerical parameters have been presented. The next section is dedicated to the validation of the numerical computations.

5.3 Validation of the numerical computations

As mentioned in the introduction, previous numerical computations (with the solver Turbo3D) have been performed and validated with experimental data. Consequently, the solutions presented here are validated through comparisons with the first aforementioned numerical results, the measurements being not available. The following sub-sections compare firstly steady and unsteady solutions from both the solvers. Then sensibilities with respect to the flux limiter and the mesh density are presented.

5.3.1 Turb'Flow™/Turbo3D comparison

This sub-section compares first the steady states and then the unsteady results from Turb'Flow™ and Turbo3D solvers.

Steady state

The steady static pressure coefficient at 10%, 50% and 90% span computed with the solvers Turb'Flow™ and Turbo3D are displayed in Figure 5-7. The impingement point of the main shock on the suction side, i.e. a bow shock from the leading edge of adjacent blade, is also given as criterion for comparison. In addition, Figure 5-8 shows the turbulent kinetic energy at midspan in the blade-to-blade plane. The figures indicate the following:

- the shock wave at the leading edge is well captured by both solvers.
- Turb'Flow™ predicts stronger bow shock than Turbo3D.
- the shock at the mid-axial chord on suction side due to the bow shock at the leading edge of adjacent blade is not predicted at the same location, i.e. more downstream for Turb'Flow™.
- Turb'Flow™ exhibits higher load on blade whereas Turbo3D shows smoother evolution.
- although the extent in terms of disturbed flow is rather similar, the levels of turbulent kinetic energy are strongly different: the magnitude is much more higher for Turbo3D than Turb'Flow™.

The above discrepancies are due to different meshes and solvers as summarized in Table 5-4. Despite its robustness, Van Leer spatial scheme features high diffusion at low velocity and added to $k-\varepsilon$ turbulence model this explains the differences in terms of number of nodes and first cell sizes.

	Turbo3D	Turb'Flow™
number of nodes	1 969 033	841 739
first cell size (% of the pitch)	0.001%	0.05%
turbulence model	$k-\varepsilon$	$k-\omega$
spatial scheme	Van Leer	Liou

Table 5-4: Comparisons of numerical parameters (TBF versus T3D)

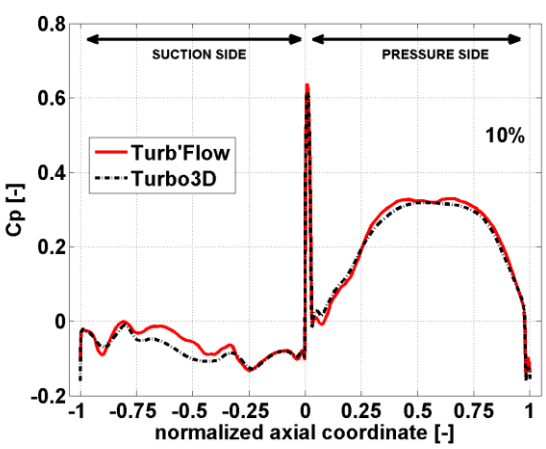

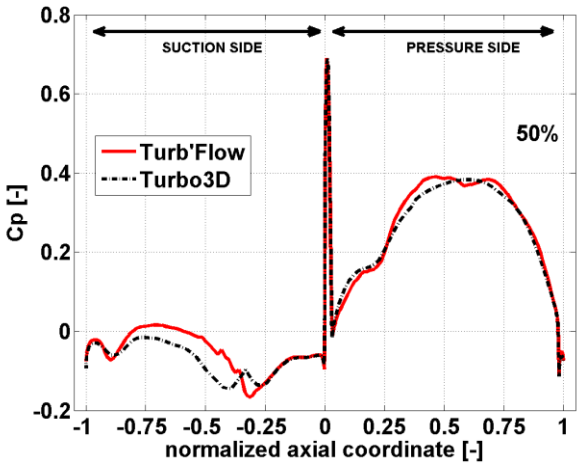

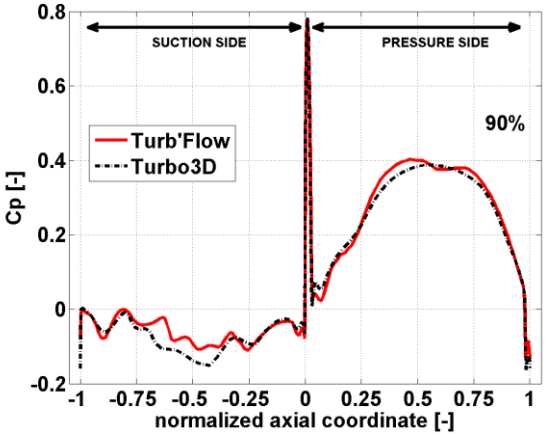

impingement point of the bow shock generated at the leading edge of adjacent blade [% of axial chord]		
span	Turb'Flow™	Turbo3D
10%	25	22
50%	31	26
90%	25	22

Figure 5-7: Comparison of steady static pressure coefficient (TBF versus T3D)

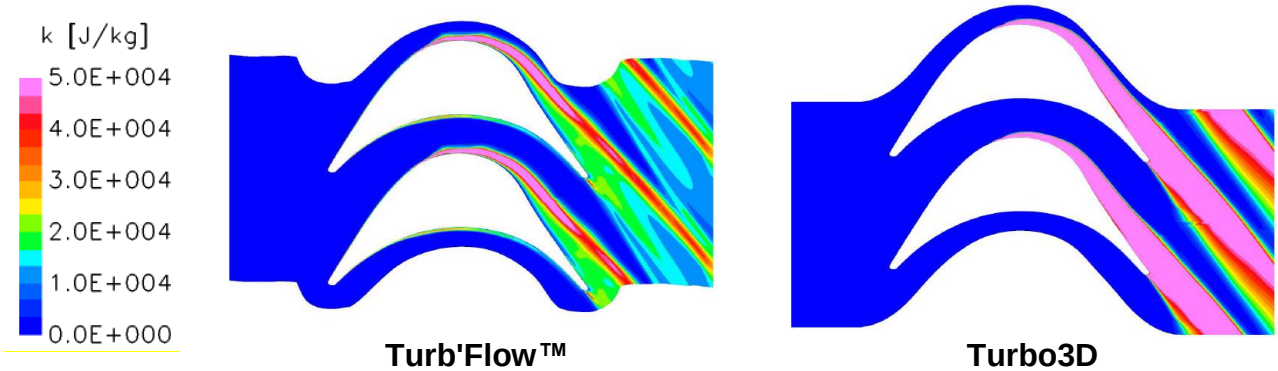

Figure 5-8: Comparison of turbulent kinetic energy at midpsan (TBF versus T3D)

The numerical results have been validated regarding the steady state. The next sub-section aims at validating the unsteady results.

Unsteady state

Stability parameter computed from Turb'Lin™ and Turbo3D is plotted in Figure 5-9 versus the nodal diameters, each one corresponding to the frequency summarized in Table 5-2. In order to compare, the stability parameter is therefore normalized by the oscillation frequency. All backward modes are predicted unstable whereas forward modes are stable. The results depict consistent features: the modes -3ND and +3ND are the most unstable and stable modes respectively. It has been concluded, despite the differences, that the unsteady computations are valid for this study.

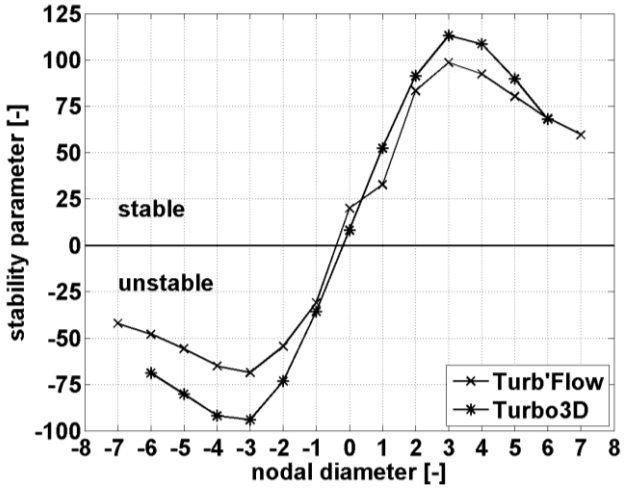

Figure 5-9: Comparison of stability parameter (TBF versus T3D)

The consistency has been evaluated through comparisons with previous numerical results. The next sub-section is dedicated to the evaluation of the effects of numerical parameters on the results.

5.3.2 Effect of numerical parameters

This sub-section is dedicated to the sensitivity to the flux limiter and mesh density in the steady computations.

Flux limiter

Flux limiter is used in order to avoid any oscillation or overshoot nearby a discontinuity or high gradients of the solution, typically such as shock waves. This is a non-linear function bounded and continuously varying between 0 and 1 that ensures a monotone behavior of the spatial scheme by limiting the amplitude of local gradients. The effect of spatial accuracy limiter on the steady load and thus on the shock wave position is presented in Figure 5-10 through the steady static pressure coefficient at 10%, 50% and 90% span. The main effect of the limiters would be to induce different patterns of the shock in terms of scattering. Based on (Soulat, 2010) and (Waterson and Deconinck, 2007), the two second order limiters considered are:

- MUSCL: Monotone Upstream-centered Scheme for Conservation Laws

- SMARTER: Sharp and Monotonic Algorithm for Realistic Transport Efficiently Revised

Although the latter is more diffusive, the differences between each curve are unnoticeable indicating that the two limiters have the same effect. This is highlighted in the right bottom figure with the difference of the pressure coefficients which is well below 0.02, except at 10% span, at the shock position, a local peak is observed with a difference of about 0.055. The use of SMARTER limiter leads to less rough convergence, it has been therefore use for the steady computations.

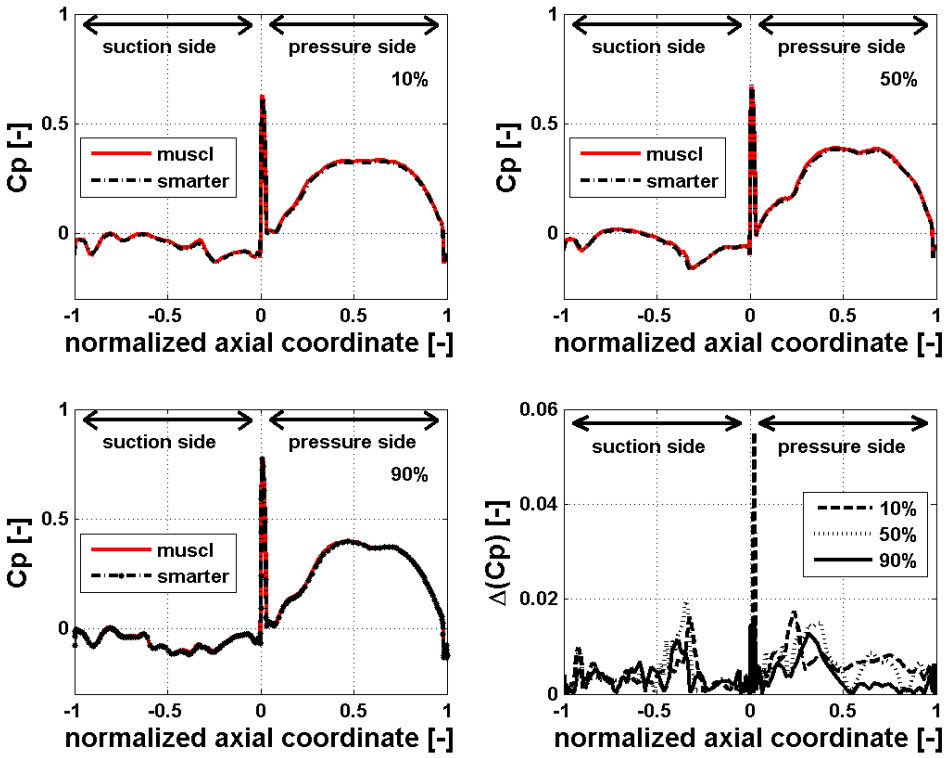

Figure 5-10: Effect of flux limiter on steady static pressure coefficient

Mesh density

A comparison between a fine grid referenced as "grid 1x" and a coarse grid referenced as "grid 2x" is presented. The coarse grid is based on the fine grid but one every two points is deleted in each direction. The comparison consists in evaluating the aerodynamic work on each mesh for the most unstable nodal diameter, i.e. -3ND, as displayed in Figure 5-11. The trend is fairly well conserved as shown in the left hand side figure, the relative difference on the global coefficient is about 7.7%. However, although the stability parameter remains globally negative, its evolution along the span exhibits positive values at 70% span and especially close to tip and hub which correspond to high gradient regions and thus very sensitive to mesh density. Finally, given the CPU time and the results associated to each grid, linearized unsteady computations have been performed on "grid 2x".

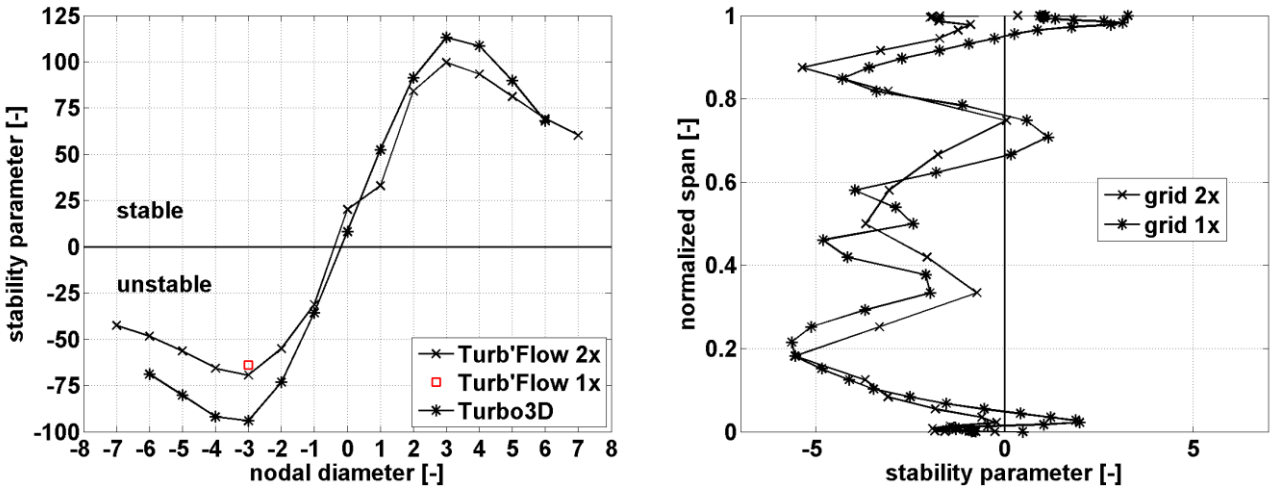

Figure 5-11: Effect of mesh density on stability parameter

The industrial case has been presented. The blade motion has been described and will be the source of excitation in the linearized unsteady computations. As a validation, steady and unsteady results have been compared to previous computations that were validated with measurements. The comparison has been found good enough and despite the lack of direct comparison with experimental data, the use of Turb'Lin™ has been approved.

The next sections are dedicated to the results. First the steady state is introduced.

5.4 Steady state results

This section is dedicated to the steady state results that will be displayed at 10%, 50% and 90% span as highlighted by white lines in Figure 5-12. The black arrow represents the direction of the flow which will be for that matter from left to right in 2D blade-to-blade planes. First the shock waves pattern is described, then the steady load and finally the shock wave/boundary layer interaction.

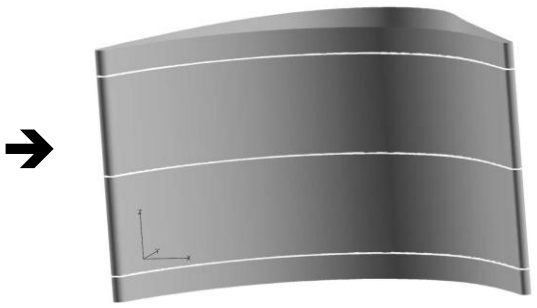

Figure 5-12: 3D blade profile and localisation of radial cuts

5.4.1 Description of the shock waves pattern

The steady supersonic flow involves a complex pattern of shock waves with reflexions. Schlieren visualization is a helpful way to highlight shock waves, boundary layers and wakes through the variations of density. A first type of Schlieren is suggested in order to emphasize the intensity of shock waves through the modulus of density gradient. A second

type of Schlieren identifies both compression and expansion waves through the projection of density gradient on the normalized relative velocity vector:

- $\overrightarrow{\nabla\rho} \cdot \frac{\overrightarrow{V_r}}{\|\overrightarrow{V_r}\|} > 0$: compression waves
- $\overrightarrow{\nabla\rho} \cdot \frac{\overrightarrow{V_r}}{\|\overrightarrow{V_r}\|} < 0$: expansion waves

Figure 5-13 displays such numerical Schlieren visualizations and Figure 5-14 gives the relative Mach number, the sonic lines are highlighted in black.

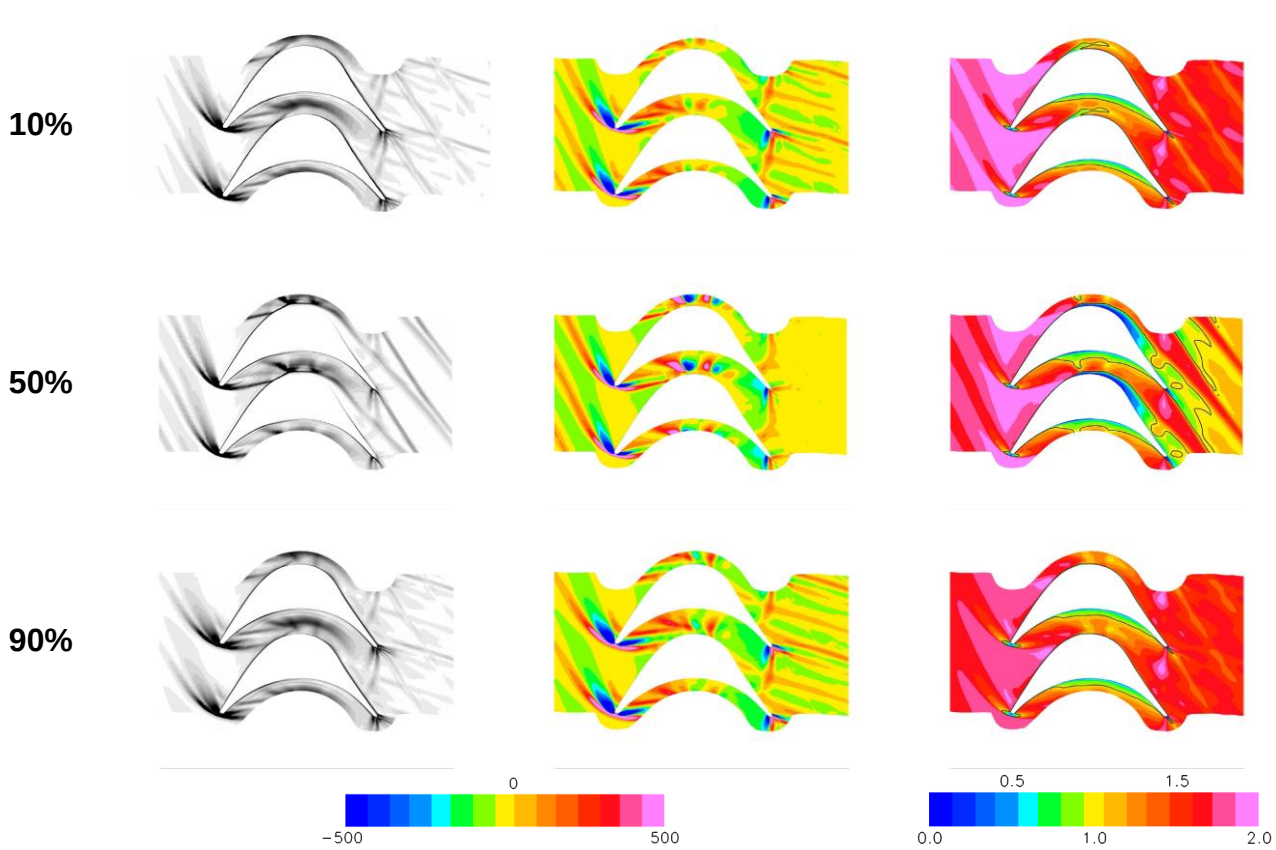

Figure 5-13: Schlieren visualizations

Figure 5-14: Relative Mach number

The three radial cuts at 10%, 50% and 90% span show the following:

- the supersonic inlet flow induces a detached bow shock ahead of the curved leading edge with a subsonic pocket around the stagnation point.
- behind the shock, locally, the convex surface generates expansion waves both on the pressure and suction sides.
- then the curvature on the suction side leads to flow acceleration ending at the impingement point of the downward branch of the bow shock from adjacent blade through a weak shock and causing boundary layer separation (described further down).
- on the pressure side just after the leading edge, the flow starts to decelerate on the first third axial chord then it becomes subsonic. The extend of that subsonic layer is larger at midspan and exhibits a sonic line over almost the entire section passage close to the separation point of suction side (described further down).

- two weak shocks appear at the trailing edge and impinge the suction side of the adjacent blade. The interaction is much more pronounced close to the walls, i.e. hub and tip.
- at mid-channel the flow is characterized by successive "spots" of compressions and expansions especially at midspan.

The bow shock at the leading edge impinges on the suction side of the adjacent blade and causes boundary layer separation as displayed in Figure 5-15: the regions with negative axial velocity are emphasized in order to highlight how large the separation is. Although separation occurs over the entire channel height, the flow is mostly disturbed at mid-channel. The separation close to the walls, i.e. hub and shroud, are of lower magnitude meaning a different topology of the flow in terms of shock waves intensity (Figure 5-13).

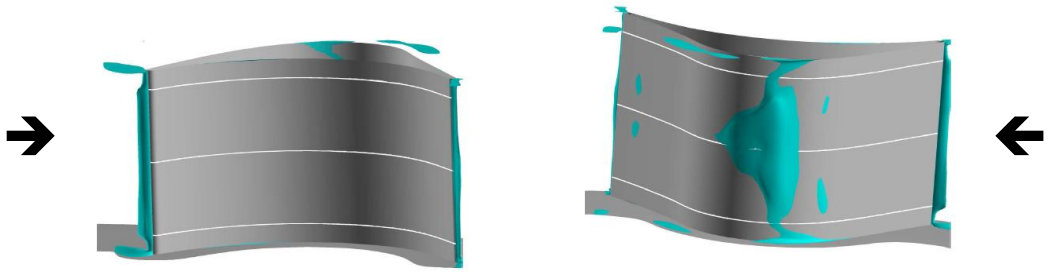

Figure 5-15: Separation regions

5.4.2 Steady load

Figure 5-16 displays the static pressure coefficient on blade surface at 10%, 50% and 90% of channel height versus the normalized axial coordinate and over the span in a 3D view. This shows the following:

- the pressure jump at the leading edge increases while approaching the tip.
- the suction side shows slight difference of the impingement point of bow shock from the adjacent blade. This is located at 31% axial chord at midspan and slightly upstream (25% axial chord) when approaching either the hub or the tip. This observation is in line with the above comment, namely the shock waves at leading edge are of lower magnitude close to the walls.
- after the shock, still on the suction side, the pressure gradually increases, reaches a maximum at 71% axial chord, decreases up to 89% axial chord and starts again to rise through a weak shock originated from the trailing edge shock wave of the adjacent blade.
- the 3D views indicate that on the pressure side there is no strong radial evolution, whereas on the suction side two static pressure spots appear both at the hub and tip.

These positive pressure gradients result in sucking fluid particles with low kinetic energy towards the mid-channel where pressure is lower as illustrated with the streamlines in Figure 5-17. Two passage vortices start developing from the hub and tip slightly upstream of the mid-axial-chord. They appear as counter-rotating pairs and grow in size while traveling downstream and moving towards the midspan; the centers of vorticity are clearly identified.

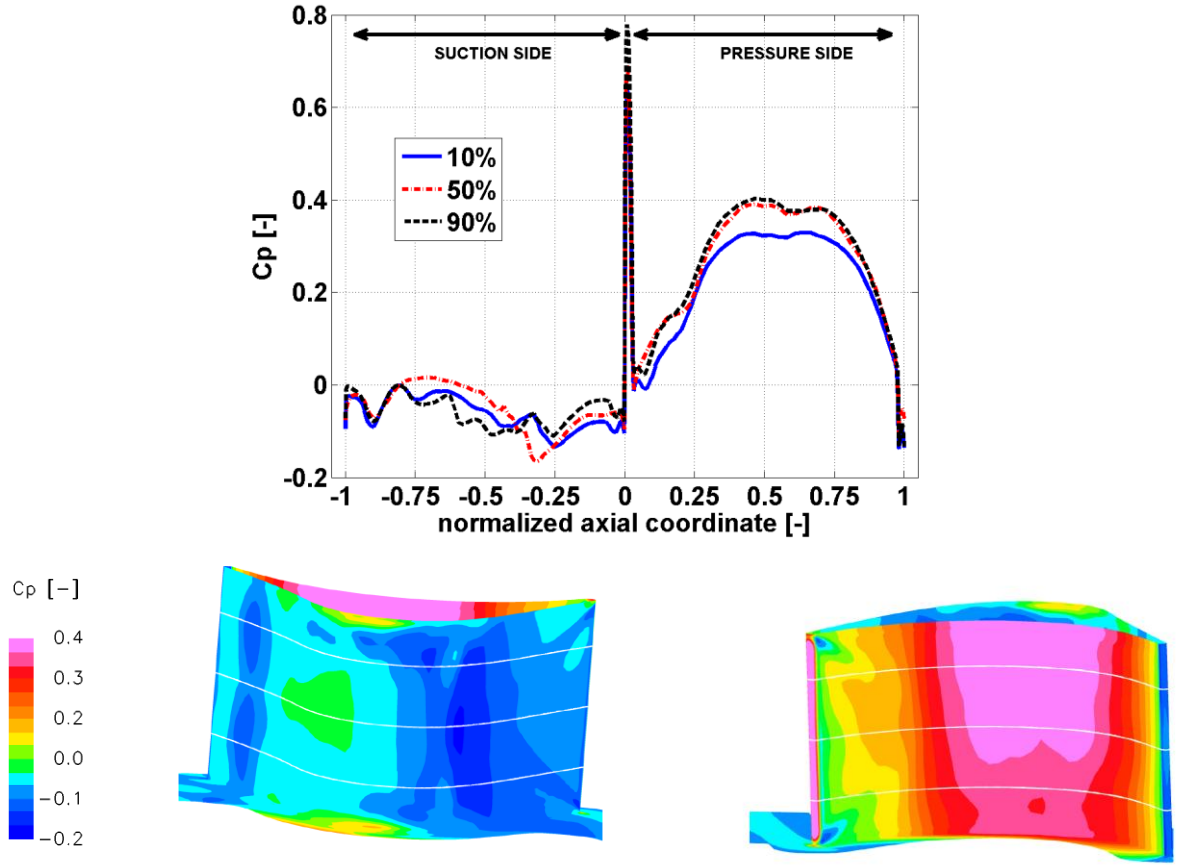

Figure 5-16: Spanwise variation of static pressure coefficient on blade surface

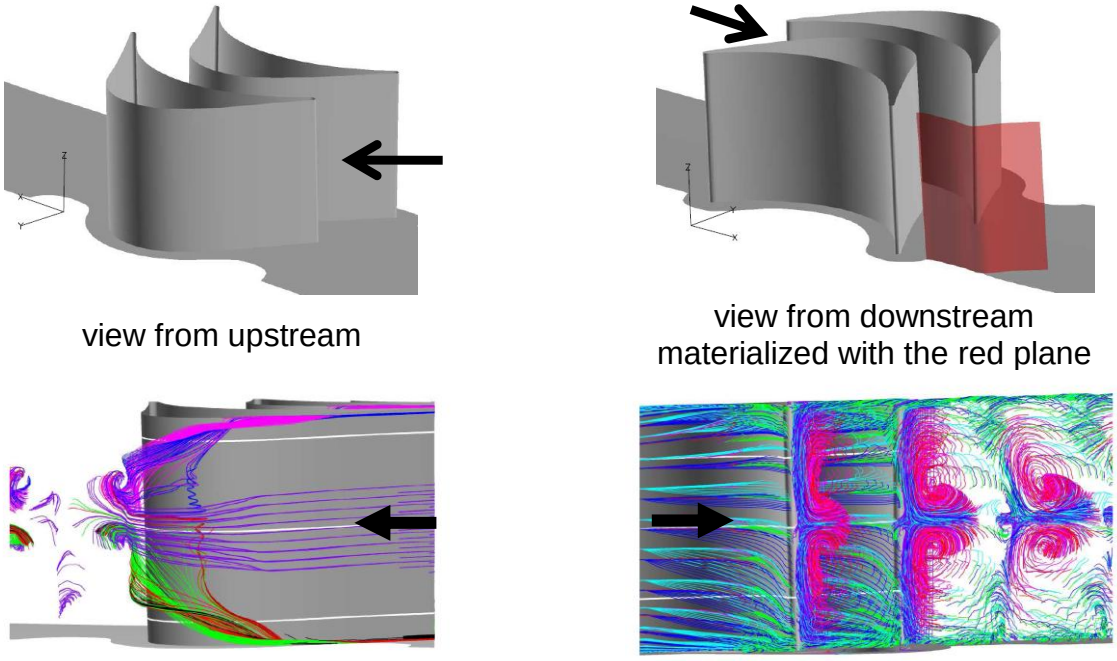

Figure 5-17: Fluid particles streamlines

5.4.3 Shock wave/boundary layer interaction

Figure 5-18 illustrates the shock wave/boundary layer interaction through the superposition of numerical Schlieren visualization and contours of the turbulent kinetic energy. As expected, thicker boundary layer is observed as soon as a wave is reflecting on the blade surface. The strongest interaction is located at the separation point on the suction side. The two red crosses will be used further as references for the quasi-steady analysis.

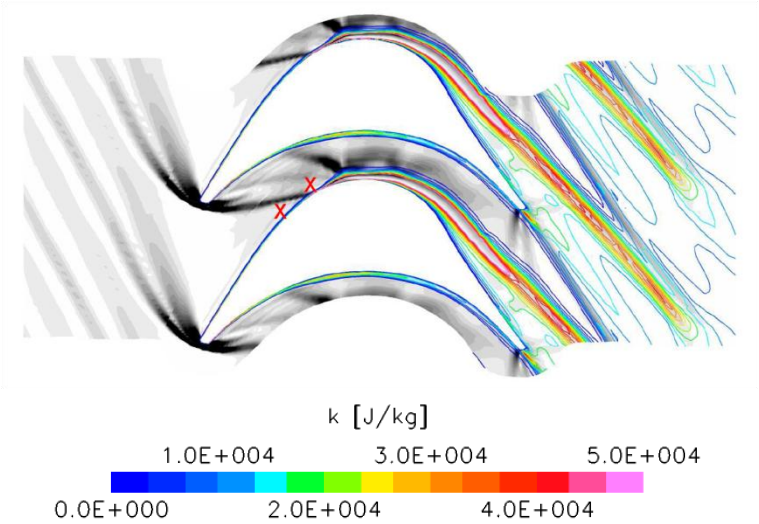

Figure 5-18: Shock wave/boundary layer interaction

5.4.4 Summary

The steady state has been presented and can be summarized as follows:

- the supersonic flow induces a detached bow shock ahead of the curved leading edge.
- the aforementioned shock impinges the suction side of the adjacent blade and this results in boundary layer separation.
- the separated region extends from hub to tip, nevertheless this is much larger at midspan than close to the walls.
- the flow at midspan experiences strong compression and expansion regions.
- the corner vortices at hub and tip develop such that they start to disturb the flow at midspan close to the mid-chord.

The next section is dedicated to the unsteady state. The aerodynamic response to a prescribed motion of the blade is computed over the aforementioned restricted nodal diameters range.

5.5 Unsteady state results

The unsteady results are presented as follows:

- the stability parameter is firstly presented over the restricted range of nodal diameters.
- then, the focus is put on the most unstable and stable coefficients (±3ND) and a quasi-steady analysis is suggested in order to highlight the mechanisms responsible for flutter.

- the effect of the nodal diameters and the cut-on/cut-off conditions are finally evaluated.

5.5.1 Stability parameter

The aerodynamic damping coefficient versus the nodal diameter is displayed in Figure 5-19. All the backward modes are predicted unstable; whereas forward modes are all stable. The -3ND and +3ND are respectively the most unstable and the most stable mode. These two extremes are analyzed in the following sub-section.

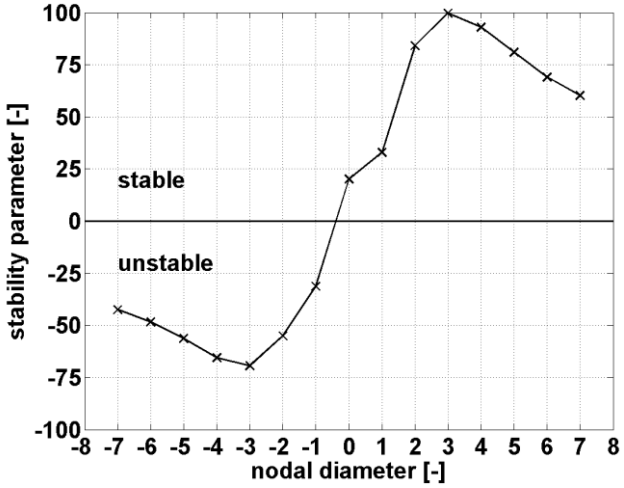

Figure 5-19: Stability parameter

5.5.2 Analysis of the ±3 nodal diameters pattern

This part focuses on the ±3 nodal diameters. First the stability parameter is evaluated over the span, then the focus is put on the unsteady pressure fluctuations and finally a quasi-steady analysis is suggested.

Stability parameter

The stability parameter along the normalized span is plotted in Figure 5-20 as well as on blade surface in a 3D view:

- the distributions appear symmetric with respect to the marginal stability, i.e. the most stable regions at +3ND correspond to the most unstable ones at -3ND.
- the stability parameter exhibits three domains: close to hub, at mid-channel and close to tip with an extremum at 18%, 50% and 87% span respectively.
- although there are significant drops in stability close to hub and tip as well as at 33% and 75% span, the +3ND remains stabilizing over the span, whereas the -3ND displays locally positive values (at 75% span and tip).
- the stability/instability (positive/negative) contributions result from geometric considerations due to the axial nature of the blade motion. The changes in sign have to be directly related to the horizontal tangents on the blade profile.
- on the pressure sides, there is no pronounced radial evolution and the change in sign occurs at mid-axial-chord. The fore and aft 50%-axial-chord are respectively stable and unstable when traveling waves move forward (+3ND) whereas the opposite is observed for the backward mode -3ND.

- the suction side is much less homogenous. Although there is no differences between the two nodal diameters on the fore part, i.e. without energy exchange up to 30% axial chord, disparities occur at the impingement point of the bow shock. Then, as mentioned, the horizontal tangent coupled to the axial motion of the blade cause a narrow strip of no aerodynamic work. Next, the 50% aft part seems to be determinant in terms of stability since -3ND and +3ND are unstable and stable respectively on almost the entire aft suction side. The aforementioned three-domains feature is clearly highlighted through three spots of intense magnitude.

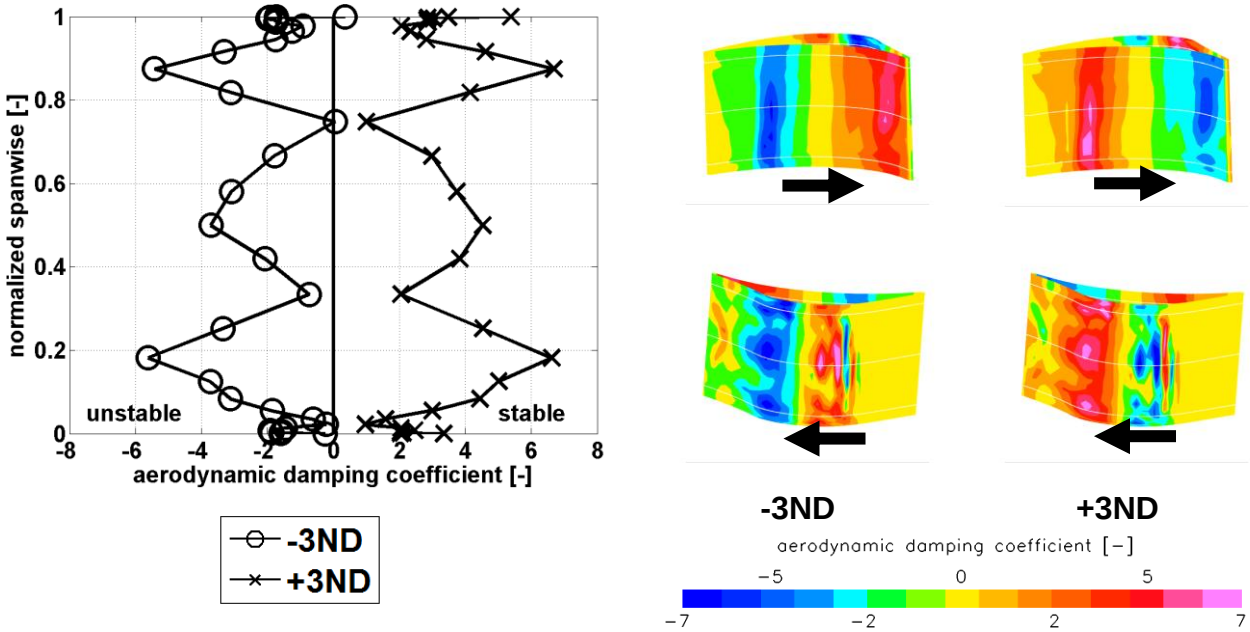

Figure 5-20: Stability of blade along the span ±3ND

In order to investigate in a more intimate way the stability behavior, the next sub-section focuses on the unsteady static pressure fluctuations.

Unsteady static pressure fluctuations

The magnitude and phase of the unsteady static pressure fluctuations from the nodal diameters ±3 are displayed in Figure 5-21 in a 3D view. The blade surface shows the following:

- the magnitudes of the fluctuations are very close with each other on both sides.
- the highest levels appear at the impingement point of the shock wave, whereas the levels are much lower on the fore and aft suction sides as well as on the fore pressure side right downstream of the shock.
- the phases behave also very similarly on the fore suction side although the amplitudes are rather low.
- a change in phase arises at the impingement point on the suction sides when comparing the two nodal diameters. At -3ND, the phase remains in the range [-180; 0]deg whereas it rotates in the range [0; 180]deg at +3ND.
- the phases on pressure side do not exhibit the same change: they remain in the aforementioned ranges.

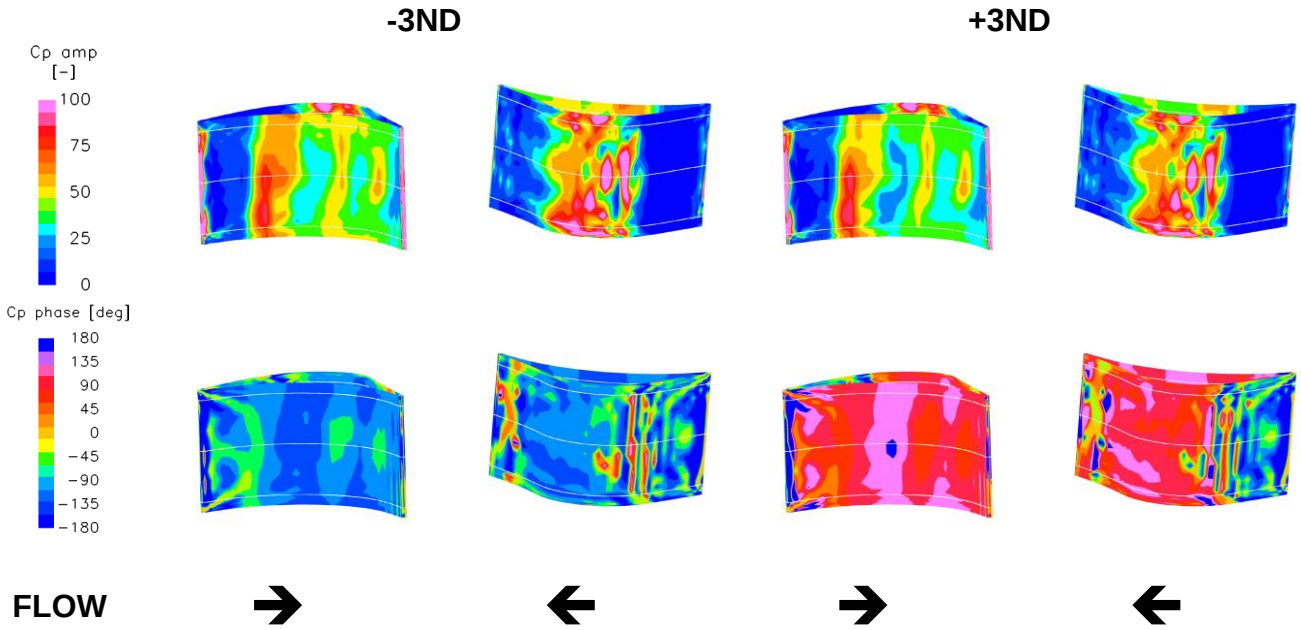

Figure 5-21: Unsteady pressure fluctuations ±3ND, 3D view

The magnitude and phase are now displayed at midspan along the normalized axial coordinate as well as in the blade-to-blade plane in Figure 5-22 and suggest the following:

- the magnitudes are very similar between the two cases. The peaks at the leading edge and on the suction side are predicted at the same position. This is also evidenced within the channel on the blade-to-blade plane.
- these two strong peaks on the suction side are located at 35% and 43% axial chord, that is to say right behind the shock. The level of fluctuations coincides with the shock wave pattern described above, the highest amplitudes are located at the leading and trailing edge as well as behind the impingement point of the bow shock; furthermore the blade-to-blade plane suggests a more pronounced correlation between compression regions in the mean flow and high fluctuations than expansion regions.
- although the magnitudes are very low, the phases on the fore suction side display very similar and shaky behaviors.
- on the pressure side and the aft suction side, the phases indicate opposite and symmetric trends. Whereas the phase at +3ND remains mainly in the range 0deg-180deg, the phase at -3ND is comprised between 0deg and -180deg.
- the aft suction side exhibits nevertheless a strong drop in phase for both the nodal diameters from 88% to 93% axial chord and corresponds to the impingement point of the shock generated at the trailing edge of the adjacent blade.

The low reduced frequencies and the phases suggest to analyze the problem from a quasi-steady point of view. The next sub-section proposes such an approach.

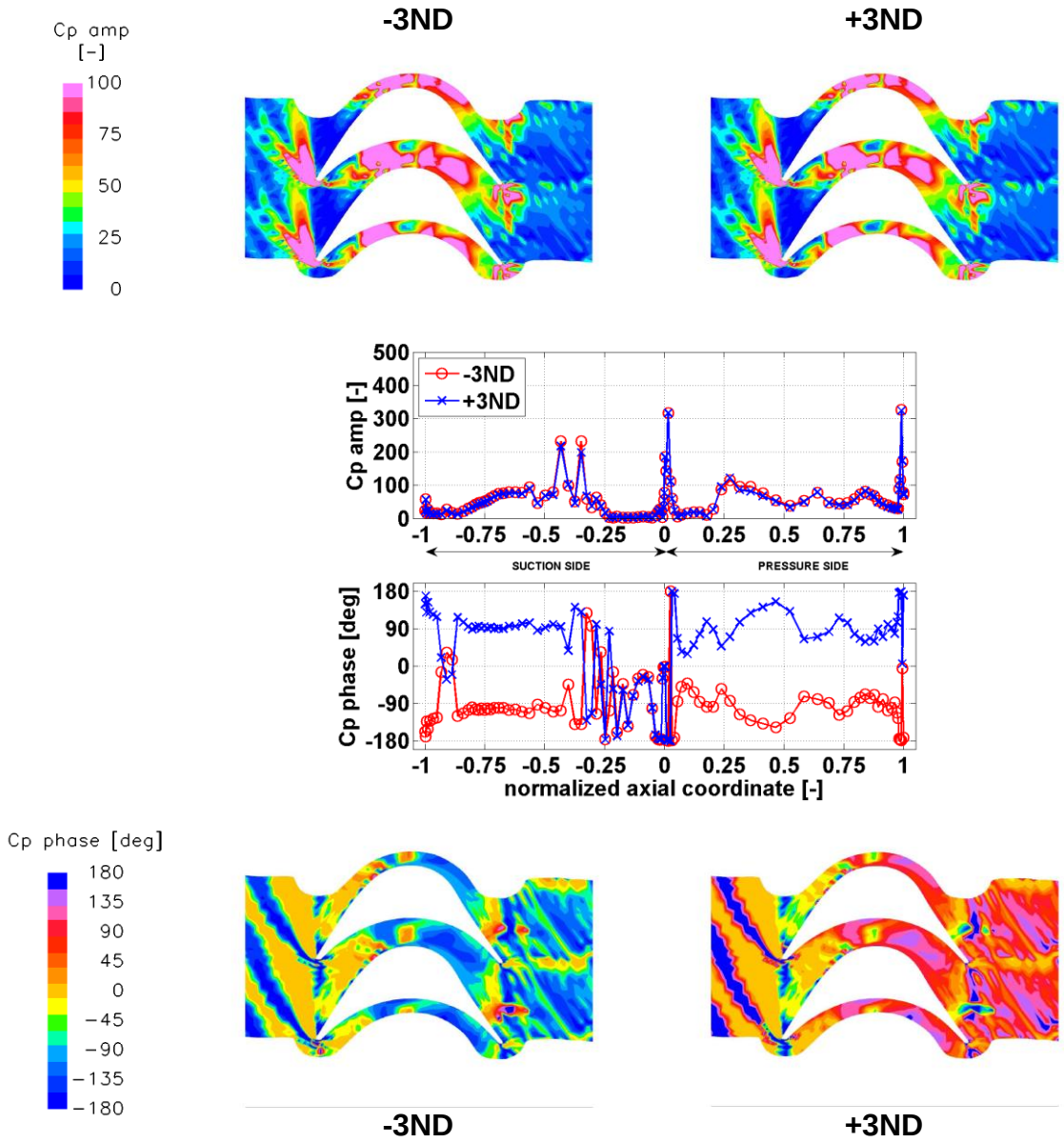

Figure 5-22: Unsteady pressure fluctuations at midspan ±3ND

Quasi-steady analysis

Quasi-steady condition implies that the shock wave follows the blade motion. Figure 5-23 illustrates the change in section due to interblade phase angle (the motion is amplified); the ±3ND are displayed at the same time t in the oscillation cycle both in a blade-to-blade plane and in temporal view described by sinusoidal curve. The solid lines represent the steady blade, i.e. the reference position, whereas the dotted lines describe the actual position of the blade. For each nodal diameter blade 0 is the reference. Quasi-steady analysis on these configurations at time t as described in Figure 5-23 leads to the following:

- blades +1 and -1 are in delay and in advance respectively for the -3ND case. When the shock is moving in the opposite direction of the flow, its magnitude increases and the induced pressure fluctuation is thus out-of-phase with respect to the speed of shock wave motion which is itself 90deg shifted with respect to the movement. Therefore, blade motion and pressure fluctuations are in-phase.

- in contrast, for the case +3ND, blades +1 and -1 are respectively in advance and in delay. When the shock is moving streamwise, the relative flow velocity in the shock frame of reference decreases resulting in weakening the shock. Therefore, blade motion and pressure fluctuations are out-of-phase.

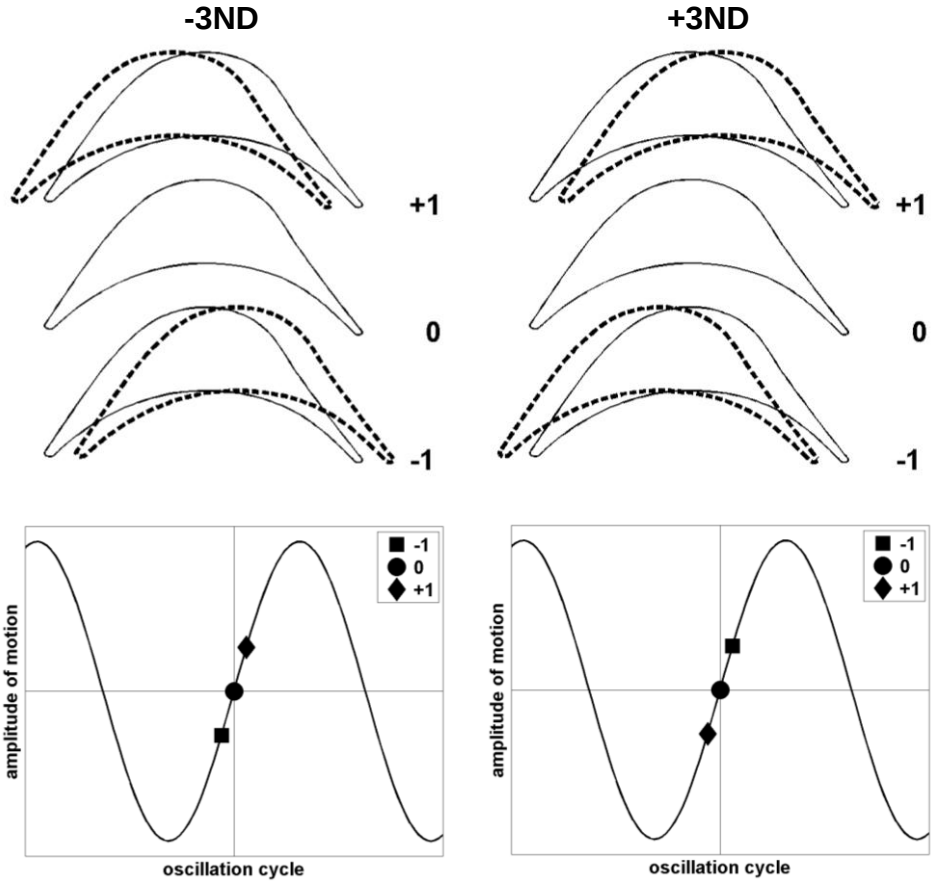

Figure 5-23: Illustration of the ±3ND

Furthermore, despite the low level of pressure fluctuations, the drop in phase around 90% axial chord (Figure 5-22) is believed to be due to the impingement of expansion waves generated at the trailing edge of the adjacent blade. The blade oscillation induces oscillation of the expansion waves and when they move in the same direction than the flow, the relative velocity in the expansion wave frame of reference decreases and this results in weakening its intensity. As a result, the pressure downstream increases: pressure fluctuation and expansion wave motion are in-phase.

The shock wave motion appears as a key driver in the stability. Based on (Tijdeman, 1977) and (Ferrand et al., 1998), the shock motion is therefore analyzed. Assuming inviscid flow, normal shock wave and without upstream perturbation, the pressure fluctuation downstream of the shock can be related to the shock motion as follows,

$$\frac{\delta p_{s,dw}}{p_{s,up}} = \frac{2\gamma M_{r,up}^2}{\gamma+1}\left[\frac{3+\gamma-2M_{r,up}^2}{2+(\gamma-1)M_{r,up}^2}\frac{\partial ln\left(M_{r,up}\right)}{\partial x^*} - 2ik\right]\delta x_{shock}^* \qquad \text{Eq. 5-8}$$

The subscripts up and dw denote the values taken just up- and downstream of the shock wave respectively (these two positions are highlighted with the red crosses in Figure 5-18).

Figure 5-24 displays the unsteady pressure coefficient at midspan for the ±3ND superposed on the density gradient. Besides, the amplitude and phase of the shock motion are included in Figure 5-25 (the amplitude is normalized by the maximum amplitude of vibration). Eq. 5-8 establishes a correlation between stationary velocity gradient and shock movement and reveals that dominant Mach number gradient induces pressure fluctuation in-phase with shock motion. The figures indicate the following:

- the amplitude of shock motion is increasing with increasing reduced frequency, i.e. with increasing variation of the section. Backward modes exhibit slightly higher shock motion amplitude. In terms of stability, a system is more prone to be unstable when the shock features large motion.
- the phase suggests that the shock motion and the pressure fluctuation downstream of the shock are out-of-phase for the forward modes, i.e. the pressure decreases upon movement of the shock in direction of the flow, whereas in-phase feature are observed for the backward modes.

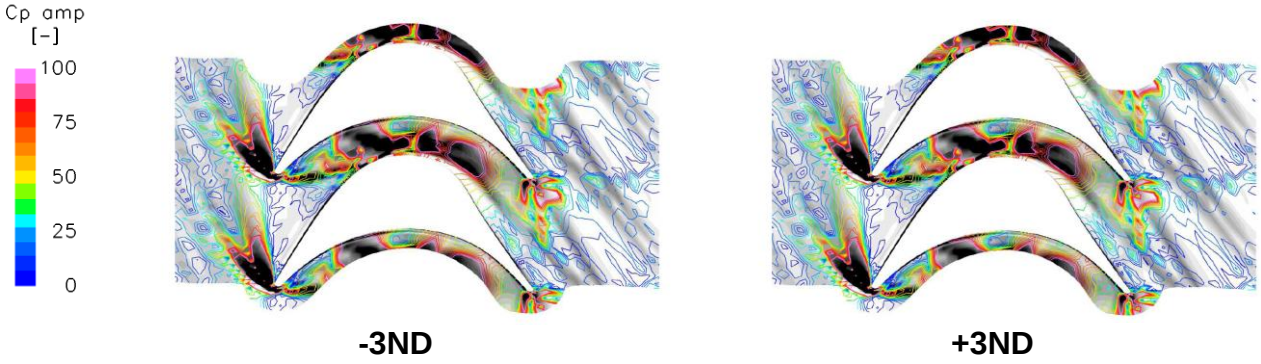

Figure 5-24: Pressure fluctuations superposed on Schlieren visualization (midspan)

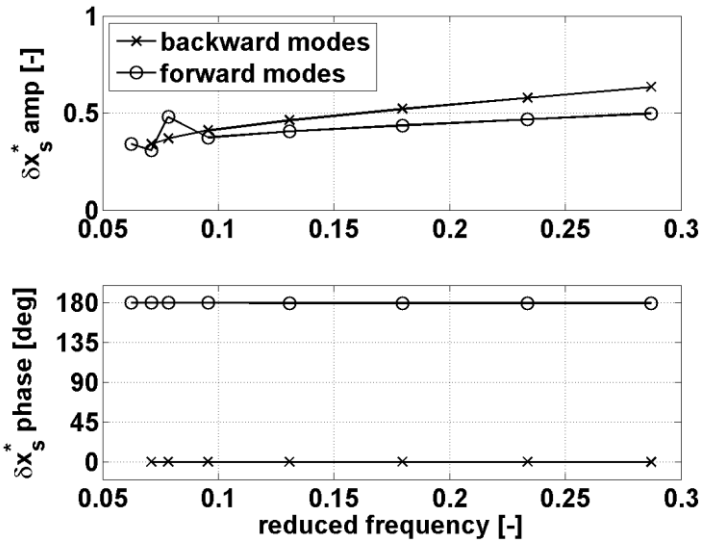

Figure 5-25: Shock wave motion versus reduced frequency

At this point, the focus has been put on the ±3ND. It has been shown that the stability is directly related to the shock motion with respect to the blade motion. The next sub-sections investigate first the unsteady pressure fluctuations and then the cut-on/cut-off modes over the IBPA range.

5.5.3 Effect of the interblade phase angle

It is recalled that all the blades vibrate with the same amplitude, the same frequency and constant phase angle between two adjacent blades. That defines the interblade phase angle (IBPA). Two cases can be described:

- the IBPA is different from zero. This implies a variation of the section of the flow passage. In particular, when the IBPA is equal to 180deg, the variation of the section of the flow passage is maximal.
- the IBPA is equal to zero. This implies a variation of the incidence.

An illustration of the IBPA effects is suggested in Appendix B. In the following, the magnitude and phase for the 0deg IBPA are firstly presented and then completed by the interblade phase angles different from zero.

Zero degree interblade phase angle

The 0 nodal diameter results at midspan is presented in order to highlight the incidence effect on the unsteady response. Figure 5-26 and Figure 5-27 display respectively the stability parameter over the span and the unsteady pressure in terms of amplitude and phase at midspan:

- the blade remains stable along the span with a maximum value at 40% of the channel height. At 50% span, the coefficient is equal to about 18% of the +3ND case. This suggests that the effect of incidence is of lower magnitude than the effect of variation in section.
- the magnitude of the pressure fluctuations exhibits similar feature than the ±3ND, i.e. strong level at the leading edge as well right behind the impingement point.
- the phase is comprised between 0deg and -180deg and exhibits strong variations. Nevertheless it remains negative on the entire blade surface except on the aft suction side. This has been mentioned above and corresponds to the impingement point of the shock generated at the trailing edge of the adjacent blade.

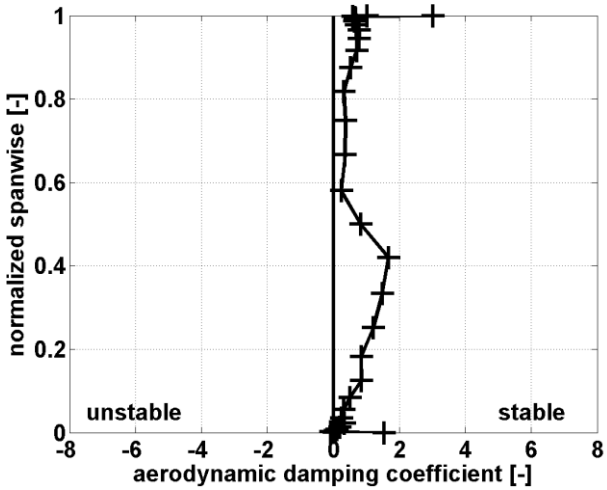

Figure 5-26: Stability parameter, 0ND

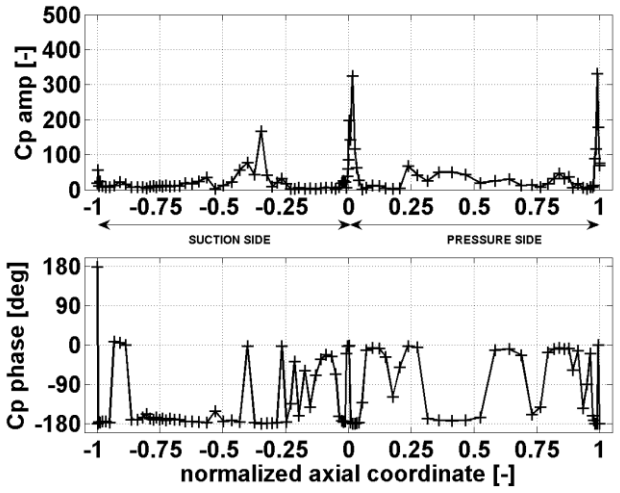

Figure 5-27:Unsteady pressure fluctuations, magnitude and phase, 0ND

Non-zero interblade phase angles

The unsteady pressure fluctuations (magnitude and phase) for the interblade phase angles different from zero are included in Figure 5-28, which shows the following:

- similar behaviors are observed on the magnitude with an increase in amplitude with increasing interblade phase, i.e. with increasing section.
- the phases also show analogous features. On the pressure side, the phases of backward and forward modes remain respectively negative and positive. On the fore suction side where the amplitudes are very low, phases are again wavering, then all phases are consistent within the IBPA range: they remain negative and positive for backward and forward modes respectively with the aforementioned drop on the aft part. In contrast, the +1ND case depicts positive phase on the fore suction side whereas the phases of the other positive nodal diameters are negative.
- these results suggest that the bow shock at the leading edge is unaffected by the change in incidence and remains in phase with respect to the blade motion. Its impingement on the adjacent blade is therefore shifted by the value of the IBPA. This explains the similarity of results with respect to the IBPA.
- the antisymetric behavior of the ±3ND (Figure 5-20) can be explained by the low influence of the zero degree interblade phase angle.

The IBPA effect has been highlighted. It appears that the effect of the change in incidence has a stabilizing effect, whereas the change in section is destabilizing. In the same manner than in the previous chapter, the aerodynamic damping is investigated with respect to cut-on/cut-off modes. This is addressed in the next sub-section.

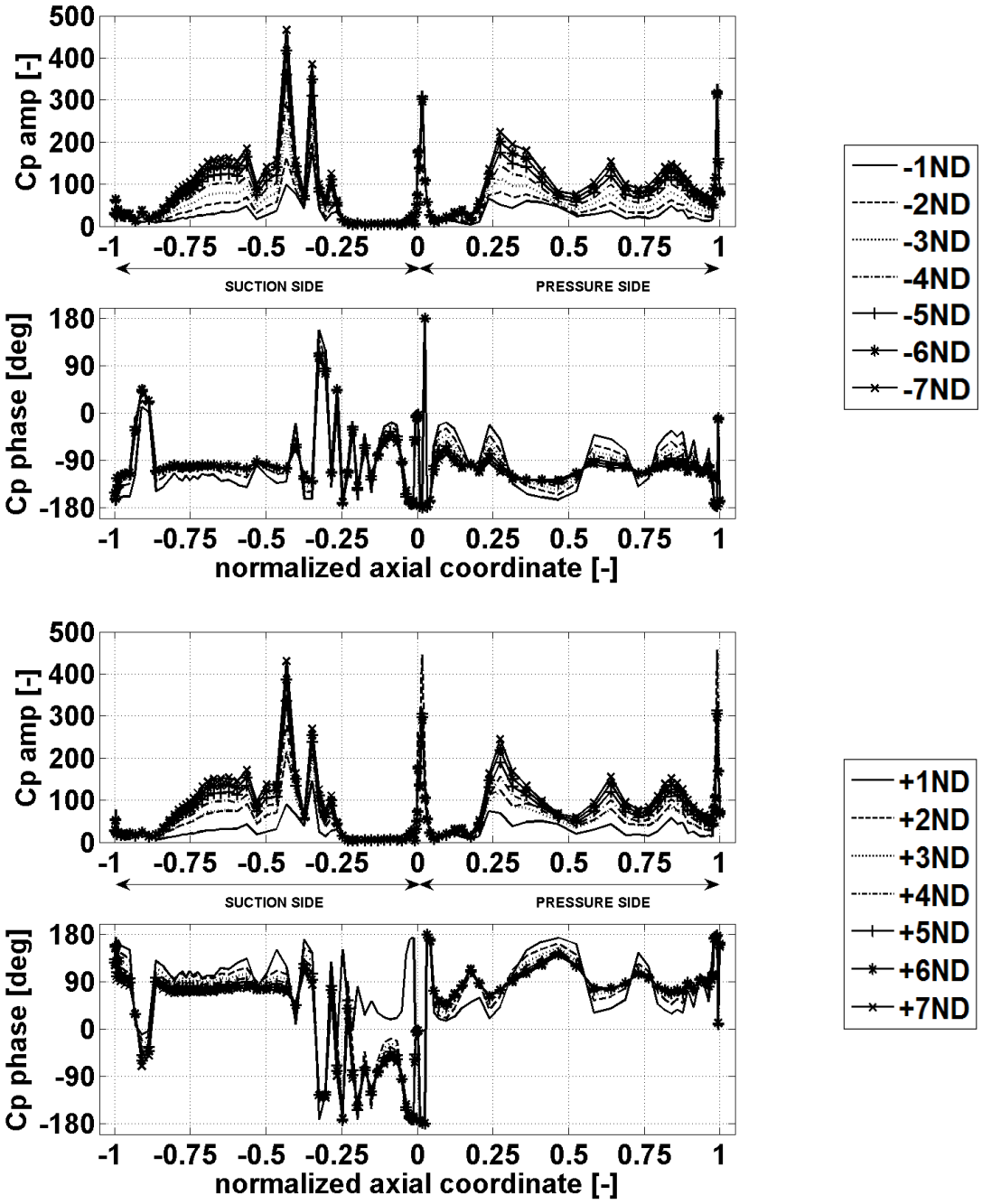

Figure 5-28: Unsteady pressure fluctuations, magnitude and phase, all IBPA

5.5.4 Analysis of cut-on/cut-off modes

In the same manner than the subsonic flutter studied in chapter 4, the nature of waves are evaluated at midspan. The linearized unsteady computations lead to the following results (Table 5-5):

- backward modes propagate with constant amplitude both at the in- and outlet indicating cut-on condition.
- magnitudes of forward modes decay at the inlet and imply therefore cut-off conditions, whereas they remain constant at the outlet. Nevertheless, the +1ND

case gives the same conditions than the backward modes, i.e. cut-on condition at the in- and outlet.

nodal diameter [-]	inlet	outlet
$-7 \leq n \leq -1$	cut-on	cut-on
0	cut-off	cut-on
1	cut-on	cut-on
$+7 \leq n \leq +2$	cut-off	cut-on

Table 5-5: Cut-on/cut-off conditions at midspan

The same conditions have been found at the outlet whatever the nodal diameter, i.e. the waves propagate with constant amplitude. This suggests that the stability is insensitive to the outlet. In contrast, the stability appears to be correlated to the inlet conditions. In particular, the backward modes, which have been predicted unstable, are characterized by cut-on conditions; this observation is in line with previous studies (Ferrand et al., 1995) which showed that cut-on conditions at the inlet lead to critical cases. An explanation of the particular case of +1ND is however still outstanding.

5.6 Conclusion

An isolated rotor blade from an industrial supersonic space turbine has been numerically investigated. The study was based on 3D unsteady computations linearized in the frequency domain. The blade was part of a shrouded assembled bladed disk and connected to the disk through fir tree attachment.

The steady results have shown that the aerodynamic field exhibits strong non-linearities with a detached bow shock at the leading edge resulting in boundary layer separation on the suction side of adjacent blade. The separated region extended from hub top tip but was much larger at midspan. The steady field was rather severe, whereas the blade motion was of elementary nature, i.e. purely axial.

Linearized unsteady computations have been performed over a restricted nodal diameters range (from -7ND to +7ND) and have shown the following:

- the blade motion itself does not generate significant static pressure fluctuations. The results show for instance that only the stripe around the geometric throat gives strong fluctuations.
- the fluctuations are mainly caused in regions where high gradients occur (boundary layer separation).
- the amplitudes of pressure fluctuations increase with increasing IBPA, i.e. with increasing section. However, comparisons between forward and backward modes gives negligible differences.
- the region upstream of the shock has no effect on the stability.
- considerable reorganization of the unsteady flow takes place in regions of shocks that are critical in terms of stability.
- cut-on/cut-off conditions suggest that the waves which propagate upstream without decaying may induce instability, this has been demonstrated in the acoustic blockage theory.

- despite the robust character of the blades, the combination of high pressures and high velocities with a flexible disk leads to flutter. This is believed to be due to a disk dominated effect: the reduced frequency of the blades itself would be much higher and not leading to flutter. However, as the blades sit on a comparatively flexible disk, the reduced frequency comes down and this results to instability.

6 CONCLUSION

6.1 Summary

The present research work was dedicated to the investigation of subsonic and supersonic flutters in turbines. Analyses were conducted experimentally and numerically.

Experimental investigations were performed at the Division of Heat and Power Technology at the Royal Institute of Technology, Sweden. A worldwide unique annular turbine sector cascade was employed. The cascade was non-rotating and consisted of seven low pressure gas turbine profiles one of which could be made oscillating in different rigid-body modes. The aim was to experimentally obtain time-dependent pressures on a vibrating turbine blade at realistic Mach numbers and reduced frequencies. The unsteady pressures were measured on the oscillating blade and its direct neighbors at different span positions using the influence coefficient technique. The following modes were considered:

- pure axial bending
- pure circumferential bending
- pure torsion
- combined axial bending/torsion
- combined circumferential bending/torsion

For each modeshape, a set of different parameters was investigated:

- two outlet Mach numbers from low to high subsonic: 0.4 and 0.8 respectively.
- three inflow incidence angles: nominal and off-designs such as to force the flow to separate.
- four oscillation frequencies yielding to maximum reduced frequencies of 0.4 and 0.2 for the low and high subsonic case respectively.

In addition, hot-wire measurements were carried out upstream of the cascade in order to characterize the turbulence level.

The experimental data will help the basic understanding of aeroelastic response to a prescribed motion in a 3D flow, and will also serve as a database for the validation of numerical design tools. This represents an extensive database of unsteady measurements for many future studies. The main results are summarized below:

- the steady blade loading revealed a suction peak on the fore suction side. The flow is accelerated in this region and this generates high aeroelastic responses on suction sides of blade 0 and -1. This could correspond to the laminar to turbulent transition.
- the major aeroelastic responses appear on the oscillating blade and its direct adjacent surfaces; however, once the torsion is involved in the blade motion, the pressure fluctuations magnitudes are no longer negligible on suction side of blade +1, i.e. facing away the oscillating blade.
- pure axial bending and pure torsion motions involve the largest changes in section at the throat, which are of the same order of magnitude. This results in qualitatively similar features with each other. In particular, pressure and suction sides of the oscillating blade are respectively out-of- and in-phase with respect to the blade motion. This also agrees with the direct adjacent surfaces. Quasi-steady analysis are well adapted to put light on the phenomenon.

- in contrast, pure circumferential bending features differently and quasi-steady analysis are no longer adapted. It is believed to be due to the transition point on the suction side as well as to the relative steady circumferential gradient, in addition of the fact that the motion induces lower change in section at the throat than axial and torsion.
- the major aeroelastic response results from pure axial bending, pure torsion or when one of them is part of a combination. Response at pure circumferential is of lower order of magnitude.
- the lowest reduced frequency involves distinct high response at pure axial and pure torsion. An increase in reduced frequency results in decreasing response at M08. A clear explanation of the phenomenon is however still outstanding.
- the flow velocity strongly affects the oscillating blade and leads to similar feature whatever the modeshape. On blade -1, the phases on aft suction side are highly disturbed whereas the aft part is much less affected.
- separated flow leads to change in phase and considerable response in magnitude. However, steady state is needed for deeper investigations.
- the 3D effects have been highlighted through measurements at different span positions. Pure axial bending mode is the most affected in terms of magnitude and phase.
- the linear superposition principle has led to good agreement and has been confirmed. This will therefore allow decomposing more complex motions into elementary movements.
- out-of-phase combination of pure modes can lead to destabilizing configurations even if the pure modes are stable. Furthermore, the stability of combined modes appear to strongly depend on the nature of the combination in terms of ratio bending-to-torsion amplitude and phase angle between bending and torsion.

Numerical simulations were performed at the "Laboratoire de Mécanique des Fluides et d'Acoustique" at "Ecole Centrale de Lyon", France. The steady states were computed using Turb'Flow™, which solves the 3D compressible RANS equations based on a finite volume formulation. The unsteady computations linearized in the frequency domain were performed using Turb'Lin™ based on linearity principle assuming small amplitude of perturbation. This results in superposition of an unsteady linear field generated by a harmonic perturbation upon a non-linear steady field. The unsteady pressure response to a prescribed motion is computed in the traveling wave mode and then the aerodynamic damping is assessed. Two industrial space turbines were numerically studied and chosen because they reflect the technological progresses in modern engines and make them particularly sensitive to flutter.

First, a low subsonic space turbine was investigated, which consisted of a blisk. The quasi non-existence of viscous damping makes the aerodynamic damping evaluation even more critical. The reduced frequency was high (6.4) and the blade motion consisted of in-phase combined modes originating from the blisk eigenmode. The 2D unsteady responses were computed over a restricted IBPA range. The results that emerge from this study are summarized below:

- the stability margin can be improved and the flutter foreseen by decomposing the blade motion into elementary movements and then determine the most destabilizing contributions.

- the classical bending/torsion flutter, namely the torsion is a potential source of instability, is prone to occur in blisks.
- the stability conditions highly depend on the interblade phase angle as well as the cut-on/cut-off modes that are themselves strongly correlated to the IBPA. Furthermore, the presence of adjacent rows in real engines need to be taken into account because they will modify the cut-on/cut-off conditions.
- the change in section acts destabilizing whereas the change in incidence do not.

Then the focus was put on a supersonic space turbine. The flow featured strong non-linearities such as shock wave/boundary layer interaction and the motion was of elementary nature, i.e. purely axial. The 3D unsteady responses were computed over a restricted nodal diameter range (from -7ND to +7ND) yielding to a maximum reduced frequency of 0.28. The main results are summarized below:

- quasi-steady analysis and linearized computations are still relevant for supersonic flows.
- the blades are aeroelastically unstable and stable for backward and forward modes respectively.
- flutter appears with the change in phase between forward and backward modes.
- the least stable configuration corresponds to cut-on modes both at the in- and outlet.

The blade design process can be improved and designers can act on the structure with specific targets by geometric elementary decompositions. Combined to linearized computations, the 2D methodology provides useful information on stabilizing or/and self-exciting behaviors of the blade relative motion. Indeed the occurrence of classical flutter in blisk was not expected given first the robust character of such a structure and second, the fact that this kind of flutter often appear in external flows with lower stiffness. Moreover, violent changes in propagating waves occur according to the interblade phase angle. The study of the propagating waves to the far field provide essential knowledge on the pressure disturbance while in the near field highly non-uniform features take place. Nevertheless, in real engines, the influence of the adjacent blade rows will lead to different conclusions.

6.2 Future work

The next steps of this investigation are of two natures: experimental and numerical.

From the experimental side,

- in the light of the unsteady responses observed on suction side of blade +1, data on blade +2, especially for the combined modes, will provide more confidence on the fact that it was excluded from the experimental plan. The off-design results suggest as well to complete the database by steady measurements at M04 and M08. Finally hot-wire measurements downstream of the cascade will provide useful information for comparisons with CFD.
- the instrumentation of the oscillating blade over the span will provide a more detailed picture of the 3D effects during flutter. Furthermore, it would be of great interest to evaluate also the principle of linear superposition over the span and especially close to the tip.

- the motion evaluation during blade oscillation suffers from the distorted refracted laser signal due to the Plexiglas windows of test section and from the vibration of the facility itself. Despite its high advantage to be not intrusive, it must be improved.
- The facility is unique because rather close to realistic conditions. However, both high subsonic velocity and high reduced frequency are difficult to reach due to mechanical issues of the actuator mechanism. The reduced frequency can therefore be increased by increasing the oscillation frequency, but also by replacing the profile inside the test section with a larger chord for instance.

From the numerical side,

- all the computations have been performed with the turbulence set to frozen. It is believed that the stability strongly depends on the turbulence especially for separated flows. Therefore, computations with variable turbulence are recommended.
- in the light of the experimental database, linearized unsteady computations are recommended for comparisons as well as non-linear unsteady computations in order to evaluate the non-linearities in the aerodynamic field.
- perform unsteady computations on the supersonic flow to evaluate the linear contribution and the non-linear part.
- in the light of the cut-on/cut-off investigations, it appears essential to include the adjacent blade rows.
- Despite the limitations of CFD capabilities, parametric approaches can help to understand results. Parametric studies enable to assess the trends by drawing stability map and then change for instance frequencies, interblade phase angles, operating conditions.

7 REFERENCES

Armstrong, E. K.; Stevenson, R.E.; 1960
“Some Practical Aspects of Compressor Blade Vibration”
Journal Royal Aeronautical Society, Vol. 64, p.117f

Aubert S.; 1993
"Etude de Schémas à Haute Précision pour la Simulation d'Ecoulements Transsoniques Instationnaires ou Visqueux. Application aux Turbomachines";
PhD thesis, Ecole Centrale de Lyon, Ecully, France

Atassi, H.M.; Fang, J.; Ferrand, P., 1995
“Acoustic blockage effects in unsteady transonic nozzle and cascade flows”
The 7th International Symposium on Unsteady Aerodynamics and Aeroelasticity of Turbomachines, Tanida and Namba editors, Elsevier, pp.777-794

Bendiksen O.O.; Friedmann P.P.; 1980
“Coupled Bending-Torsion Flutter in Cascades”
AIAA Journal, Vol. 18, N°2, pp.194-201

Bendiksen O.O.; Friedmann P.P.; 1982
“The Effect of Bending-Torsion Coupling on Fan and Compressor Blade Flutter”
ASME Journal of Engineering for Gas Turbines and Power, Vol. 104, pp.617-623

Beretta, A.; Rottmeier, F.; Ott, P.; 2005
"Combined/simultaneous gust and oscillating aerodynamics in subsonic flow"
Experimental Thermal and Fluid Science, Vol. 30, 2006, pp.393-401

Bölcs A.; Fransson T.H.; 1986
”Aeroelasticity in Turbomachines – Comparison of Theoretical and Experimental Results”
Technical Report No.13, EPFL, Lausanne, Switzerland

Bron, O.; Fransson T.H.; Ferrand P.; 2003
“Experimental and Numerical Study of Non-linear Interactions in Two Dimensional Transonic Nozzle Flow”
The 10th International Symposium on Unsteady Aerodynamic, Aeroacoustics and Aeroelasticity in Turbomachines, Duke University, Durham, NC, USA

Bron, O.; 2004
“Experimental and Numerical Study of Shock Boundary Layer Interaction in Unsteady Transonic Flow”
Dual PhD thesis, HPT/LMFA, Royal Institute of Technology, Stockholm, Sweden, Ecole Centrale de Lyon, France

Bruun, H.H.; 1995
“Hot-Wire Anemometry Principles and Signal Analysis"
Oxford University Press

Collar, A.; 1946

“The Expanding Domain of Aeroelasticity”
The Royal Aeronautical Society

Comte-Bellot, G.; 1976
"Les Méthodes de Mesure Physique de la Turbulence"
Journal de Physique, Colloque C1, supplément au n°1, Tome 37, Janvier 1997, pp.C1-67

Jørgensen, F.E.; 2002
“Probes for Hot-wire Anemometry"
Dantec

Dantec; 2005
“How to Measure Turbulence with Hot-Wire Anemometers"
Dantec Dynamics

Dowell, E.H.; Clark, R.; Cox, D.; Curtiss, H.C.; Edwards, J.W.; Hall, K.C.; Peters, D. A.; Scanlan, R.; Simiu, E.; Sisto, F.; Strganac, T.W.; 2004
"A Modern Course in Aeroelasticity"
Fourth Revised and Enlarged Edition, Kluwer Academic Publishers, p.275

Fang J.; Atassi H.M.; 1991
”Compressible Flows with Vortical Disturbances Around a Cascade of Loaded Airfoils"
Unsteady Aerodynamics and Aeroelasticity of Turbomachines and Propellers, 6th International Symposium, University of Notre Dame, USA, pp.149-176

Ferrand P.; 1984
”Linearized Theory of the Choked Flow in an Annular Oscillating Cascade”
Unsteady Aerodynamics and Aeroelasticity of Turbomachines and Propellers, 3rd International Symposium, Ed Cambridge University, pp.41-52

Ferrand P.; 1987
”Etude phénoménologique du flottement de blocage sur la base des résultats d'une théorie linéarisée”
Advanced Technology for Aero Gas Turbine Components, AGARD CP 421, paper n°30

Ferrand P.; Atassi H.M.; Aubert S.; 1996
”Unsteady Flow Amplification Produced by Upstream or Downstream Disturbances”
The 85th Symposium on Loss Mechanisms and Unsteady Flows in Turbomachines, AGARD CP 571, paper n°31

Ferrand P.; Aubert S.; Smati L.; Bron O.; Atassi H.M.; 1998
”Nonlinear Interaction of Upstream Propagating Sound with Transonic Flows in a Nozzle”
AIAA paper 98-2213, 4th AIAA/CEAS Aeroacoustics Conference, June 2-4, Toulouse, France

Ferrand P.; 2007
”Ecoulement 3D et Instationnaires en Turbomachine"
Lecture material, Ecole Centrale de Lyon, Ecully, France

Fluorem SAS; 2006

Report SNA0613, Confidential

Fransson, T.H.; 1999
"Aeroelasticity in Axial Flow Turbomachines"
Basic Introduction to Aeroelasticity, Lecture Series 1999-05, Von Karman Institute for Fluid Dynamics, May 3-7

Frey K.K.; Fleeter S.; 1997
"Rotating Blade Row Oscillating Airfoil Aerodynamics"
Unsteady Aerodynamics and Aeroelasticity of Turbomachines, Proceedings of the 8th International Symposium, pp.67-82

George, W.K.; Beuther P.D.; Shabbir A.; 1987
"Polynomial Calibrations for Hot-wire in Thermally-Varying Flows"
The 1987 ASME Applied Mechanics, Bioengineering, and Fluid Engineering Conference, Cincinnati, Ohio, USA

Gerolymos, G.A.; Vallet, I.; 1996
"Implicit Computation of the Three-Dimensional Compressible Navier-Stokes Equations Using k-ε Turbulence Closure"
AIAA Journal, Vol. 34, No. 7, pp.1321-1330

Gerolymos, G.A.; Tsanga, G.; Vallet, I.; 1998
"Near-Wall k-ε Computation of Transonic Turbomachinery Flows with Tip Clearance"
AIAA Journal, Vol. 36, No. 10, pp.1769-1777

Glodic, N.; Bartelt M.; Vogt D.; Fransson T.H.; 2009
"Aeroelastic Properties of Combined Mode Shapes in an Oscillating LPT Cascade"
Proceedings of the 12th International Symposium on Unsteady Aerodynamics, Aeroacoustics & Aeroelasticity of Turbomachines, London, UK

Groth, P.J.; Mårtensson, H.E.; Edin N.; 2008
"Experimental and CFD Based Determination of Flutter Limits in Supersonic Space Turbines"
Proceedings of ASME Turbo Expo 2008: Power for Land, Sea and Air, GT2008-50675, Berlin, Germany

Jameson, A.; Schmidt, W.; Turkel, E.; 1981
"Numerical Solution of the Euler Equations by Finite Volume Using Runge-Kutta Time-Stepping Schemes"
The 14th Fluid and Plasma Dynamics Conference, AIAA 81-1259, Palo Alto, CA, USA

Kerrebrock, J. L.; 1977
"Aircraft Engines and Gas Turbines"
The MIT Press, p.203

Kok, J. C.; 1999
"Resolving the Dependence of Free-Stream Values for the k-omega Turbulence Model"
National Aerospace Laboratory, NLR-TP-99295

Körbächer, H.; 1996
”Experimental Investigation of the Unsteady Flow in an Oscillating Annular Compressor Cascade”
PhD thesis N°1512, Ecole Polytechnique Fédérale de Lausanne, Switzerland

Liou, M. S.; 1996
”A Sequel to AUSM: AUSM+”
Journal of Computational Physics, 129, pp.364-382

Liou, M. S.; 2006
”A Sequel to AUSM, Part II: AUSM+ -up for all speed”
Journal of Computational Physics, 214, pp.137-170

Lomas, C.; 1986
“Fundamentals of Hot-wire Anemometry”
Cambridge University Press

Marshall, J. G.; Imregun, M.; 1996
"A Review of Aeroelasticity Methods with Emphasis on Turbomachinery Applications"
Journal of Fluids and Structures, 10, pp.237-267

Mårtensson, H.; 2006
"Flutter Free Design of Aerodynamically Unstable Supersonic Turbines"
42nd AIAA/ASME/SAE/ASEE Joint Propulsion Conference & Exhibit, 9-12 July 2006, Sacramento, California, USA

Meingast, M.; Kielb, R.E.: Thomas, J.P.; 2009
"Preliminary Flutter Design Method for Supersonic Low Pressure Turbines"
Proceedings of ASME Turbo Expo 2009: Power for Land, Sea and Air, GT2009-59177, Orlando, Florida, USA

Norryd M.; Bölcs A.; 1997
“Experimental Investigation of Unsteady Pressure Behaviors in a Linear Turbine Cascade”
Unsteady Aerodynamics and Aeroelasticity of Turbomachines, Proceedings of the 8th International Symposium, pp.103-116

Nowinski, M.; Panovsky, J.; 2000
"Flutter Mechanisms in Low Pressure Turbine Blades"
Journal of Engineering for Gas Turbine and Power, 122, January 2000, pp.82-88

Olsson, U.; 2006
"Aerospace Propulsion from Insects to Spaceflight"
Computerized Educational Platform, Heat and Power Technology, Lecture Series Volume No.3

Pacull F.; 2007
”Cut-on/cut-off modes analysis"
Internal report, Fluorem

Panovsky J.; Kielb R.E.; 2000

”A Design Method to Prevent Low Pressure Turbine Blade Flutter”
Journal of Engineering for Gas Turbines and Power, Vol. 122, p.89

Platzer M.; 1990
”Aeroelasticity: Lecture Notes"
EPFL, Lausanne, Switzerland

Smati L.; 1997
"Contribution au Développement d'une Méthode Numérique d'Analyse des Ecoulements Instationnaires. Applications aux Turbomachines"
PhD thesis, Ecole Centrale de Lyon, Ecully, France

Soulat, L.; 2010
“Définition, Analyse et Optimisation Aérodynamique d'un Nouveau Concept de Traitement de Carter au Moyen d'Outils Numériques. Application aux Turbomachines Basse Vitesse”
PhD thesis, Ecole Centrale de Lyon, Ecully, France

Srinivasan, A.; 1997
“Flutter and Resonant Vibration Characteristics of Engine Blades”
ASME Journal of Engineering for Gas Turbine and Power, pp.119:742-775

Tavoularis, S.; 1986
"Techniques for Turbulence Measurement"
in Encyclopedia of fluid mechanics, Volume 1 (A86-33401 14-34), Houston, TX, Gulf Publishing Co., pp.1207-1255

Tchernycheva O.V.; Fransson T.H.; Kielb R.E. and Barter J.; 2001
“Comparative Analysis of Blade Mode Shape Influence on Flutter of Two-Dimensional Turbine Blades”
ISABE-2001-1243, XV ISOABE conference, Bangalore, India

Tijdeman, H.; 1977
"Investigations of the Transonic Flow Around Oscillating Airfoils"
National Aerospace Laboratory, NLR TR 77090 U, Amsterdam, The Netherlands

TSI; 2000
“IFA 300 Constant Temperature Anemometer System - Instruction Manual"
TSI

TurbLin™; 2009
“User Manual of Turb'Lin™ Version 1.6.3"
Fluorem

Verdon, J. M.; 1987
”Linearized Unsteady Aerodynamic Theory”
AGARD Manual on Aeroelasticity in Axial Flow Turbomachines, Volume 1, Unsteady Turbomachinery Aerodynamics, No. 298, pp.2-1–2-30

Vogt, D. M.; Fransson, T. H.; 2000

“Aerodynamic Influence Coefficients on an Oscillating Turbine Blade in Three-Dimensional High Speed Flow”
The 15th Symposium on Measuring Techniques in Transonic and Supersonic Flows in Cascades and Turbomachines, Florence, Italy

Vogt, D. M.; Fransson, T. H.; 2004
“Effect of Blade Mode Shape on the Aeroelastic Stability of a LPT Cascade”
The 9th National Turbine Engine High Cycle Fatigue (HCF) conference, March 16-19, Pinehurst, North California, USA

Vogt, D. M.; Fransson, T. H.; 2004
“A technique for using recessed-mounted pressure transducers to measure unsteady pressure”
The 17th Symposium on Measuring Techniques in Transonic and Supersonic Flows in Cascades and Turbomachines, Stockholm, Sweden

Vogt, D.; 2005
”Experimental Investigation of Three-Dimensional Mechanisms in Low-Pressure Turbine Flutter”
PhD thesis, Royal Institute of Technology, Department of Heat and Power Technology, Stockholm, Sweden

Vogt D.M.. Fransson T.H.; 2007
”Experimental Investigation of Mode Shape Sensitivity of an Oscillating Low-Pressure Turbine Cascade at Design and Off-Design Conditions”
ASME Journal of Engineering for Gas Turbine and Power, Vol. 129, pp.530-541

Waterson N.P.; Deconinck H.; 2007
”Design Principles for Bounded Higher-Order Convection Schemes - a Unified Approach”
Journal of Computational Physics,224, pp.182-207

Wilcox, D.C.; 1993
”Turbulence Modeling for CFD”
DCW Industries, La Cañada, CA, USA

A DETERMINATION OF FLUTTER STABILITY

In the present context, the term "flutter stability" denotes the stabilizing character of the flow rather than the stability of the entire fluid-structure system. On the other hand, the traveling wave formulation implies that all the blades of the row are oscillating at the same frequency, at constant amplitude and constant interblade phase angle.

The parameter commonly used for blade flutter stability is the aerodynamic work per oscillation cycle (Verdon, 1987), W_{cycle}, which represents the work done by the fluid on a given blade over one period of its motion.

$$W_{cycle} = \oint \frac{dW}{dt} dt \qquad \text{Eq. A-1}$$

where

$$\frac{dW}{dt} = - \oint_{Surface} \tilde{p} \cdot \tilde{\vec{V}} \cdot \vec{n} \cdot ds \qquad \text{Eq. A-2}$$

is the rate at which this work is done.

Furthermore, assuming that the blade is oscillating in traveling wave mode without deformation, the harmonic motion of the blade can be described by a complex vector consisting of three orthogonal components as follows,

$$\left\{\tilde{\vec{h}}\right\} = \begin{Bmatrix} \hat{h}_x \\ \hat{h}_y \\ \hat{h}_z \end{Bmatrix} \qquad \text{Eq. A-3}$$

whose the components represent the axial bending, the circumferential bending and the torsion modes respectively.

Moreover, assuming small perturbations, the unsteady pressure due to the harmonic blade motion can be represented as a harmonic oscillation as well,

$$p(X,t) = \bar{p}(X) + \tilde{p}(X,t) = \bar{p}(X) + \hat{p}e^{i(\omega t + \varphi_{p \to h})} \qquad \text{Eq. A-4}$$

- $\bar{p}(X)$ is the steady mean pressure
- $\tilde{p}(X,t)$ is time-varying perturbation
- $\hat{p}$ is the complex pressure perturbation amplitude of the harmonic oscillation
- $\varphi_{p \to h}$ is the phase angle of response with respect to excitation, i.e. the blade motion. The phase angle is per definition positive if the response is leading the excitation.

A common way to present the unsteady results is to normalize the unsteady pressure amplitude by a reference dynamic head and the amplitude of the blade motion. This provides a complex unsteady pressure coefficient,

$$\hat{C}_p = \frac{\hat{p}}{A \cdot p_{dyn}} \qquad \text{Eq. A-5}$$

The reference dynamic head is defined as the difference between the total pressure $p_{t,ref}$ and the static pressure $p_{s,ref}$, taken upstream of the blade row.

In the same way, a normalized force is defined as follows,

$$\hat{\vec{f}} = \frac{\hat{\vec{F}}}{A \cdot p_{dyn}} \qquad \text{Eq. A-6}$$

$\hat{\vec{F}}$ is the unsteady aerodynamic force which is also of harmonic nature. The force results from integration around the blade surface,

$$\hat{\vec{f}} = \oint_S d\hat{\vec{f}}\, ds = \int_S \begin{Bmatrix} d\hat{f}_x \\ d\hat{f}_y \\ d\hat{f}_z \end{Bmatrix} ds \qquad \text{Eq. A-7}$$

The work per oscillation cycle can therefore be expressed as the product of the force and the motion,

$$W_{cycle} = \int_T \tilde{\vec{F}} \cdot \tilde{\vec{h}} \cdot dt = \int_T \hat{\vec{F}} \cdot \hat{\vec{h}} \cdot e^{i\omega t} dt \qquad \text{Eq. A-8}$$

where $\hat{\vec{h}}$ represents the complex motion of the blade. After integration, Eq. A-8 writes as follows,

$$W_{cycle} = \pi \left[|h_x| \cdot |f_x| \cdot \sin \varphi_{f_x \to h_x} + |h_y| \cdot |f_y| \cdot \sin \varphi_{f_y \to h_y} + |h_z| \cdot |f_z| \cdot \sin \varphi_{f_z \to h_z} \right] \qquad \text{Eq. A-9}$$

The aerodynamic work depends only on the value of the phase-related terms, i.e. the imaginary parts of the perturbation force. As a result, this means that if the response is lagging the excitation, i.e. the imaginary part is negative, the flow has a stabilizing effect.

W_{cycle} denotes therefore the energy that is transferred either from the fluid to the blade, i.e. positive work, or from the blade to the fluid, i.e. negative work. Using the nomenclature introduced by Verdon (1987), a normalized stability parameter is introduced. This is based on the negated work per oscillation cycle and is made dimensionless with the oscillation amplitude and the constant number π.

$$\Xi = \frac{-W_{cycle}}{\pi h}\bigg|_x + \frac{-W_{cycle}}{\pi h}\bigg|_y + \frac{-W_{cycle}}{\pi h}\bigg|_z \qquad \text{Eq. A-10}$$

B INTERBLADE PHASE ANGLE

The blades being all coupled to the disk, each blade experience the same motion resulting from the disk. All the blades vibrate with the same amplitude, the same frequency and constant phase angle between two adjacent blades. That defines the InterBlade Phase Angle (IBPA), noted σ, which represents the phase lag between the blades within a row oscillating in traveling wave mode. Because of the blade row periodicity in terms of time and space, the IBPA cannot be random; it is equal to a part of the total number of blades N. There are as many IBPA as blades and can thus take discrete values. For each nodal diameter forwards traveling waves (Eq. B-1) and backwards traveling waves (Eq. B-2) are defined as follows

$$\sigma = 2\pi \frac{n}{N} \qquad \text{Eq. B-1}$$

$$\sigma = 2\pi \frac{(N-n)}{N} \qquad \text{Eq. B-2}$$

n refers to the nodal diameter ($n = 0..N$).

For $n = 0$, the IBPA is equal to 0deg, i.e. all the blades are in-phase. Using this particular case, Kerrebrock (1977) suggests, assuming the flow as incompressible, that flutter in cascade can be considered as the superposition of two contributions:

- the first one can be related to the effect of an isolated blade. The blade oscillation generates a velocity $\delta\vec{V}$, which is small compared to the velocity of the steady flow $\vec{V}$. The superposition of these two velocities, $\vec{V} + \delta\vec{V}$, creates small variations of the incidence and thus a change in forces applied on the blade. When the IBPA is equal to 0deg, all the channels between each blade are identical and this case can therefore be represented by an isolated blade (Figure B-1).

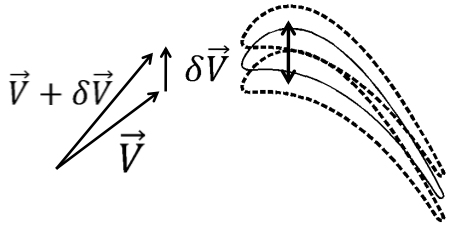

isolated blade → change in incidence
(↔ IBPA = 0deg)

Figure B-1: Schematic representation of the interblade phase angle effects

- the second contribution can be related to the variation of the section of the flow passage. When the IBPA is not equal to zero, a second effect appears due to the difference of the channels between each blade in terms of flow passage. This implies a change in axial flow velocity, i.e. a change in mass flow. Consider three blades that are part of a row represented in Figure B-2(a). They are referenced "0", "-1" and "+1" for the reference blade and its direct neighbours respectively. Each

blade vibrates in the same mode, amplitude and frequency but at a certain phase lag (180deg) between two adjacent blades (Figure B-2(b)). The main consequence is the following: in addition of the variation of the incidence involved by the oscillation of a single blade (typically when the IBPA is equal to 0deg), it arises a variation of the section of the flow passage as illustrated in Figure B-2(c). The blades +1 and -1 are in their high position whereas the blade 0 is in its low position. As a result the section comprised between the blades 0 and +1 increases ($\delta S>0$) whereas the section comprised between the blades -1 and 0 decreases ($\delta S<0$).

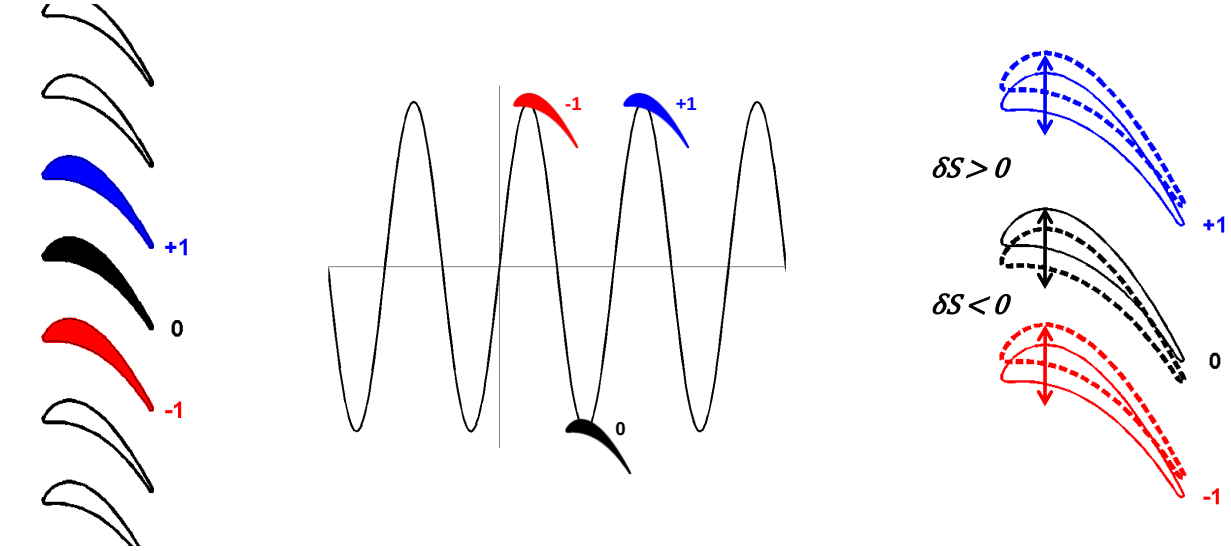

(a) blade row (b) 180deg phase lag (c) variation of the passage section

Figure B-2: Schematic representation of 180deg IBPA

C INFLUENCE COEFFICIENT TECHNIQUE

Contrary to the traveling wave formulation, the so-called influence coefficient technique assumes that every single blade of the row is oscillating separately. The total unsteady pressure on a blade consists therefore of the individual response from itself and from the other blades which are lagged by respective phase angle. This assumes small perturbations such that the influences of the various blades superimpose linearly. The unsteady response expressed in terms of aerodynamic influence coefficients can thus be related to the traveling wave formulation as follows,

$$\hat{C}_{p,twm}^{m,\sigma}(X,t) = \sum_{n=-\frac{N}{2}}^{n=+\frac{N}{2}} \hat{C}_{p,infc}^{n,m}(X,t) \cdot e^{-i\sigma n} \qquad \text{Eq. C-1}$$

where

- $\hat{C}_{p,twm}^{m,\sigma}$ is the complex unsteady pressure coefficient acting on blade m with the cascade oscillating in the traveling wave mode with interblade phase angle σ.

- $\hat{C}_{p,infc}^{n,m}$ is the complex unsteady pressure coefficient of the vibrating blade n acting on the non-oscillating reference blade m.

- σ is the interblade phase, in the traveling wave mode, between the blade n and the reference blade m.

The analyze of Eq. C-1 suggests the following and is illustrated in Figure C-1 below:

- the influence of the reference blade 0 on stability is of constant nature.

- the direct neighbors, i.e. blades ±1, give a harmonically varying contribution, which can be interpreted as first harmonic oscillation in interblade phase angle.

- the further blade pairs, i.e. indices ±2 and so on, contribute their respective higher harmonic variation.

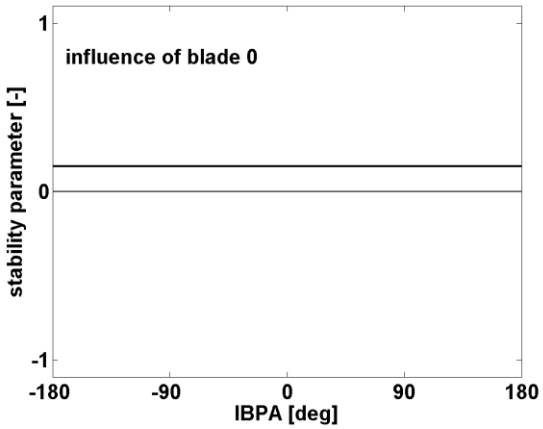

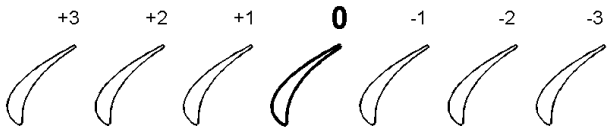

average offset represents blade's influence on itself (blade 0)

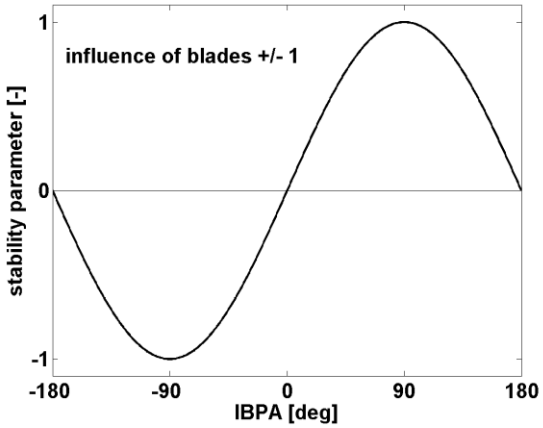

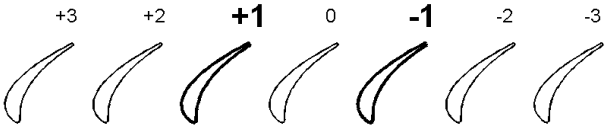

first harmonic represents neighboring blades influence (blades ±1)

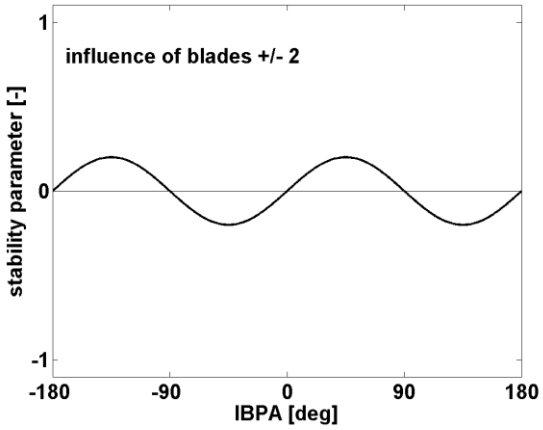

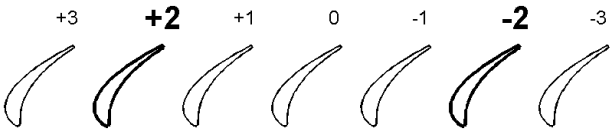

second harmonic represents influence of blades two stations away (blades ±2)

Figure C-1: Schematic influence of blade pairs on blade row aeroelastic stability

D NUMERICAL MODEL

This appendix gives a short description of the numerical tools used to compute the steady and unsteady states. More details can be found in (Aubert, 1993), (Smati, 1997), (Bron, 2004) and (Soulat, 2010).

The motion of a compressible viscous Newtonian fluid is governed by the Navier-Stokes equations, which come from the fundamental principle of mechanics and thermodynamics. Those equations are determined from the conservation laws for mass, momemtum, and energy and the thermodynamic relation for a perfect gas. The instantaneous Navier-Stokes equations are written in a conservative form and statistically averaged to account for turbulence effect. The turbulent compressible flow is thus modelled by a partial differential equations system, which is numerically resolved. The system is replaced by an algebraic equations system for variables calculated only at a finite number of discrete positions in time and space. The next sub-sections describe therefore the spatial and time discretizations as well as the turbulence model used for steady computations. Then the linearized unsteady computations are introduced.

D.1 Spatial discretization

The spatial discretization is based on a finite volume formulation with vertex storage on structured mesh. The convective terms are evaluated using an upwind flux vector splitting scheme coupled to a MUSCL approach, whereas the viscous and turbulent terms are computed using a second order finite difference scheme. The hyperbolic nature of the viscous terms involves a system of waves, with specific propagations in terms of directions and velocities. The numerical computation of these terms is more accurate and more physical with upwind schemes. This kind of scheme allows a good capture of discontinuities and has an artificial intrinsic dissipation. Two types of schemes are commonly considered: those based on flux splitting and those based on the resolution of the Riemann problem. The former have the advantage of being simpler and more effective, but they are known to be less accurate.

The AUSM+ (Advection Upstream Splitting Scheme) scheme from Liou (1996, 2006) has been employed in this study. The idea is based on taking into account the specificity of the velocity (pure convection) and pressure (acoustic wave propagation). The convective flux is indeed separated into two contributions related to either the velocity or pressure. Furthermore, Liou scheme is not very diffusive both through shock waves and in low speed regions. For the second order computations, the spatial scheme is coupled to a non-linear function called limiter. The limiter allows automatic detection of discontinuities of the solution and prevents parasitical numerical oscillations by reducing the spatial accuracy to first order. There are many limiters in the literature and the choice is not easy because it determines the treatment of discontinuities and the quality of the results. If the limiter is too sensitive, many regions will be calculated with first order accuracy resulting in excessive numerical dissipation. In contrast, if the limiter is too insensitive, parasitical oscillations will emerge from the discontinuities. In this study, the limiter SMARTER (Waterson and Deconinck, 2007) has been adopted, it is a relatively diffusive limiter and therefore sensitive to discontinuities.

A note shall be made on the numerical parameters of the study of the industrial subsonic space turbine, i.e. the blisk (chapter 1). The spatial scheme used was the upwind Roe scheme, which is well adapted for high Mach number or transonic flows. Roe scheme is usually associated to a Flux Difference Splitting method in which the fluxes are separated into an upstream and downstream propagating parts (in opposition to a Variable Difference Splitting). Roe scheme solves a Riemann problem at the interface between two cells of the discretized domain by approaching the solution only. Roe schemes are robust and accurate especially for flows with shock waves, but they can produce non-physical solutions.

D.2 Time discretization

The time integration consists in calculating the solution $q^{(n+1)}$ at the next time step $(n+1)$, from the solution q at one or several previous time steps $q^{(n)}$, $q^{(n-1)}$, $q^{(n-2)}$, ... From a numerical point of view, there exists two main types of time discretization scheme:

- implicit schemes: the solution on one node at the time step $(n+1)$ depends on the entire flow field creating a spatial dependency. This type of scheme allows large time step and necessitates the resolution of a complex linear system, extremely consuming in CPU and memory resources. Usually, matrix conditioning are used to simplify the resolution of the system.

- explicit schemes: the solution at the next time step $(n+1)$ is calculated from solutions at previous time steps only. The resolution of the system is simpler, straightforward and does not require a large amount of CPU and memory resources. The main drawback is the need to use small time step to keep the system numerically stable.

In the present work, expect for the industrial subsonic space turbine, i.e. the blisk (chapter 1), explicit time marching methods have been employed. One of those, the Runge-Kutta scheme has the advantage to be a second order precision technique for a simple and straightforward application. The method consists on the evaluation of p intermediate solutions between the current (n) and next $(n+1)$ time step. Each intermediate time step correction is calculated from the previous one. In the present work, a five time steps Runge-Kutta scheme has been used. As any explicit time marching technique, the Runge-Kutta scheme obeys the CFL (Courant, Friedrichs, Levy) condition.

$$CFL = (U + c)\frac{\Delta t}{\Delta x} \leq 1 \qquad \text{Eq. D-1}$$

Basically, this stipulates that the numerical propagation of information ($\frac{\Delta x}{\Delta t}$) cannot be faster than the physical propagation $(U + c)$. U represents a characteristic velocity scale, c corresponds to the speed of sound and Δx is a characteristic length scale (typically the mesh size). The time step Δt between each time marching iteration is then calculated based on the CFL value and the local velocity and length scales.

D.3 Turbulence modeling

Statistical methods are commonly applied to the governing equations in order to take into account the natural turbulence of the flow. The equations are then linearized revealing double correlation terms and leading to an unclosed mathematical system. In the present study a two equations turbulent model $k-\omega$ has been employed. This consists of solving the transport equations for the turbulent kinetic energy and the specific dissipation, which represent respectively velocity (fluctuations) and time (decay of large structures) scales.

The main advantages of such model are:

- a simplified numerical computation in near wall regions because it requires less nodes and it does not need damping functions.
- a better prediction of separated flows.

The disadvantages of such model are:

- a delicate numerical treatment of the theoretical infinite value of ω on the wall.
- a high sensitivity of the free stream values.

There are two $k-\omega$ turbulence models available in Turb'Flow™:

- Wilcox $k-\omega$ (Wilcox, 1993)
- Kok Turbulent/Non-Turbulent (TNT) $k-\omega$ (Kok, 1999)

The first model is known to be dependent of the free-stream values of the turbulence variables. The second one provides a different set of calibration coefficients in order to resolve this free-stream dependency and has been employed in the computations.

D.4 Linearized unsteady computations

D.4.1 Principle

A steady aerodynamic field is first computed with Turb'Flow™ and represents the reference field. This reference field is then used for the unsteady computations, which are linearized in the frequency domain. The aerodynamic response to a prescribed blade motion is finally calculated with Turb'Lin™, which computes the complex magnitude of the harmonic fluctuations of the conservative variables by solving a linear system of the form (Turb'Lin™, 2009),

$$AX = B \qquad \text{Eq. D-2}$$

where,

- A is a matrix assumed invertible.
- B is a vector.
- X is the unknown vector.

D.4.2 Linear system resolution

The resolution can be summarized into the following steps:

1. set a initial value X^0.
2. solve $A\Delta X = B - AX^n$.
3. compute $X^{n+1} = X^n + \Delta X$.
4. do steps 2 and 3 until convergence, i.e. $\Delta X \to 0$ when $X^n \to X$, solution of $AX = B$.

The linear system in step 2 is solved using an external linear solver with Krylov methods. Krylov methods refer to algorithms that are based on Krylov subspace to converge by successive approximations towards the solution of the linear system from a initial estimation (step 1). GMRES method is one of the major iterative methods for numerically solving large and sparse nonsymmetric problems (it is not limited to positive symmetric matrices only). The convergence of Krylov subspace methods depends on a large degree on the distribution of eigenvalues. There exists different approaches and below those used in the current work are briefly described, more details can be found in (Soulat, 2010):

- Deflated GMRES is an improvement of the restarted GMRES methods by deflating eigenvalues for matrices that have a few small eigenvalues. The restarted GMRES methods suffer from the fact that the information of some eigenvectors composing the approximation disappears and because of this restart a good approximate solution cannot be obtained. In deflation algorithms, there exists two approaches. The first method consists in adding the desired eigenvectors directly to the Krylov subspace, whereas the second method suggests to explicitly deflate the eigenvectors from the matrix with a preconditioner.
- BiCGStab is a biconjugate gradient method for which the matrix A does not need to be symmetric.

D.4.3 Spatial scheme

The Jameson-Schmidt-Turkel JST scheme (Jameson et al., 1981) has been used for the linearized unsteady computations. This is a cell-centered finite volume scheme and contrary to upwind schemes, it does not privilege particular directions. However it is naturally non-dissipative: this gives good accuracy but this makes the scheme naturally unstable. The JST scheme can generate numerical oscillations with alternate signs that may be initiated by discontinuities such as shock waves. An additional artificial dissipation is therefore added in order to avoid divergence. The main difference with upwind schemes is in that case it is possible to control the magnitude and the order of the dissipation. Furthermore, in order to prevent oscillations in areas of high gradients, pressure sensors are added.

D.4.4 Turbulence modeling

Two approaches are possible, either the turbulence is variable or frozen. This results in two different configurations. When the turbulence is set to variable, the turbulence model is derived and this implies that the turbulence reacts quasi-steadily to the excitation generated by the blade vibration. This means that the frequency associated to the turbulence is higher than the one associated to the excitation. In contrast, if the excitation frequency is higher than the turbulence frequency, the turbulence will not react and will remain, i.e. frozen, in its steady state. The choice depends obviously on the flow, on CPU time, and memory resources. All the unsteady computations have been performed with frozen turbulence due to computer considerations. No comparisons with variable turbulence have been carried out.

D.5 Parallelization

Parallel computations have been employed. This technique leads to a consequent decrease in memory load per processor, and most important, to reasonable computing times. This is indeed a requirement considering the huge need of an unsteady turbulent

3D Navier-Stokes simulation on a fine mesh. Moreover, the use of a structured mesh makes the parallel architecture of the code optimal. The mesh is then divided into several sub-domains that are individually mastered by a single process on its respective processor. Each process thereafter manages its respective sub-domain and communicate with its surrounding neighbors to exchange information on their collocative boundaries.

E STEADY COMPUTATIONS OF THE EXPERIMENTAL SETUP

Steady computations of the experimental annular cascade have been performed at nominal incidence angle and prior the measurements. The operating point and the numerical parameters are described in the sections below.

E.1 Operating conditions

The operating conditions are summarized in Table E-1.

PARAMETER	SYMBOL	M04		M08		UNIT
		inlet	*outlet*	*inlet*	*outlet*	
mass flow	$\dot{m}$	1.97	1.97	4.05	4.05	[kg/s]
total temperature	T_t	303	303	303	303	[K]
static temperature	T_s	300.57	293.60	296.84	267.08	[K]
total pressure	P_t	120.0	120.0	160.0	160.0	[kPa]
static pressure	P_s	11664	107474	148.903	102.880	[kPa]
density	ρ	1.352	1.275	1.748	1.342	[kg/m^3]
Mach number	M	0.2	0.4	0.32	0.82	[-]
flow angle	α	-26	61	-26	61	[deg]
velocity	V	69.88	137.39	111.24	268.62	[m/s]
axial component of velocity	V_x	62.81	66.61	99.98	130.23	[m/s]
radial component of velocity	V_r	0	0	0	0	[m/s]
circumferential component of velocity	V_θ	-30.64	120.16	-48.76	234.94	[m/s]

Table E-1: Operating conditions for numerical simulations

E.2 Computation grid

One blade sector is meshed with a periodic multi-blocks structured grid (Figure E-1 and Figure E-2). An O-grid is geometrically extruded from the blade profile, starting from a first cell size of 4µm. H-grids are added up- and downstream of the blade on about 2 axial chords. The tip clearance is also included (118929 nodes). The grid counts 882214 nodes in total.

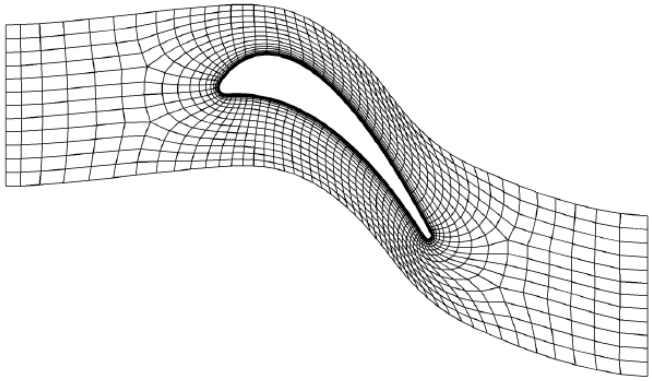

Figure E-1: Computation grid at midspan (1 every 2 points)

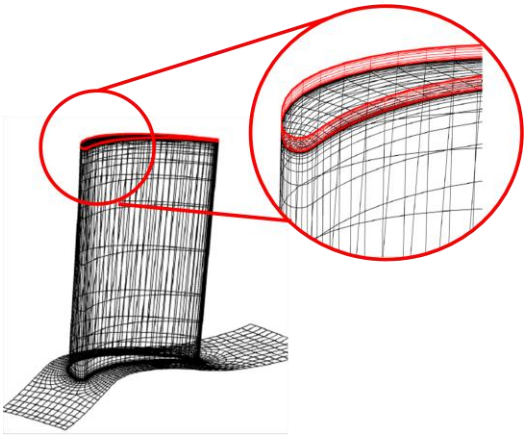

Figure E-2: Computation grid with tip clearance (1 every 2 points)

E.3 Numerical parameters

The aerodynamic field is initialized using a boundary layer thickness of 5% of the channel height both at the hub and the casing. At the inlet, four conditions are imposed: the total pressure, the total temperature, the tangent of the inlet angle and no radial velocity is assumed; moreover, the turbulent kinetic energy k and the turbulent dissipation ω are also imposed. At the outlet, a pressure gradient profile is imposed.

The numerical computation of the Navier-Stokes equations by the solver Turb'Flow is based on a finite volume formulation on structured grid in which convective terms are evaluated using a separation flow technique, whereas a centered scheme is used to calculate the viscous and turbulent terms. The spatial and time discretizations are described in Appendix D. The $k-\omega$ turbulence was used.

F EFFECT OF REDUCED FREQUENCY

The present appendix focuses on the effect of the reduced frequency on the aeroelastic response on blade 0 and blades ±1 in terms of magnitude and phase of the unsteady pressure coefficient. Four reduced frequencies are investigated: 0.05, 0.1, 0.15 and 0.2. The appendix gathers experimental unsteady results for the outlet Mach number 0.8 (M08), the nominal incidence (nom) and the five modeshapes: pure axial bending, pure torsion, pure circumferential bending, combined axial/torsion and combined circumferential/torsion.

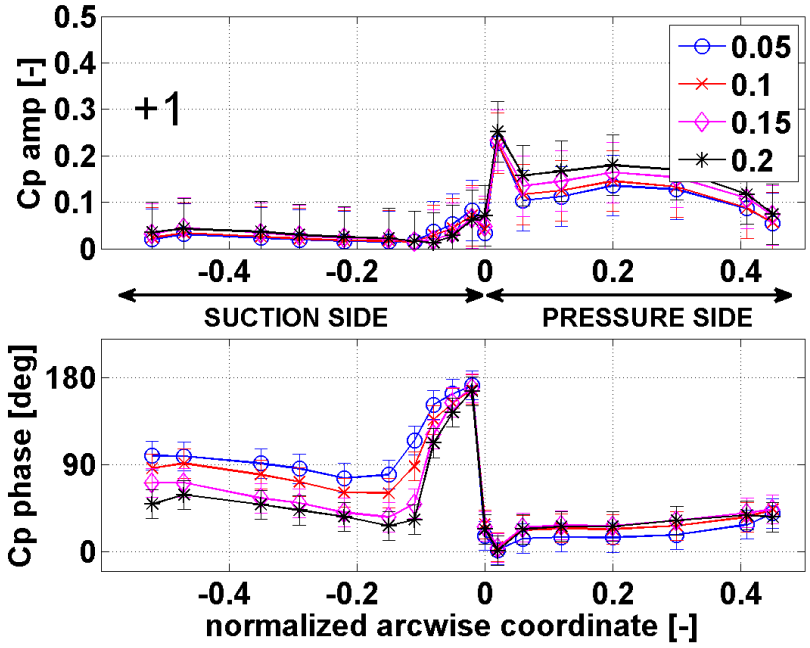

M08, nominal, pure axial bending

blade +1

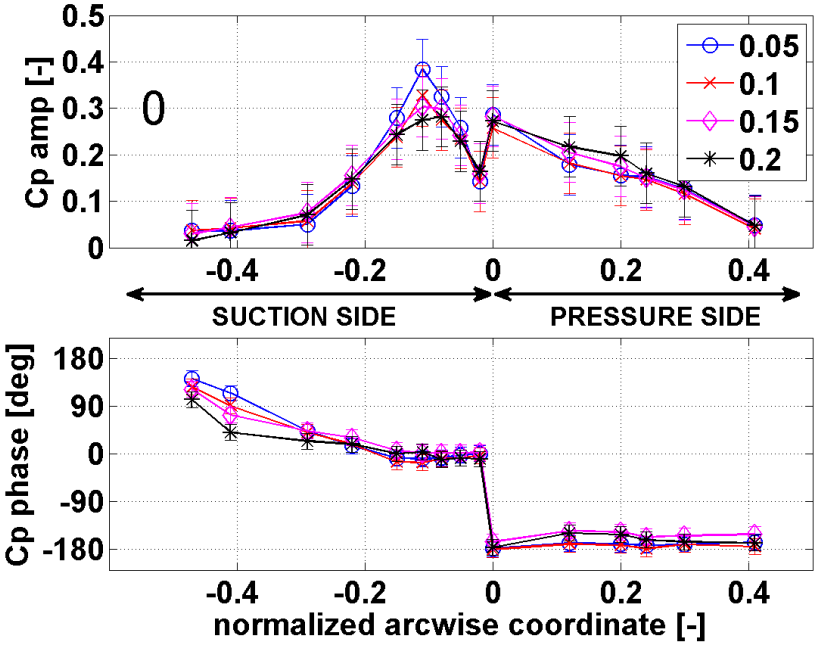

M08, nominal, pure axial bending

blade 0

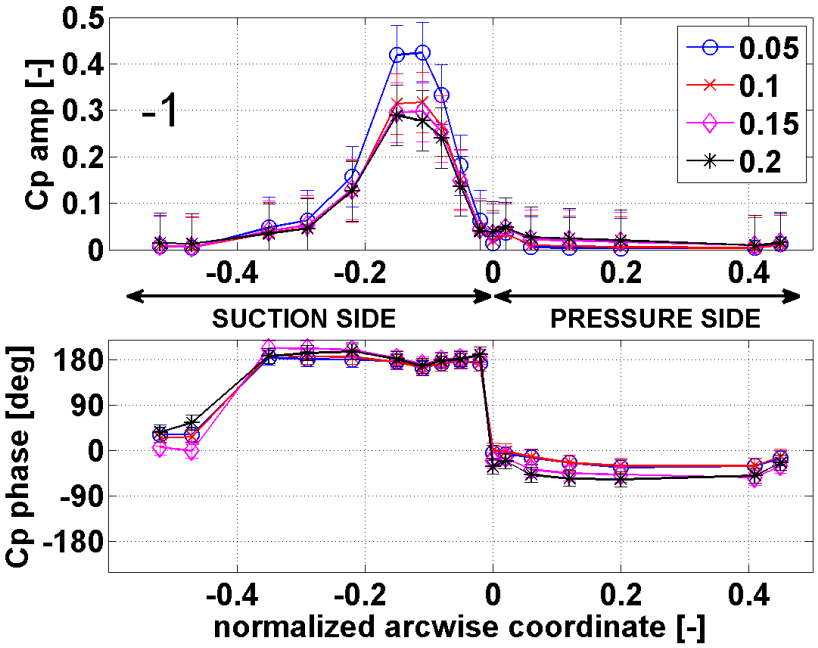

**M08,
nominal,
pure axial bending**

blade -1

Figure F-1: Effect of reduced frequency, M08, nom, pure axial bending

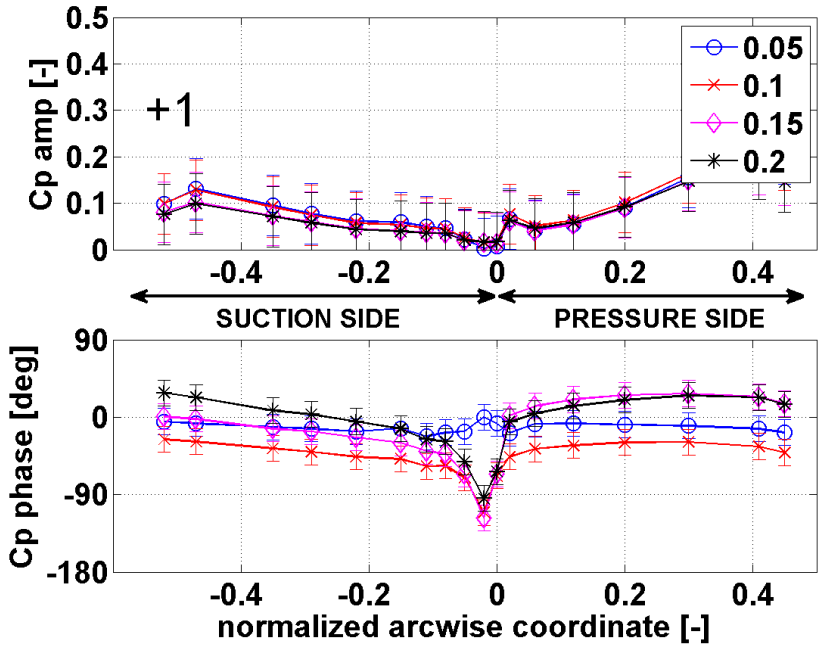

M08, nominal, pure torsion

blade +1

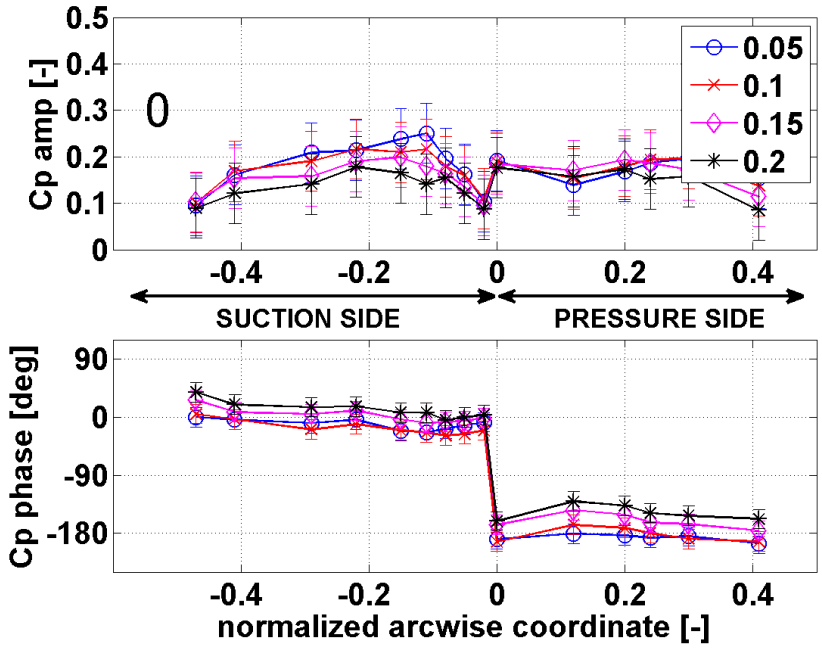

M08, nominal, pure torsion

blade 0

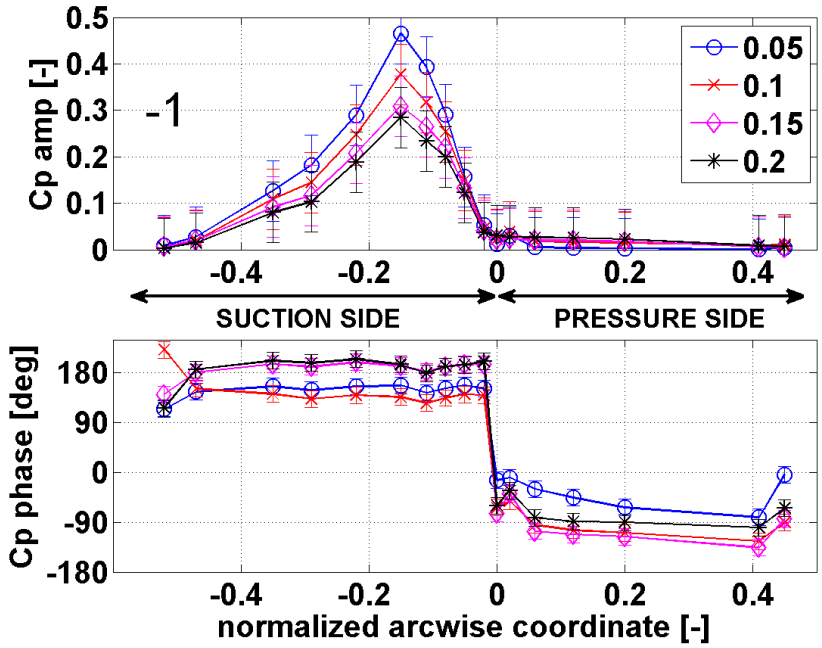

Figure F-2: Effect of reduced frequency, M08, nom, pure torsion

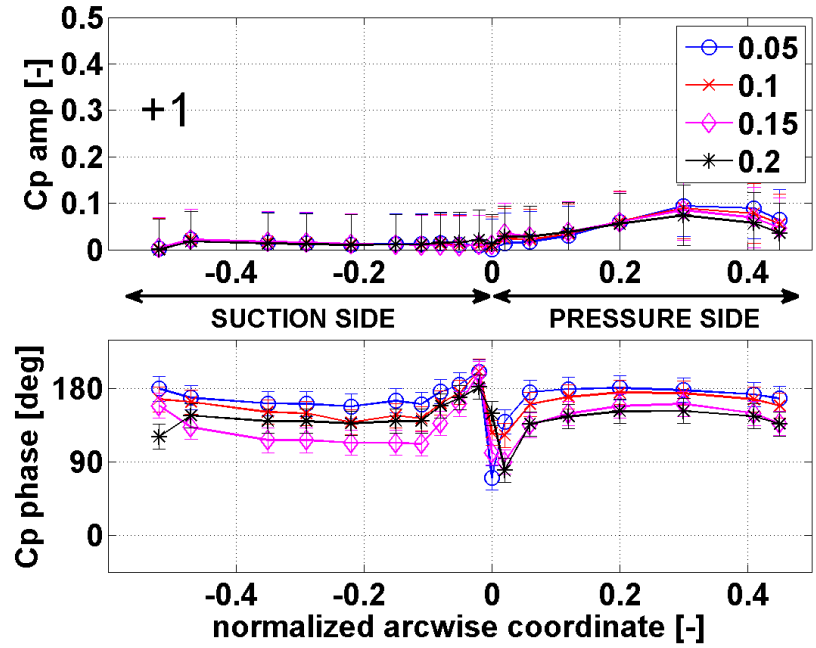

**M08,
nominal,
pure circumferential
bending**

blade +1

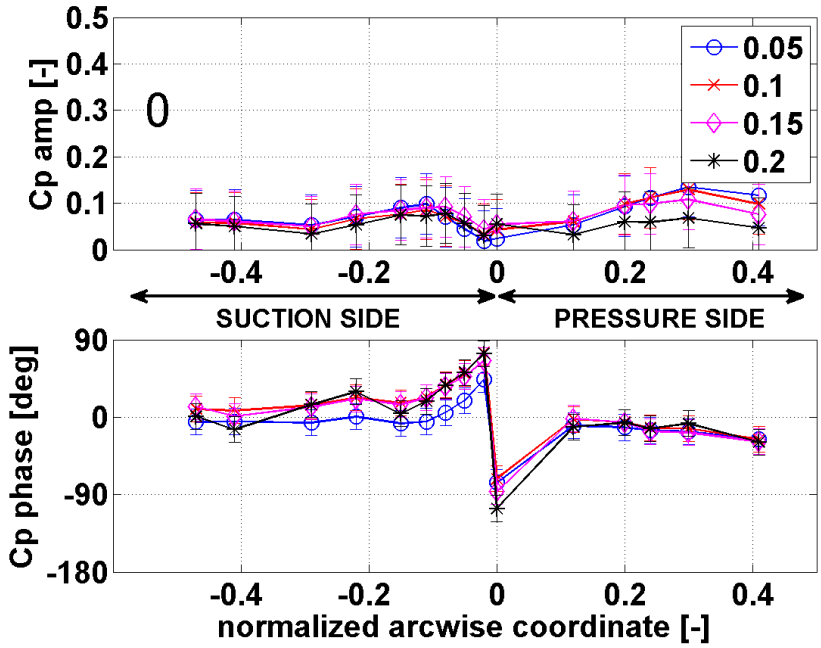

**M08,
nominal,
pure circumferential
bending**

blade 0

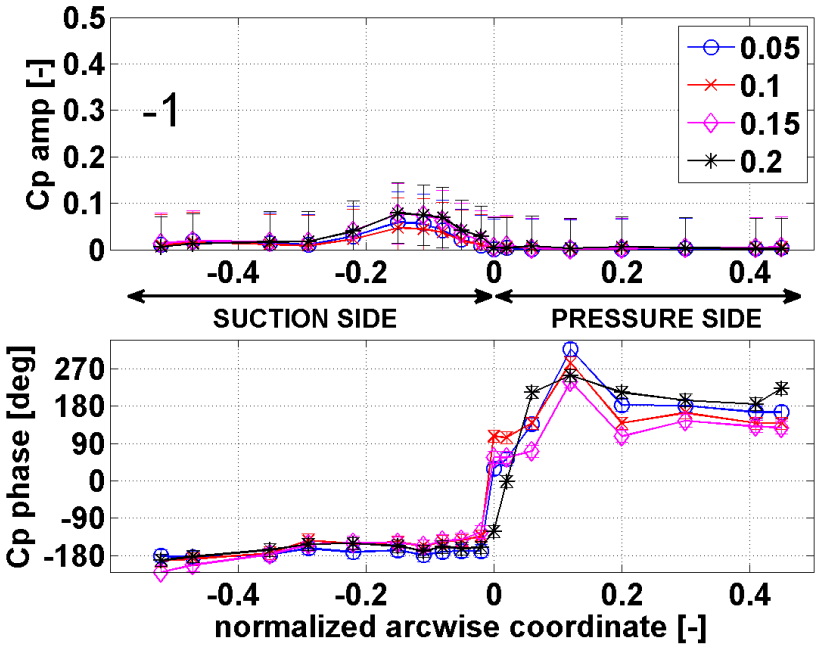

**M08,
nominal,
pure circumferential
bending**

blade -1

Figure F-3: Effect of reduced frequency, M08, nom, pure circ. bending

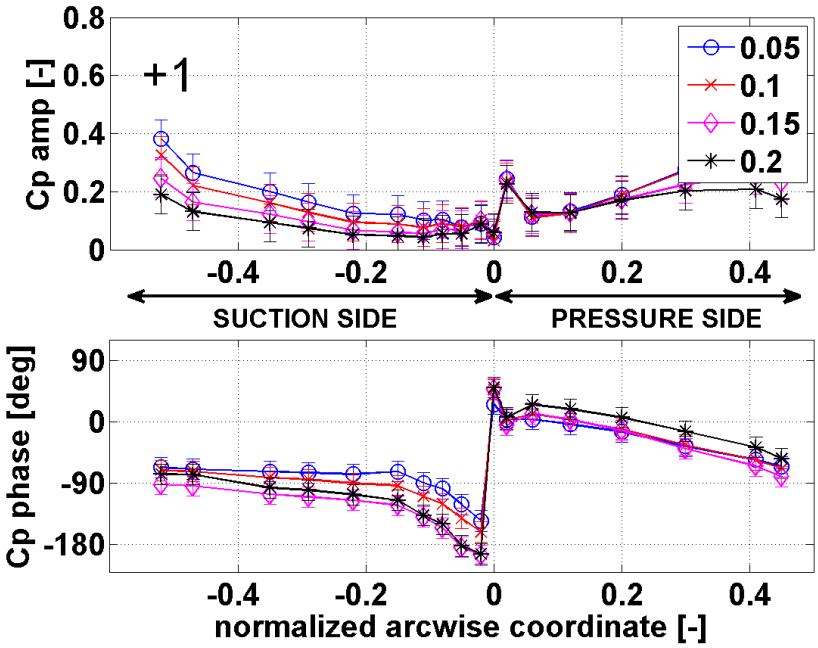

M08, nominal, combined axial/torsion

blade +1

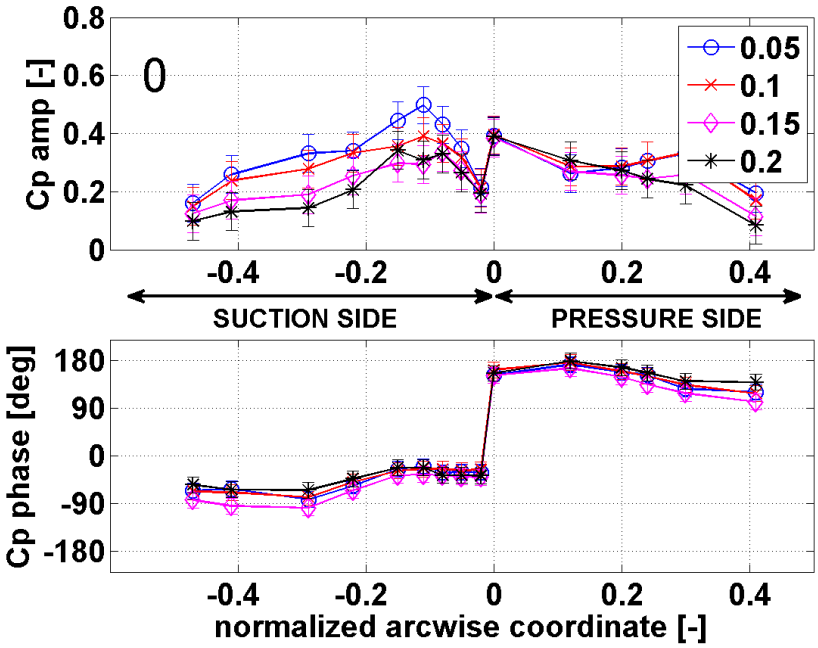

M08, nominal, combined axial/torsion

blade 0

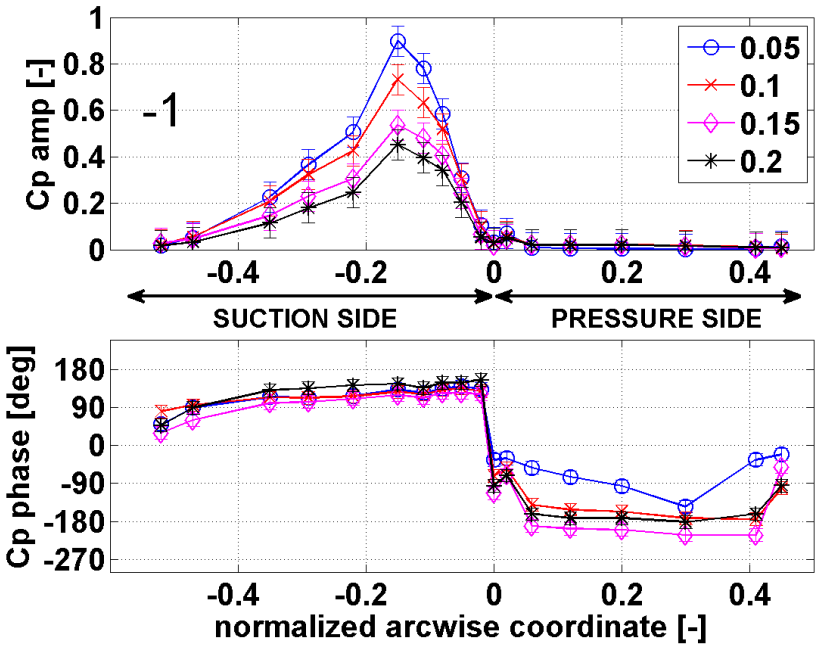

M08, nominal, combined axial/torsion

blade -1

Figure F-4: Effect of reduced frequency, M08, nom, combined axial/torsion

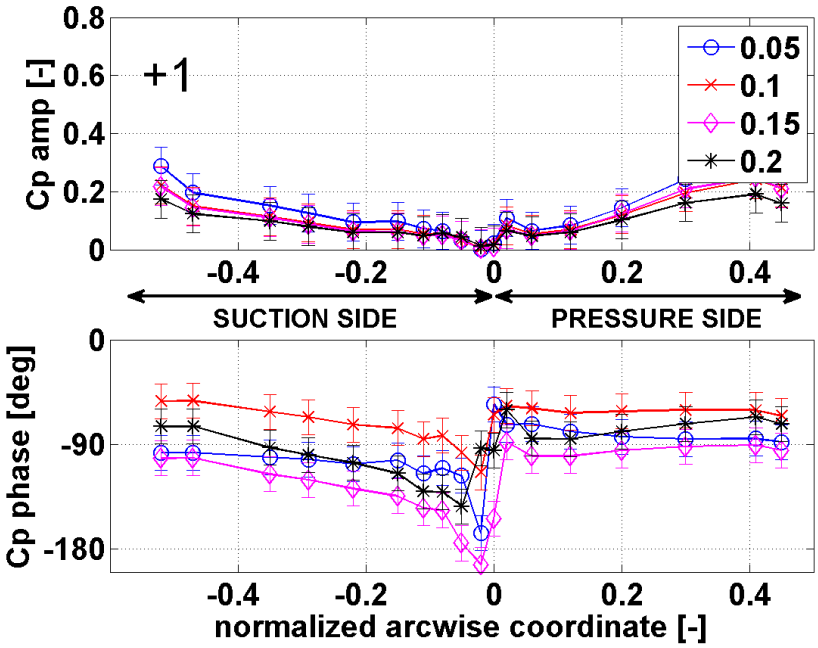

M08, nominal, combined circumferential /torsion

blade +1

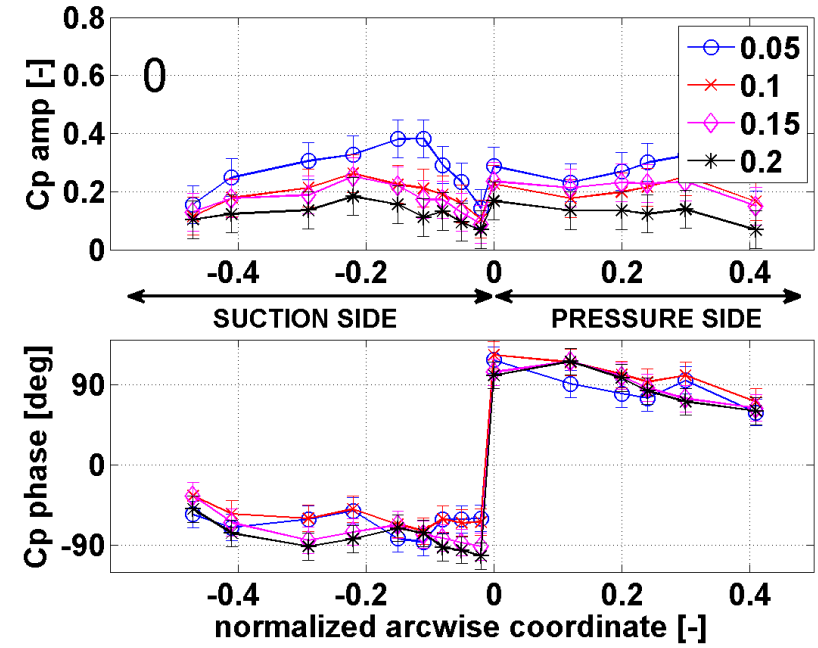

M08, nominal, combined circumferential /torsion

blade 0

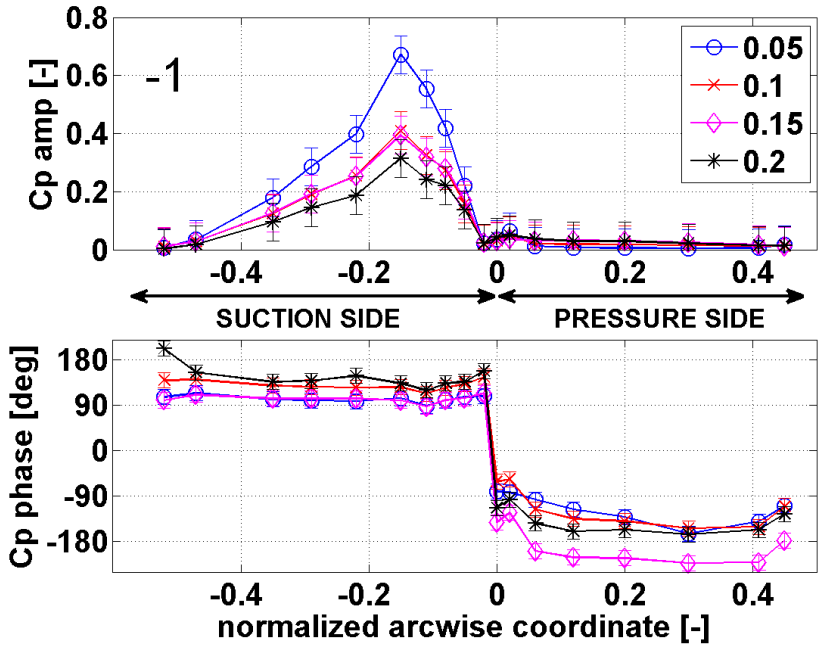

M08, nominal, combined circumferential /torsion

blade -1

Figure F-5: Effect of reduced frequency, M08, nom, combined circ./torsion

G EFFECT OF STEADY FLOW VELOCITY

The present appendix focuses on the effect of the steady flow velocity on the aeroelastic response on blade 0 and blades ±1 in terms of magnitude and phase of the unsteady pressure coefficient. Two outlet Mach number are investigated: 0.4 and 0.8. The appendix gathers experimental unsteady results for the reduced frequency 0.2, the nominal incidence and the five modeshapes: pure axial bending, pure torsion, pure circumferential bending, combined axial/torsion and combined circumferential/torsion.

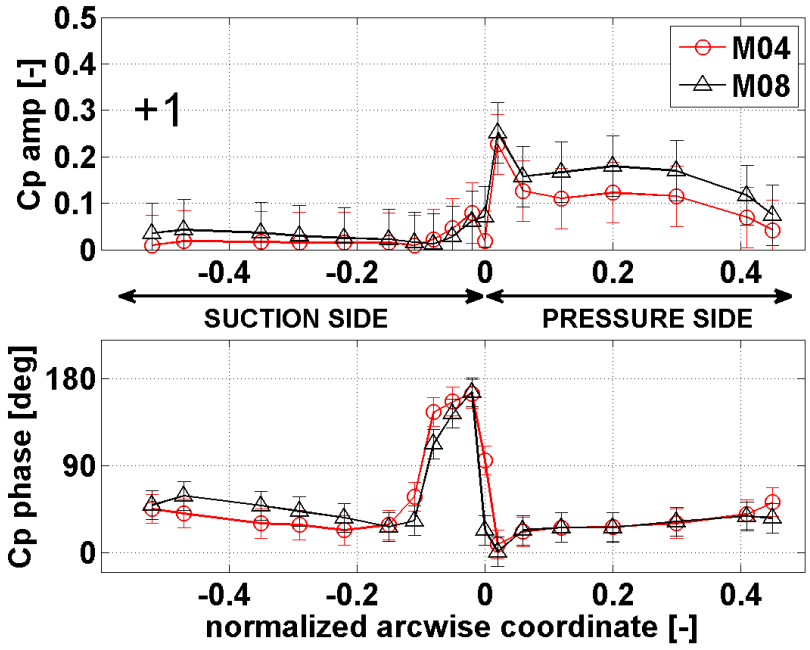

nominal, k=0.2, pure axial bending

blade +1

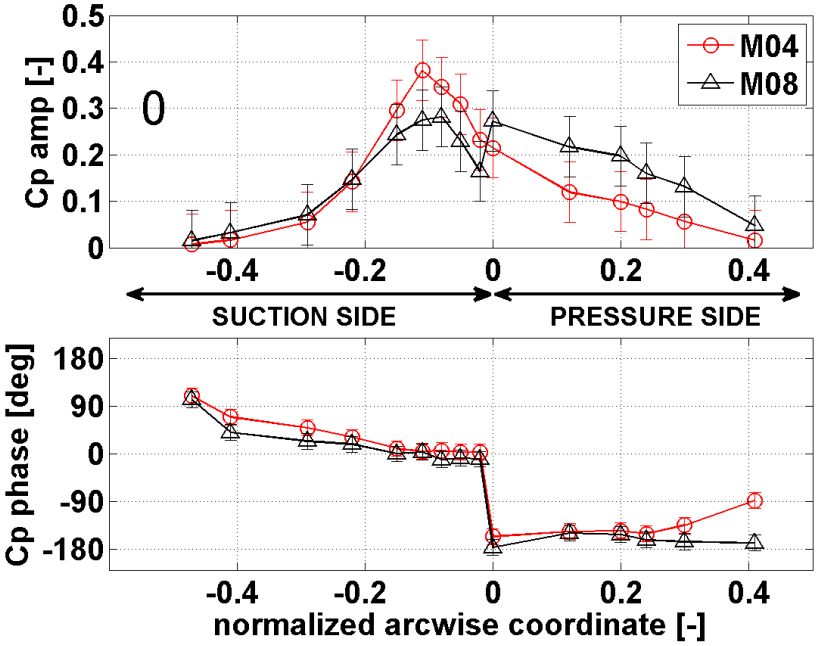

nominal, k=0.2, pure axial bending

blade 0

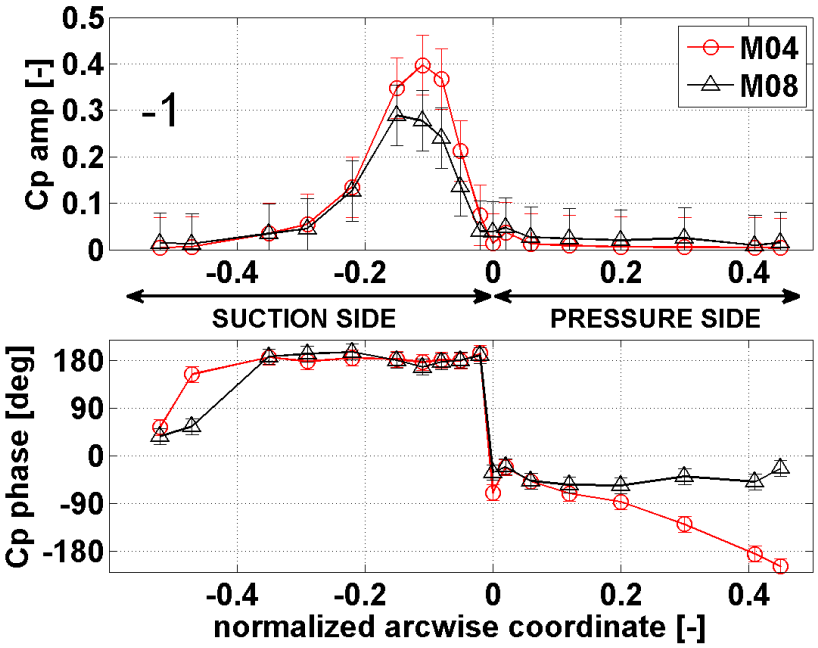

nominal,
k=0.2,
pure axial bending

blade -1

Figure G-1: Effect of flow velocity, nom, k=0.2, pure axial bending

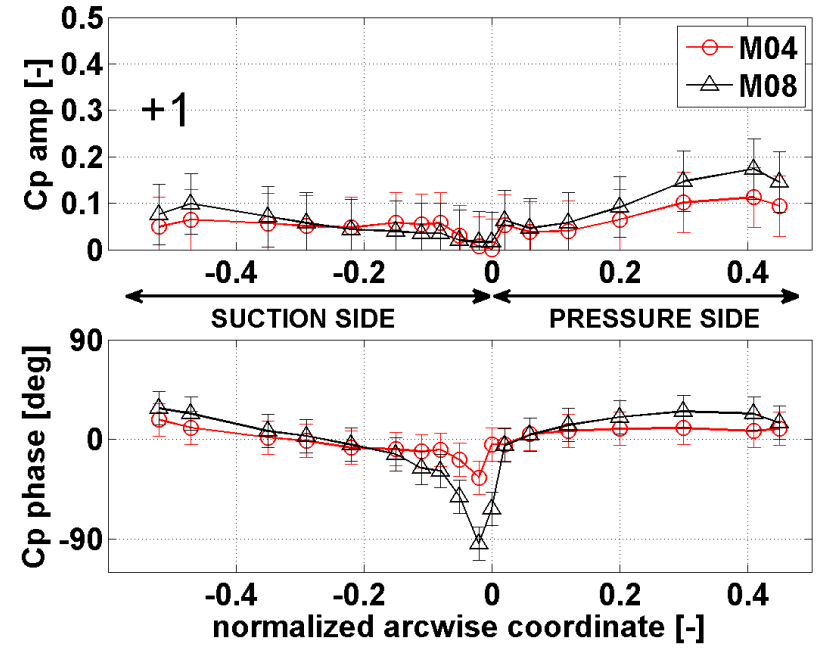

nominal, k=0.2, pure torsion

blade +1

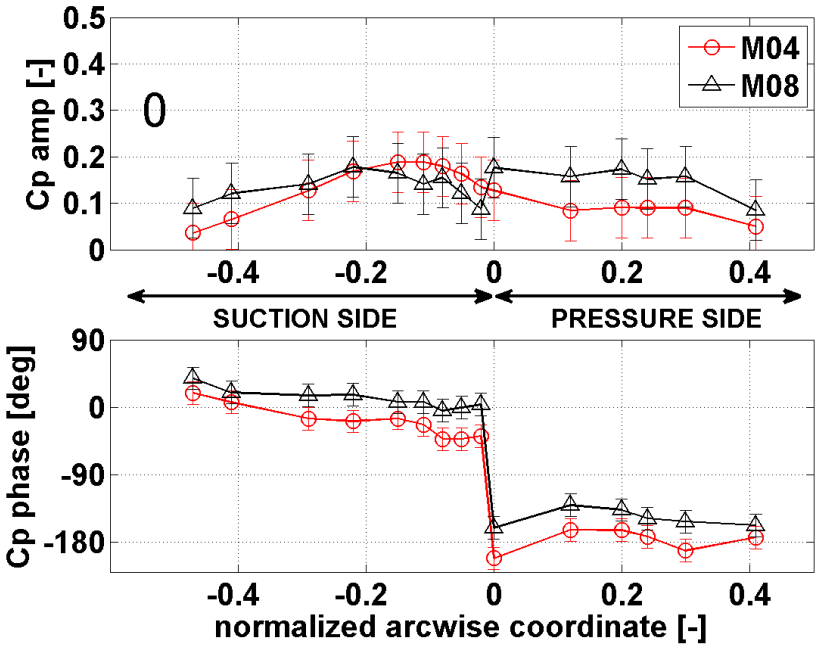

nominal, k=0.2, pure torsion

blade 0

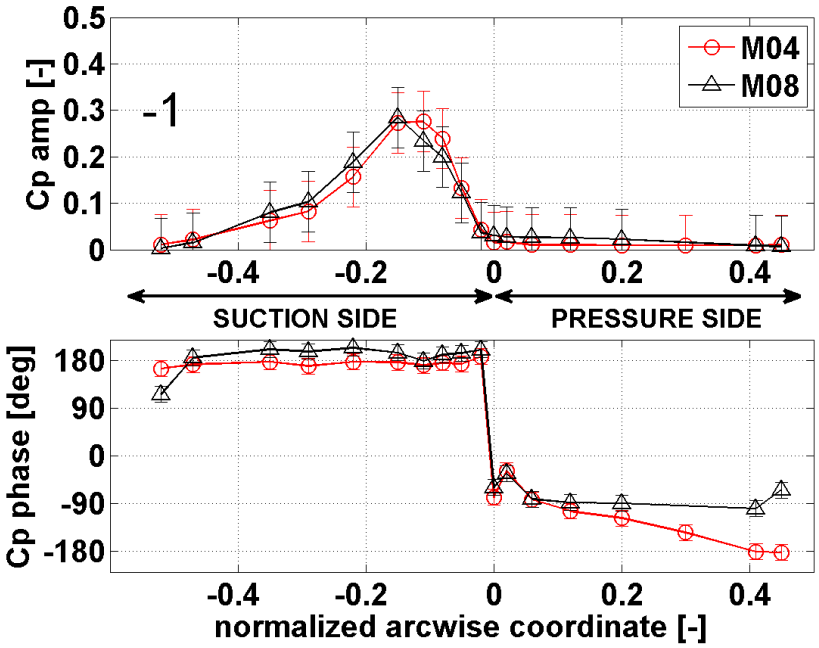

nominal, k=0.2, pure torsion

blade -1

Figure G-2: Effect of flow velocity, nom, k=0.2, pure torsion

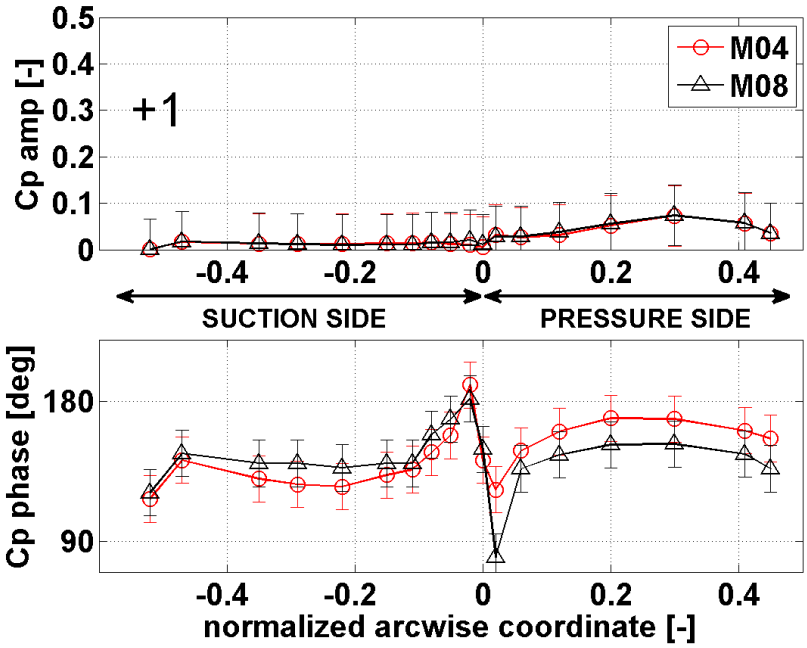

**nominal,
k=0.2,
pure circumferential
bending**

blade +1

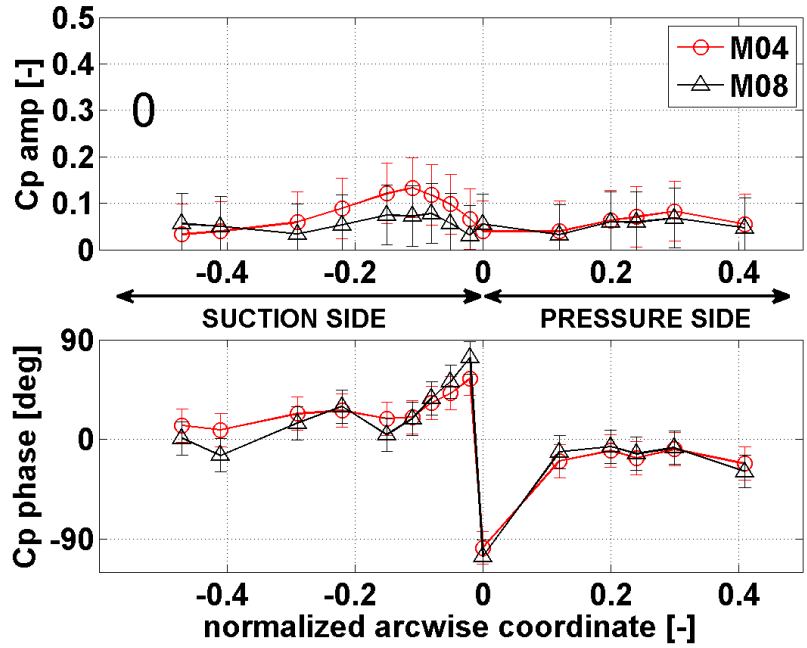

**nominal,
k=0.2,
pure circumferential
bending**

blade 0

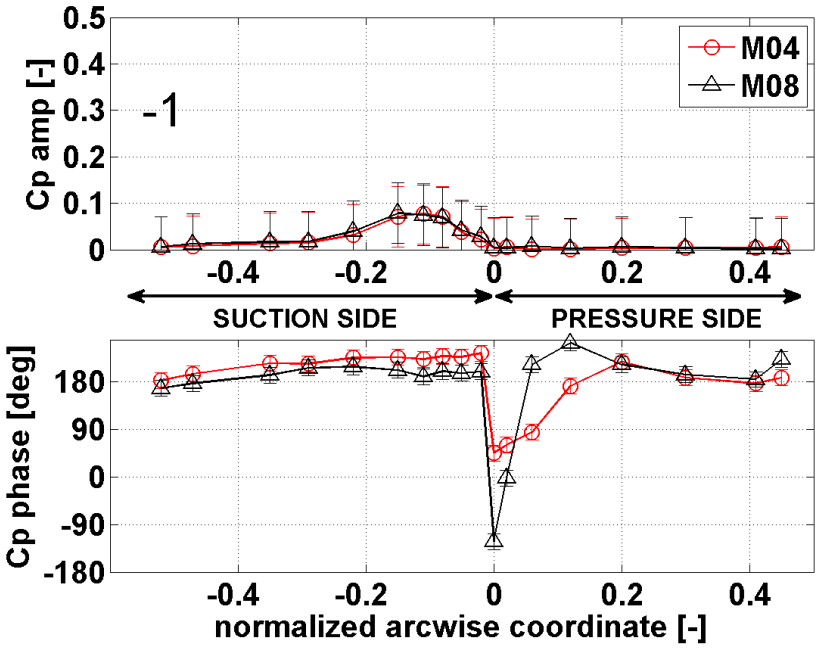

nominal, k=0.2, pure circumferential bending

blade -1

Figure G-3: Effect of flow velocity, nom, k=0.2, pure circ. bending

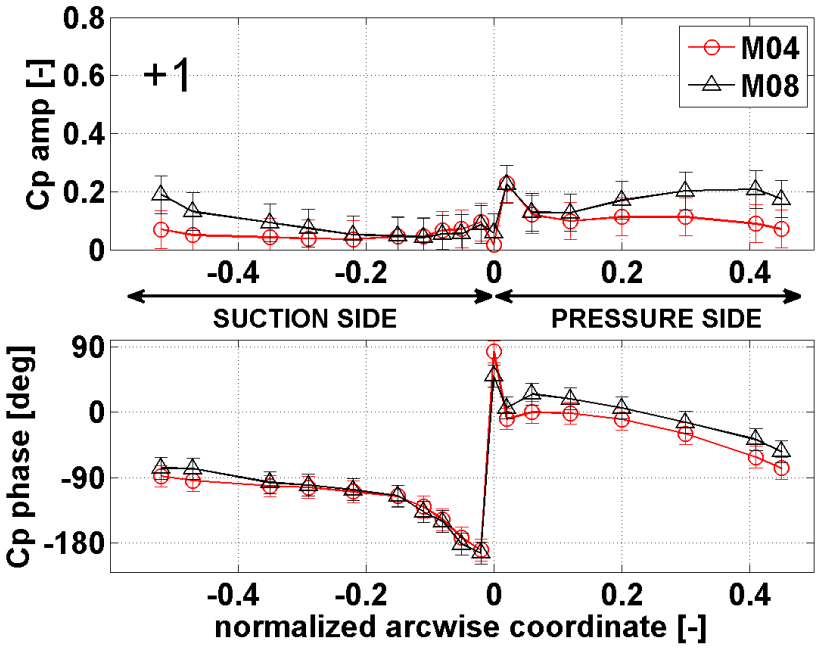

nominal, k=0.2, combined axial/torsion

blade +1

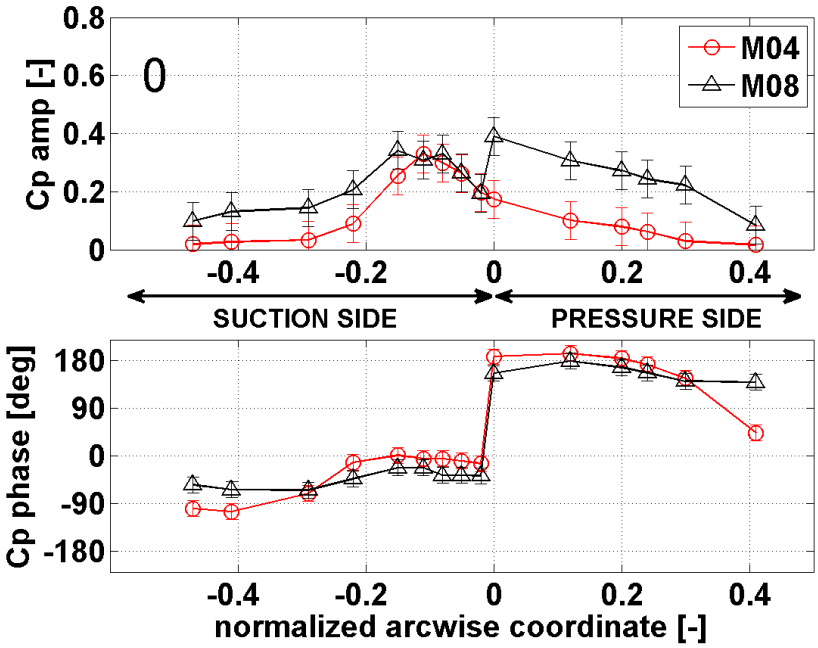

nominal, k=0.2, combined axial/torsion

blade 0

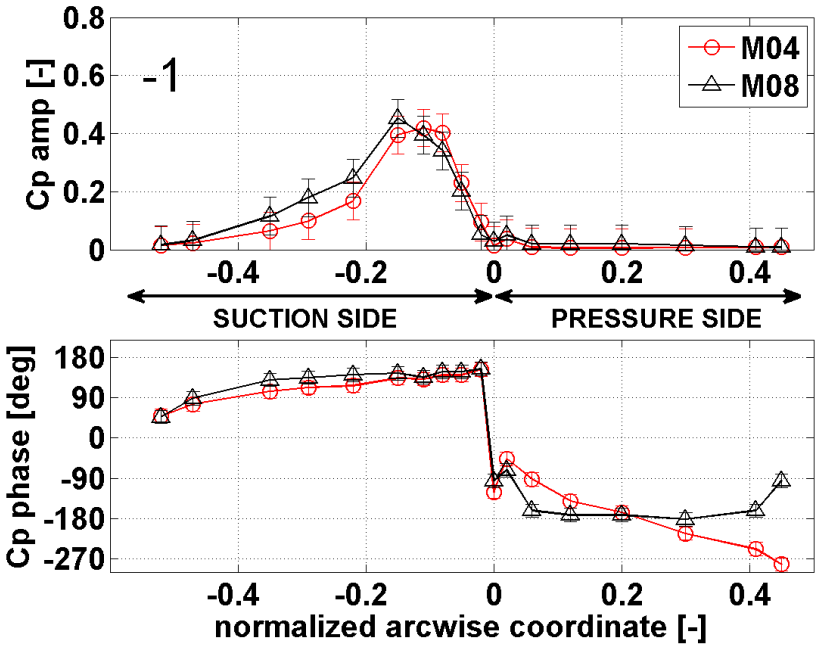

nominal, k=0.2, combined axial/torsion

blade -1

Figure G-4: Effect of flow velocity, nom, k=0.2, combined axial/torsion

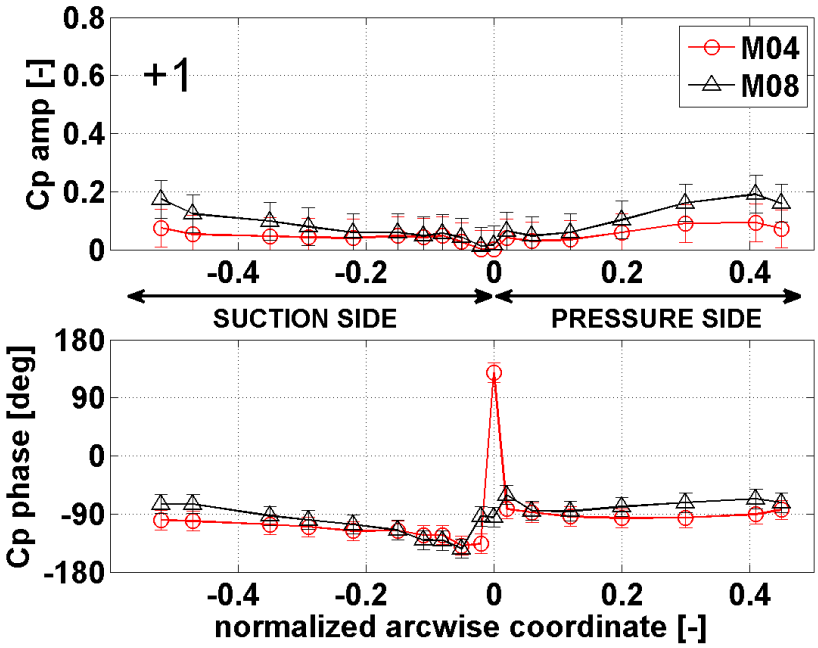

nominal, k=0.2, combined circumferential /torsion

blade +1

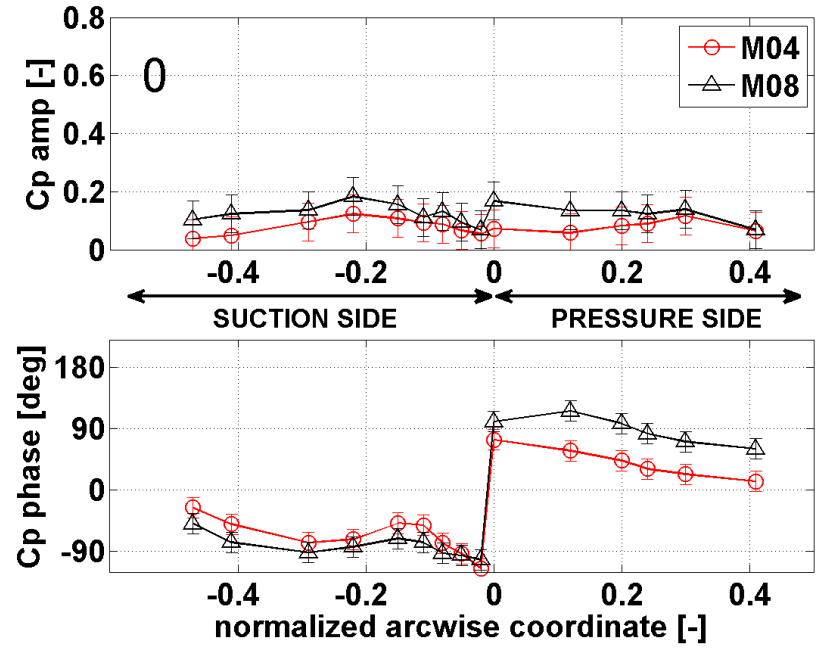

nominal, k=0.2, combined circumferential /torsion

blade 0

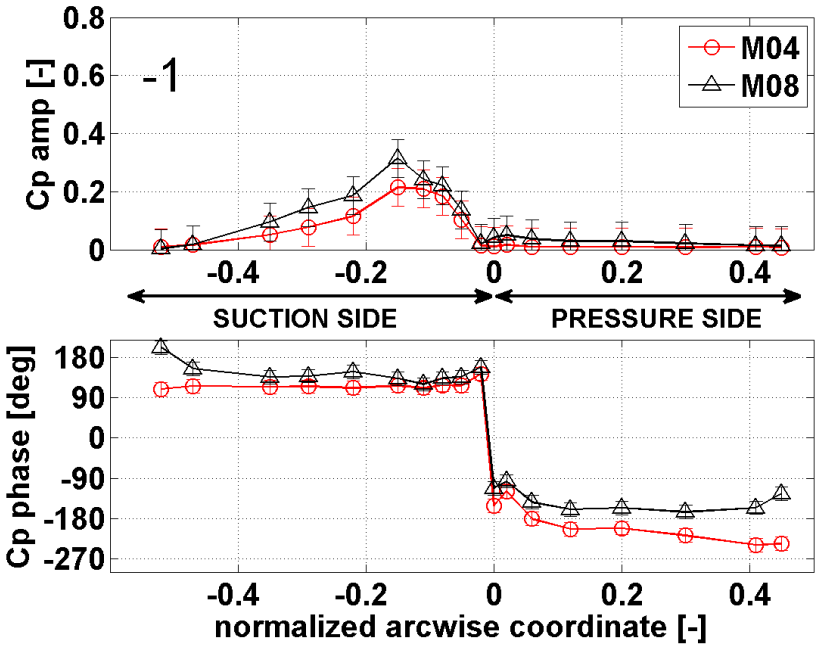

nominal, k=0.2, combined circumferential /torsion

blade -1

Figure G-5: Effect of flow velocity, nom, k=0.2, combined circ./torsion

H EFFECT OF INCIDENCE ANGLE

The present appendix focuses on the effect of the incidence angle on the aeroelastic response on blade 0 and blades ±1 in terms of magnitude and phase of the unsteady pressure coefficient. Three incidence angles are investigated: nominal, off-design 1 and off-design 2. From nominal over off-design 1 to off-design 2, the incidence increases such that the boundary layer on the pressure side separates. The appendix gathers experimental unsteady results for the outlet Mach number 0.8, the reduced frequency 0.2 and the five modeshapes: pure axial bending, pure torsion, pure circumferential bending, combined axial/torsion and combined circumferential/torsion.

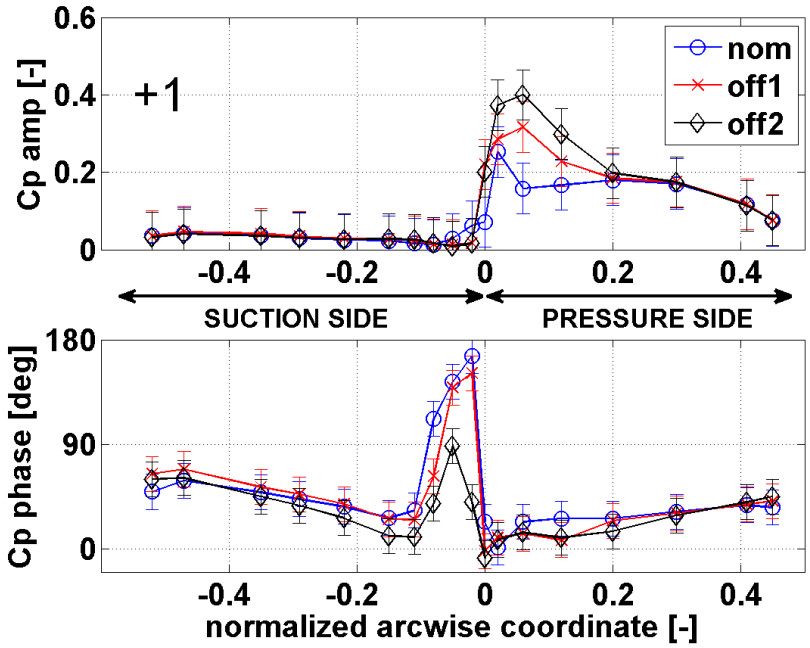

M08,
k=0.2,
pure axial bending

blade +1

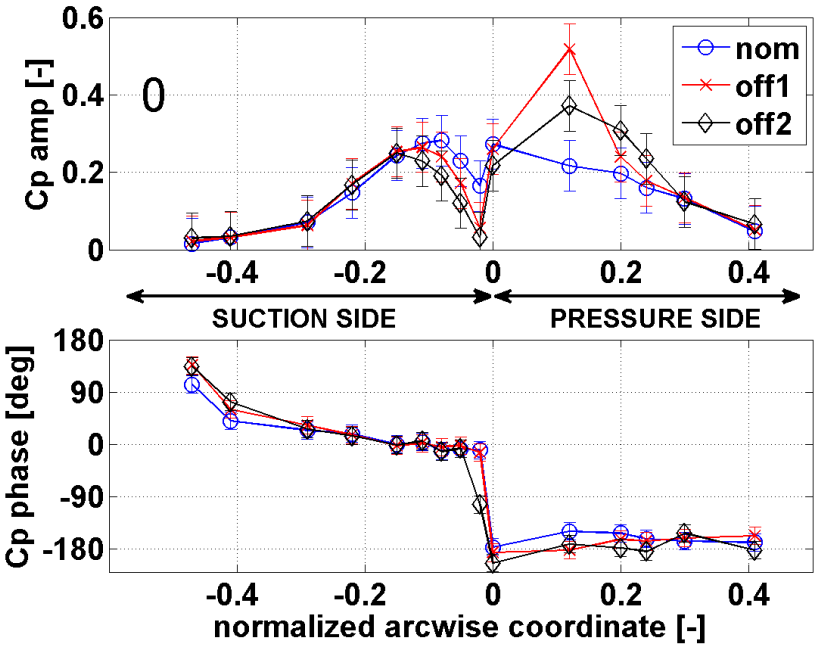

M08,
k=0.2,
pure axial bending

blade 0

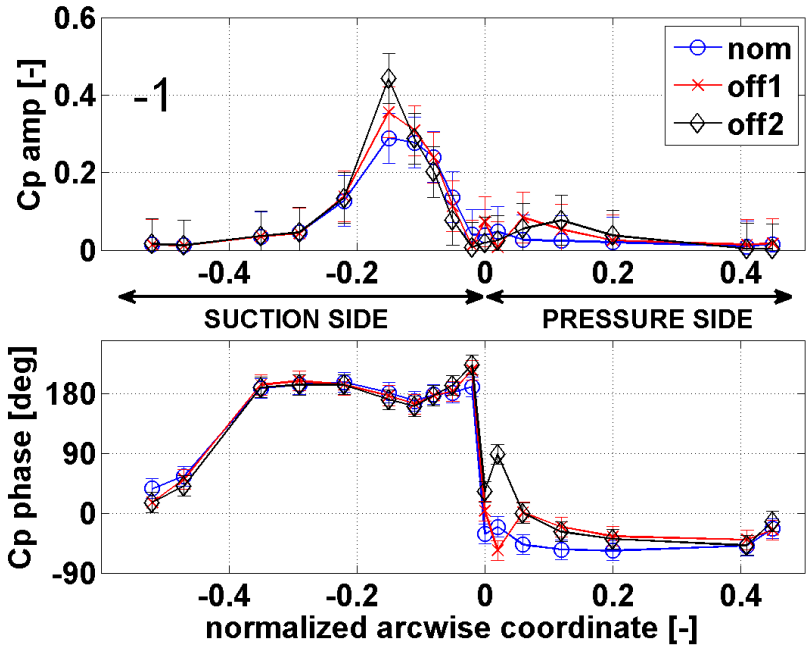

M08,
k=0.2,
pure axial bending

blade -1

Figure H-1: Effect of flow incidence, M08, k=0.2, pure axial bending

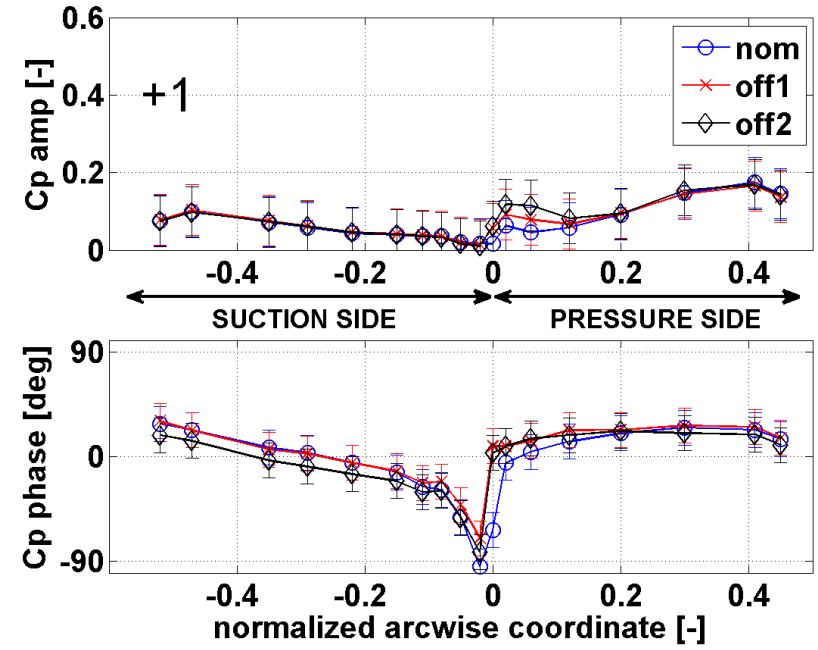

M08,
k=0.2,
pure torsion

blade +1

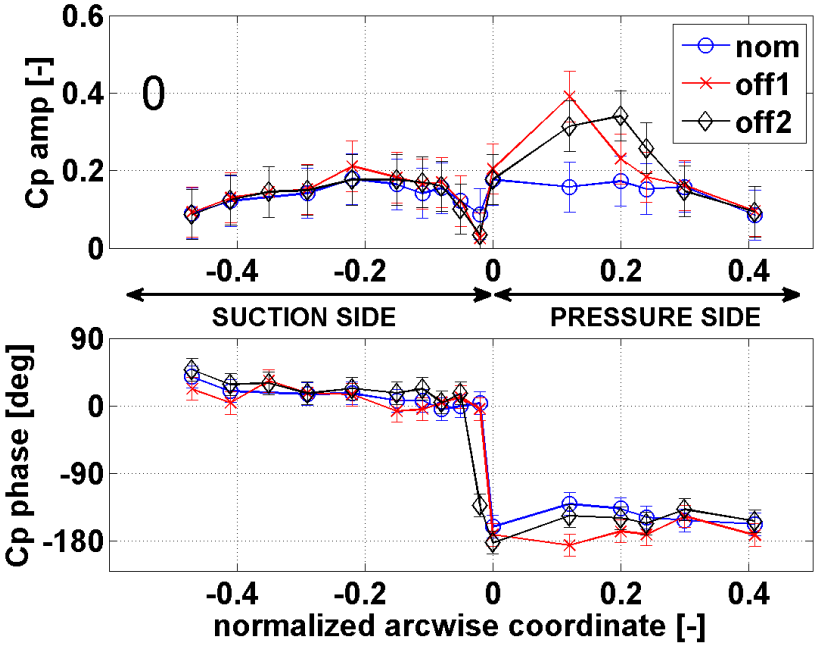

M08,
k=0.2,
pure axial bending

blade 0

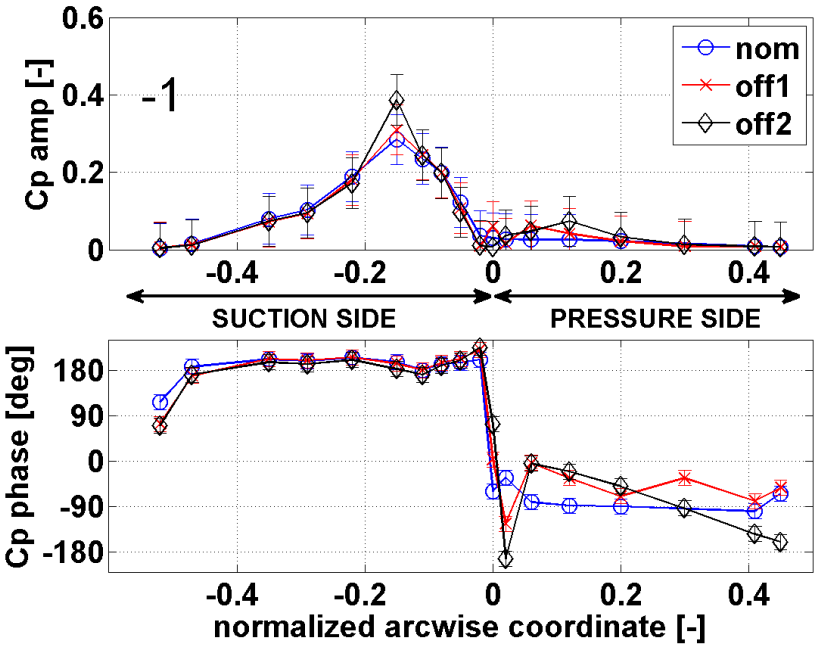

M08,
k=0.2,
pure axial bending

blade 0

Figure H-2: Effect of flow incidence, M08, k=0.2, pure torsion

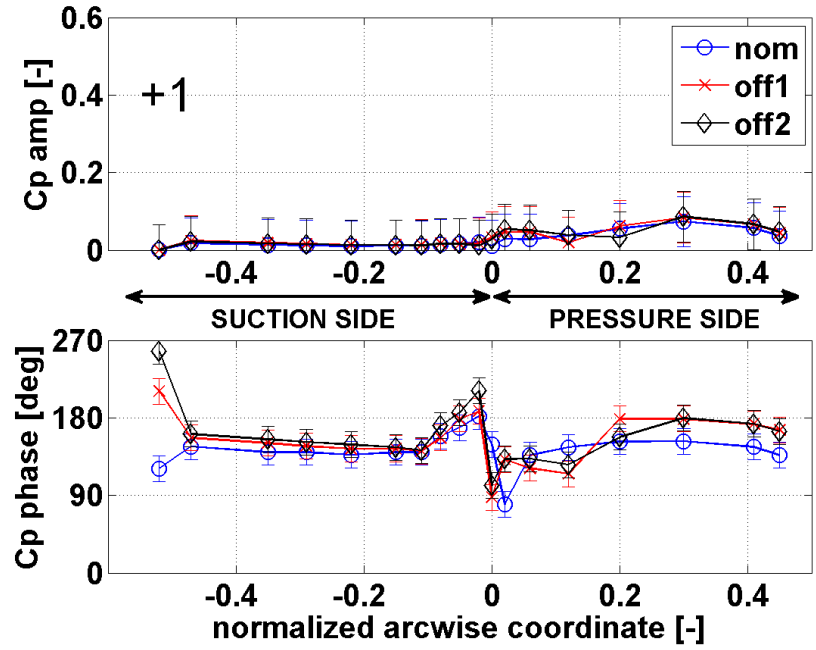

**M08,
k=0.2,
pure circumferential
bending**

blade +1

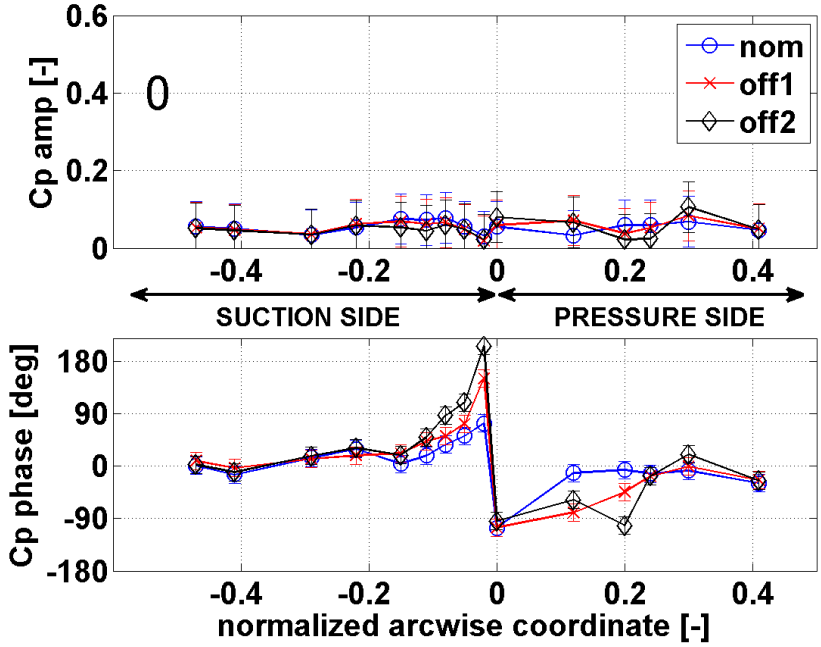

**M08,
k=0.2,
pure circumferential
bending**

blade 0

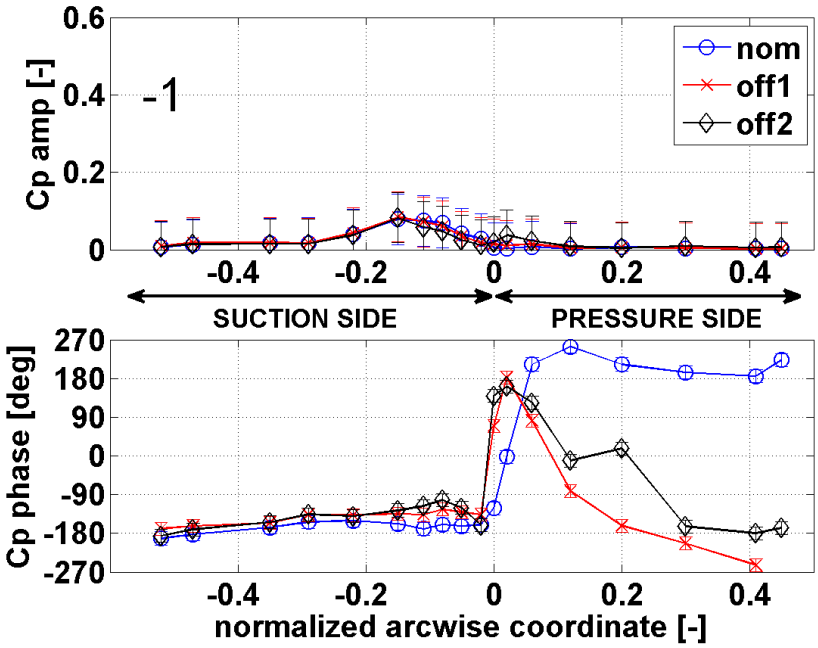

M08,
k=0.2,
pure circumferential bending

blade -1

Figure H-3: Effect of flow incidence, M08, k=0.2, pure circ. bending

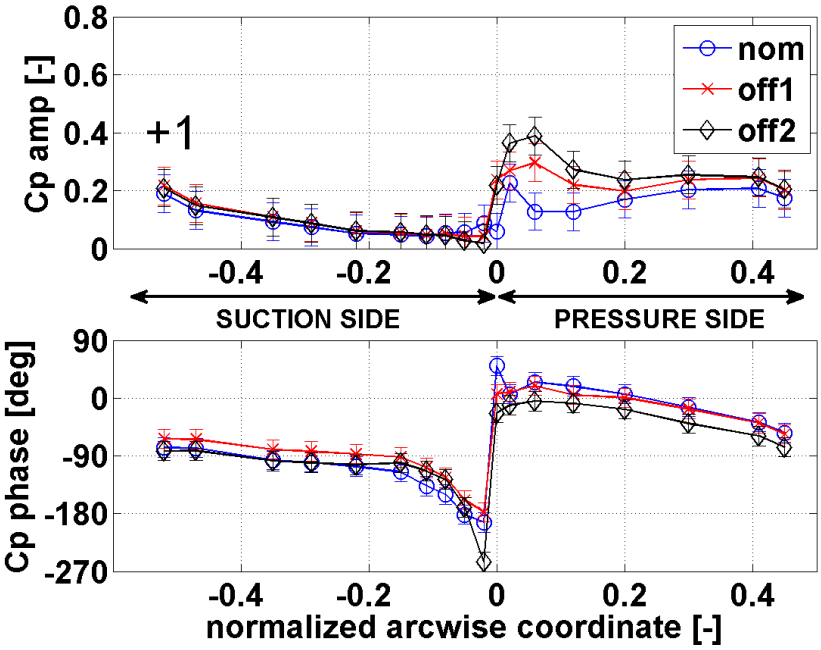

M08, k=0.2, combined axial/torsion

blade +1

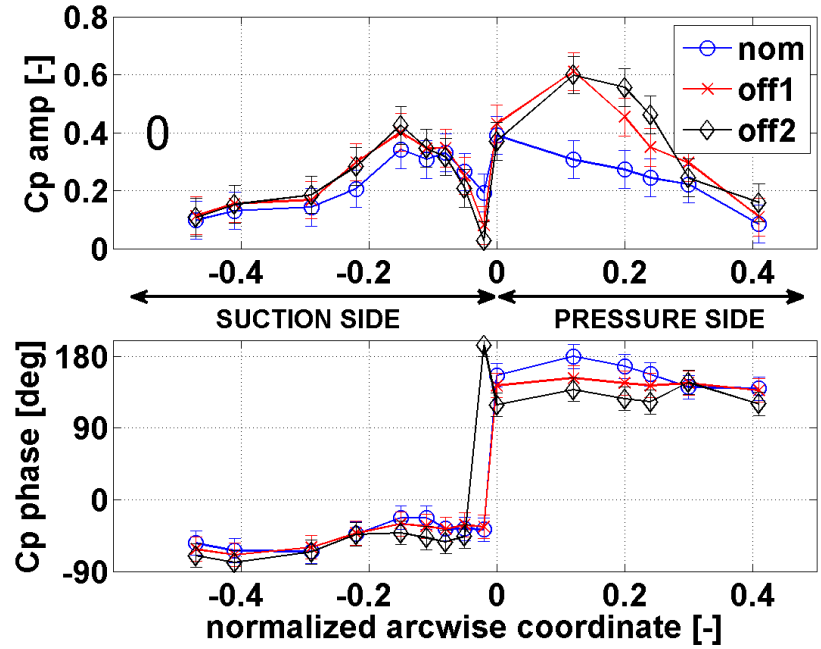

M08, k=0.2, combined axial/torsion

blade 0

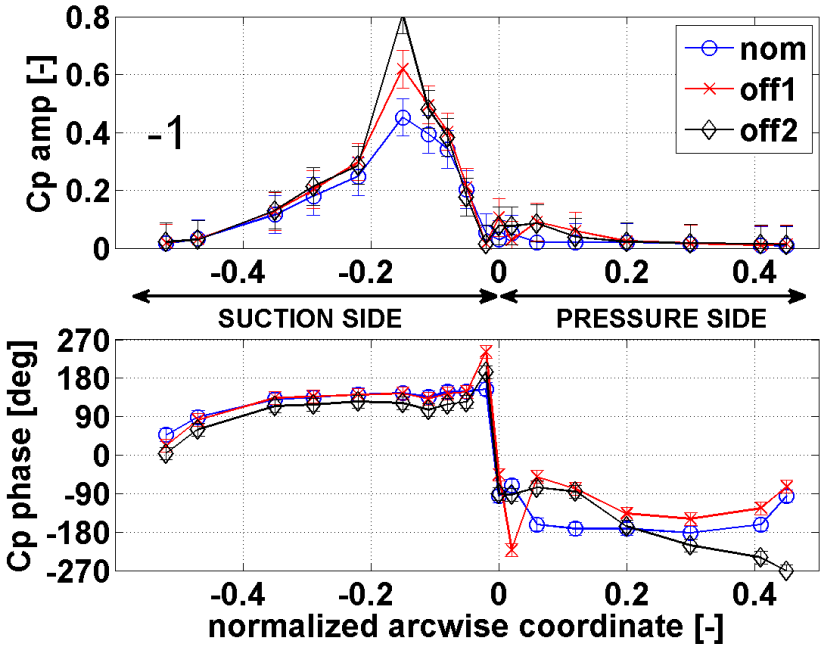

M08, k=0.2, combined axial/torsion

blade -1

Figure H-4: Effect of flow incidence, M08, k=0.2, combined axial/torsion

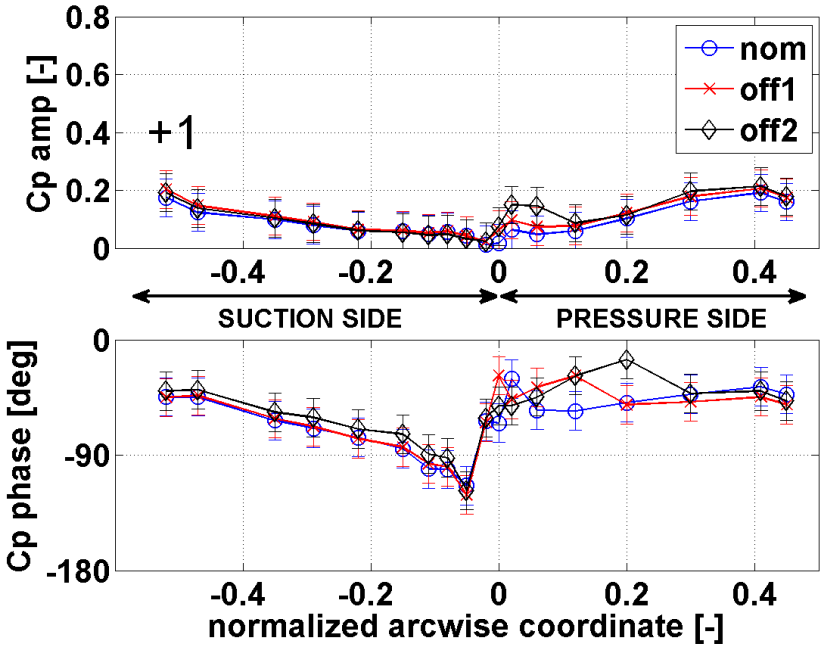

M08, k=0.2, combined circumferential /torsion

blade +1

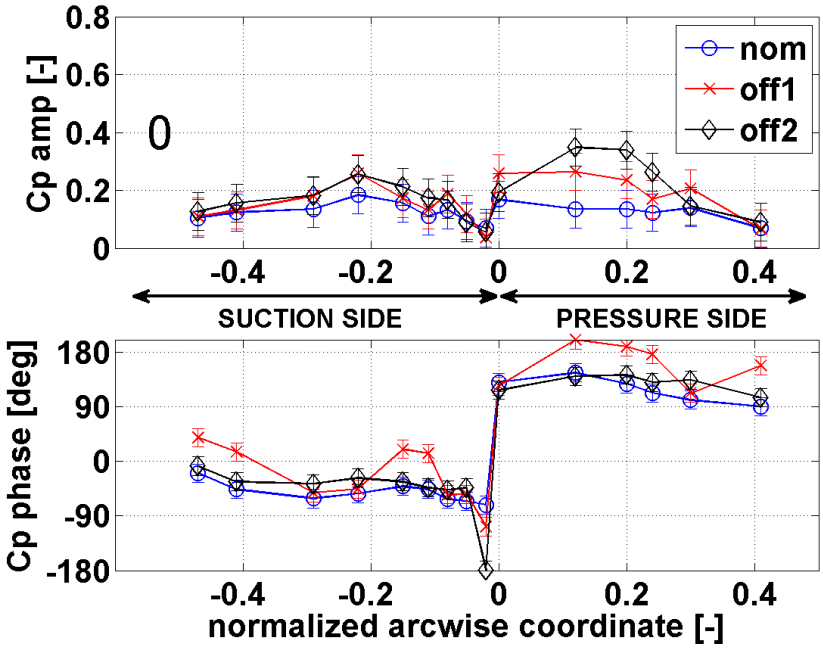

M08, k=0.2, combined circumferential /torsion

blade 0

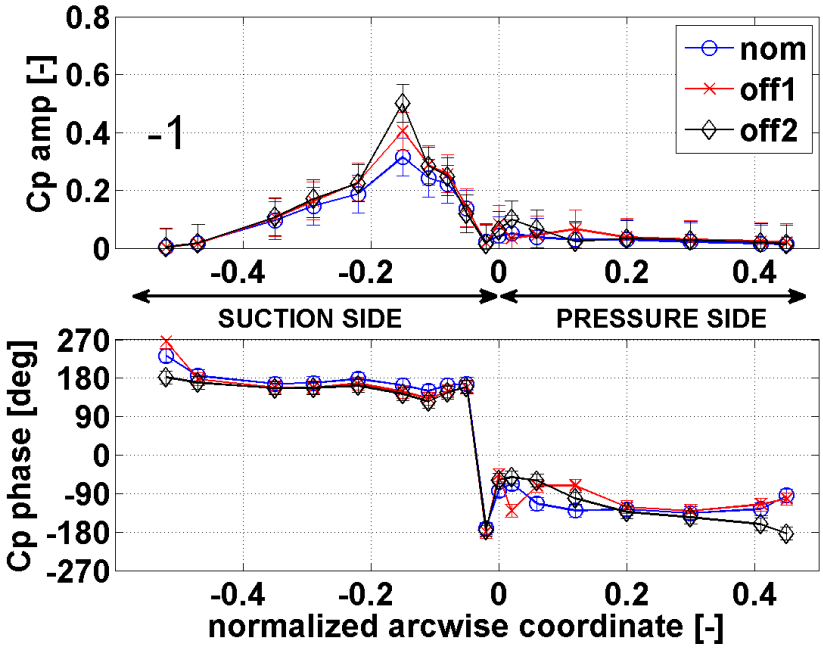

M08, k=0.2, combined circumferential /torsion

blade -1

Figure H-5: Effect of flow incidence, M08, k=0.2, combined circ./torsion

I THREE-DIMENSIONAL EFFECTS

The present appendix focuses on the three-dimensional effects on the aeroelastic response on blade 0 and blades ±1 in terms of magnitude and phase of the unsteady pressure coefficient. Three span positions are investigated: 10%, 50% and 90%. The appendix gathers experimental unsteady results for the outlet Mach number 0.8, the reduced frequency 0.2, the nominal incidence and four modeshapes: pure axial bending, pure torsion, pure circumferential bending and combined axial/torsion.

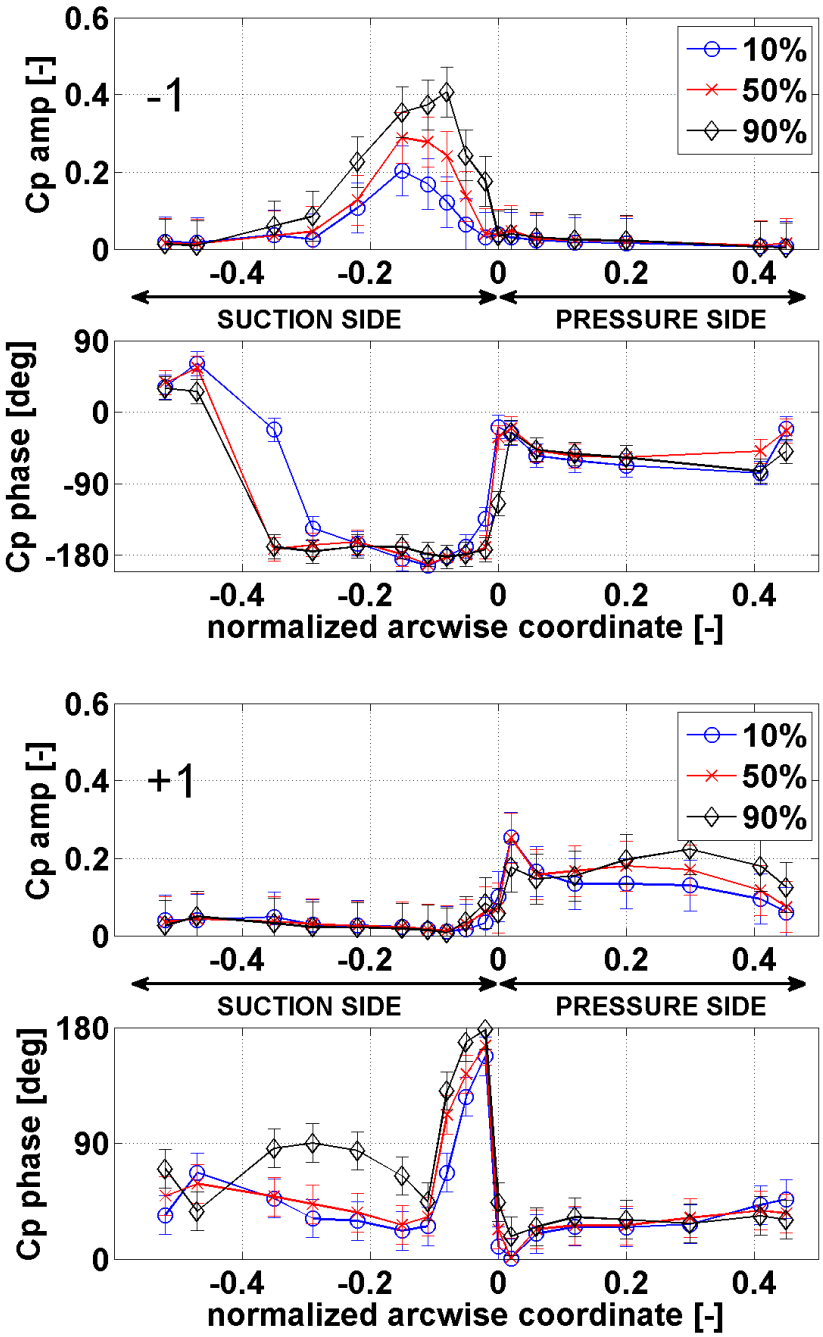

M08, nominal, k=0.2, pure axial bending

blade -1

Figure I-1: Spanwise variations, M08, nom, k=0.2, pure axial bending

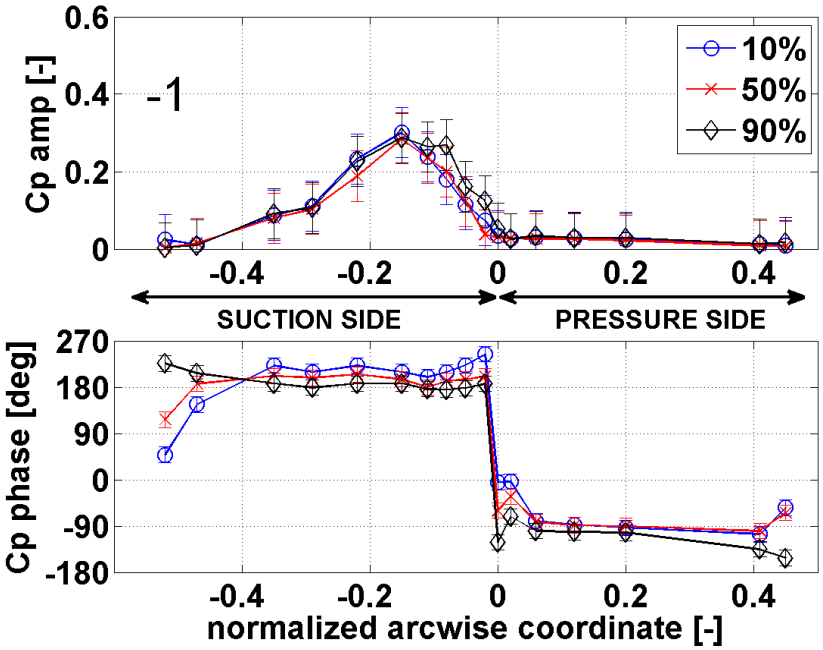

M08, nominal, k=0.2, pure torsion

blade -1

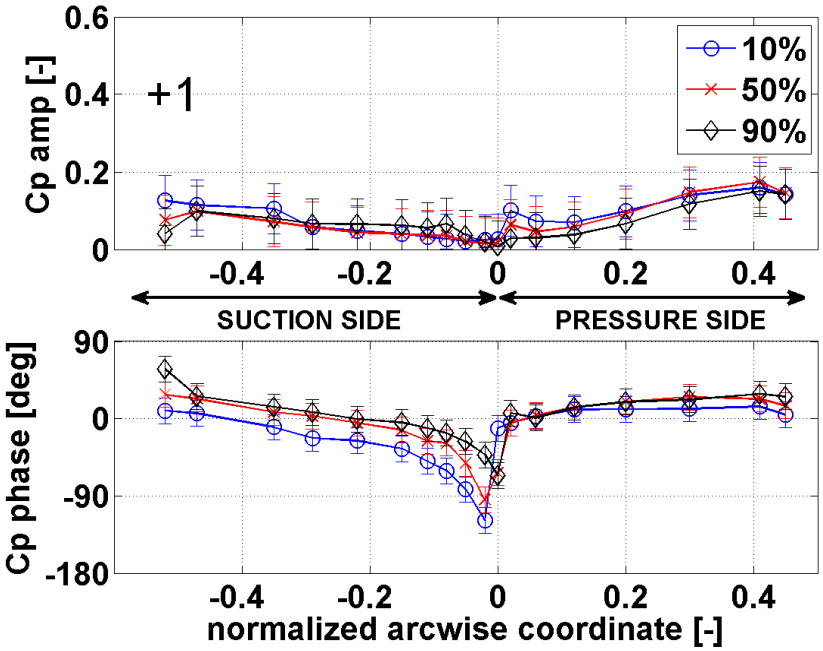

M08, nominal, k=0.2, pure torsion

blade +1

Figure I-2: Spanwise variations, M08, nom, k=0.2, pure torsion

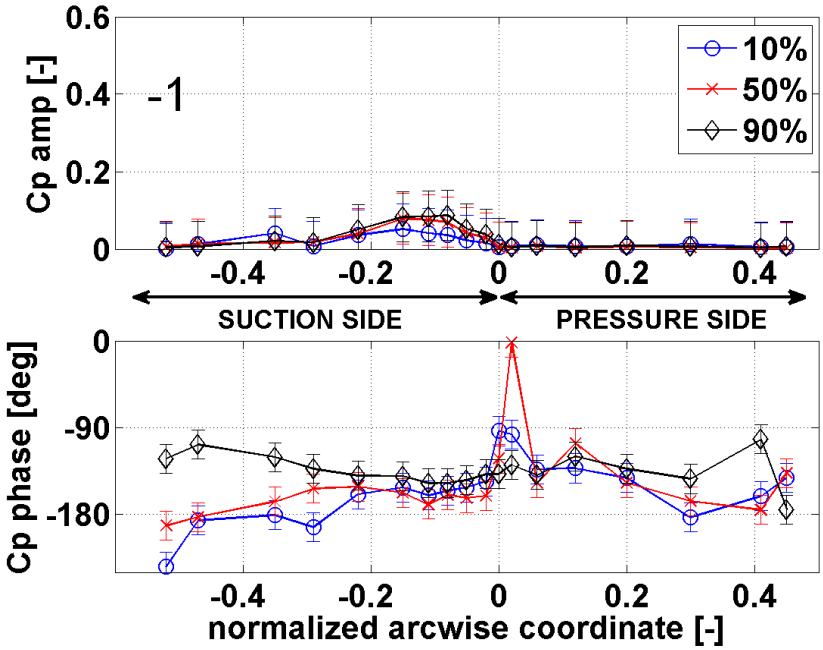

M08, nominal, k=0.2, pure circumferential bending

blade -1

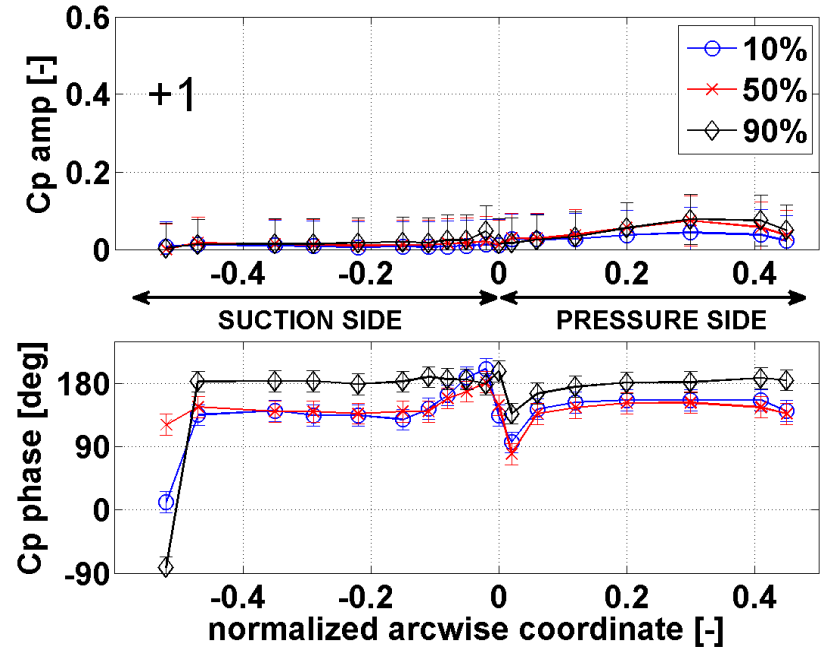

M08, nominal, k=0.2, pure circumferential bending

blade +1

Figure I-3: Spanwise variations, M08, nom, k=0.2, pure circ. bending

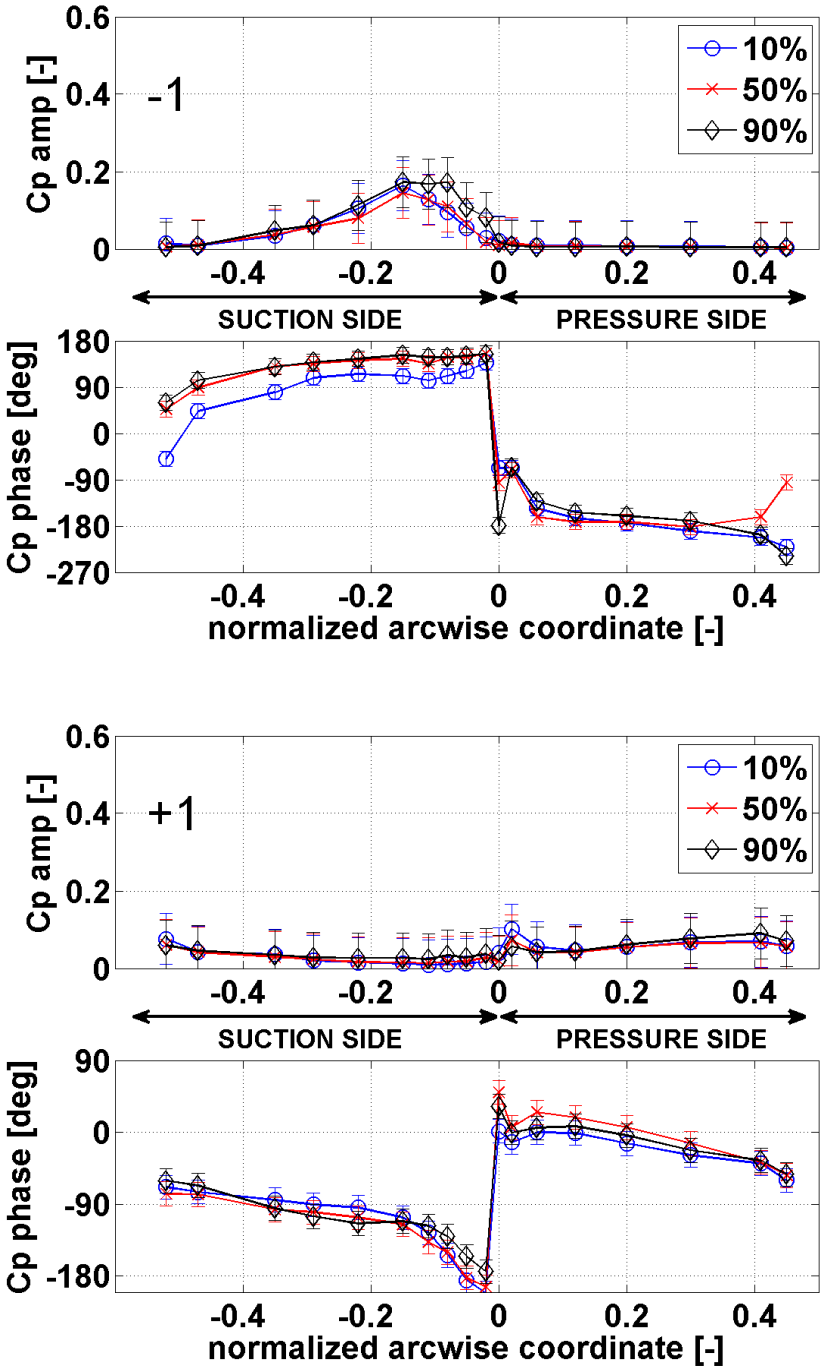

M08, nominal, k=0.2, combined axial/torsion

blade -1

M08, nominal, k=0.2, combined axial/torsion

blade +1

Figure I-4: Spanwise variations, M08, nom, k=0.2, combined axial/torsion

J LINEAR SUPERPOSITION

The present appendix focuses on the linear superposition of the magnitude and phase of the unsteady pressure coefficient on blade 0 and blades ±1. The appendix gathers experimental unsteady results for the outlet Mach number 0.8, the reduced frequency 0.05 and the nominal incidence. For each case, i.e. axial bending/torsion and circumferential bending/torsion, the pure bending and the pure torsion are measured and displayed. Then the combined modes are also measured and presented. Finally the analytical superposition is plotted for comparison.

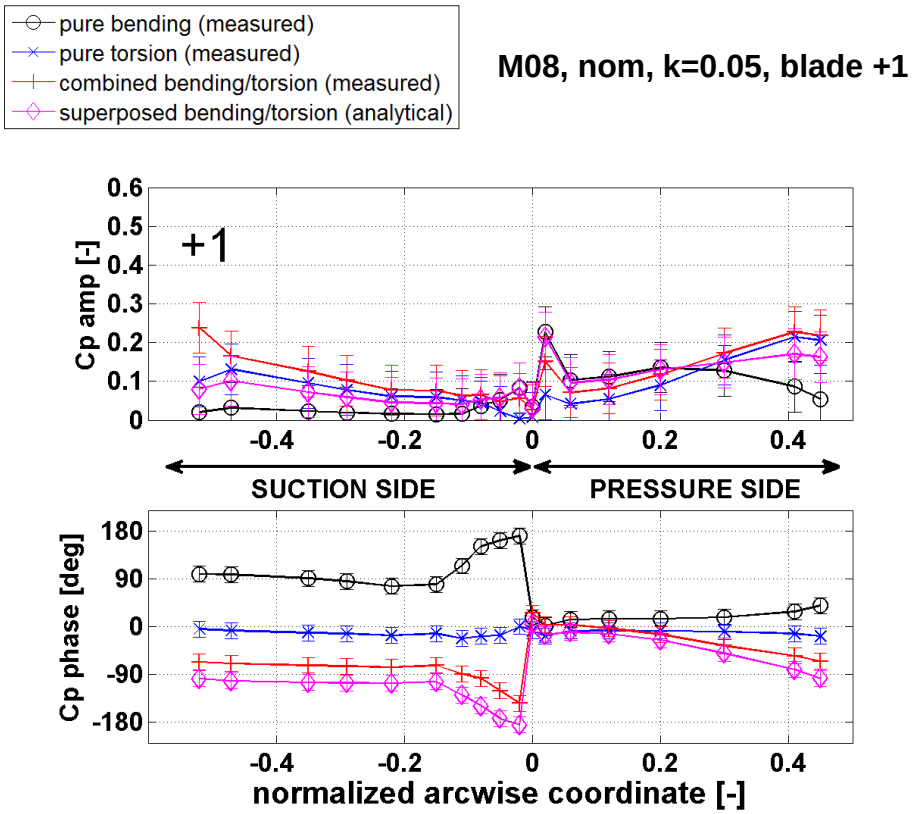

Figure J-1: Linear superposition, combined axial bending/torsion, blade +1

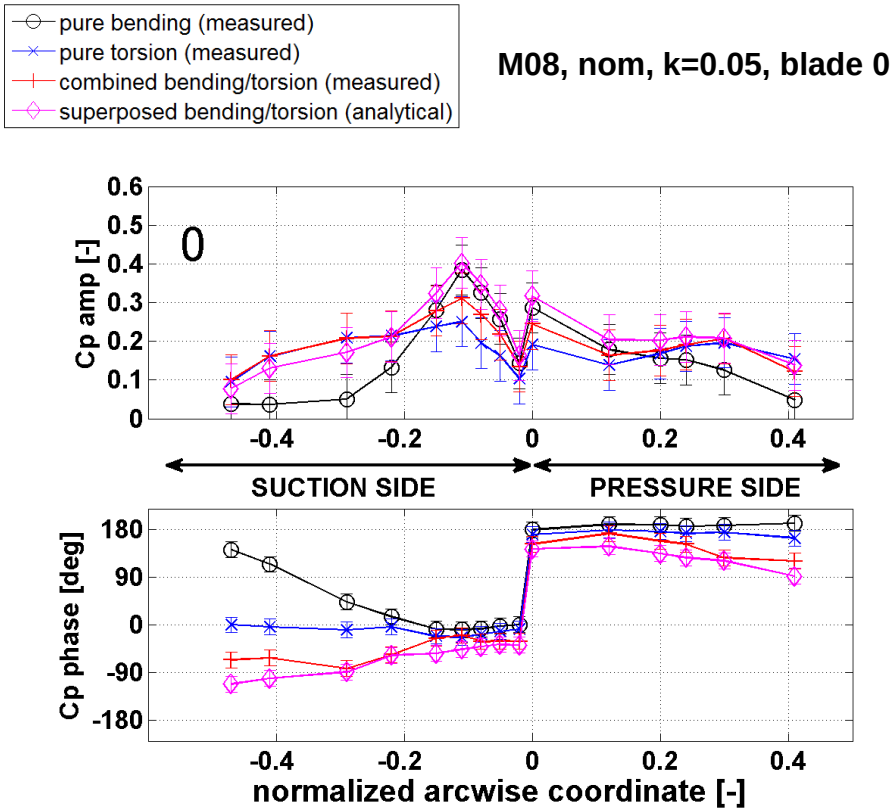

Figure J-2: Linear superposition, combined axial bending/torsion, blade 0

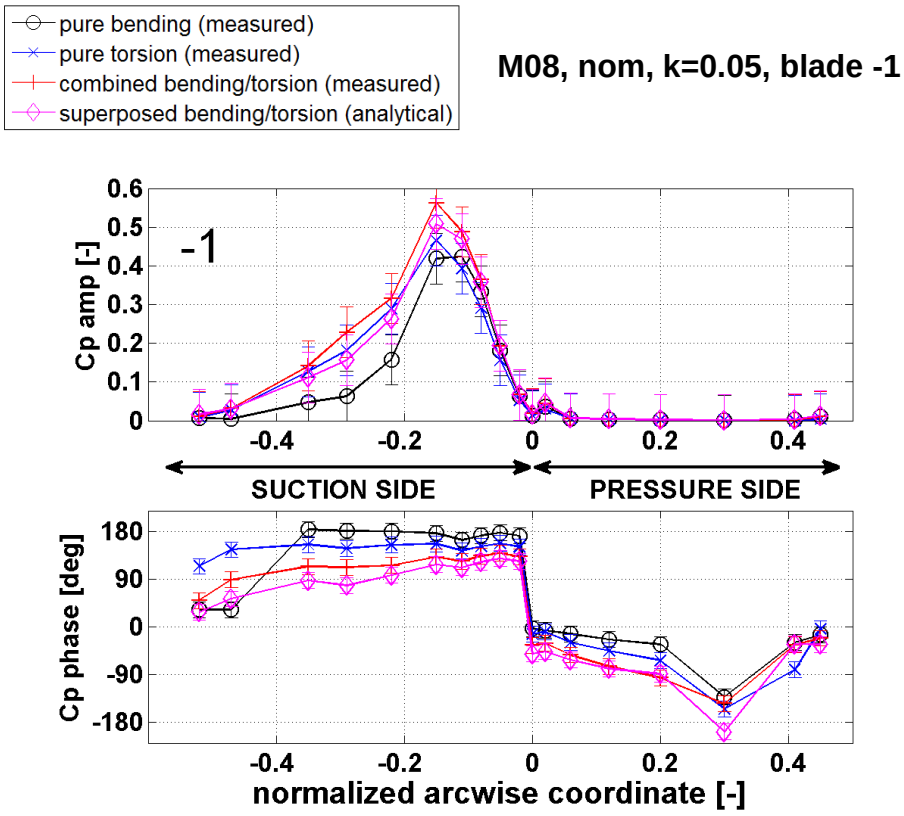

Figure J-3: Linear superposition, combined axial bending/torsion, blade -1

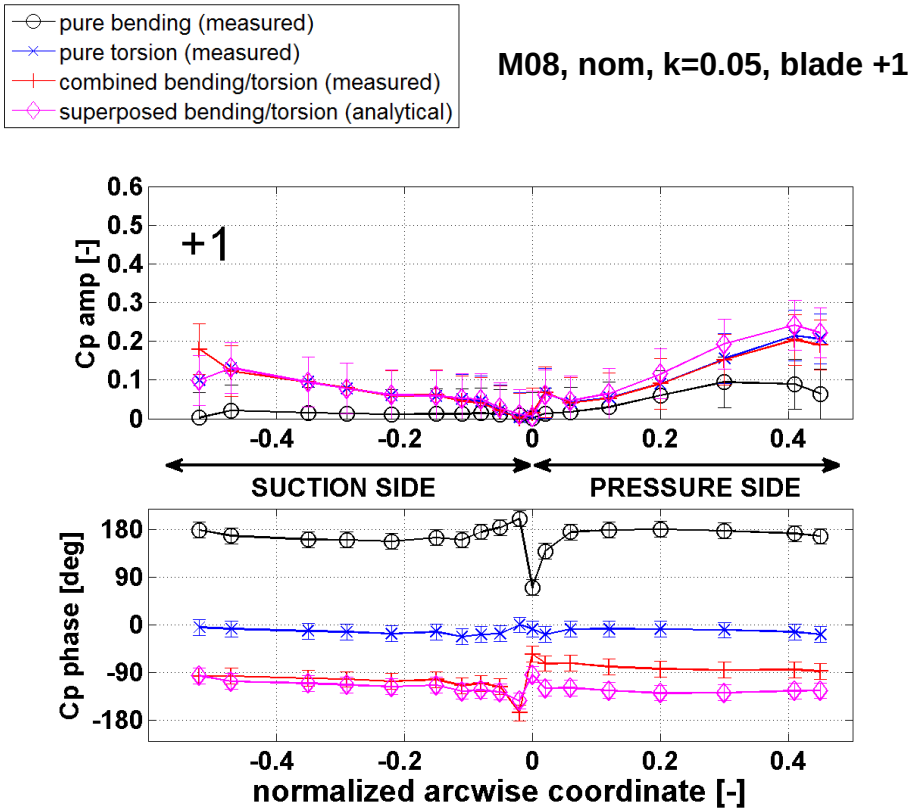

Figure J-4: Linear superposition, combined circumferential bending/torsion, blade +1

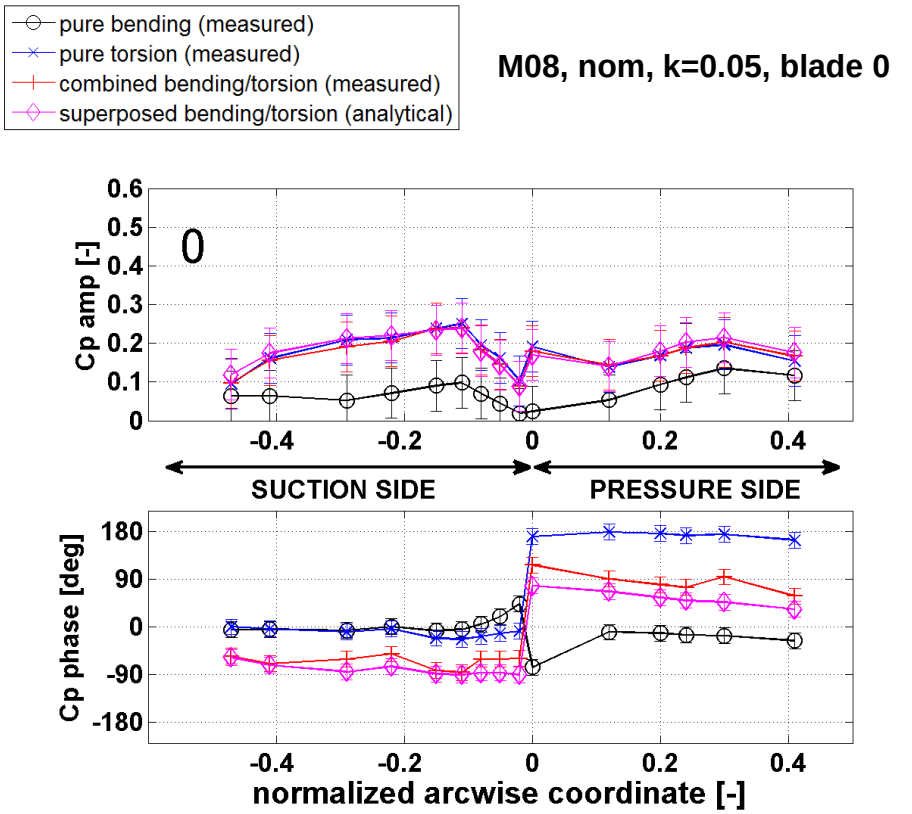

Figure J-5: Linear superposition, combined circumferential bending/torsion, blade 0

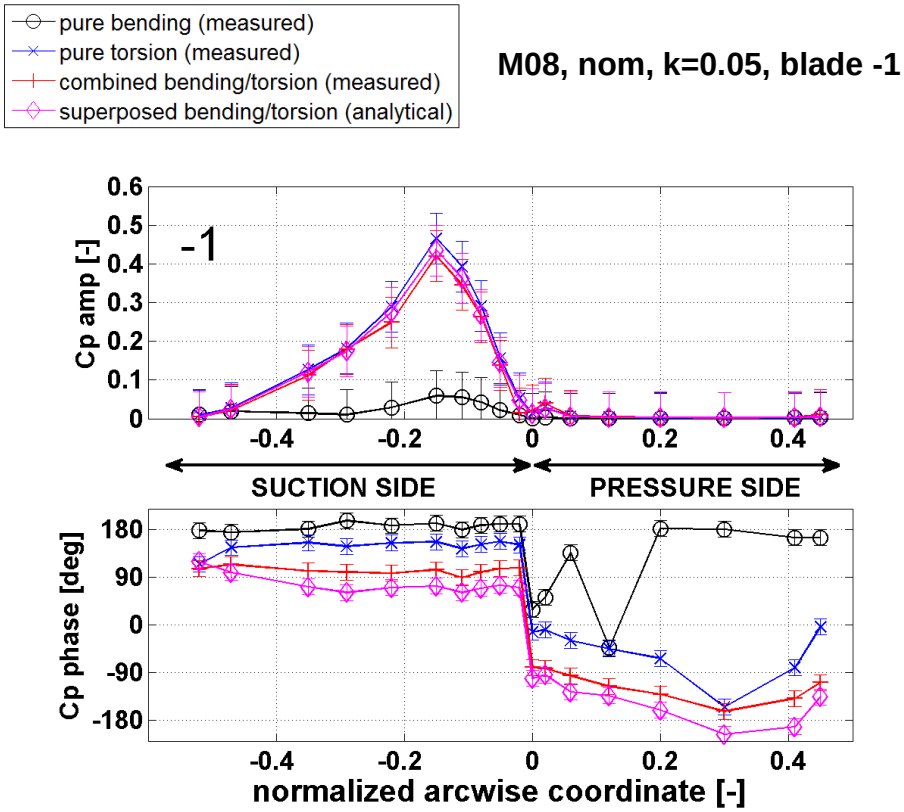

Figure J-6: Linear superposition, combined circumferential bending/torsion, blade -1

ÉCOLE CENTRALE LYON

Direction de la recherche

Liste des personnes Habilitées à Diriger des Recherches en poste à l'Ecole Centrale de Lyon

Nom-Prénom	*Corps grade*	Laboratoire ou à défaut département ECL	Etablissement
AURIOL Philippe	*professeur*	AMPERE	ECL
BEROUAL Abderrahmane	*professeur*	AMPERE	ECL
BURET François	*professeur*	AMPERE	ECL
JAFFREZIC-RENAULT Nicole	*directeur de recherche*	AMPERE	CNRS/ECL
KRÄHENBÜHL Laurent	*directeur de recherche*	AMPERE	CNRS/ECL
MARTELET Claude	*professeur*	AMPERE	ECL
NICOLAS Alain	*professeur*	AMPERE	ECL
NICOLAS Laurent	*directeur de recherche*	AMPERE	CNRS/ECL
SCORLETTI Gérard	*professeur*	AMPERE	ECL
SIMONET Pascal	*chargé de recherche*	AMPERE	CNRS/ECL
THOMAS Gérard	*professeur*	AMPERE	ECL
VOLLAIRE Christian	*professeur*	AMPERE	ECL
		Nbre Ampère 12	

HELLOUIN Yves	*maître de conférences*	DER EEA	ECL
LE HELLEY Michel	*professeur*	DER EEA	ECL
		Nbre DER EEA 2	

GUIRALDENQ Pierre	*professeur émérite*	DER STMS	ECL
VINCENT Léo	*professeur*	DER STMS	ECL
		Nbre DER STMS 2	

LOHEAC Jean-Pierre	*maître de conférences*	ICJ	ECL
MAITRE Jean-François	*professeur émérite*	ICJ	ECL
MARION Martine	*professeur*	ICJ	ECL
MIRONESCU Elisabeth	*professeur*	ICJ	ECL
MOUSSAOUI Mohand	*professeur*	ICJ	ECL
MUSY François	*maître de conférences*	ICJ	ECL
ZINE Abdel-Malek	*maître de conférences*	ICJ	ECL
		Nbre ICJ 7	

DAVID Bertrand	*professeur*	ICTT	ECL
		Nbre ICTT 1	

CALLARD Anne-Ségolène	*maître de conférences*	INL	ECL
CLOAREC Jean-Pierre	*maître de conférences*	INL	ECL
GAFFIOT Frédéric	*professeur*	INL	ECL
GAGNAIRE Alain	*maître de conférences*	INL	ECL
GARRIGUES Michel	*directeur de recherche*	INL	CNRS/ECL
GENDRY Michel	*directeur de recherche*	INL	CNRS/ECL
GRENET Geneviève	*directeur de recherche*	INL	CNRS/ECL
HOLLINGER Guy	*directeur de recherche*	INL	CNRS/ECL

JOSEPH Jacques	*professeur*	INL	ECL
KRAWCZYK Stanislas	*directeur de recherche*	INL	CNRS/ECL
LETARTRE Xavier	*chargé de recherche*	INL	CNRS/ECL
MARTIN Jean-René	*professeur émérite*	INL	ECL
O'CONNOR Ian	*professeur*	INL	ECL
PHANER-GOUTORBE Magali	*professeur*	INL	ECL
ROBACH Yves	*professeur*	INL	ECL
SAINT-GIRONS Guillaume	*chargé de recherche*	INL	CNRS/ECL
SEASSAL Christian	*chargé de recherche*	INL	CNRS/ECL
SOUTEYRAND Eliane	*directeur de recherche*	INL	CNRS/ECL
TARDY Jacques	*directeur de recherche*	INL	CNRS/ECL
VIKTOROVITCH Pierre	*directeur de recherche*	INL	CNRS/ECL

Nbre INL 20

CHEN Liming	*professeur*	LIRIS	ECL

Nbre LIRIS 1

BAILLY Christophe	*professeur*	LMFA	ECL
BERTOGLIO Jean-Pierre	*directeur de recherche*	LMFA	CNRS/ECL
BLANC-BENON Philippe	*directeur de recherche*	LMFA	CNRS/ECL
BOGEY Christophe	*chargé de recherche*	LMFA	CNRS/ECL
CAMBON Claude	*directeur de recherche*	LMFA	CNRS/ECL
CARRIERE Philippe	*chargé de recherche*	LMFA	CNRS/ECL
CHAMPOUSSIN J-Claude	*professeur émérite*	LMFA	ECL
COMTE-BELLOT geneviève	*professeur émérite*	LMFA	ECL
FERRAND Pascal	*directeur de recherche*	LMFA	CNRS/ECL
GALLAND Marie-Annick	*professeur*	LMFA	ECL
GODEFERD Fabien	*chargé de recherche*	LMFA	CNRS/ECL
GOROKHOVSKI Mikhail	*professeur*	LMFA	ECL
HENRY Daniel	*directeur de recherche*	LMFA	CNRS/ECL
JEANDEL Denis	*professeur*	LMFA	ECL
JUVE Daniel	*professeur*	LMFA	ECL
LE RIBAULT Catherine	*chargée de recherche*	LMFA	CNRS/ECL
LEBOEUF Francis	*professeur*	LMFA	ECL
PERKINS Richard	*professeur*	LMFA	ECL
ROGER Michel	*professeur*	LMFA	ECL
SCOTT Julian	*professeur*	LMFA	ECL
SHAO Liang	*chargé de recherche*	LMFA	CNRS/ECL
SIMOENS Serge	*chargé de recherche*	LMFA	CNRS/ECL
TREBINJAC Isabelle	*maître de conférences*	LMFA	ECL

Nbre LMFA 23

BENAYOUN Stéphane	*professeur*	LTDS	ECL
CAMBOU Bernard	*professeur*	LTDS	ECL
COQUILLET Bernard	*maître de conférences*	LTDS	ECL
DANESCU Alexandre	*maître de conférences*	LTDS	ECL
FOUVRY Siegfrid	*chargé de recherche*	LTDS	CNRS/ECL
GEORGES Jean-Marie	*professeur émérite*	LTDS	ECL
GUERRET Chrystelle	*chargé de recherche*	LTDS	CNRS/ECL
HERTZ Dominique	*past*	LTDS	ECL
ICHCHOU Mohamed	*professeur*	LTDS	ECL
JEZEQUEL Louis	*professeur*	LTDS	ECL
JUVE Denyse	*ingénieur de recherche*	LTDS	ECL
KAPSA Philippe	*directeur de recherche*	LTDS	CNRS/ECL
LE BOT Alain	*chargé de recherche*	LTDS	CNRS/ECL

LOUBET Jean-Luc	*directeur de recherche*	LTDS	CNRS/ECL
MARTIN Jean-Michel	*professeur*	LTDS	ECL
MATHIA Thomas	*directeur de recherche*	LTDS	CNRS/ECL
MAZUYER Denis	*professeur*	LTDS	ECL
PERRET-LIAUDET Joël	*maître de conférences*	LTDS	ECL
SALVIA Michelle	*maître de conférences*	LTDS	ECL
SIDOROFF François	*professeur*	LTDS	ECL
SINOU Jean-Jacques	*maître de conférences*	LTDS	ECL
STREMSDOERFER Guy	*professeur*	LTDS	ECL
THOUVEREZ Fabrice	*professeur*	LTDS	ECL
TREHEUX Daniel	*professeur*	LTDS	ECL
VANNES André-Bernard	*professeur émérite*	LTDS	ECL
VINCENS Eric	*maître de conférences*	LTDS	ECL
		Nbre LTDS 26	
	Total HdR ECL	91	

AUTORISATION DE SOUTENANCE

Vu les dispositions de l'arrêté du 7 août 2006,

Vu la demande du Directeur de Thèse

Monsieur P. FERRAND

et les rapports de

Monsieur J-G. PERSSON
Professeur - Machine Design - KTH (Royal Institute of Technology) - Brinellvägen 68 - SE-100 44 Stockholm - Suède

Et de

Monsieur D. VOGT
Docteur - HPT - KTH (Royal Institute of Technology) - Brinellvägen 68 - SE-100 44 Stockholm - Suède

Monsieur FERRIA Hakim

est autorisé à soutenir une thèse pour l'obtention du grade de **DOCTEUR**

Ecole doctorale MECANIQUE, ENERGETIQUE, GENIE CIVIL ET ACOUSTIQUE

Fait à Ecully, le 21 janvier 2011

P/Le Directeur de l'E.C.L.
La Directrice des Etudes

M-A. GALLAND